Circumstellar Material in Young Stellar Objects

Circumstellair materiaal in jonge stellaire objecten
(met een samenvatting in het Nederlands)

Academisch Proefschrift

ter verkrijging van de graad van doctor aan de Universiteit van Amsterdam op gezag van de rector magnificus prof. dr. J.J.M. Franse ten overstaan van een door het college voor promoties ingestelde comissie in het openbaar te verdedigen in de Aula der Universiteit, op dinsdag 14 september 1999 te 15.00 uur

door

Mario Enrico van den Ancker

geboren te Amsterdam

Promotiecomissie:

Promotor:	prof. dr. A.G.G.M. Tielens
Co-promotor:	prof. dr. L.B.F.M. Waters
Overige leden:	prof. dr. E.F. van Dishoeck
	dr. H.F. Henrichs
	prof. dr. E.P.J. van den Heuvel
	prof. dr. P.S. Thé
	prof. dr. C. Waelkens
	dr. P.R. Wesselius

Faculteit der Wiskunde, Informatica, Natuurkunde en Sterrenkunde
Universiteit van Amsterdam

ISBN: 9-05776-027-4

Cover illustration: Reproduction of Palomar Observatory Sky Survey print of the BD+40°4124 region (cf. Chapter 8)

Contents

Chapter 1

Star Formation: An Overview

1.1 Introduction

One of the basic tasks of science is to understand how we and the world around us have come into existence. The thesis presented here deals with a small part of that question: how do stars form? In the eighteenth century the French astronomer Laplace asked himself the same question, and came up with the answer we still consider essentially correct today: stars form out of large clouds of gas (and dust) in interstellar space which collapse under the influence of their own gravity. However, after more than two centuries of research many important questions regarding the star formation process, and the fundamentals of planet formation, still remain unanswered. Nonetheless, the rapid progress in our knowledge of star formation in the last few decades, mainly due to the availability of a new generation of astronomical instruments, as well as a number of surprising discoveries, show that we are now at the brink of a fundamentally better understanding of the origins of our own solar system. Therefore the subject of star formation is one of the most exciting fields of astrophysics today.

Today, the standard picture of the process of low-mass star formation (Shu et al. 1987) is divided in four distinct phases. First, a number of dense cores develop within a molecular cloud. At some point, the dense cores collapse to form embedded protostars which accumulate material by accretion from the surrounding cloud. As the embedded protostars accrete mass, they also lose mass due to a strong stellar wind, which eventually leads to the dispersion of the reservoir of mass from the protostellar envelope and the end of accretion. The former protostar, now a pre-main sequence star, begins to contract slowly, increasing its central temperature until hydrogen ignition takes place and it has become a stable star on the main sequence.

Collapse of a cloud naturally leads to disk structures as material with significant angular momentum will be unable to fall directly onto the central star, and will instead accumulate in a rotating disk. The star can only accrete this material if the disk can shed angular momentum; as the mass moves inwards, the angular momentum has to move outwards and be stored in larger rotating bodies like the planets in our own solar system. Although the detailed physics behind this is by no means clear, there is strong observational evidence that in all astronomical objects where accretion disks

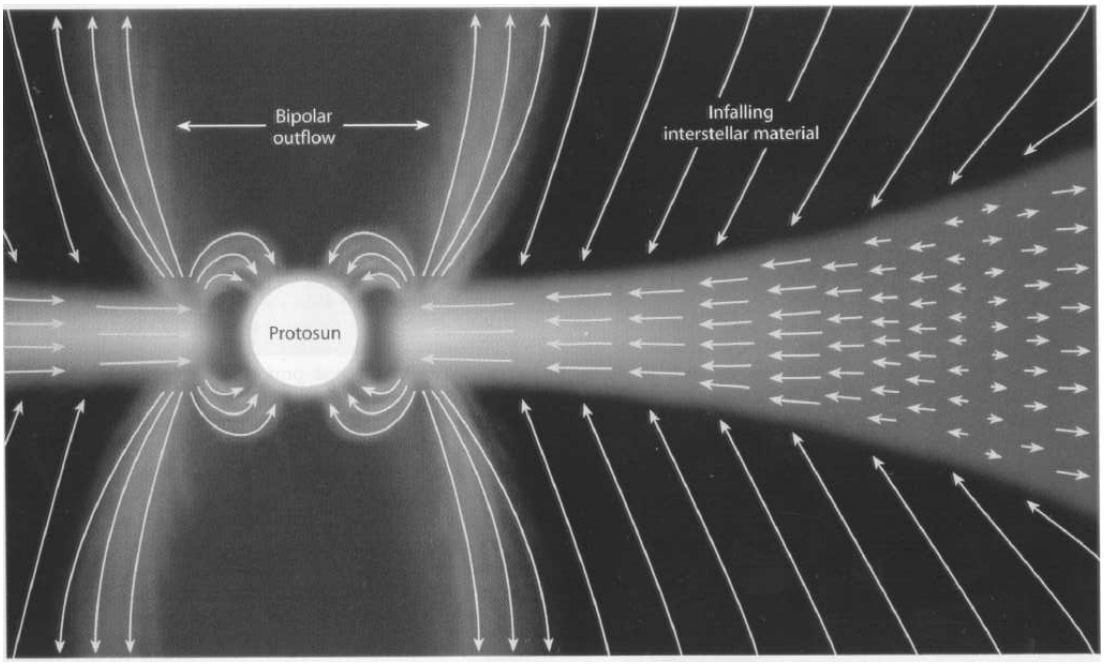

Fig. 1.1. Schematic picture of the environment of a young stellar object. Infall of matter onto the circumstellar disk, accretion onto the central star and accretion-driven outflow are indicated by arrows [from Wood 1997].

are formed, energetic ejecta of material along the rotation axis of the system are also present. The ejecta can also carry away part of the angular momentum of the system, allowing accretion of mass onto the central object. These jets, commonly seen in young stellar objects (YSOs), may accelerate ambient molecular material and drive a more or less collimated bipolar molecular outflow. A schematic picture of this view of the environment of a YSO is shown in Fig. 1.1.

1.2 Pre-main sequence stellar evolution

The first numerical simulations of stellar evolution were done by Henyey et al. (1955). They followed the evolution of pre-main sequence stars to the main sequence, showing that a young star remains nearly constant in brightness with increasing temperature as it contracts towards the main sequence. Later, Hayashi (1961) pointed out that these evolutionary tracks were incomplete since they assumed the star would be fully radiative until the onset of core hydrogen burning, whereas the star would be fully convective prior to the radiative phase described by Henyey et al. Subsequent pre-main sequence evolutionary computations (Hayashi 1961; Iben 1965; Larson 1969) started at low temperature and high luminosity and are vertical in the Hertzsprung-Russell (HR) diagram until the luminosity of the star drops below the stability criterion. At this point, the star becomes radiative and evolves along a nearly horizontal track to the main sequence. The starting point in these pre-main sequence evolutionary calculations will be determined by the outcome of the cloud collapse phase, which was

not incorporated in these early models, but was assumed to be at low temperature and high luminosity. The first one to incorporate the physics of cloud collapse into a numerical evolution code was Shu (1977), who showed that it would start in the cloud center and work from the inside-out, due to the limited sound speed in the cloud. The timescale for this collapse would be determined by the accretion rate, which is dependent on the local sound speed.

Shortly after the Shu model gained general acceptance as the standard star formation scenario, Cohen & Kuhi (1979) constructed HR diagrams for several nearby star forming regions, and showed that, even in the youngest systems, there is an upper bound on the Hayashi tracks above which stars are not found. Stahler (1983) suggested that pre-main sequence stars would be first seen in a narrow locus, the "birthline", determined by the mass-radius relationship of the protostar at the end of accretion, and equated the birthline with the upper limit seen by Cohen & Kuhi. Stahler (1988) later showed that deuterium burning would start during the accretion process and continue until after accretion ends. This has important consequences for protostellar evolution, since it will keep the central object convective: the newly accreted matter will be brought deep into the interior of the star, providing new fuel for the deuterium burning. The situation for high-mass stars is somewhat different: the collapse timescale is longer than the pre-main sequence contraction timescale so that the star reaches the main sequence before the accretion is complete. Stars more massive than the limit for which this will be the case will not be observable in their pre-main sequence phase. Depending on the accretion rate (which is assumed constant and independent of the stellar mass in the evolutionary model computations), the mass limit at which this would happen is now estimated to be between 7 and 15 solar masses (Palla & Stahler 1992, 1993).

With this general picture of star formation in mind, Lada & Wilking (1984) grouped infrared sources in the ρ Ophiuchus cloud into three now commonly used classes, based on their spectral energy distribution (SEDs). Class I sources have strong infrared excesses (i.e. broader than a blackbody), peaking at far-infrared wavelengths. The optical source is heavily embedded and is generally not visible in the optical. Class II sources are stars with strong infrared excesses, but with flat or decreasing slopes (in λF_λ) at wavelengths longer than 2 μm. Class II sources are usually optically visible and many show emission lines. Class III objects have decreasing slopes in their infrared energy distribution, consistent with a reddened stellar photosphere. These sources are also optically visible, and many still show traces of youth in their spectra. An illustration of typical SEDs of these Lada classes for YSOs is given in Fig. 1.2. In recent years, some authors have extended this classification scheme by introducing Class 0 sources (e.g. André et al. 1999 and references therein): sources which are only visible at submm wavelengths. These are believed to be the cores of parental clouds of gas and dust which are heated up by gravitational contraction, and in which protostars are forming.

Adams & Shu (1985, 1986) developed models for the spectral energy distribution of protostars and showed they are consistent with Class I spectra. Adams et al. (1987) extended this argument to strengthen the connection between the sequence of Class I, Class II, Class III and the evolutionary stages of embedded protostar, exposed pre-

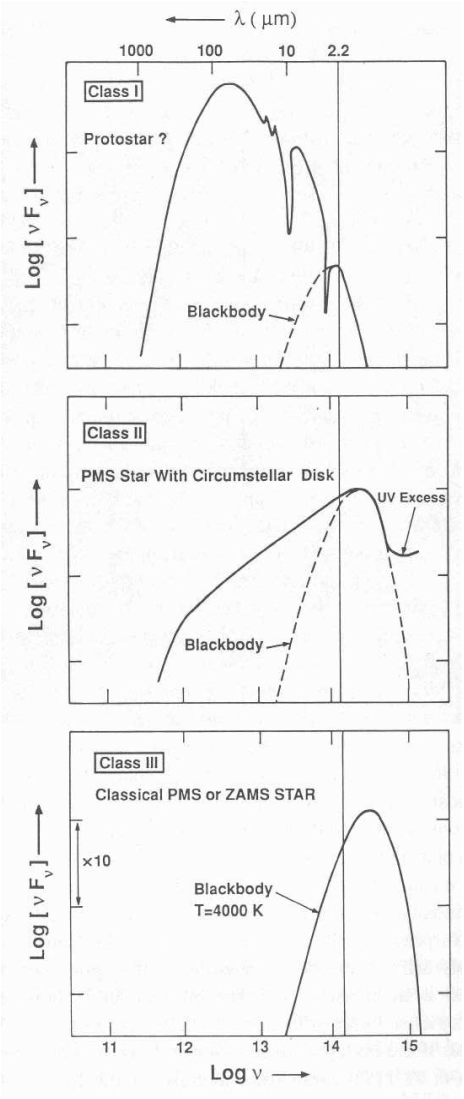

Fig. 1.2. Classification scheme for YSO spectral energy distributions [from Lada 1987].

main sequence star with circumstellar material, and isolated pre-main sequence star. They also showed that to fit the energy distribution of a Class II source, it is essential to include a disk in the system. While these and other models generally compare well with the observed shape of the SEDs, they do not agree at a high level of precision. Existing models still make too many simplifying assumptions about the geometry of the emitting material to achieve a high level of accuracy (see e.g. Calvet et al. 1994).

1.3 Molecular clouds

The regions of enhanced density in the interstellar medium known as molecular clouds are the birthgrounds of young stars. Historically, molecular, or dark, clouds were discovered through the obscuration of the light of background stars by the dust associated

with the cloud. However, the study of molecular clouds did not reach its full growth until it became possible to observe mm and submm transitions of molecular species such as CO and NH_3 (Cheung et al. 1968; Wilson et al. 1970; Kutner et al. 1977), allowing more detailed studies of the kinematics and distribution of the molecular gas to be made. Today, more than 100 different molecular species have been found to exist in molecular clouds.

Molecular clouds are usually divided in two groups. Most stars in our galaxy are thought to have formed in a Giant Molecular Cloud. These are located in the spiral arms of our galaxy and have masses up to 10^6 $M_\odot$. The Orion complex is the best-known and nearest example of such a Giant Molecular Cloud. However, stars are also found to form in smaller molecular clouds, not necessarily confined to the spiral arms, of which the Taurus-Auriga complex is the best studied example. These smaller molecular cloud complexes can probably survive one or more rotation periods of our galaxy and thus exist long enough to allow the star formation process to take place (e.g. Shu et al. 1973).

The material in a molecular cloud is not distributed in a homogeneous way. Giant molecular clouds are actually cloud complexes, composed of smaller clouds with masses 10^3–10^4 $M_\odot$, in which the density is an order of magnitude higher than in the inter-cloud medium. Myers & Benson (1983) were the first to perform a systematic search for denser cores of molecular gas in star forming regions. These cores, with masses between 1 and 100 $M_\odot$ are now believed to be on the verge of gravitational collapse and eventually will form a single star. They are often clustered and may share a common envelope.

Star formation occurs when a clump in a molecular cloud collapses under the influence of its own gravity. However, gravitational collapse is an efficient process, so from a theoretical point of view no such clumps should be visible if the cloud had no means to support itself. The fact that we still observe clumps in molecular clouds means that some form of cloud support must be present. It is believed that the process known as ambipolar diffusion is the main mechanism which slows down cloud collapse. In the presence of magnetic fields, the bulk of the material, which is neutral, will still try to collapse under its own gravity. However, it will interact with a trace fraction of ionized material, supported by the magnetic field, and the neutrals can be supported against their self gravity through the frictional drag they experience as they slip relative to the ions. Due to ion-neutral collisions, magnetic energy is slowly lost and eventually cloud collapse will take place, although at a much slower rate than expected from gravity alone. For a more detailed description of the physical conditions in molecular clouds the reader is referred to the recent work by Evans (1999).

1.4 T Tauri Stars

When spectrographs became available in the last century, a class of stars was found, often located in nebulous regions and showing variations in brightness, which have late-type absorption spectra on which strong emission lines of hydrogen, calcium and

iron are superposed. Soon after their discovery, it was speculated that these T Tauri stars, named by Joy (1945) after the brightest member of the class, could be identified with young stars, still contracting towards the main sequence. However, definitive proof of their pre-main sequence nature had to wait until Walker (1956) made the first colour-magnitude diagrams of star forming regions that were sufficiently accurate to prove the presence of late-type stars located above the main sequence. Walker noted that many of these pre-main sequence stars were T Tauri stars and suggested that all T Tauri stars might be low-mass pre-main sequence stars.

Since then, the T Tauri stars have been intensely studied. Optical studies of emission lines have shown that matter is not only being accreted, but that some lines also exhibit P Cygni profiles, characteristic of mass loss. Absorption line spectra of the central late-type star often appear superposed on a blue continuous spectrum, an effect known as veiling. After the development of UV and infrared instrumentation in the 1960's and 1970's, it was shown that T Tauri stars also possess both excess ultraviolet and infrared emission above photospheric levels. In the classification scheme of young stars they are Class II sources. Subsequent modelling successfully explained the total energy distribution of T Tauri stars as arising in a late-type star which is accreting matter through a circumstellar disk. The infrared excess is believed to come from continuum emission from gas as well as from heated dust particles in the disk. The excess ultraviolet emission is believed to arise in the boundary layer between the star and the disk, where the gas is heated to high temperatures by frictional forces. Both accretion disk and boundary layer will give rise to the blue continuum in the optical responsible for the veiling. The amount of ultraviolet excess is correlated with the strength of the emission lines and so does, to a lesser extent, the near-infrared part of the infrared excess. In T Tauri stars, emission lines like the Balmer lines are usually explained as arising in a strong wind, either from the disk or from the central star, although some lines, most noticeably the forbidden atomic transitions, probably arise in the surface layers of the circumstellar disk. The correlation between excesses and emission line strength therefore suggests that in T Tauri stars outflow strength depends on accretion rate.

The advent of X-ray astronomy showed the T Tauri stars to be strong X-ray emitters, linked to strong magnetic activity (flares) on the stellar surface. It also revealed a population of late-type field stars in star forming regions which show very weak, if any, emission lines, no ultraviolet excess, and little or no infrared excess and yet show comparable levels of X-ray emission to the T Tauri stars. These are now usually referred to as weak-line T Tauri stars (WTTS), whereas the T Tauri stars with strong emission lines are nowadays often referred to as classical T Tauri stars (CTTS). It should be stressed, however, that in reality there exists a continuous range of emission line strengths in T Tauri stars between the extreme cases of CTTS and the WTTS, so the distinction between the two groups is somewhat artificial. The distribution of WTTS and CTTS in the HR diagram was shown to be not significantly different. The discovery of the WTTS thus showed that the low-mass pre-main sequence population of star forming regions is not limited to stars with accretion disks, but also contains stars which are essentially stripped of all circumstellar material.

From the veiling and the optical emission lines, a large spread in accretion rates (typically 10^{-6} to 10^{-8} $M_\odot$ yr^{-1}) was derived for classical T Tauri stars of similar ages, suggesting that the accretion rate is not constant in time. This suggestion is confirmed by the existence of an interesting subgroup of the T Tauri stars, the FU Orionis stars or FUORS. First identified as a class of young stars with large increases (about 4^m) in optical light lasting several decades (Herbig 1966, 1977), they are now recognized as systems in which the mass accretion rate through the circumstellar disk increases by orders of magnitude to $\approx 10^{-4}$ $M_\odot$ yr^{-1} during a short period of time, probably due to thermal instabilities in the accretion disk. For further details on T Tauri and FU Orionis stars, the reader is referred to the excellent reviews by Bertout (1989) and Hartmann & Kenyon (1996).

1.5 Herbig Ae/Be Stars

Soon after Walker's (1956) discovery that T Tauri stars are low-mass pre-main sequence stars, Herbig (1960) identified a class of "Be and Ae stars associated with nebulosity" which he suggested to be likely high-mass counterparts to the T Tauri stars on the basis of their general similarity to the T Tauri stars and their spectral similarities with each other. For an object to be included in this class of stars, now known as Herbig Ae/Be stars (HAeBes), Herbig proposed the following membership criteria: (1) spectral type earlier than F0, (2) presence of emission lines, (3) located in an obscured region, and (4) illuminating a fairly bright reflection nebula.

For a long time, the pre-main sequence nature of the HAeBes was doubted because the early stellar evolution models suggested that stars heavier than 3–6 solar masses would have collapse timescales longer than the pre-main sequence contraction timescale and would therefore not be observable in their pre-main sequence phase. This, and the fact that the proposed membership criteria would not only select young stars, but also some classes of post-main sequence objects (as was already pointed out by Herbig himself), made an entire generation of astronomers virtually ignore the existence of Herbig Ae/Be stars. Not until the recognition of the nature of the observational birthline for intermediate-mass stars by Stahler in 1988, was it realized that the upper mass limit for which a star ends up on its Hayashi track, is in fact much higher than that predicted by the early evolutionary models and intermediate-mass pre-main sequence stars do in fact exist.

Nonetheless, the original HAeBe membership criteria were clearly not sufficient to select only intermediate-mass pre-main sequence stars. Also, an increasing number of stars which clearly resembled the Herbig Ae/Be stars, but were located in more isolated regions, were found by the IRAS satellite as well as in ground-based surveys (Hu et al. 1991; Oudmaijer et al. 1992; Bogaert 1994; Thé et al. 1994), so it became evident that Herbig's original criteria did not select all intermediate-mass young stars. Therefore many subsequent authors have re-interpreted the criteria for membership of the Herbig Ae/Be stellar group and even use the term more loosely to indicate young intermediate-mass stars. Probably the most reliable membership criteria de-

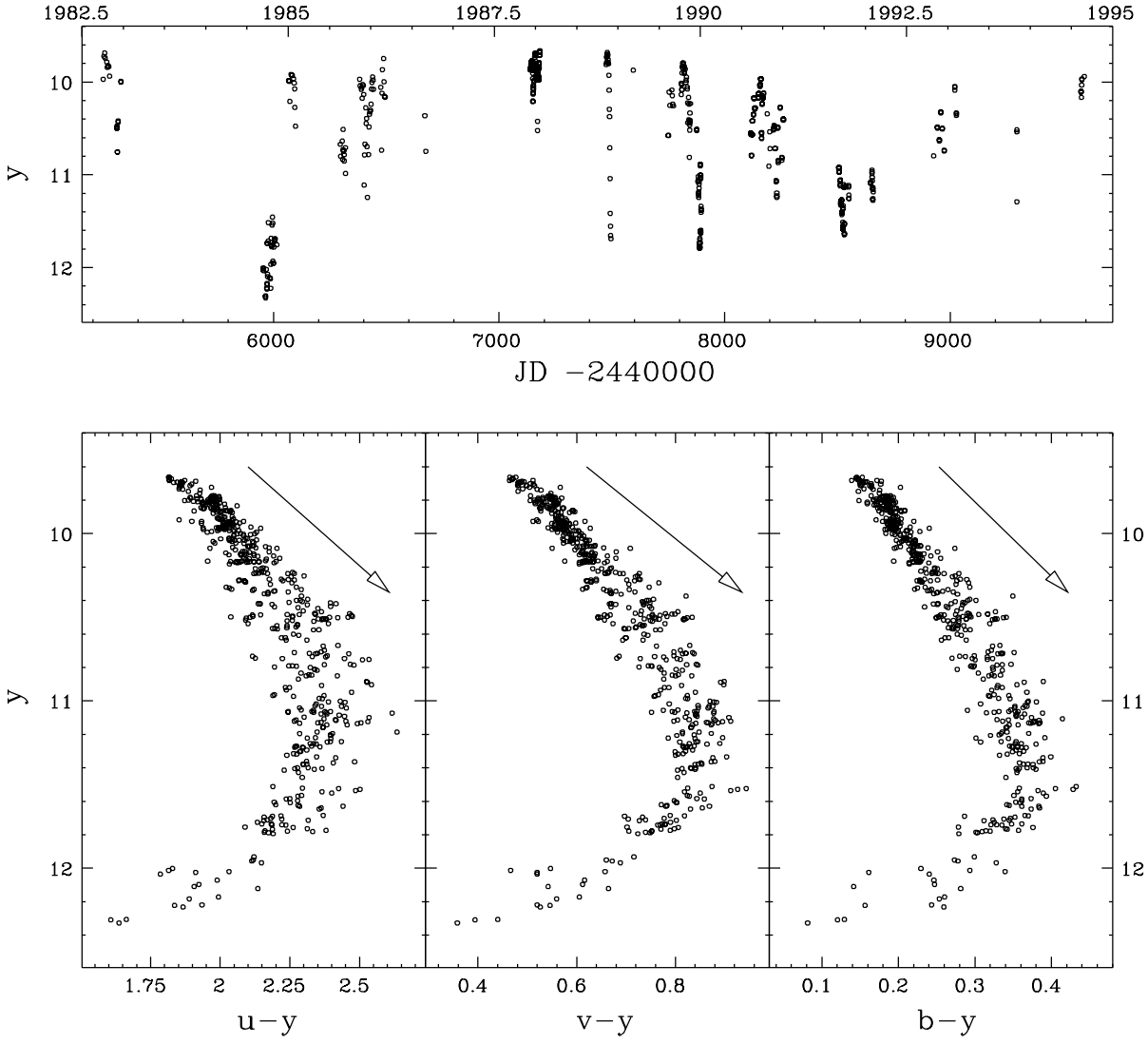

Fig. 1.3. Lightcurve (top) and colour-magnitude diagrams (bottom) of the Herbig Ae star UX Ori in the Strömgren $uvby$ system. Data courtesy of ESO's long-term photometry of variables programme (Manfroid et al. 1991, 1995; Sterken et al. 1993, 1995).

fined nowadays are those given by Waters & Waelkens (1998) in their review of Herbig Ae/Be stars: (1) spectral type A or B with emission lines, (2) presence of infrared excess due to hot or cool circumstellar dust or both, and (3) luminosity class III to V. In the thesis presented here we will adhere to this definition.

One of the main criteria for membership of the Herbig Ae/Be stellar group is the presence of emission lines, especially in the Balmer lines of hydrogen. Apart from these, many HAeBes also show lines like Ca II, O I, [O I], [N II], as well as many metallic lines in emission. The first systematic investigation of the line profiles of HAeBes was done by Finkenzeller & Mundt (1984), who found that most have a "double-peaked" Hα profile, consisting of a, sometimes shifted, emission peak with an almost unshifted absorption component superposed. However, some stars with single emission peaks, as well as HAeBes which show P Cygni and inverse P Cygni profiles were also found. Later, it became clear that in at least some cases these line profiles are highly variable on time scales of days (e.g. Grinin et al. 1994).

Most of the emission lines observed in the HAeBe spectra can be well understood as arising in a stellar wind, although in analogy with the T Tauri stars some, most noticeably the forbidden atomic lines, are believed to be formed at the surface layer of the circumstellar disk. The emission lines are seen superposed on an absorption spectrum of a stellar photosphere. Since the contrast in brightness between accretion disk and stellar photosphere is much higher in Herbig Ae/Be stars than in T Tauri stars, veiling in HAeBes is limited to a small number of extremely rapidly accreting systems, possibly going through a prolonged FUOR-like accretion phase. However, for the vast majority of HAeBes the absorption line spectrum is entirely photospheric (e.g. Böhm & Catala 1993; Corcoran & Ray 1997).

One of the best studied properties of the HAeBe stellar group is the photometric variability exhibited by many, though not all, HAeBes. This may either be explained by rotational modulation of cool spots on the stellar surface, variable accretion, or by variable amounts of circumstellar extinction (Bibo & Thé 1991; Herbst et al. 1994). A particularly interesting subgroup of the Herbig Ae/Be stars are the UX Orionis-type stars, or UXORs. These are systems which show deep (up to $\Delta V \approx 3^{\mathrm{m}}$), irregular, variations in brightness. The aperiodic minima of UXORs have faster declines than recoveries and there usually is a very tight correlation of the magnitude with the colours, which get redder as the star fades. This behaviour is characteristic of variable, presumably circumstellar, extinction of the starlight by dust particles. During very deep minima, the photometric behaviour of UXORs may change and there is a colour reversal or blueing effect: the colours get bluer as the star fades even further. Furthermore, there exists a perfect anticorrelation between the brightness and the degree of linear polarization for UXORs (e.g. Grinin et al. 1991).

The photometric behaviour of UXORs can easily be understood by assuming the presence of patchy dust clouds, orbiting in Keplerian orbits around the star (Wenzel 1968; Grinin 1988). When such a dust cloud passes our line of sight, the light from the star becomes fainter and redder due to extinction by the particles in the dust cloud. Sub-μm dust grains in the dust clouds will also scatter the starlight, providing a constant, faint, blue emission. Below some brightness, the scattered blue light will start to

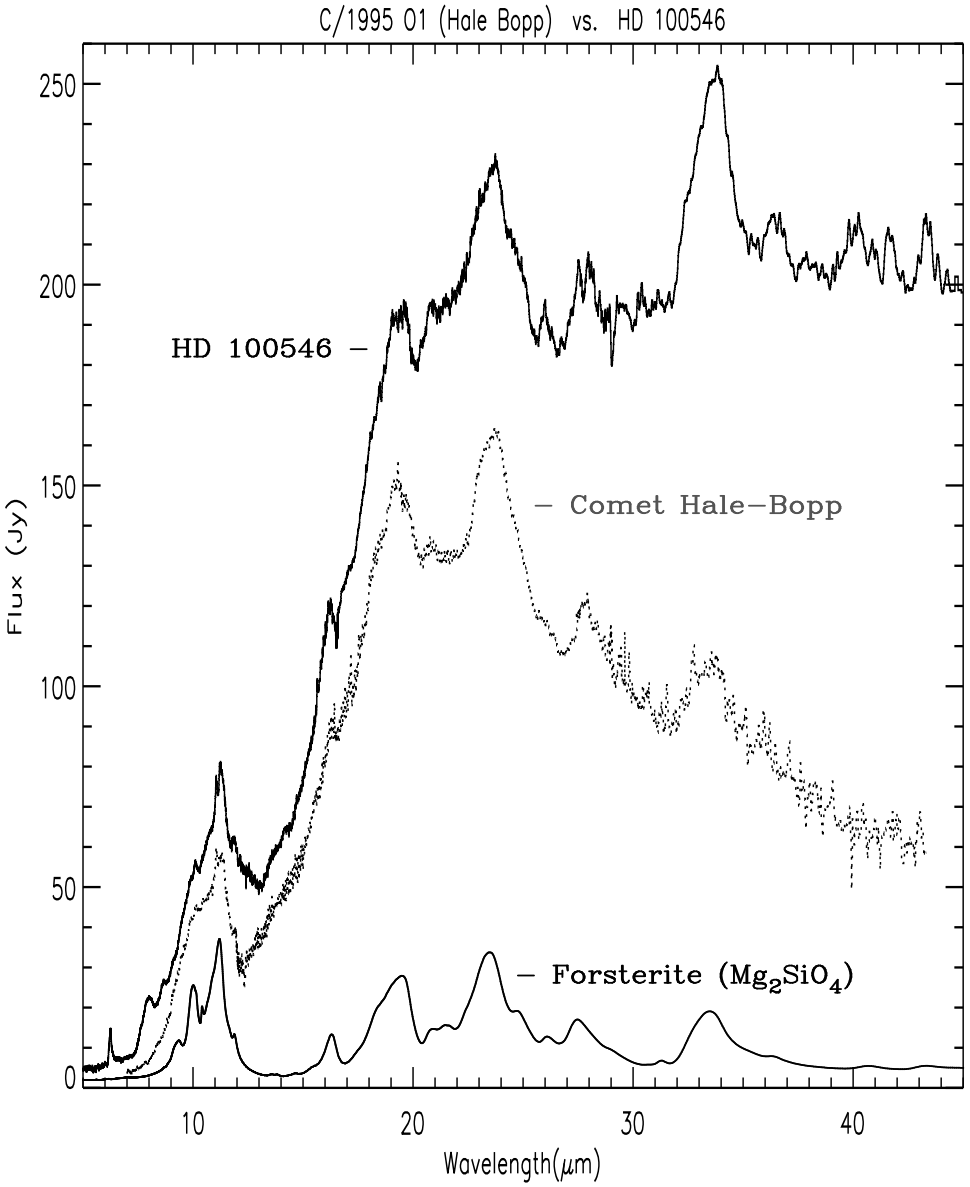

Fig. 1.4. ISO spectra of HD 100546 (top curve) compared to those of comet Hale-Bopp (middle) and lab spectra of Forsterite (bottom curve) [adapted from Malfait et al. 1998].

dominate, and produce the observed blueing effect. The scattered light will also have a higher degree of polarization than the light that reaches us directly from the star, so this picture will also explain the observed anticorrelation between brightness and degree of linear polarization. Deviations from the perfect correlation between magnitude and colour predicted by this model can be accounted for by additional variations due to cool spots or variable accretion. The photometric behaviour of UXORs is illustrated in Fig. 1.3, where we show a lightcurve and colour-magnitude diagrams of the UXOR prototype UX Ori.

Studies of the photometric variability of Herbig Ae/Be stars by Finkenzeller & Mundt (1984) and Bibo & Thé (1991) have shown that the UXOR phenomenon is limited to HAeBes with a spectral type later than A0. This result is still not well understood. It has been suggested, however, that this is merely a selection effect (Grady et al. 1996). In Chapter 3 it will be shown that this is not the case, and we will offer an explanation for the fact the the UXOR phenomenon is only observed in Herbig Ae stars by showing that it is limited to giants.

At wavelengths longer than about 1 μm HAeBe stars show strong excess emission above photospheric levels, due to circumstellar dust heated by the central star. For a long time, the geometry of this material has been a controversial subject. Whereas one would expect such hot dust ($\approx$ 1500 K) to be located close to the star, where it can only be stable in a disk-like geometry, some authors have proposed that this emission arises in an extended dust shell containing very small dust grains not in thermal equilibrium with the stellar radiation field (Hartmann et al. 1993; Natta et al. 1993). However, submm interferometry in the ^{13}CO 1–0 transition by Mannings & Sargent (1997) clearly show the molecular emission to be blue-shifted, indicative of approaching gas, on one side of the star, whereas red-shifted emission (receding gas) is strictly confined to the other side of the star. These results are difficult, if not impossible, to explain with anything but a rotating disk-like structure, so it appears that the presence of circumstellar disks around HAeBes is now proven beyond doubt. However, more extended envelopes are also present in some systems and will show up as an additional cool component in the energy distribution.

One of the most exciting recent developments in the field of Herbig Ae/Be stars is the progress in the field of infrared spectroscopy. Ground-based spectroscopy as well as the results from the IRAS mission have shown that both C-rich (as seen in Polycyclic Aromatic Hydrocarbons; PAHs) and O-rich (as seen in silicates) dust particles are a common component in the circumstellar environment of HAeBes. In particular, many UXORs show the 10 μm amorphous silicate feature strongly in emission. However, after the launch of the *Infrared Space Observatory* (ISO), our understanding of the circumstellar dust in these objects has become more blurred, since it was shown that the exact nature of the circumstellar dust of HAeBes varies widely and dust properties do not correlate well with one another (c.f. Chapter 5). An especially spectacular ISO result is the infrared spectrum of the Herbig B9 star HD 100546 (Waelkens et al. 1996; Malfait et al. 1998; Fig. 1.4). In this object, part of the circumstellar dust must consist of magnesium-rich crystalline olivines, the mineral forsterite (Mg_2SiO_4). This is exactly the same material as is found in comets in our own solar system (e.g. Crovisier et al.

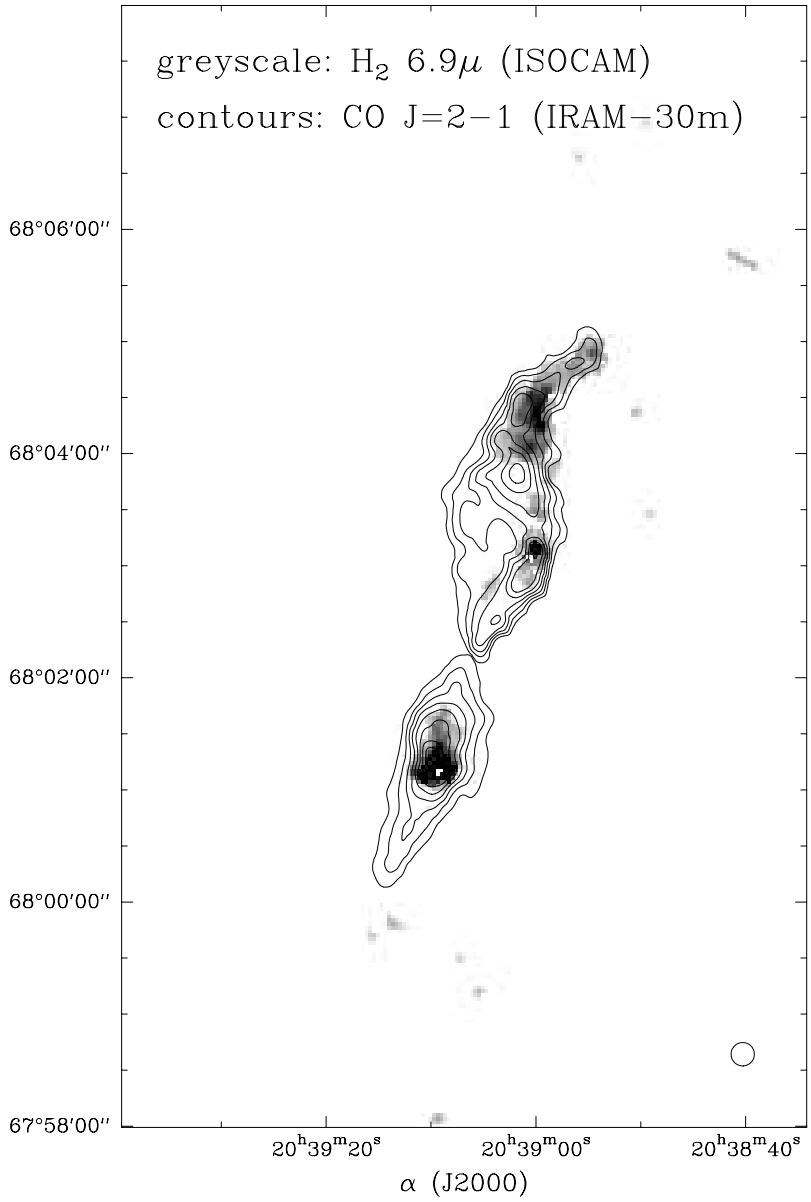

Fig. 1.5. Molecular outflow in L1157, mapped in H_2 0–0 S(5) emission with ISOCAM (grey scale). Superposed are contours of the CO 2–1 emission. The circle at the bottom right corner shows the beam size of the CO observations [from Richer et al. 1999].

1997), suggesting that the processing of circumstellar dust in the primitive solar system bears similarity to that in HAeBes.

The general picture of the phenomena seen in Herbig Ae/Be stars outlined above is not significantly different from that seen towards T Tauri stars, although both groups are fairly heterogeneous: strongly accreting HAeBes such as V380 Ori or Z CMa show a high degree of analogy to the classical T Tauri stars, whereas the HAeBe systems in which accretion has nearly stopped, such as AB Aur or UX Ori, are reminiscent of T Tauri stars with a low degree of veiling. The influence of the fundamental difference between Herbig Ae/Be and T Tauri stars, the presence of a convective atmosphere, does not seem to affect the evolution of the circumstellar disk. The weak-line T Tauri stars do not have a direct analogue in the formal Herbig Ae/Be stellar group, but studies of the HR-diagram of young OB associations (e.g. van den Ancker et al. 1997; de Winter et al. 1997) show that typically 90% of pre-main sequence intermediate-mass cluster members are not recognizable as HAeBes. These may be the analogues of the WTTS, although they cannot be easily recognized as being young in X-rays because of the absence of a convective envelope. As a final note, we refer the reader to the recent reviews by Pérez & Grady (1997) and by Waters & Waelkens (1998) for a more detailed overview of Herbig Ae/Be stars.

1.6 Outflows and jets

It has been known for a long time that mass loss is a common phenomenon in pre-main sequence stars. Optical spectra of T Tauri stars showed early on the presence of strong winds (Joy 1945; Herbig 1960; Kuhi 1964). In 1971, Luyten pointed out the large proper motion of small bullets of intense nebular emission, known as Herbig-Haro objects, associated with the dark cloud L1551. Nowadays these Herbig-Haro objects are understood as fast-moving (a few hundred km s^{-1}) bullets of shocked gas in the outflow of a young star. Cudworth & Herbig (1979) confirmed the Luyten (1971) result and made several suggestions for the cause of the large proper motion, including the suggestion that the objects were moving away from the position of the infrared source L1551 IRS 5.

It is ironic that a search for *infalling* material around protostellar candidates resulted in the first discovery of molecular *outflows*. In a classic paper, Snell et al. (1980) reported the discovery of a bipolar CO outflow from L1551 IRS 5 and presented all of the modern components of an accreting YSO system: large lobes of the molecular outflow driven by a fast, ionized wind collimated by a thick torus of material surrounding the central star. Once this model was presented, many objects, in a luminosity range as wide as 0.2 to 10^6 $L_\odot$, were found to drive molecular outflows. They usually have a bipolar morphology, but often appear poorly collimated in CO. In Fig. 1.5 we show an example of a bipolar molecular outflow, observed in CO in the submm and in pure rotational transitions of H_2 with ISO.

There is strong observational evidence that accretion is linked to outflow phenomena. Deduced orientations of outflows are invariably found to be perpendicular to the

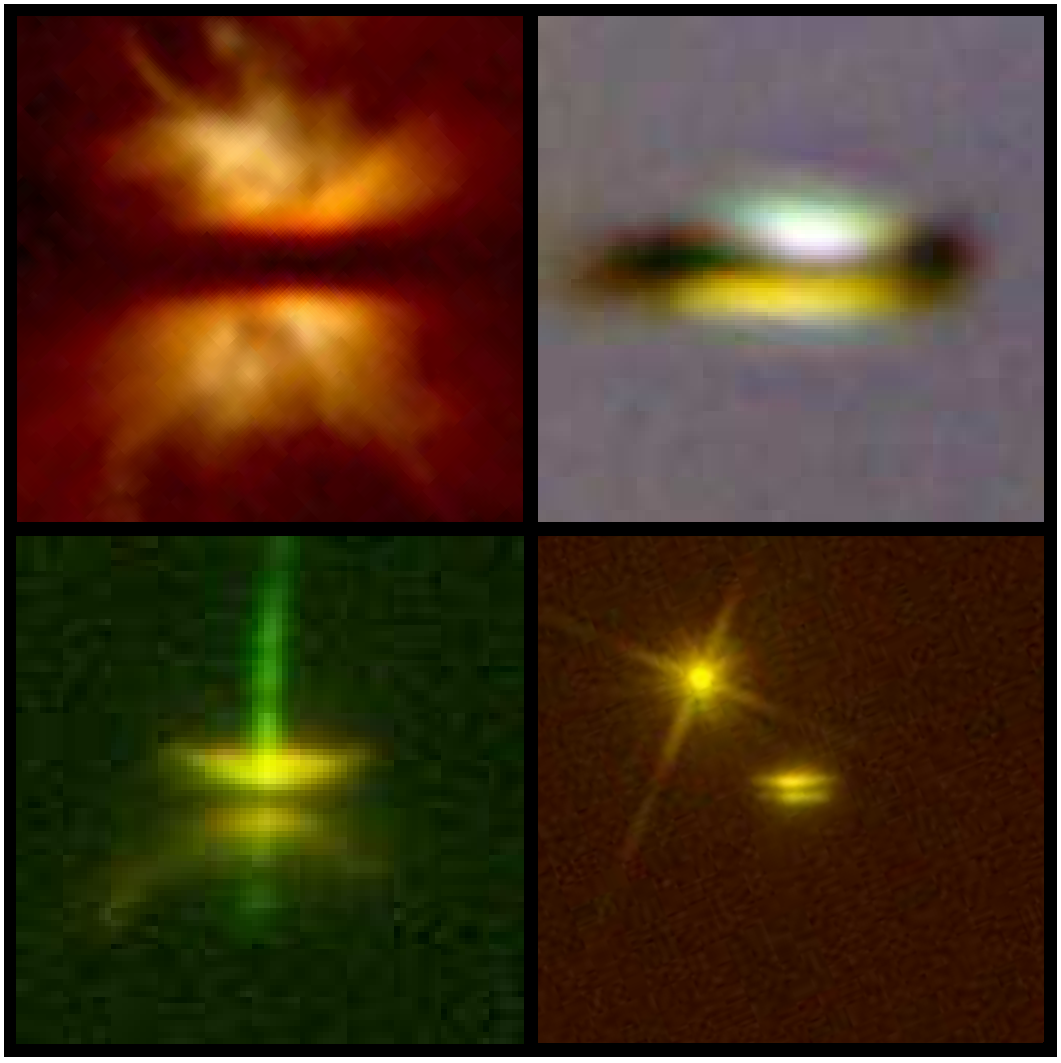

Fig. 1.6. Continuum HST images of the edge-on disks surrounding IRAS 04302+2247 (top left), Orion 114-426 (top right), HH Tau (bottom left) and HK Tau/c (bottom right). Each panel is 1200 AU squared and all intensities are logarithmically scaled [from McCaughrean et al. 1999].

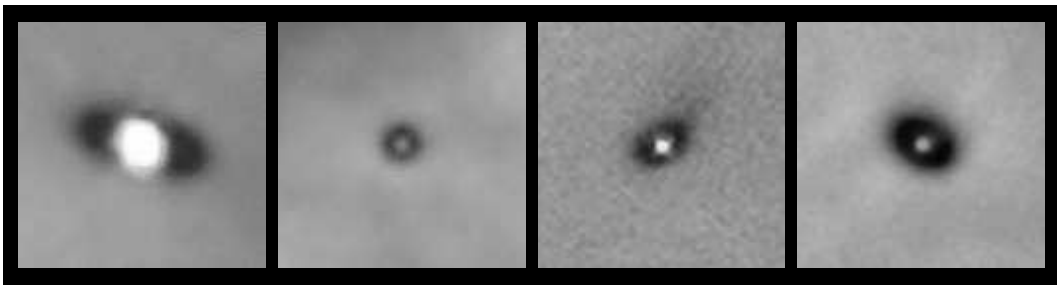

Fig. 1.7. HST images of four silhouette disks in the Orion nebula. All are seen against the nebular Hα background. Each panel is 900 AU squared [from McCaughrean & O'Dell 1996].

rotation axis of an accreting source, with a good correlation between indicators of accretion activity and the mass loss rate. This is an important result, since the end of accretion is one of the most important phases in the formation of a young star. The point at which accretion stops determines the mass of the star which will develop. The accretion process is thought te be interrupted by the presence of a strong outflow as the source cloud from which the circumstellar disk is being replenished is disrupted. Hence the end of accretion also marks the transition between the embedded and exposed phases of evolution. The transition between these two stages is apparently quite rapid, as evidenced by the lack of sources with very flat far-IR SEDs.

Perhaps the most spectacular visual phenomena related to star formation are optical jets of ionized gas. These have much smaller opening angles (typically a few degrees) than the molecular outflows and usually show a knotty structure. They often contain Herbig-Haro objects and may extend many parsecs away from the driving source. Occasionally they are also seen in extremely high velocity molecular material (e.g. Bachiller et al. 1990). These fast jets from YSOs are usually interpreted as accretion-powered, centrifugally driven winds from magnetized accretion disks (e.g. Königl & Pudritz 1999). Recent results (see for example the review by Richer et al. 1999) suggest that at least for low-mass systems this jet may drive the molecular outflow. In turn, this may accelerate ambient molecular cloud material, causing a shock if the material reaches supersonic velocities. In Chapters 7 to 10 we will study the infrared emission line spectra of a number of YSOs and show that these are commonly dominated by material heated in such a shock.

1.7 Protoplanetary disks

At about the same time that outflows were recognized, observational evidence was mounting for the presence of disks in YSO systems. These disks may be present in a variety of shapes and sizes. On the largest scales, the envelope of molecular gas may be rotating slowly around the central object. Evidence for such large scale (10^3–10^4 AU) bulk motions has been seen in the CO velocity fields for several embedded YSOs (see Staude & Elsässer 1993 for a review). More recent CO submm-interferometry has also revealed the presence of much smaller (a few hundred AU) rotating structures around several optically visible YSOs (Mannings & Sargent 1997), which may probe the circumstellar disk directly.

The spectral energy distribution models of Adams & Shu (1985) implied the presence of warm circumstellar disks to explain the amount of mid-IR emission. The large observed amounts of mid- and far-IR emission in systems with relatively low extinction to the central star also imply a disk geometry. Furthermore, early millimeter continuum interferometry (Keene & Masson 1990; Lay et al. 1994) revealed compact (100 AU size) structures which were strongly suggestive of disks. Several systems such as L1551 IRS 5 and R Mon show evidence for axisymmetric dust distributions in the pattern of light reflected off nearby reflection nebulae. These patterns are explained as shadow patterns cast by a star shining through the polar regions of a disk-like struc-

ture. Polarization observations show that in several systems, the bulk of the emission is seen only through scattering, while the direct line of sight is heavily obscured (Bastien 1989 and references therein). The shape of emission line profiles, in which only blue-shifted wings are seen, particularly in forbidden lines formed relatively far from the central star, are further evidence of obscuring circumstellar disks (e.g. Mundt 1984). These pieces of evidence imply the presence of moderately large disks with scales of hundreds of AU. Recently, the *Hubble Space Telescope* (HST) has produced spectacular images of disks around low-mass YSOs in the Orion nebula, seen in their direct IR emission (e.g. Beckwith et al. 1989; Chen et al. 1998), or via the shadows cast on background emission (McCaughrean & O'Dell 1996). Examples of such disks are shown in Figs. 1.6 and 1.7.

If YSO circumstellar disks can survive long enough, the dust particles in the disk are expected to grow into km-sized bodies, planetesimals, and eventually into full-fledged planetary systems (Weidenschilling 1980; Weidenschilling et al. 1989; Wetherill 1990). The discovery of extrasolar planets around main sequence stars through reflex proper motions (Mayor & Queloz 1995; Marcy & Butler 1998) suggests that this is indeed a common phenomenon. Because they are believed to be the site for planet formation, non-accreting disks around young stellar objects are often called protoplanetary disks (not to be confused with the disks in protoplanetary nebulae). An interesting consequence of planet formation in YSO disks is that the newly formed planet will sweep up its surrounding material and open up a gap in the disk at the radial distance of the planet (Artymowicz 1987; Lin et al. 1999). The size of the gap will depend on the mass of the planet. These gaps in YSO disks may be observed indirectly by the derivation of the surface density in the disk as a function of radial distance from modelling of the energy distribution. In the next chapter we will suggest that evidence for the presence of disk gaps corresponding to Jupiter sized planets is present in some Herbig Ae/Be stars. An interesting future prospect is that the next generation of infrared and millimeter interferometers should be able to map these gaps directly and thus provide solid proof for the formation of planets in YSO disks.

References

Adams, F.C., Shu, F.H. 1985, ApJ 296, 655 in *"Protostars & Planets IV"*, eds. V. Mannings, A.P. Boss & S.S. Russell, (Tucson: University of Arizona Press), in press.

Adams, F.C., Shu, F.H. 1986, ApJ 308, 836

Adams, F.C., Lada, C.J., Shu, F.H. 1987, ApJ 312, 788

André, P., Ward-Thompson, D., Barsony, M. 1999,

Artymowicz, P. 1987, Icarus 70, 303

Bachiller, R., Cernicharo, J., Martín-Pintado, J., Tafalla, M., Lazareff, B. 1990, A&A 231, 174

Bastien, P. 1989, in *"Polarized Radiation of Circumstellar Origin"*, eds G.V. Coyne et al., (Vatican City: Vatican Observatory), p. 541

Beckwith, S.V., Sargent, A.I., Koresko, C.D., Weintraub, D.A. 1989, ApJ 343, 393

Bertout, C. 1989, ARA&A 27, 351

Bibo, E.A., Thé, P.S. 1991, A&AS 89, 319

Bogaert, E. 1994, PhD thesis, Kathol. Univ. Leuven
Böhm, T., Catala, C. 1993, A&AS 101, 629
Calvet, N., Hartmann, L.W., Kenyon, S.J., Whitney, B.A. 1994, ApJ 434, 330
Calvet, N., Hartmann, L.W., Strom, S.E. 1999, in *"Protostars & Planets IV"*, eds. V. Mannings, A.P. Boss & S.S. Russell, (Tucson: University of Arizona Press), in press.
Chen, H., Bally, J., O'Dell, C.R. et al. 1998, ApJ 492, L173
Cheung, A.C., Rank, D.M., Townes, C.H., Thornton, D.D., Welch, W.J. 1968, Phys. Rev. Lett. 21, 1701
Cohen, M., Kuhi, L.V. 1979, ApJS 41, 743
Corcoran, M., Ray, T.P. 1997, A&A 321, 189
Crovisier, J. Leech, K., Bockelée-Morvant, D. et al. 1997, Science 275, 1904
Cudworth, K.M., Herbig, G.H. 1979, AJ 84, 548
de Winter, D., Koulis, C., Thé, P.S., van den Ancker, M.E., Pérez, M.R. 1997, A&AS 121, 223
Evans, N.J. 1999, ARA&A, in press
Finkenzeller, U., Mundt, R. 1984, A&AS 55, 109
Fukui, Y., Iwata, T., Mizuna, A., Bally, J., Lane, A.P. 1993, in: *"Protostars and Planets III"*, eds. E.H. Levy & J.I. Lunine, (Tucson: University of Arizona Press), p. 603
Grady, C.A., Pérez, M.R., Talavera, A. et al. 1996, A&AS 120, 157
Grinin, V.P. 1988, SvA 14, L27
Grinin, V.P., Kiselev, N.N., Minikulow, N.K., Chernova, G.P., Voshchinnikov, N.V. 1991, Ap&SS 186, 283
Grinin, V.P., Thé, P.S., de Winter, D., Giampapa, M., Rostopchina, A.N., Tambovsteva, L.V., van den Ancker, M.E. 1994, A&A 292, 165
Hartmann, L., Kenyon, S.J. 1996, ARA&A 34, 207
Hartmann, L., Kenyon, S.J., Calvet, N. 1993, ApJ 407, 219
Hayashi, C. 1961 PASP 13, 450
Henyey, L.G., LeLevier, R., Levee, R.D. 1955, PASP 67, 154
Herbig, G.H. 1960, ApJS 4, 337
Herbig, G.H. 1966, Vistas Astron. 8, 109
Herbig, G.H. 1977, ApJ 217, 693
Herbst, W., Herbst, D.K., Grossman, E.J., Weinstein, D. 1994, AJ 108, 1906
Hu, J.Y., Thé, P.S., de Winter, D. 1991, A&A 208, 213
Iben, I. 1965, ApJ 141, 933
Joy, A.H. 1945, ApJ 102, 168
Keene, J., Masson, C. 1990, ApJ 355, 635
Königl, A., Pudritz, R.A. 1999, in *"Protostars & Planets IV"*, eds. V. Mannings, A.P. Boss & S.S. Russell, (Tucson: University of Arizona Press), in press.
Kuhi, L.V. 1964, ApJ 140, 1409
Kutner, M.L., Tucker, K.D., Chin, G., Thaddeus, P. 1977, ApJ 215, 521
Lada, C.J. 1987, IAU Symposium 115: *"Star Forming Regions"*, p. 1
Lada, C.J., Wilking, B.A. 1984, ApJ 287, 610
Larson, R.B. 1969, MNRAS 145, 271
Lay, O.P., Carlstrom, J.E., Hills, R.E., Phillips, T.G. 1994, ApJ 434, L75
Lin, D.C.N., Papaloizou, J.C.B., Bryden, G., Ida, S., Terquem, C. 1999, in *"Protostars & Planets IV"*, eds. V. Mannings, A.P. Boss & S.S. Russell, (Tucson: University of Arizona Press), in press.
Luyten, W.J. 1971, *"The Hyades"* (Minneapolis: Univ. Minnesota Press)

Malfait, K., Waelkens, C., Waters, L.B.F.M., Vandenbussche, B., Huygen, E., de Graauw, M.S. 1998, A&A 332, L25
Manfroid, J, Sterken, C., Bruch, A., et al. 1991, A&AS 87, 481
Manfroid, J, Sterken, C., Cunow, B. et al. 1995, A&AS 109, 329
Mannings, V., Sargent, A.I. 1997, ApJ 490, 792
Marcy, G.W., Butler, R.P. 1998, ARA&A 36, 57
Mayor, M., Queloz, D. 1995, Nature 378, 355
McCaughrean, M.J., O'Dell, C.R. 1996, AJ 111, 1977
McCaughrean, M.J., Stapelfeldt, K., Close, L. 1999, in *"Protostars & Planets IV"*, eds. V. Mannings, A.P. Boss & S.S. Russell, (Tucson: University of Arizona Press), in press.
Mundt, R. 1984, ApJ 280, 749
Myers, P.C., Benson, P.J. 1983, ApJ 266, 309
Natta, A., Prusti, T., Krügel, E. 1993, A&A 275, 527
Oudmaijer, R.D., van der Veen, W.E.C.J., Waters, L.B.F.M., Trams, N.R., Waelkens, C., Engelesman, E. 1992, A&AS 96, 625
Palla, F., Stahler, S.W. 1992, ApJ 392, 667
Palla, F., Stahler, S.W. 1993, ApJ 418, 414
Pérez, M.R., Grady, C.A. 1997, Space Science Reviews 82, 407
Richer, J., Shepherd, D., Cabrit, S., Bachiller, R., Churchwell, E. 1999, in *"Protostars & Planets IV"*, eds. V. Mannings, A.P. Boss & S.S. Russell, (Tucson: University of Arizona Press), in press.
Serkowski, K., Mathewson, D.S., Ford, V.L. 1975, ApJ 196, 263
Shu, F.H. 1977, ApJ 214, 488
Shu, F.H., Millione, V., Roberts, W.W. 1973, ApJ 183, 819
Shu, F.H., Adams, F.C., Lizano, S. 1987, ARA&A 25, 23
Snell, R.L., Loren, R.B., Plambeck, R.L. 1980, ApJ 239, L17
Staude, H.J., Elsässer, H., 1993, A&AR 5, 165
Stahler, S.W. 1983, ApJ 274, 822
Stahler, S.W. 1988, ApJ 332, 804
Stahler, S.W. 1994, PASP 106, 337
Stahler, S.W., Shu, F.H., Taam, R.E. 1980, ApJ 241, 637
Sterken, C., Manfroid, J., Anton, K., et al. 1993, A&AS 102, 79
Sterken, C., Manfroid, J., Beele, D., et al. 1995, A&AS 109, 329
Thé, P.S., de Winter, D., Pérez, M. 1994, A&AS 104, 315
van den Ancker, M.E., Thé, P.S., Feinstein, A., Vázquez, R.A., de Winter, D., Pérez, M.R. 1997, A&AS 123, 63
Waelkens, C., Waters, L.B.F.M., de Graauw, M.S. et al. 1996, A&A 315, L245
Walker, M.F. 1956, ApJS 2, 365
Waters, L.B.F.M., Waelkens, C. 1998, ARA&A 36, 233
Weidenschilling, S.J. 1980, Icarus 44, 172
Weidenschilling, S.J., Donn, B., Meakin, P. 1989, in *"The Formation and Evolution of Planetary Systems"*, eds. H.A. Weaver & L. Danly (Cambridge Univ. Press), p. 131
Wenzel, W. 1968, IAU Coll. *"Non-periodic Phenomena in Variable Stars"*, Budapest, p. 61
Wetherill, G.W. 1990, Ann. Rev. Earth Planet. Sci. 18, 205
Wilson, R.W., Jefferts, K.B., Penzias, A.A. 1970, ApJ 161, L43
Wood, J.A. 1997, Sky & Telescope 97, No. 1, 37

Chapter 2

Hipparcos Data on Herbig Ae/Be Stars: An Evolutionary Scenario

M.E. van den Ancker, P.S. Thé, H.R.E. Tjin A Djie, C. Catala, D. de Winter, P.F.C. Blondel and L.B.F.M. Waters, A&A 324, L33 (1997)

Abstract

Fundamental astrophysical parameters (distance, temperature, luminosity, mass, age) of a sample of 10 Herbig Ae/Be candidates and 3 non-emission line A and B stars in star forming regions were computed combining Hipparcos parallaxes with data from literature. All genuine Herbig stars in our sample are located between the birthline and the zero-age main sequence (ZAMS) in the Hertzsprung-Russell diagram (HRD), in accordance with what is expected for pre-main sequence stars. The region in the HRD close to the birthline is relatively devoid of stars when compared to the region closer to the ZAMS, in agreement with the expected evolutionary time scales. The Herbig Ae/Be stars not associated with star forming regions were found to be located close to the ZAMS. Additionally we discuss a possible evolutionary scenario for the circumstellar environment of Herbig stars.

2.1 Introduction

In a historical paper Herbig (1960) was the first to realize that the "Be and Ae stars associated with nebulosity" are in fact stars of intermediate mass still in their pre-main sequence (PMS) phase of evolution: stars which have lost most of their envelope of infalling gas and dust, and whose energy is mainly supplied by gravitational contraction. Criteria for membership of this class of stars, now more commonly known as Herbig Ae/Be (HAeBe) stars, are (Thé et al. 1994): (1) spectral type earlier than F8; (2) presence of emission lines; (3) presence of IR-excess in the spectral energy distribution; (4) location in or near a probable star formation region.

Table 2.1. Astrophysical parameters of programme stars.

(1) HIP	(2) Other Name	(3) π [mas]	(4) $f_{\rm rej}$ [%]	(5) d [pc]	(6) Association D.C.	(7) Association R.N.	(8) Association S.A.	(9) $d_{\rm lit}$ [pc]	(10) Ref.	(11) Sp. Type	(12) Ref.	(13) A_V [m]	(14) $\log T_{\rm eff}$	(15) $\log L_\star/L_\odot$	(16) M [$M_\odot$]	(17) Age [Myr]
22910	AB Aur	6.9±1.0	0	144^{+23}_{-17}	L1519,(L1517)		Tau R2	140	(1)	A0Ve	(11)	0.50	4.00	$1.72^{+0.13}_{-0.11}$	2.4±0.2	2.5±1.0
34116	HD 53367	4.1±1.4	8	250^{+120}_{-60}	L1657	S292	CMa R1	1150	(2)	B0IVe	(12)	2.23	4.50	$4.04^{+0.34}_{-0.26}$	13±3	> 0.05
54413	HD 97048	5.7±0.8	0	180^{+30}_{-20}	DC297.2-15.6	S135	CED 111	160	(3)	B9–A0ep+sh	(3)	1.24	4.00	$1.61^{+0.13}_{-0.10}$	2.5±0.2	> 2
54557	HD 97300	5.3±1.0	1	190^{+40}_{-30}			CED 112	160	(3)	B9V	(13)	1.33	4.02	$1.54^{+0.17}_{-0.15}$	2.5±0.3	> 3
56379	HD 100546	9.7±0.6	0	103^{+7}_{-6}	(DC296.2-7.9)			170	(4)	B9Vne	(14)	0.28	4.02	$1.51^{+0.06}_{-0.05}$	2.4±0.1	> 10
58520	HD 104237	8.6±0.5	0	116^{+8}_{-7}			Cha III	84	(4)	A0Vpe	(4)	0.71	3.98	$1.77^{+0.06}_{-0.06}$	2.5±0.1	2.0±0.5
79080	HR 5999	4.8±0.9	0	210^{+50}_{-30}	DC339.7+9.2	S14	Lupus 3	140	(5)	A5–7III/IVe+sh	(12)	0.37	3.88	$1.89^{+0.17}_{-0.15}$	3.1±0.5	0.6±0.4
80462	HD 147889	7.4±1.2	0	140^{+30}_{-20}	L1687	IC 4603	Sco R1	160	(6)	B2V	(15)	3.32	4.34	$3.32^{+0.16}_{-0.13}$	7.5±1.0	> 0.1
81624	HD 150193	6.7±1.7	3	150^{+50}_{-30}	L1729		Sco R1	160	(6)	A1Ve	(16)	1.61	3.97	$1.47^{+0.25}_{-0.19}$	2.3±0.2	> 2
87819	HD 163296	8.2±1.0	0	122^{+17}_{-13}				150	(7)	A1Ve	(16)	0.25	3.97	$1.48^{+0.12}_{-0.10}$	2.3±0.1	> 2.5
93425	HD 176386	7.4±1.2	0	140^{+30}_{-20}	DC359.8-17.9	NGC 6727		130	(8)	B9IV	(17)	0.62	4.03	$1.69^{+0.14}_{-0.13}$	2.7±0.2	> 2
100289	BD+40 4124	9.3±2.2	18	110^{+30}_{-20}	L888/L895	NGC 6910	Cyg R1	980	(9)	B2Ve	(18)	3.16	4.34	$2.04^{+0.23}_{-0.19}$	–	–
103763	HD 200775	2.3±0.6	0	430^{+160}_{-90}	L1174	NGC 7023	Cep R2	440	(10)	B2.5IVe	(19)	1.92	4.31	$3.89^{+0.26}_{-0.21}$	10±2	0.02±0.01

References to Table 2.1: (1) Elias (1978); (2) Herbst et al. (1982); (3) Whittet et al. (1997); (4) Hu et al. (1989); (5) Hughes et al. (1993); (6) Whittet (1974); (7) Thé et al. (1985); (8) Marraco & Rydgren (1981); (9) Shevchenko et al. (1991); (10) Whitcomb et al. (1981); (11) Böhm & Catala (1993); (12) Finkenzeller (1985); (13) Rydgren (1980); (14) Houk et al. (1975); (15) Cohen (1973); (16) Houk et al. (1988); (17) Houk et al. (1982); (18) Hillenbrand et al. (1995); (19) Rogers et al. (1995).

Later, stars were found which are not near any plausible star formation region, but show all other characteristics of HAeBe stars. Whether these so-called isolated Herbig Ae/Be stars are young stellar objects remains controversial. Moreover, the membership criteria outlined above do not uniquely select intermediate-mass pre-main sequence stars, but will also select evolved massive stars (Davies et al. 1990) which are still located in the region where they formed. Therefore one has to be careful in identifying Herbig stars with pre-main sequence objects (Herbig 1992).

In this chapter we will derive astrophysical parameters of a sample of 10 Herbig Ae/Be candidates as well as 3 non emission-line A and B-type stars in star formation regions for which the Hipparcos mission resulted in better than 3σ detections of the parallax. An attempt will be made to construct an evolutionary scenario for the circumstellar environment of HaeBe stars. In Chapter 3 we will study the photometric behaviour of the Herbig Ae/Be stellar group as a whole using the photometric data on all Herbig stars provided by Hipparcos.

2.2 Data analysis

Accurate absolute astrometry as well as photometry was obtained by Hipparcos on a sample of 38 A- and B-type stars in nearby star forming regions. This sample is a subset of a list of objects (Thé et al. 1982) which was accepted in 1982 by the Hipparcos consortium and which was released to the P.I. prior to the publication of the Hipparcos Catalogue (ESA 1997), in which a full description of the data products will be given. Table 2.1 lists the stars for which a better than 3σ detection of the parallax was achieved. A full analysis of the complete sample will be given in the next chapter.

The first two columns in Table 2.1 give the Hipparcos number and the name of each star. The third column lists the trigonometric parallax measured by Hipparcos and the 1σ uncertainty in this (both in milliarcseconds). The fourth column lists the percentage of measurements that had to be rejected to arrive at the solution for the parallax given in the third column. The next column in Table 2.1 gives the distance, with its 1σ uncertainty, computed from the parallax. Columns 6–8 contain names of the star forming region in which the star is located. In column 6 an association with a dark cloud from the catalogue of Lynds (1962), or its extension to the southern hemisphere (Hartley et al. 1986) is given. When the name of the dark cloud is in parentheses, this indicates that the star is located near the edge, so the association of the star with the cloud might be doubtful. The next column in Table 2.1 lists the reflection nebula with which the star is associated, whereas the $8^{\rm th}$ column in Table 2.1 gives the name of a stellar aggregate with which the star is associated. A literature distance and a reference to the paper in which this was derived is provided in columns 9 and 10.

2.3 Astrophysical parameters

In order to compute the total luminosity of the sample stars, photometric data, from the ultraviolet (ANS, TD1, IUE), through the optical (Walraven $WULBV$, Johnson/Cousins

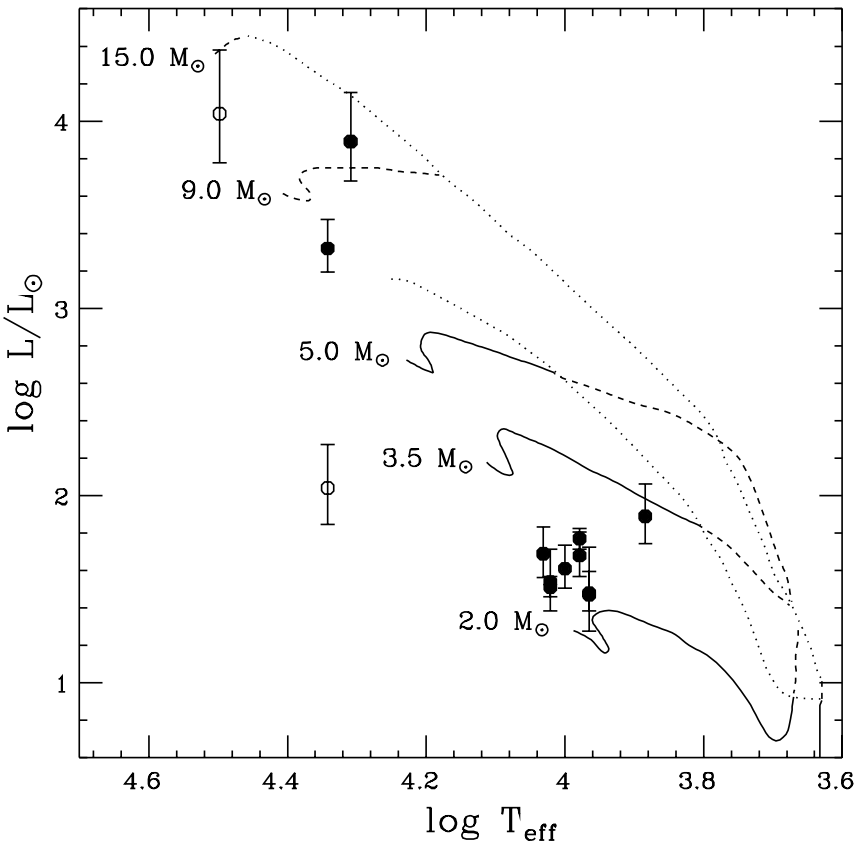

Fig. 2.1. Hertzsprung-Russell diagram of Herbig Ae/Be stars with parallaxes measured by Hipparcos. Open plot symbols indicate stars with $f_{\rm rej} > 3\%$. Also shown are the theoretical pre-main sequence evolutionary tracks (solid lines and dashed lines) and the birthlines for 10^{-4} (upper dotted line) and 10^{-5} $M_\odot$ yr^{-1} (lower dotted line) by Palla & Stahler (1993).

$UBVRI$) to the infrared ($JHKLMNQ$, IRAS), were collected from literature. Since many of the stars show strong variations in brightness, only optical and UV data obtained near maximum brightness were used. The stellar luminosity, extinction and effective temperature were computed following the method outlined in van den Ancker et al. (1997). This method includes a correction for a possible anomalous extinction law towards the object. Since in HAeBes one often overestimates stellar temperatures from UV spectra due to the presence of heated layers in the immediate surroundings of the stars' photospheres (e.g. Blondel & Tjin A Djie 1994), and photometric methods to estimate stellar temperatures often yield erroneous results when the extinction law for the circumstellar material is anomalous, as is often the case for such stars (e.g. Thé et al. 1996), we only use spectral types based on optical spectra (Table 2.1). The computed visual extinction at maximum brightness A_V, effective temperature $T_{\rm eff}$ and stellar luminosity $L_\star$ are listed in columns 13–15 of Table 2.1.

In Figure 2.1, we plot the programme stars in the HR diagram. The error in $\log T_{\rm eff}$ is about 0.05 (or one subclass in spectral type), but individual data points may have larger errors. The error in luminosity is dominated by the error in the distance. Also

shown in Fig. 2.1 are the pre-main sequence evolutionary tracks and the birthline (i.e. the line where a star first becomes optically visible on its evolution to the zero-age main sequence) computed by Palla & Stahler (1993). Using these evolutionary tracks and the isochrones given by the same authors, we can make an estimate of the masses and ages of our programme stars. These are listed in the last two columns of Table 2.1. Note that for HD 200775 the given age, based on it being a pre-main sequence star, is rather dubious. Given the short main sequence life time of a 10 $M_\odot$ star and the fact that the post-main sequence lifetime of such a star is much longer than its pre-main sequence contraction time, it seems more likely that HD 200775 is already evolving away from the ZAMS, in which case its age would be around 20 Myr.

2.4 Discussion and conclusions

The observed distribution of stars fits well with what is expected for pre-main sequence stars: they are almost all located between (or at) the zero-age main sequence (ZAMS) and the birthline. There is a good correlation between the luminosity class (Table 2.1) and the position in the HRD: All giants are located to the right of the ZAMS. The clustering of stars around the evolutionary track of mass 2.5 $M_\odot$ in Fig. 2.1 is probably due to a selection effect: There are no Herbig Be stars in the nearest star forming regions. Since the pre-main sequence evolution of B-type stars proceeds much faster than those of their A-type counterparts this could reflect a difference in age between nearby and more distant star forming regions.

Peculiar is the position of BD+40°4124 in Fig. 2.1, far below the ZAMS. Such a position seems impossible for a young stellar object. BD+40°4124 illuminates a reflection nebula, in which many other young stellar objects can be found (Hillenbrand et al. 1995), so the possibility of this being an extremely rare evolved object seen projected towards a star forming region can be excluded. Therefore one or more of our assumptions used for deriving this position in the HRD must be wrong. Different authors in literature agree well on the spectral type of BD+40°4124, B2–3e. Also, a spectral type which would place it near the zero-age main sequence is not compatible with the observed spectral energy distribution. However, the distance as measured by Hipparcos (110^{+30}_{-20} pc) differs greatly from the literature value of the distance to the star forming region in which BD+40°4124 is located (1000 pc). Therefore we conclude that, although formally the Hipparcos data products give a 4σ detection for the parallax of BD+40°4124, this must be wrong. We note that for BD+40°4124 and HD 53367 the percentage of measurements that was rejected to arrive at the solution for the trigonometric parallax given in the Hipparcos Catalogue is very high, $f_{\rm rej} > 3\%$ (indicated by open circles in Fig. 2.1). Furthermore, BD+40°4124 was flagged as a variability induced mover in the Hipparcos Catalogue, most probably indicating problems with the astrometric solution. This case may reflect the difficulty of parallax determinations by Hipparcos in nebulous regions. For HD 53367 the discrepancy between the literature and Hipparcos distance that can be seen in Table 2.1 is statistically hardly significant.

A fair number of stars in our sample cluster around the 2.5 $M_\odot$ track (Fig. 2.1). This

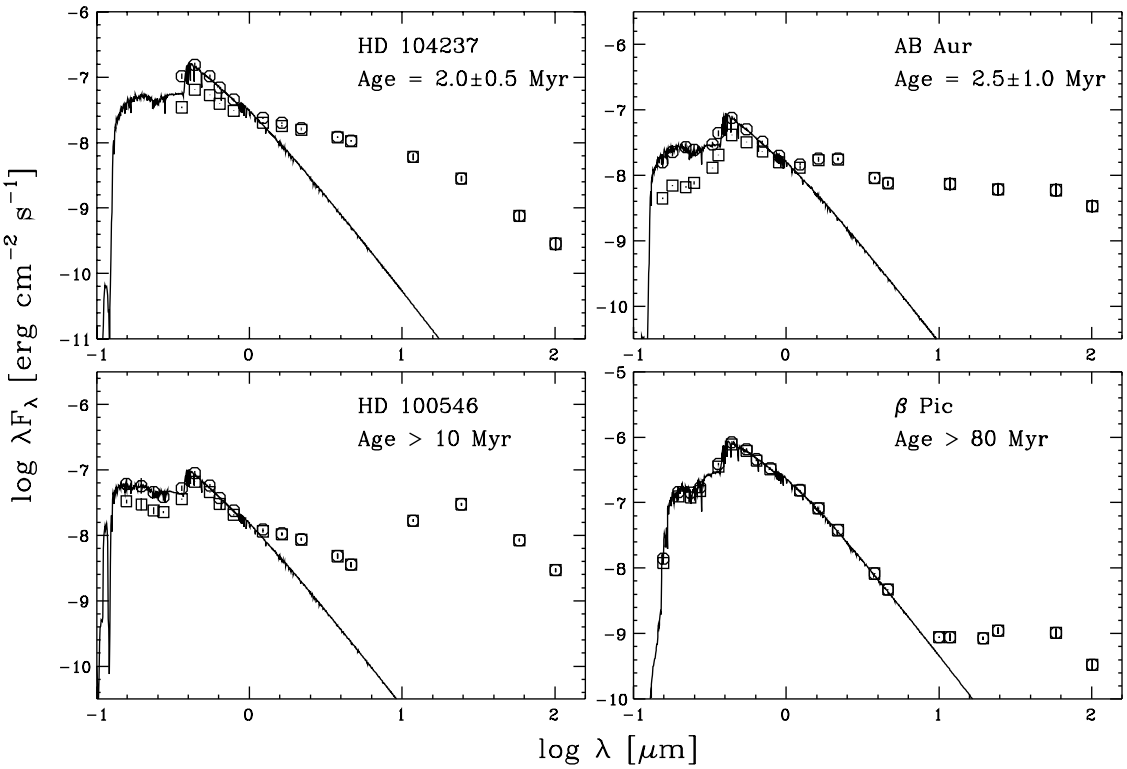

Fig. 2.2. Observed (squares) and extinction-corrected (circles) SEDs for (a) HD 104237, (b) AB Aur, (c) HD 100546, (d) β Pic. Also shown are Kurucz (1991) models fitted to the extinction-corrected SEDs.

allows us to construct an evolutionary sequence for their circumstellar environment. We select the objects HD 104237, AB Aur and HD 100546 for which reliable ages were estimated (Table 2.1), and plot their spectral energy distributions (SEDs) in Figure 2.2. Included in Figure 2.2 is the SED of β Pic which is even older than HD 100546 (Crifo et al. 1997), but has a slightly lower mass. The younger stars in our sample have SEDs that tend to be more or less flat in the infrared, whereas for the more evolved ones the dust excess tends to have a double-peaked structure, with a broad dip in the energy distribution around 10 μm. Extrapolating such a behaviour, we would expect to end up with a higher-mass equivalent of a star like β Pic. Interestingly, Waelkens et al. (1992) showed that the SEDs of Herbig stars can be classified as "flat" or "double-peaked" in the infrared and proposed an evolutionary scenario in which a broad dip around 10 μm develops with time. The ages derived from the Hipparcos data are consistent with such a scenario.

Spectroscopic evidence for evolution of the circumstellar dust component comes from observations with the *Infrared Space Observatory* ISO (Waelkens et al. 1996): HD 100546 shows a strong crystalline silicate component, similar to those seen in the ground-based 10 μm spectra of β Pic (Knacke et al. 1993) and of comets (Hanner et al. 1994). A recent ISO spectrum of the comet Hale-Bopp also shows strong crystalline silicates (Crovisier et al. 1997). In contrast, the object HD 104237 shows little evidence for such a crystalline dust component (Malfait, private communication). The occurrence

of crystalline dust is an indication for the degree of "processing" which the circumstellar material underwent after accretion from the molecular cloud, and is thus a measure of age. We find that for the small sample discussed here, the age derived from Hipparcos is consistent with the degree of processing seen in the ISO spectra.

We stress that the timescales for the evolution of the central star and the circumstellar material are probably not well coupled: studies of very young open clusters show that only a small percentage of the cluster stars, many of which are undoubtedly pre-main sequence in nature, show circumstellar gas and dust (e.g. van den Ancker et al. 1997). Furthermore, it is known that some giants, with presumably lower stellar ages than dwarfs, do show a double-peaked infrared excess, making the construction of evolutionary sequences difficult. Provided that the initial configuration and spatial distribution of the circumstellar dust envelopes of the Herbig Ae/Be stars are similar, some unknown physical mechanism regulates the timescale at which the circumstellar matter is dispersed. So, while the *timescales* may be very different for individual stars, it is quite possible that the *sequence* is as proposed in Fig. 2.2.

It is tempting to speculate about the origins of the formation of a 10 μm dip. From the presence of 10 μm amorphous silicate emission in most Herbig Ae/Be stars, we know that the dust envelopes surrounding these stars must be optically thin, and that the presence of a broad dip around 10 μm must correspond to a physical gap in the radial distribution of dust around HAeBes. Such a gap can only be caused by perturbations by another body surrounding the central star. This could either be a low-mass star outside the dust shell, clearing the region between the inner and outer Lindblad resonances through long-range resonance effects (Lin & Papaloizou 1979), or a Jupiter-sized planet forming inside the dust envelope, clearing $2\sqrt{3}$ Roche lobe radii on either side of the planet (Artymowicz 1987). Since many of the HAeBes with faint companions detected in recent years by speckle interferometry as well as by Hipparcos (Chapter 3) do not show a dip in their energy distributions, we consider the latter explanation more likely.

Acknowledgements. This chapter is based on data from the Hipparcos astrometry satellite. The authors would like to thank K. Malfait, C. Waelkens and P.R. Wesselius for many useful discussions on the ISO spectra of Herbig Ae/Be stars.

References

Artymowicz, P. 1987, Icarus 70, 303
Blondel, P.F.C., Tjin A Djie, H.R.E. 1994, ASP Conf. Ser. 62, 211
Böhm, T., Catala, C. 1993, A&AS 101, 629
Cohen, J.G. 1973, ApJ 186, 149
Crifo, F., Vidal-Madjar, A., Lallement, R., Ferlet, R., Gerbaldi, M. 1997, A&A 320, L29
Crovisier, J., Leech, K., Bockelée-Morvan, D., Brooke, T.Y., Hanner, M.S., Altieri, B., Keller, H.U., Lellouch, E. 1997, Science 275, 1904
Davies, J.K., Evans, A., Bode, M.F., Whittet, D.C.B. 1990, MNRAS 247, 517
Elias, J.H. 1978, ApJ 224, 857
ESA, 1997, The Hipparcos Catalogue, ESA SP-1200

Finkenzeller, U. 1985, A&A 151 340
Hanner, M.S., Lynch, D.K., Russell, R.W. 1994, ApJ 425, 274
Hartley, M., Manchester, R.N., Smith, R.M., Tritton, S.B., Goss, W.M. 1986, A&AS 63, 27
Herbig, G.H. 1960, ApJS 4, 337
Herbig, G.H. 1992, ASP Conf. Ser. 62, 3
Herbst, W., Miller, D.P., Warner, J.W., Herzog, A. 1982, AJ 87, 98
Hillenbrand, L.A., Meyer, M.R., Strom, S.E., Skrutskie, M.F. 1995, AJ 109, 280
Houk, N., Cowley, A.P. 1975, Michigan Spectral Survey, Vol. 1, Univ. Michigan Press
Houk, N. 1982, Michigan Spectral Survey, Vol. 3, Univ. Michigan Press
Houk, N., Smith-Moore, A. 1988, Michigan Spectral Survey, Vol. 4, Univ. Michigan Press
Hu, J.Y., Thé, P.S., de Winter, D. 1989, A&A 208, 213
Hughes, J., Hartigan, P., Clampitt, L. 1993, AJ 105, 571
Knacke, R.F., Fajardo-Acosta, S.B., Telesco, C.M., Hackwell, J.A., Lynch, D.K., Russell, R.W. 1993, ApJ 418, 440
Kurucz, R.L. 1991, in *"Stellar atmospheres–Beyond classical models"* (eds. A.G. Davis Philip, A.R. Upgren, K.A. Janes), L. Davis press, Schenectady, New York, p. 441
Lin, D.N.C., Papaloizou, J. 1979, MNRAS 188, 191
Lynds, B.T. 1962, ApJS 7, 1
Marraco, H.G., Rydgren, A.E. 1981, AJ 86, 62
Palla, F., Stahler, S.W. 1993, ApJ 418, 414
Rogers, C., Heyer, M.H., Dewdney, P.E. 1995, ApJ 442, 694
Rydgren, A.E. 1980, AJ 85, 444
Shevchenko, V.S., Ibragimov, M.A., Chernysheva, T.L. 1991, SvA 35, 229
Thé, P.S., Felenbok, P., Cuypers, H., Tjin A Djie, H.R.E. 1985, A&A 149, 429
Thé, P.S., Tjin A Djie, H.R.E., Praderie, F., Catala, C. 1982, ESA SP-177, 105
Thé, P.S., de Winter, D., Pérez, M. 1994, A&AS 104, 315
Thé, P.S., Pérez, M.R., Voshchinnikov, N.V., van den Ancker, M.E. 1996, A&A 314, 233
van den Ancker, M.E., Thé, P.S., Feinstein, A., Vázquez, R.A., de Winter, D., Pérez, M.R. 1997, A&AS 123, 63
Waelkens, C., Bogaert, E., Waters, L.B.F.M. 1992, ASP Conf. Ser. 62, 405
Waelkens, C., Waters, L.B.F.M., de Graauw, M.S. et al. 1996, A&A 315, L245
Whitcomb, S.E., Gatley, I., Hildebrand, R.H., Keene, J., Sellgren, K., Werner, M.W. 1981, ApJ 246, 416
Whittet, D.C.B. 1974, MNRAS 168, 371
Whittet, D.C.B., Prusti, T., Franco, G.A.P., Gerakines, P.A., Kilkenny, D., Larson, K.A., Wesselius, P.R. 1997, A&A 327, 1194

Chapter 3

Hipparcos Photometry of Herbig Ae/Be Stars

M.E. van den Ancker, D. de Winter and H.R.E. Tjin A Djie,
A&A 330, 145 (1998)

Abstract

The photometric behaviour of a sample of 44 Herbig Ae/Be (HAeBe) candidate stars was studied using a uniform set of optical photometry obtained by the Hipparcos mission. Astrophysical parameters (distance, temperature, luminosity, mass, age) of this sample of stars were derived as well by combining the astrometric data provided by Hipparcos with data from literature. Our main conclusions can be summarized as follows: (1) More than 65% of all HAeBe stars show photometric variations with an amplitude larger than $0\overset{\mathrm{m}}{.}05$; (2) HAeBes with a spectral type earlier than A0 only show moderate (amplitude $< 0\overset{\mathrm{m}}{.}5$) variations, whereas those of later spectral type can (but not necessarily have to) show variations of more than $2\overset{\mathrm{m}}{.}5$. We explain this behaviour as being due to the fact that stars with lower masses become optically visible, and hence recognizable as Herbig Ae stars, while still contracting towards the zero-age main sequence (ZAMS), whereas their more massive counterparts only become optically visible after having reached the ZAMS; (3) The Herbig stars with the smallest infrared excesses do not show large photometric variations. This can be understood by identifying the stars with lower infrared excesses with the more evolved objects in our sample; (4) No correlation between the level of photometric variability and the stellar $v \sin i$ could be found. If the large photometric variations are due to variable amounts of extinction by dust clouds in the equatorial plane of the system, the evolutionary effects probably disturb the expected correlation between the two.

3.1 Introduction

Lately, the group of Herbig Ae/Be (HAeBe) stars, objects which are believed to be intermediate mass (2–10 $M_\odot$) stars still in their phase of pre-main sequence (PMS) con-

traction, has received a great deal of interest. In his original paper, Herbig (1960a) selected a sample of candidate intermediate-mass young stellar objects with the following properties: (1) spectral type earlier than F0; (2) presence of emission lines; (3) location in an obscured region; (4) association with a fairly bright reflection nebula. Later, these criteria were extended to include less massive stars, as well as stars which are situated in more isolated regions. Nowadays, some authors also include stars without strong emission lines in samples of HAeBe stars (Malfait et al. 1998), making the distinction with the Vega-type stars somewhat vague. Here, we will adopt the following criteria for inclusion of stars in our sample: (1) spectral type B, A or F; (2) luminosity class III–V; (3) emission component(s) in Hα; (4) presence of infrared emission due to circumstellar dust. The first two criteria will eliminate most confusion with evolved objects, the third characteristic will eliminate confusion with Vega-type stars, and the last criterion will exclude the classical Be stars from our sample. Yet these criteria may still select a small fraction of evolved massive stars, so one has to be careful in identifying HAeBe stars with PMS objects.

One of the best studied characteristics of the group of HAeBe stars is their photometric behaviour. A significant fraction of HAeBes shows usually irregular variations up to several magnitudes in the visual. These have been explained using several models. The large ($> 0\overset{\mathrm{m}}{.}5$) irregular variations in brightness seen in the UXOR subgroup (named after their prototype UX Ori) of the Herbig stars, with a typical time scale of weeks, can be explained as being due to variable amounts of extinction by, presumably circumstellar, dust of the starlight (e.g. Bibo & Thé 1991). Superimposed on this, variations on the $0\overset{\mathrm{m}}{.}1$ level, with a time scale from hours to days, can be explained as due to clumpy accretion (Pérez et al. 1992) or as due to chromospheric activity (star spots; Catala et al. 1993). More regular variations at the millimagnitude level have been explained as caused by stellar pulsations when a PMS star is in the same instability strip in the Hertzsprung-Russell diagram (HRD) as the evolved δ Scuti objects (Kurtz & Marang 1995).

In Chapter 2 we studied fundamental astrophysical parameters of a small sample of HAeBe stars using Hipparcos data, released to the P.I. prior to the publication of the Hipparcos Catalogue (ESA 1997). In addition to measuring astrometric data, the Hipparcos mission also resulted in roughly one hundred optical broadband photometric measurements for each of these targets (van Leeuwen et al. 1997). The recent release of the final version of the Hipparcos Catalogue makes it possible to use these data to study the photometric behaviour of the HAeBe stellar group as a whole in a more systematic and unbiased way than has been done so far. In this chapter we will therefore study the level of photometric variability on time scales up to a few years for all HAeBe candidates identified up to date, included in the Hipparcos Catalogue.

3.2 Data analysis

Our initial sample of stars to include in the present study consisted of all HAeBe candidates from the catalogue of Thé et al. (1994), measured by Hipparcos, together with

all emission-line stars from the sample of HAeBe and Vega-type stars from the papers by Sylvester et al. (1996), Grady et al. (1996) and Malfait et al. (1998), as well as a few individual probable HAeBes which were overlooked in these studies. In going through the literature for all these stars, it was noted that several of the stars included in this sample are probably not young stars, although they fulfill all membership criteria of the HAeBe class: ω Ori most definitely is a classical Be star with a history of mass loss (Sonneborn et al. 1988). HD 76534 was suggested to be a classical Be star as well (Oudmaijer & Drew 1997) since it does not have the significant near-IR excess due to hot circumstellar dust found in most HAeBes. A similar conclusion was reached for BD+41°3731 by Bernacca et al. (1995). Our analysis of literature data showed that the same applies for the stars GU CMa, HD 53367 and IL Cep. HD 283817 was shown to be a post-main sequence binary system (Martín 1993), and not a pre-main sequence member of the Taurus-Auriga complex, as suggested by Walter et al. (1990). This is confirmed by the lower limit on the distance towards this star measured by Hipparcos. MWC 137 was once believed to be a Planetary Nebula (Acker et al. 1987), and its true nature is still disputed. The PMS nature of many stars showing B[e] characteristics, like HD 45677 or HD 50138, remains controversial as well. Furthermore, several stars included in the previous studies of HAeBe stars were found to have masses, obtained from their position in the HRD or from literature data, which put them in the range of T Tauris (taken as less massive than 1.5 $M_{\odot}$), rather than HAeBes. Although young objects as well, these low-mass stars do not belong in an analysis aimed at studying the PMS evolution of intermediate-mass stars. Hence, all these stars were not included in our analysis. An overview of our complete sample and the main results of the Hipparcos measurements are given in Table 3.1. In the remainder of this chapter we will only indicate the probable HAeBe candidates from this Table when referring to our sample.

The first two columns in Table 3.1 list the number of the star in the Hipparcos Catalogue and a more common identifier. The third column lists the trigonometric parallax measured by Hipparcos and the 1σ uncertainty in this (both in milliarcseconds). The fourth column lists the percentage of measurements that had to be rejected to arrive at the solution for the parallax. In case this percentage is high, the error in the listed parallax can be much higher than that given by the formal standard deviation (Chapter 2). The fifth column in Table 3.1 gives the distance, with its 1σ uncertainty, computed from the parallax in the 17 cases in which a 3σ detection was achieved by Hipparcos. In other cases, a 3σ lower limit on the distance is indicated. A dash in this column indicates stars with $f_{\rm rej} > 3\%$, for which the astrometric data was excluded from our discussion. Note that the distances listed in column 6 are simply the inverse of the listed parallax. No correction for the Lutz-Kelker effect (Lutz & Kelker 1973) was applied because this correction will depend on the distribution of the true distances of the sample under consideration (Brown et al. 1997; Oudmaijer et al. 1998), which is essentially unknown for a sample of stars not only concentrated towards galactic star-forming regions, but also selected on historical (i.e. studied previously in literature) rather than on more rational grounds. Since we are only considering cases in which the Hipparcos mission resulted in a better than 3σ detection of the parallax, the correc-

Table 3.1. Astrophysical parameters of programme stars.

Probable Herbig Ae/Be candidates

(1) HIP	(2) Name	(3) π [mas]	(4) $f_{\rm rej}$ [%]	(5) d [pc]	(6) Association D.C.	(7) B.N.	(8) S.A.	(9) $d_{\rm lit}$ [pc]	(10) Ref.	(11) $H_{\rm p,min.}$ [$^{\rm m}$]	(12) δH_p [$^{\rm m}$]
3401	V594 Cas	3.3(1.6)	0	> 120	L1302	NGC 225	RSF1 Cas	650	(1)	10.45	0.36
16243	BD+30°549	2.6(1.9)	2	> 120	L1450,L1452	NGC 1333	Per R1	350	(2)	10.48	0.13
17890	XY Per	8.3(3.5)	17	–	L1442,L1449	Anon.	RSF Per B	350	(2)	9.23	0.38
22910	AB Aur	6.9(1.0)	0	144^{+23}_{-17}	L1519,(L1517)	Anon.	Tau R2	140	(3)	7.06	0.06
23143	HD 31648	7.6(1.2)	0	131^{+24}_{-18}						7.75	0.11
23602	UX Ori	0.6(2.5)	0	> 130	(L1616)	Anon.				10.12	1.21
24552	HD 34282	6.1(1.6)	2	160^{+60}_{-40}						9.87	0.77
25253	HD 35187	6.7(2.5)	7	–						7.85	0.21
25299	V346 Ori	1.6(2.0)	0	> 130		(Anon.)	Ori OB1 a	400	(4)	10.21	0.14
25540	CO Ori	−1.8(2.8)	0	> 120		C54				10.47	1.28
25546	HD 35929	0.9(0.9)	2	> 360	(L1641)		Ori OB1 c	430	(4)	8.19	0.05
25793	HD 36112	4.9(1.2)	0	200^{+60}_{-40}						8.33	0.06
26327	V380 Ori	3.7(5.5)	8	–	L1641	NGC 1999	Ori OB1 c	430	(4)	10.26	0.33
26403	BF Ori	−0.7(1.8)	0	> 210	L1641	NGC 1980	Ori OB1 c	430	(4)	9.70	2.49
26752	HD 37806	1.1(1.1)	0	> 230	L1630	(Anon.)	Ori OB1 b1	500	(4)	7.91	0.07
27059	V351 Ori	3.5(1.6)	2	> 210	L1630		Ori OB1 b1	500	(4)	8.91	0.14
28582	HD 250550	1.7(1.5)	0	> 160	L1586,L1587		Gem OB1	280	(5)	9.49	0.10
31042	HD 46060	4.6(2.5)	10	–		Anon.	Mon R2	760	(6)	8.85	0.15
31235	HD 259431	3.5(1.4)	0	> 130	L1605	NGC 2247	Mon R1	800	(7)	8.67	0.08
34042	Z CMa	−0.9(2.2)	0	> 180	L1657	S295	CMa R1	1150	(7)	9.56	0.47
35488	NX Pup	2.0(2.4)	33	–	DC256.2-14.4	Anon.		450	(8)	9.55	1.18
36068	HD 58647	3.6(0.8)	1	280^{+80}_{-50}						6.85	0.03
48269	HD 85567	1.0(0.7)	1	> 480	(DC281.7-4.4)					8.54	0.06
54413	HD 97048	5.7(0.8)	0	180^{+30}_{-20}	DC297.2-15.6	S135	CED 111	160	(9)	8.50	0.05
55537	HD 98922	1.0(0.6)	0	> 540	(DC288.3+7.3)					6.77	0.04
56379	HD 100546	9.7(0.6)	0	103^{+7}_{-6}	(DC296.2-7.9)			170	(10)	6.68	0.19
58520	HD 104237	8.6(0.5)	0	116^{+8}_{-7}			Cha III	84	(10)	6.59	0.11
77542	HD 141569	10.1(0.8)	2	99^{+9}_{-8}	(L169)	Anon.				7.14	0.03
78092	HD 142527	5.0(1.2)	0	200^{+60}_{-40}		Anon.				8.42	0.09
78943	HD 144432	4.0(1.5)	0	> 200			Sco R1			8.24	0.05
79080	HR 5999	4.8(0.9)	0	210^{+50}_{-30}	DC339.7+9.2	S14	Lupus 3	270	(11)	6.87	1.02
81624	HD 150193	6.7(1.7)	3	150^{+50}_{-30}	L1729		Sco R1	160	(12)	8.91	0.05
82747	AK Sco	6.9(1.4)	0	150^{+40}_{-30}	DC348.0+3.7			200	(13)	9.01	0.60
85755	51 Oph	7.7(0.9)	0	131^{+17}_{-13}						4.79	0.02
87819	HD 163296	8.2(1.0)	0	122^{+17}_{-13}						6.88	0.07
90617	V431 Sct	−2.1(4.2)	6	–	(L481)					11.41	0.60
93449	R CrA	122(68)	5	–	DC359.9-17.9	NGC 6729		130	(14)	10.63	1.67
94260	HD 179218	4.1(0.9)	0	240^{+70}_{-40}	(L693)					7.41	0.03
98719	V1295 Aql	0.2(1.1)	2	> 290						7.85	0.05
100289	BD+40°4124	9.3(2.2)	18	–	L888/L895	NGC 6910	Cyg R1	980	(15)	10.47	0.26
103763	HD 200775	2.3(0.6)	0	430^{+160}_{-90}	L1174	NGC 7023	Cep R2	440	(16)	7.39	0.04
107207	V361 Cep	3.0(6.1)	0	> 50		NGC 7129		1250	(17)	10.85	0.13
107983	BD+46°3471	−0.8(1.5)	0	> 280	L1055	S125	(IC 5146)	900	(18)	10.17	0.11
114995	MWC 1080	−7.0(3.3)	6	–	L1238	S158		2200	(19)	11.31	0.39

(13) n_H	(14) Var.	(15) Sp. Type	(16) Ref.	(17) Hα	(18) Ref.	(19) $v \sin i$ [km s^{-1}]	(20) Ref.	(21) A_V [m]	(22) $\log T_{\rm eff}$	(23) $\log L_\star/L_\odot$	(24) M [M$_\odot$]	(25) log(Age) [yr]	(26) Remarks
167	•	B8eq	(20)	P	(46)	55(5)	(46)	2.14	4.08	> 1.13			
83		B8Vpe	(21)					1.89	4.08	> 0.93			
99	•	A2II+B6e	(22)	D	(46)	95+130	(62)	2.26	4.15	–			vis. bin.
40	•	A0Ve+sh	(23)	P	(46)	80(5)	(46)	0.50	3.98	$1.68^{+0.13}_{-0.11}$	2.4(2)	6.3(2)	
44	•	A3ep+sh	(24)	P	(47)			0.25	3.94	$1.51^{+0.15}_{-0.13}$	2.2(3)	6.4(2)	
73	•	A3IIIe	(25)	D	(48)	70(6)	(46)	0.37	3.93	> 0.40			
79	•	A0e	(26)					0.59	3.98	$0.68^{+0.27}_{-0.21}$	–	–	
68	•	A2–3IV/Ve	(27)	D	(27)	105(9)	(46)	0.65	3.95	–			vis. bin.
141	•	A5III:e	(28)	S	(49)			0.43	3.91	> 0.21			
66	•	F9:e	(29)	P	(50)			1.83	3.79	> 0.53			vis. bin.
85		F0IIIe	(29)	S	(51)	150(30)	(49)	0.40	3.86	> 1.92			
77		A5IVe	(30)	S	(52)			0.22	3.91	$1.35^{+0.24}_{-0.18}$	2.0(3)	6.5(3)	
98	•	A1:e	(22)	S	(50)			1.43	3.97	–			IR bin.
92	•	A5–6IIIe	(29)	D	(49)	100(10)	(46)	0.26	3.90	> 0.56			
128	•	A2Vpe	(31)	D	(53)	120(30)	(46)	0.03	3.95	> 1.51			
62	•	A7 IIIe	(32)	D	(32)			0.50	3.88	> 1.14			
77		B4–5IIIe	(29)	P	(54)	110(9)	(46)	0.71	4.20	> 1.33			
176	•	B3ne	(21)					1.61	4.27	–			
58		B1Ve	(29)	D	(55)	90(8)	(46)	1.61	4.41	> 2.37			
78	•	F6IIIe	(29)	P	(50)	< 130:	(63)	2.42	3.80	> 1.72			IR bin.
107	•	A9–F0Ve	(20)	D	(49)	120(10)	(46)	0.59	3.87	–			vis. bin.
97		B9IVe	(26)	D	(49)	280(50)	(49)	0.50	4.03	$2.48^{+0.22}_{-0.17}$	4.2(6)	5.2(4)	
133	•	B7–8Ve	(29)	P	(51)			0.81	4.10	> 2.54			
106		B9–A0ep+sh	(33)	P	(51)	140(20)	(46)	1.24	4.00	$1.61^{+0.13}_{-0.10}$	2.5(2)	> 6.3	
165	•	B9Ve	(34)	P	(51)			0.34	4.02	> 2.96			Sp. bin.
131	•	B9Vne	(35)	D	(49)	250(50)	(49)	0.28	4.02	$1.51^{+0.06}_{-0.05}$	2.4(1)	> 7.0	
134	•	A4IVe+sh	(29)	D	(51)			0.31	3.93	$1.55^{+0.06}_{-0.05}$	2.3(1)	6.3(1)	
91		B9.5Ve	(36)	D	(56)	236(9)	(27)	0.47	4.00	$1.35^{+0.08}_{-0.07}$	2.3(1)	> 7.0	IR bin.
91	•	F7IIIe	(29)	S	(51)			1.49	3.80	$1.84^{+0.23}_{-0.19}$	3.5(6)	5.0(5)	
102		A5Ve	(29)	D	(57)	74(2)	(27)	0.56	3.91	> 1.48			
126	•	A5–7III/IVe+sh	(37)	D	(58)	180(20)	(19)	0.47	3.90	$1.93^{+0.19}_{-0.14}$	3.2(5)	5.7(3)	vis. bin.
94		A1Ve	(38)	D	(51)	100(30)	(20)	1.61	3.97	$1.47^{+0.25}_{-0.19}$	2.3(2)	> 6.3	vis. bin.
55	•	F5+F5IVe	(13)	C	(51)	19(1)	(13)	0.62	3.81	$0.88^{+0.20}_{-0.16}$	–	–	Sp. bin.
66		B9.5Vne	(39)	D	(51)	267(5)	(27)	0.15	4.00	$2.39^{+0.11}_{-0.09}$	4.0(3)	5.5(2)	
95	•	A1Ve	(38)	D	(59)	120(30)	(20)	0.25	3.97	$1.48^{+0.12}_{-0.10}$	2.3(1)	6.6(4)	
35		B1e	(40)					–	4.05	–			
69	•	A1e–F7e var	(29)	D	(50)			1.64	3.93	–			Sp. var.
77		B9e	(41)			60(6)	(64)	1.27	4.02	$2.50^{+0.22}_{-0.17}$	4.3(5)	5.0(6)	
100	•	A2IIIe	(42)	P	(42)			0.19	3.95	> 1.80			
129	•	B2Ve	(43)	C	(60)	180(20)	(20)	3.16	4.34	–			IR bin.
108	•	B2.5IVe	(44)	D	(61)	40(4)	(46)	1.92	4.31	$3.89^{+0.26}_{-0.21}$	10(2)	4.2(3)	IR bin.
49		B3ne	(20)	D	(46)	180(50)	(46)	1.89	4.27	> 0.71			
110		A4e+sh	(20)	P	(46)	150(12)	(46)	0.90	3.93	> 1.17			
104	•	B0e	(45)	P	(60)	100(30)	(62)	5.27	4.48	–			vis. bin.

Table 3.1. (Continued)

Low-mass young stellar objects

(1) HIP	(2) Name	(3) π [mas]	(4) $f_{\rm rej}$ [%]	(5) d [pc]	(6) Association D.C.	(7) Association B.N.	(8) Association S.A.	(9) $d_{\rm lit}$ [pc]	(10) Ref.	(11) $H_{\rm p,min.}$ [$^{\rm m}$]	(12) δH_p [$^{\rm m}$]
24855	HD 34700	0.9(1.8)	0	> 180						9.29	0.05
26295	CQ Tau	10.1(2.0)	0	100^{+25}_{-17}			Tau T4	130	(65)	9.96	1.07
58285	T Cha	15.1(3.3)	0	66^{+19}_{-12}	DC300.2-16.9		Cha I	160	(9)	10.73	2.69

Isolated B[e] stars

(1) HIP	(2) Name	(3) π [mas]	(4) $f_{\rm rej}$ [%]	(5) d [pc]	(6) Association D.C.	(7) Association B.N.	(8) Association S.A.	(9) $d_{\rm lit}$ [pc]	(10) Ref.	(11) $H_{\rm p,min.}$ [$^{\rm m}$]	(12) δH_p [$^{\rm m}$]
30800	HD 45677	2.8(1.1)	0	> 300						7.89	0.46
32923	HD 50138	3.5(0.8)	0	290^{+90}_{-50}						6.55	0.10
53444	GG Car	-1.8(1.7)	2	> 200						8.59	0.42
63547	CD$-48°7859$	-1.6(2.3)	3	> 140						10.52	0.18
87136	HD 316285	-0.1(1.5)	0	> 220	L34					8.93	0.13

Stars lacking evidence for circumstellar dust

(1) HIP	(2) Name	(3) π [mas]	(4) $f_{\rm rej}$ [%]	(5) d [pc]	(6) Association D.C.	(7) Association B.N.	(8) Association S.A.	(9) $d_{\rm lit}$ [pc]	(10) Ref.	(11) $H_{\rm p,min.}$ [$^{\rm m}$]	(12) δH_p [$^{\rm m}$]
21768	HD 283817	2.5(1.8)	0	> 180	L1538		Tau R2	140	(3)	10.46	0.16
26594	ω Ori	2.0(0.9)	2	> 210		DG 70	Ori OB1 a	400	(4)	4.44	0.09
28816	17 Lep	3.1(0.7)	0	330^{+90}_{-60}		Anon.		44	(75)	4.96	0.05
25950	HD 36408	2.9(1.6)	7	–						5.49	0.07
29988	MWC 137	-4.5(4.5)	0	> 110	(L1586,L1587)	S266		1100	(76)	11.78	0.17
33868	GU CMa	1.1(1.7)	10	–	L1657	S293	CMa R1	1150	(7)	6.52	0.22
34116	HD 53367	4.1(1.4)	8	–	L1657	S292	CMa R1	1150	(7)	7.03	0.24
43792	HD 76534	2.4(1.3)	1	> 160	DC264.3+1.5	Anon.	Vela R2	830	(77)	8.04	0.08
72616	HD 130437	-0.6(1.9)	0	> 180	DC318.2-0.6					9.91	0.15
100628	BD+41°3731	0.4(1.2)	3	> 260	L895	NGC 6914	Cyg R1	980	(15)	9.87	0.09
113017	IL Cep	1.2(1.7)	1	> 160	L1216	DG188	Cep OB3	690	(78)	9.28	0.08

S: Single Peak Hα profile; D: Double-peaked; P: P-Cygni or inverse P-Cygni profile; C: Complex Hα profile.

References to Table 3.1: (1) Hagen (1970); (2) Herbertz et al. (1991); (3) Elias (1978); (4) Warren & Hesser (1978); (5) Cantó et al. (1984); (6) Kutner et al. (1980); (7) Herbst et al. (1982); (8) Brandt et al. (1971); (9) Whittet et al. (1997); (10) Hu et al. (1989); (11) Thé & Tjin A Djie (1978); (12) Whittet (1974); (13) Andersen et al. (1989); (14) Marraco & Rydgren (1981); (15) Shevchenko et al. (1991); (16) Whitcomb et al. (1981); (17) Shevchenko & Yabukov (1989); (18) Dobashi et al. (1994); (19) Levreault (1988); (20) Finkenzeller (1985); (21) Racine (1968); (22) Finkenzeller & Mundt (1984); (23) Böhm & Catala (1993); (24) Jaschek et al. (1991); (25) Timoshenko (1985); (26) Cannon & Mayall (1949); (27) Dunkin et al. (1997); (28) Herbig (1960b); (29) de Winter, D., personal communication; (30) Houk, N. 1995, personal communication with B. Zuckerman; (31) Guetter (1981); (32) van den Ancker et al. (1996); (33) Whittet et al. (1987); (34) Houk (1978); (35) Houk & Cowley (1975); (36) Jaschek & Jaschek (1992); (37) Tjin A Djie et al. (1989); (38) Houk & Smith-Moore (1988); (39) Abt & Morrell (1995); (40) Kukarkin (1974); (41) Slettebak (1966); (42) Ringuelet et

(13) n_H	(14) Var.	(15) Sp. Type	(16) Ref.	(17) Hα	(18) Ref.	(19) $v \sin i$ [km s^{-1}]	(20) Ref.	(21) A_V [m]	(22) $\log T_{\rm eff}$	(23) $\log L_\star/L_\odot$	(24) M [M$_\odot$]	(25) log(Age) [yr]	(26) Remarks
74	•	G0Ve	(26)	S	(52)			0.68	3.78	> 1.23			
90	•	A1–F5IVe	(66)	D	(46)	110(20)	(46)	0.96	3.84	$-0.21^{+0.19}_{-0.16}$	–	–	
91	•	G2:e	(29)	P	(67)	48(10)	(68)	1.64	3.77	$0.13^{+0.22}_{-0.17}$	1.1(2)	> 7.1	

(13) n_H	(14) Var.	(15) Sp. Type	(16) Ref.	(17) Hα	(18) Ref.	(19) $v \sin i$ [km s^{-1}]	(20) Ref.	(21) A_V [m]	(22) $\log T_{\rm eff}$	(23) $\log L_\star/L_\odot$	(24) M [M$_\odot$]	(25) log(Age) [yr]	(26) Remarks
116	•	B2III–V[e]	(69)	D	(71)	70(20)	(73)	0.87	4.33	> 2.60			
82	•	B5V[e]	(29)	D	(72)	150	(74)	0.59	4.19	$2.85^{+0.23}_{-0.18}$	5.0(1.0)	5.0(5)	
124	•	B0–2[e]+K3:	(70)	D	(51)			2.57	4.41	> 3.17			vis. bin.
161	•	B6:III[e]	(29)	S	(51)			0.74	4.15	> 0.72			
61	•	B0[e]+sh	(70)					6.29	4.48	> 4.74			vis. bin.

(13) n_H	(14) Var.	(15) Sp. Type	(16) Ref.	(17) Hα	(18) Ref.	(19) $v \sin i$ [km s^{-1}]	(20) Ref.	(21) A_V [m]	(22) $\log T_{\rm eff}$	(23) $\log L_\star/L_\odot$	(24) M [M$_\odot$]	(25) log(Age) [yr]	(26) Remarks
74	•	A3e	(79)					3.41	3.94	> 1.72			Sp. bin.
76	•	B3IIIe	(80)	D	(22)	160(20)	(20)	0.28	4.23	> 3.42			
195	•	A1Ve+sh+M3III	(81)	P	(81)	105(30)	(39)	0.20	3.97	$3.21^{+0.21}_{-0.17}$	–	–	Sp. bin.
95	•	B7III+B7IV	(82)	S	(84)	60+300	(82)	0.28	4.12	–			vis. bin.
59		Bep	(83)	S	(22)			4.53	4.48	> 2.25			
81	•	B2Vne	(22)	D	(58)	400(40)	(20)	0.87	4.34	–			vis. bin.
78	•	B0IVe	(20)	S	(22)	30(15)		2.23	4.50	–			vis. bin.
120	•	B2ne	(20)	D	(85)	110(40)	(20)	1.21	4.34	> 2.48			vis. bin.
140	•	O8–B0ep	(29)					3.22	4.52	> 3.04			
112		B2ne	(20)	S	(60)	300(20)	(20)	1.02	4.34	> 2.01			IR bin.
112	•	B3e	(20)	D	(46)	190(15)	(46)	2.88	4.27	> 2.53			vis. bin.

al. (1987); (43) Hillenbrand et al. (1995); (44) Rogers et al. (1995); (45) Cohen & Kuhi (1979); (46) Böhm & Catala (1995); (47) Morrison, N.D. private communication; (48) Grinin et al. (1994); (49) Grady et al. (1996); (50) Reipurth et al. (1996); (51) van den Ancker, M.E., unpublished spectra Coudé Auxiliary Telescope, La Silla; (52) Zuckerman (1994); (53) Pogodin (1986); (54) Hamann & Persson (1992); (55) Vieira & Cunha (1994); (56) Andrillat et al. (1990); (57) Pérez et al. (1997); (58) Praderie et al. (1991); (59) Pogodin (1994); (60) Férnandez et al. (1995); (61) Beskrovnaya et al. (1994); (62) Herbig & Bell (1988); (63) Davis et al. (1983); (64) Bernacca & Perinotto (1970); (65) Artyukhina (1959); (66) Koval'chuk & Pugach (1992); (67) Alcalá et al. (1994); (68) Chavarria et al. (1989); (69) Feinstein et al. (1976); (70) Lopes et al. (1992); (71) de Winter & van den Ancker (1997); (72) Pogodin (1997); (73) Israelian & Musaev (1997); (74) Houziaux (1960); (75) Jenkins (1952); (76) Cahn et al. (1992); (77) Herbst (1975); (78) Mel'nikov et al. (1995); (79) Walter et al. (1990); (80) Danks & Dennefeld (1994); (81) Welty & Wade (1995); (82) Levato (1975); (83) Sabbadin & Hamzaoglu (1981); (84) Wackerling (1970); (85) Oudmaijer & Drew (1997).

tion for the Lutz-Kelker effect is expected to be small and will not seriously affect our results.

Columns 6–8 in Table 3.1 contain names of the star forming region in which the star is located (although one has to keep in mind that this could be a projection effect). In column 6 an association with a dark cloud from the catalogue of Lynds (1962), or its extension to the southern hemisphere (Hartley et al. 1986) is given. When the name of the dark cloud is in parentheses, this indicates that the star is located near the edge, so the association of the star with the cloud might be doubtful. In Table 3.1 some stars are associated with several dark clouds. These are local density enhancements in a larger complex, which were given separate designations in the Lynds catalogue.

The next column in Table 3.1 lists the reflection nebula with which the star is associated, taken from the catalogue of bright nebulae by Lynds (1965). The S-designations in this column refer to the catalogue of H II regions by Sharpless (1959), the DG designations refer to the paper by Dorschner & Gürtler (1963) and the C-designations are from the catalogue of diffuse galactic nebulae by Cederblad (1956). In a number of cases a bright nebula is clearly seen in the immediate surroundings of the star on Digital Sky Survey images of the region, but no designation for this nebula could be found. In these cases the $7^{\rm th}$ column in Table 3.1 lists "Anon.". The $8^{\rm th}$ column in Table 3.1 gives the name of a stellar aggregate with which the star is associated. A literature distance to the dark cloud, reflection nebula or stellar aggregate and a reference to the paper in which this was derived are provided in columns 9 and 10.

For all stars the Hipparcos satellite obtained broadband (3500–8500 Å) photometry at an effective wavelength of 5275 Å at some 100 distinct epochs during the 37 months (from 1989.85 to 1993.21) of its mission. These observations were made by a photon-counting image dissector tube with an instantaneous field of view of 30″ diameter. Because attenuation of the image dissector tube started at about 5″ from the center, a more realistic estimate of the spatial resolution of these observations will be 10″. For multiple systems with a separation between 10 and 30″, a correction was applied to the photometric data to subtract the light from the companion(s). For multiple systems with a smaller separation, the Hipparcos photometry refers to the total light. Typical errors in the individual measurements for this photometric system are smaller than $0\overset{\rm m}{.}011$ for stars brighter than $9^{\rm th}$ magnitude. In this chapter we will only use the data in the sense of and with the accuracy of a relative photometric system, increasing the accuracy of these measurements to a few millimagnitude for such stars. A more thorough description of the Hipparcos photometric system is given in the Explanatory Supplement to the Hipparcos Catalogue. The value at measured maximum brightness of the Hipparcos magnitude, H_p, the measured range in H_p (from the $5^{\rm th}$ and $95^{\rm th}$ percentile bin of the photometry), δH_p, and the number of measurements are listed in columns 11–13 of Table 3.1. For normal, non-variable stars δH_p ranges from $0\overset{\rm m}{.}02$ for stars brighter than $5^{\rm th}$ magnitude to values up to $0\overset{\rm m}{.}1$ for $9^{\rm th}$ magnitude stars and increases sharply for fainter objects. Finally, column 14 gives a flag indicating probable variables: Stars which show a measured range in H_p larger than the accuracy of the measurements.

Five stars in our sample were found to be visual binaries by Hipparcos. HD 150193,

now definitely a member of Sco R1, is the only newly detected one. The other binary detections are in agreement with earlier observations (Reipurth & Zinnecker 1993; Bernacca et al. 1993; Leinert et al. 1997; Pirzkal et al. 1997). Some stars which have been detected as multiple systems from ground-based speckle observations in the infrared were not detected as binaries by Hipparcos because of the large magnitude difference between primary and secondary in the optical. These are indicated by the remark IR binary in the last column of Table 3.1. Known spectroscopic binaries are also listed as such in the same column. Together this brings the total fraction of known binaries in our sample at 34%.

3.3 Astrophysical parameters

To assess the stellar temperature of HAeBe stars visual spectra are essential: UV spectra often overestimate temperatures, due to the presence of heated layers in the immediate surrounding of the stars' photospheres (e.g. Blondel & Tjin A Djie 1994), and photometric methods to estimate stellar temperatures yield erroneous results when the extinction law for the circumstellar material is anomalous, as is often the case for such stars (e.g. Thé et al. 1996). Therefore a list of spectral types based on optical spectra from literature as well as on unpublished spectroscopy by the authors was assembled and is given, together with its reference, in the $15^{\rm th}$ and $16^{\rm th}$ column of Table 3.1. In a few cases (e.g. Z CMa) even the optical spectrum is heavily influenced by the circumstellar shell and may reflect the spectral type of this shell rather than that of the underlying stellar photosphere. Columns 17–20 give an identifier with the type of Hα emission profile, a literature estimate of $v \sin i$ and references to the papers in which this was derived. In a number of cases an e (for emission-line star) was added to the original classification when it was evident from other sources that the star is an Hα emitter.

To be able to compute the total luminosity of the stars in our sample, photometric data, from the ultraviolet (ANS, TD1, IUE), through the optical (Walraven $WULBV$, Johnson/Cousins $UBVRI$) to the infrared ($JHKLMNQ$, IRAS), were collected from literature. Since many of the stars in our sample show strong variations in brightness, only optical and UV data obtained near maximum brightness were used. After using the calibrations of Schmidt-Kaler (1982) to adopt an effective temperature $T_{\rm eff}$ and surface gravity $\log g$ corresponding to the star's MK spectral type, the stellar luminosity was computed following the method outlined in van den Ancker et al. (1997). This method includes a correction for a possible anomalous extinction law towards the object. An estimate of the star's infrared excess in the L and IRAS 12 micron bands was made by computing the magnitude difference between the extinction-corrected observed magnitude and a Kurucz (1991) stellar atmosphere model fitted to the extinction-corrected optical photometry. The computed visual extinction at maximum brightness A_V, effective temperature $T_{\rm eff}$ and stellar luminosity $L_\star$ are listed in columns 21–23 of Table 3.1.

In Figure 3.1, we plot the programme stars for which the Hipparcos mission re-

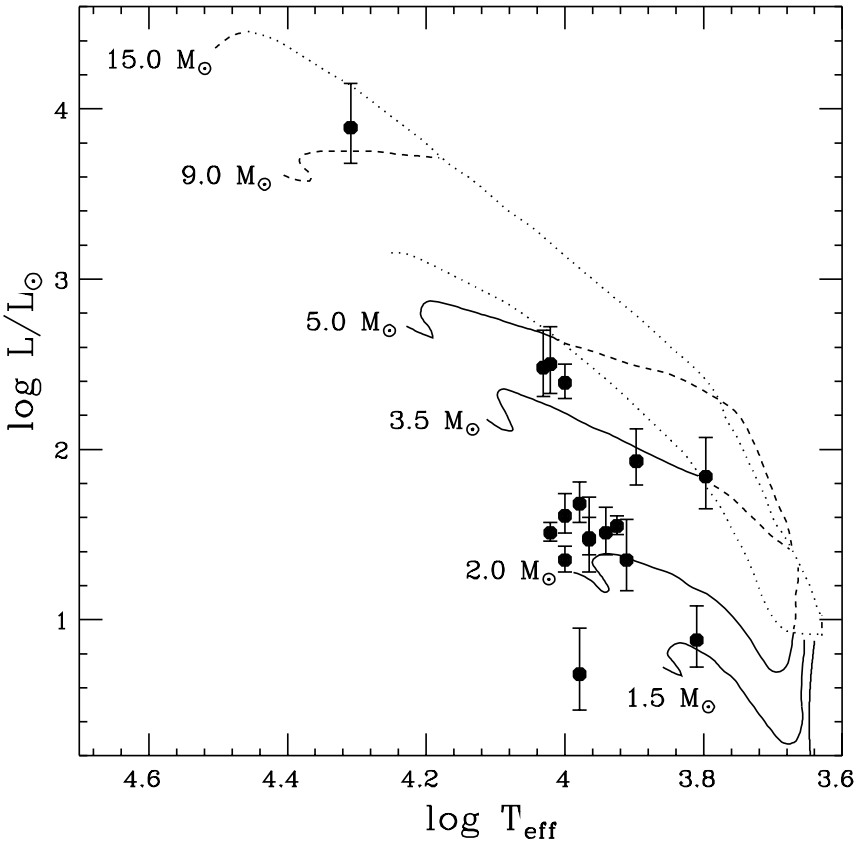

Fig. 3.1. Hertzsprung-Russell diagram of HAeBe stars with parallaxes measured by Hipparcos. Also shown are the theoretical PMS evolutionary tracks (solid lines and dashed lines) and the birthlines for 10^{-4} (upper dotted line) and 10^{-5} $M_\odot$ yr^{-1} (lower dotted line) by Palla & Stahler (1993).

sulted in a better than 3σ detection of the trigonometric parallax in the HRD. Typical errors in $\log T_{\rm eff}$ are about 0.05 (or one subclass in spectral type), but individual data points may have larger errors. The error in luminosity is dominated by the error in the distance and is indicated by the error bars. Also shown in Fig. 3.1 are the PMS evolutionary tracks and the birthline (i.e. the line where a star first becomes optically visible on its evolution to the zero-age main sequence) computed by Palla & Stahler (1993). Using these evolutionary tracks and the isochrones given by the same authors, we can make an estimate of the masses and ages of our programme stars. These are listed, together with their error estimates, in columns 24 and 25 of Table 3.1. Note that these ages are based on the assumption that we are dealing with objects that are still contracting towards the zero-age main sequence (ZAMS). If this assumption is incorrect (e.g. HD 200775, Chapter 2), the listed ages will of course be erroneous as well.

As can be seen from Fig. 3.1, one star is located slightly to the left of the ZAMS, but all other stars are located in the region between the ZAMS and the birthline, as is expected for PMS stars. The star that is located to the left of the ZAMS, HD 34282, is not well studied. Possibly its spectral type, based on data from the Henry Draper

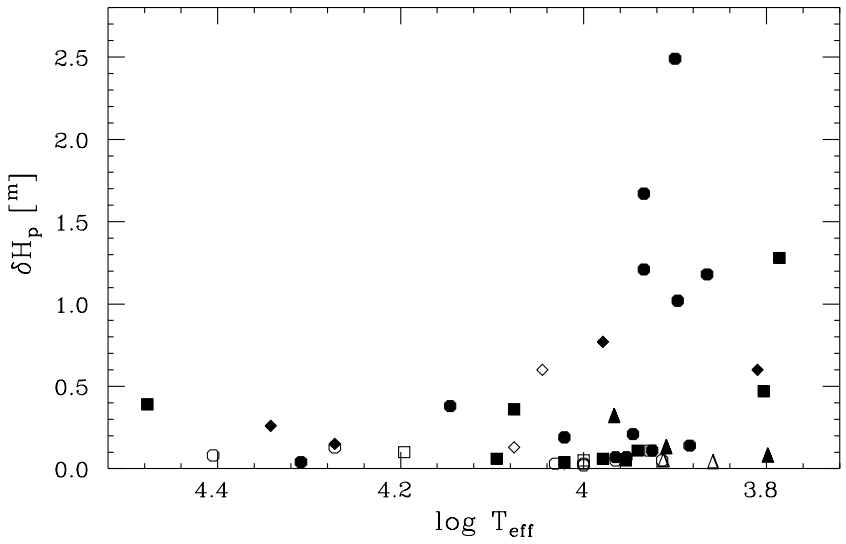

Fig. 3.2. Amplitude of the variations found in HAeBe stars as a function of stellar effective temperature. Circles indicate stars in which the Hα line is predominantly double-peaked, squares indicate stars in which Hα shows a P Cygni profile, triangles indicate stars with a single-peaked Hα line in emission and diamonds are used for stars in which Hα is in emission, but for which no information on its shape is available. Open plot symbols indicate stars for which the measured range in variability could be due to the uncertainty in the individual photometric measurements.

Memorial Catalogue, is erroneous or the photometric data set used to compute the stellar luminosity was not obtained near maximum stellar brightness. The clustering of stars in the HRD near the ZAMS can be easily explained by the fact that stars evolve much slower in the part of their PMS evolutionary track near the ZAMS than in the part near the birthline. The distribution over the different masses in this diagram, with less high-mass than intermediate-mass stars, is also in accordance with the expected ratios of a standard mass distribution.

3.4 Photometric behaviour

Bibo & Thé (1991) analysed Strömgren photometry for 23 HAeBe candidates measured in ESO's Long Term Photometry of Variables (LTPV) programme. For the stars in common with our sample, their measured range in the Strömgren y magnitude agrees within $0\overset{\text{m}}{.}1$ with our range in H_p, indicating that for these well studied cases δH_p is a good measure for the total range of variability. The number of stars in our sample is much larger than that measured by these authors (with a comparable number of measurements per star), and is much less observationally biased, which should enable us to draw statistically more significant conclusions on the level of variability of the HAeBe stellar group as a whole.

3.4.1 Inclination effects

A very strong correlation between the level of photometric variability of a HAeBe star and its spectral type was found by Finkenzeller & Mundt (1984): Nearly all strongly variable ($\Delta V > 0\overset{\mathrm{m}}{.}5$) stars in their sample have spectral types later than B8 and all stars with no significant variations ($\leq 0\overset{\mathrm{m}}{.}05$) are of spectral type earlier than A0. Later this result was reproduced by Bibo & Thé (1991), who suggested that this result was due to selection effects in their limited sample. Davies et al. (1990) showed several examples of *bona fide* Herbig Ae (HAe) stars which do not show the large variations predicted for such stars by Finkenzeller & Mundt (1984), suggesting that the link between photometric variability and spectral type may not be as well defined as implied by these authors.

Bibo & Thé (1991) pointed out that since these strongly variable stars spend most of their time near maximum brightness and the typical timescale of such photometric events is of the order of weeks, many accurate photometric measurements over a significantly longer period are needed to get a good unbiased measurement of the amount of photometric variability. This is a criterion which is not met in a systematic way for all data-sets present in literature. However, the Hipparcos photometry listed in Table 3.1 consists of roughly one hundred measurements per star, taken at essentially random time intervals with the same instrument over a 37 month period, without any bias to observe the "more interesting" cases more than others, as is often the case in ground-based work. Therefore it is much better suited to make an unbiased estimate of the level of photometric variability than the data sets used in previous studies. For this reason a new diagram of $\log T_{\mathrm{eff}}$ versus δH_p was constructed, shown in Fig. 3.2. As can be seen from this plot, some trend between stellar temperature and level of photometric variability is clearly present: Only stars with spectral type of A0 or later can show variations with an amplitude larger than $0\overset{\mathrm{m}}{.}5$. However, moderate photometric variations, of the order of several tenths of a magnitude can be seen in all spectral types present in our sample. In fact only 15 out of 44 stars in our sample are not flagged as variable and in some cases this is clearly due to the fact that they are too faint to be measured accurately by Hipparcos. We conclude that at least 65% of all HAeBes do show photometric variability with an amplitude larger than $0\overset{\mathrm{m}}{.}05$.

In the past many authors have constructed colour-magnitude diagrams for HAeBe stars, and noted that for all stars showing large and for most stars showing intermediate brightness variations, there seems to be a good correlation between colour and brightness, with a redder colour corresponding to fainter brightness. In addition to this, the linear polarization of the starlight also increases with diminishing brightness. This behaviour is characteristic of variable, presumably circumstellar, extinction of starlight by dust particles. Wenzel (1968) originally suggested that these dust particles are located in patchy dust clouds, revolving in Keplerian orbits around most HAeBes. Smaller variations superimposed on these may be explained by photospheric activity or clumpy accretion.

With this picture in mind, one possible explanation for the fact that large photometric variations only occur at spectral types later than A0 could be that since dust particles

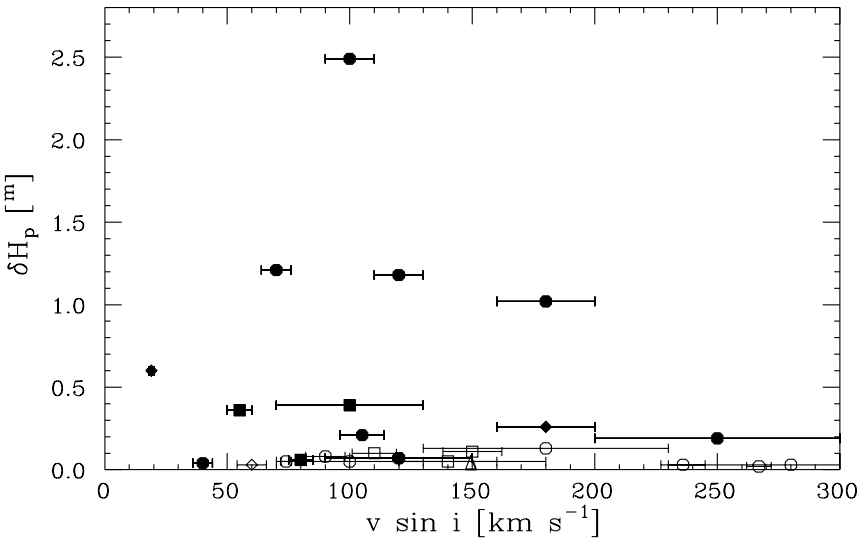

Fig. 3.3. Amplitude of the variations found in HAeBe stars as a function of stellar $v \sin i$. Plot symbols have the same meaning as in Fig. 3.2.

can survive closer to the star in cooler stars than in hot stars, the range of inclination angles under which we would have to observe such a system to have these dust clouds in our line of sight would be narrower for B-type stars than for A-type stars. In this picture all HAeBe stars would have these dust clouds orbiting them, but we will only see these in our line of sight and hence see large amplitude variations for systems seen more or less edge-on, recognizable by statistically larger value of $v \sin i$. If we combine the literature data given in Table 3.1 with the Hipparcos data to construct a diagram of $v \sin i$ versus δH_p (Fig. 3.3), no such correlation can be seen. One reason for this apparent lack of correlation could be that in a lot of HAeBes these $v \sin i$ determinations are difficult and sometimes even erroneous due to the lack of photospheric lines without (sometimes variable) emission components. Also, one would expect these young stars to continue to spin-up during their PMS contraction phase, so the spread in the intrinsic rotational velocity may have a stronger influence on the value of $v \sin i$ than the inclination. The fact that the range in quoted values on $v \sin i$ is quite similar to that seen in normal main sequence stars of the same spectral type argues against the latter effect.

Grinin & Rostopchina (1996) argued that the same inclination effect should be visible as a correlation between the level of photometric variability and the shape of the Hα line, presumably formed in a circumstellar gaseous disk: In analogy to the situation in classical Be stars, we would expect to see a single-peaked Hα profile in stars seen pole-on, thus showing little photometric variability, and the stars with large photometric variations, seen more or less edge on, should show a double-peaked Hα profile. In this scenario, the variations seen in Hα, in which this line has one preferred shape, but in some stars is occasionally seen to switch from for example double-peaked to single-peaked could be either due to inhomogeneities in the accretion of circumstellar gas, or due to a contrast effect in which part of the circumstellar gas is obscured by

inhomogeneous dust clouds (Grinin et al. 1994).

Upon closer inspection of Fig. 3.2, in which the different preferred types of Hα profiles from literature are indicated by different plot symbols, we note that indeed most stars showing large photometric variations show double-peaked Hα emission and all stars with single-peaked Hα profiles only show moderate photometric variations. However, not all stars with little or no photometric variability show a single-peaked emission profile. In fact many of these show a double-peaked emission line as well. Therefore we conclude that if a dependence on inclination is present in both δH_p and the shape of Hα, some other effect must be present as well to disturb the one to one correspondence.

3.4.2 Evolutionary hypothesis

Another possible explanation for the trend shown in Fig. 3.2 could be that we are seeing an evolutionary effect: According to the calculations by Palla & Stahler (1993), A-type stars are optically visible during their contraction towards the ZAMS, whereas B-type stars only become visible when they are very close to the ZAMS (c.f. the birthline in Fig. 3.2). In this scenario the amplitude of the variations of HAe stars would diminish with time until they would vanish after the star has finished its main sequence contraction. Support for this view comes from the observation that most stars with $\delta H_p > 0\overset{\mathrm{m}}{.}5$ are classified spectroscopically as giants, and many of them are located right of the main sequence in Fig. 3.1.

The fact that some giants do not show these strong photometric variations could be taken as evidence for the presence of an inclination effect. However, van den Ancker et al. (1996) showed that HAe stars change back and forth between a quiescent state in which they show only very moderate photometric variations and an active state in which the large amplitude variations are present many times during their evolution towards the ZAMS. The time scale over which such a star will remain in one state will be much longer than the 37 months over which our range in variability was measured. Considering the statistics in Table 3.1, in which there are only four *bona fide* HAe giants that do not show large photometric variations, we consider it more plausible that the photometrically inactive giants are in this quiescent state than to take this as an indication of an inclination effect. Since it is clear that other effects than inclination have a strong influence on the level of photometric variability as well, some caution must be taken in the current practice in literature of equating strongly variable HAeBe stars to Herbig stars seen edge-on.

3.4.3 Correlations with infrared excess

If the interpretation of the large photometric variations as being due to variable extinction by circumstellar dust is correct, one could expect some form of correlation between the infrared excess and level of photometric variability in HAeBe stars. From the typical time scales of days to weeks associated with these variations, it was shown that the dust clouds responsible for this must be at roughly one AU from the central

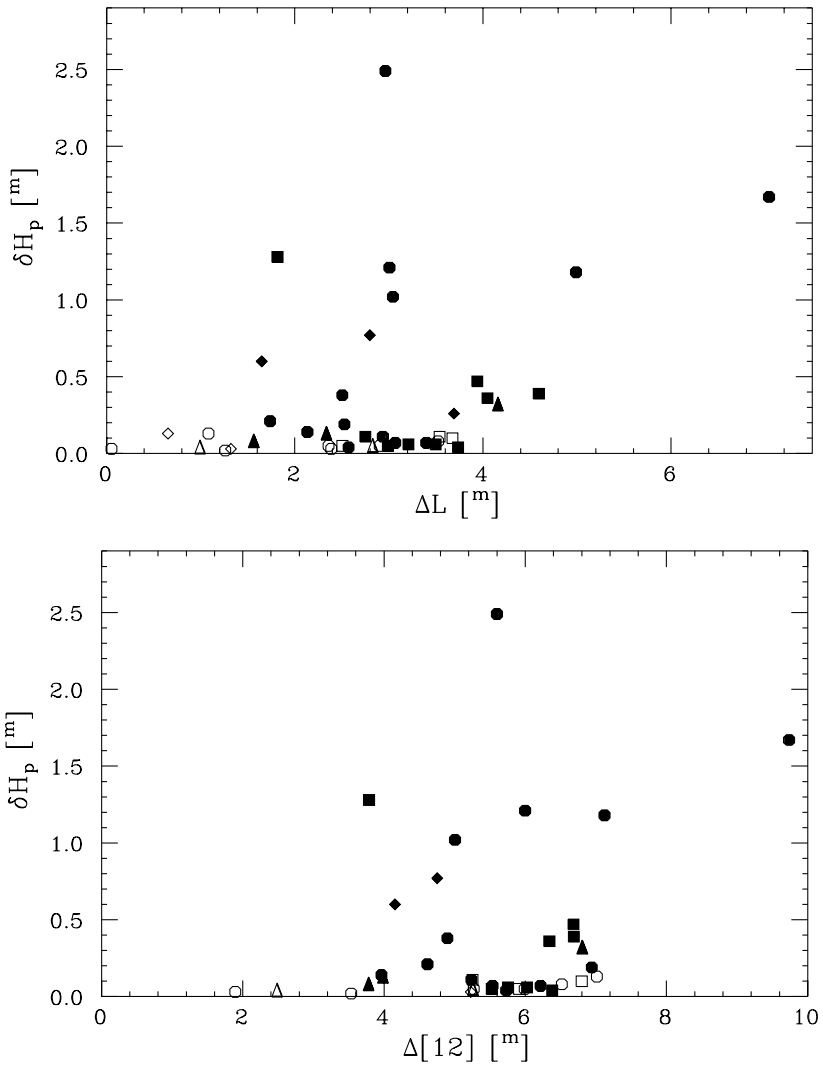

Fig. 3.4. Amplitude of the variations found in HAeBe stars as a function of infrared excess in the L (top) and IRAS 12 micron (bottom) bands. Plot symbols have the same meaning as in Fig. 3.2.

star (Thé & Molster 1994). At these distances the dust clouds should be heated up sufficiently by the central star to radiate efficiently at infrared wavelengths. Therefore one would expect that stars with smaller infrared excesses do not show photometric variations, whereas the ones with larger infrared excesses can show both large and smaller photometric variations, depending on the inclination angle under which they are seen.

To check for the presence of such a correlation we plot our δH_p against the excess at 3.6 and 12 microns (Fig. 3.4). Indeed, none of the Herbig stars with small excesses at these wavelengths shows strong photometric variability, whereas the ones with larger excesses show a large spread in δH_p. It is interesting to extrapolate this result to young stellar objects with less circumstellar material than the stars we have included in our sample. Probably these will be recognizable as β Pic-like systems (Chapter 2), with usually smaller infrared excesses and with less circumstellar gas than the HAeBes.

Therefore we compiled a list of 52 B-, A- and F-type candidates for stars with circumstellar dust and Hipparcos data. None of these stars shows a range in H_p larger than $0\overset{\mathrm{m}}{.}1$. In fact, the Hipparcos photometry of β Pic itself is constant at the millimagnitude level. This shows that the trend seen in our sample of HAeBes can be smoothly extrapolated to the Vega-type stars and that our results are compatible with an evolutionary scenario in which the two are linked.

3.5 Conclusions

In this chapter we have studied the photometric behaviour of a sample of 44 HAeBe stars using a uniform data-set, provided by the Hipparcos astrometric satellite, which is superior to those used in previous studies. We have shown that most ($> 65\%$), and possibly all, HAeBes show photometric variations at the level of at least a few hundredths of a magnitude.

As was already suggested by previous authors, Herbig stars with a spectral type earlier than A0 only show moderate (amplitude $< 0\overset{\mathrm{m}}{.}5$) photometric variability, whereas the ones of later spectral type in our sample can show variations larger than $2\overset{\mathrm{m}}{.}5$. These HAe stars showing strong photometric variability are relatively uncommon: more HAe stars show moderate than large variations. Previous studies have shown that these large photometric variations are due to variable extinction by circumstellar patchy dust clouds, whereas a variety of mechanisms could be responsible for the moderate to small ones. We suggest that these patchy dust clouds are only present during the PMS evolution of a star, and either vanish or become more homogeneous when a star has reached the ZAMS. Probably this evolutionary effect, as well as the spin-up of a star as it evolves towards the ZAMS, explains the poor correlation between $v \sin i$ or the Hα profile and the level of photometric variability.

It was found that the Herbig stars with the smallest infrared excesses in our sample do not show large photometric variations, whereas the ones with larger infrared excesses can (but not necessarily have to) show variation up to $2\overset{\mathrm{m}}{.}5$. This can be understood by identifying the stars with lower infrared excesses with the more evolved objects in our sample. Since Vega-type stars do not show these variations due to variable circumstellar extinction and also display smaller infrared excesses, this is compatible with a scenario in which these Herbig stars will in time evolve into more massive equivalents of β Pic.

Acknowledgements. This chapter is based on data from the Hipparcos astrometry satellite. The authors would like to thank Rens Waters and Mario Pérez for careful reading of the manuscript prior to publication. We would also like to thank the referees, Floor van Leeuwen and George Herbig, for many useful suggestions and comments. This research has made use of the Simbad data base, operated at CDS, Strasbourg, France.

References

Abt, H.A., Morrell, N.I. 1995, ApJS 99, 135

Acker, A., Chopinet, M., Pottasch, S.R., Stenholm, B. 1987, A&AS 71, 163
Alcalá, J.M., Covino, E., Krautter, J., Terranegra, L., Wiohmann, R. 1994, Rev. Mex. Astron. Astrofis. 29, 217
Andersen, J., Lindgren, H., Hazen, M.L., Mayor, M. 1989, A&A 219, 142
Andrillat, Y., Jaschek, M., Jaschek, C. 1990, A&A 233, 474
Artyukhina, N.M. 1959, SvA 3, 808
Bernacca, P.L., Lattanzi, M.G., Bucciarelli, B., Bastian, U., Barbaro, G., Pannunzio, R., Badiali, M., Cardini, D., Emanuele, A. 1993, A&A 278, L47
Bernacca, P.L., Lattanzi, M.G., Porro, I., Neuhäuser, R., Bucciarelli, B. 1995, A&A 299, 933
Bernacca, P.L., Perinotto, M. 1970, *"A Catalogue of Stellar Rotational Velocities"*, Contr. Asiago, 239, 1
Beskrovnaya, N.G., Pogodin, M.A., Shcherbakov, A.G., Tarasov, A.E. 1994, A&A 287, 564
Bibo, E.A., Thé, P.S. 1991, A&AS 89, 319
Blondel, P.F.C., Tjin A Djie, H.R.E. 1994, ASP Conf. Ser. 62, 211
Böhm, T., Catala, C. 1993, A&AS 101, 629
Böhm, T., Catala, C. 1995, A&A 301, 155
Brandt, J.C., Stecher, T.P., Crawford, D.L., Maran, S.P. 1971, ApJ 163, L99
Brown, A.G.A., Arenou, F., van Leeuwen, F., Lindegren, L., Luri, X. 1997, in proc. *"Hipparcos Venice '97"* symposium, ESA SP-402, p. 63
Cahn, J.H., Kaler, J.B., Stanghellini, L. 1992, A&AS 94, 399
Cannon, A.J., Mayall, M.W. 1949, *"The Henry Draper Extension"*, Harvard Ann. 112, 1
Cantó, J., Rodriguez, L.F., Calvet, N., Levreault, R.M. 1984, ApJ 282, 631
Catala, C., Böhm, T., Donati, J.F., Semel, M. 1993, A&A 278, 187
Cederblad, S. 1956, Medd. Lund 2, 119
Chavarria, C., Covino, E., Franchini, M., Stalio, R., Terranegra, L. 1989, The Messenger 58, 35
Cohen, M., Kuhi, L.V. 1979, ApJS 41, 743
Danks, A.C., Dennefeld, M. 1994, PASP 106, 382
Davies, J.K., Evans, A., Bode, M.F., Whittet, D.C.B. 1990, MNRAS 247, 517
Davis, R., Strom, K.M., Strom, S.E. 1983, AJ 88, 1644
de Winter, D., van den Ancker, M.E. 1997, A&AS 121, 275
Dobashi, K., Bernard, J.P., Yonekura, Y., Fukui, Y. 1994, ApJS 95, 419
Dorschner, J., Gürtler, J. 1963, Astron. Nachr. 287, 257
Dunkin, S.K., Barlow, M.J., Ryan, S.G. 1997, MNRAS 286, 604
Elias, J.H. 1978, ApJ 224, 857
ESA, 1997, The Hipparcos Catalogue, ESA SP-1200
Feinstein, A., Garnier, R., Vogt, N., Heck, A., Manfroid, J., Swings, J.P. 1976, A&A 51, 269
Férnandez, M., Ortiz, E., Eiroa, C., Miranda, L.F. 1995, A&AS 114, 439
Finkenzeller, U. 1985, A&A 151 340
Finkenzeller, U., Mundt, R., 1984, A&AS 55, 109
Grady, C.A., Pérez, M.R., Talavera, A., Bjorkman, K.S., de Winter, D., Thé, P.S., Molster, F.J., van den Ancker, M.E., Sitko, M.L., Calvet, N., Morrison, N.D., McCollum, B., Castelaz, M.W. 1996, A&AS 120, 157
Grinin, V.P., Rostopchina, A.N. 1996, Astron. Rep. 40, 171
Grinin, V.P., Thé, P.S., de Winter, D., Giampapa, M., Rostopchina, A.N., Tambovtseva, L.V., van den Ancker, M.E. 1994, A&A 292, 165
Guetter, H.H. 1981, AJ 86, 1057
Hagen, G. 1970, Publ. David Dunlap Obs. 4, 1

Hamann, F., Persson, S.E. 1992, ApJS 82, 285
Hartley, M., Manchester, R.N., Smith, R.M., Tritton, S.B., Goss, W.M. 1986, A&AS 63, 27
Herbertz, R., Ungerechts, H., Winnewisser, G. 1991, A&A 249, 483
Herbig, G.H. 1960a, ApJS 4, 337
Herbig, G.H. 1960b, ApJ 131, 632
Herbig, G.H., Bell, K.R., 1988, *"Third Catalog of Emission-Line Stars of the Orion Population"*, Lick Obs Bull. 1111, 1
Herbst, W. 1975, AJ 80, 683
Herbst, W., Miller, D.P., Warner, J.W., Herzog, A. 1982, AJ 87, 98
Hillenbrand, L.A., Meyer, M.R., Strom, S.E., Skrutskie, M.F. 1995, AJ 109, 280
Houk, N. 1978, Michigan Spectral Survey, Vol. 2, Univ. Michigan Press
Houk, N., Cowley, A.P. 1975, Michigan Spectral Survey, Vol. 1, Univ. Michigan Press
Houk, N., Smith-Moore, A. 1988, Michigan Spectral Survey, Vol. 4, Univ. Michigan Press
Houziaux, L. 1960, J. Obs. 43, 217
Hu, J.Y., Thé, P.S., de Winter, D. 1989, A&A 208, 213
Israelian, G., Musaev, F. 1997, A&A 328, 339
Jaschek, M., Andrillat, Y., Jaschek, C. 1991, A&A 250, 127
Jaschek, C., Jaschek, M. 1992, A&AS 95, 535
Jenkins, L.F. 1952, Gen. Cat. of Trigon. Stellar Parall., Yale Univ., New Haven
Koval'chuk, G.U., Pugach, A.F. 1992, Kinematika Fiz. Nebesn. Tel. 8, 71
Kukarkin, B.V. 1974, General Catalogue of Variable Stars, Moscow
Kurtz, D.W., Marang, F. 1995, MNRAS 276, 191
Kurucz, R.L. 1991, in *"Stellar atmospheres–Beyond classical models"* (eds. A.G. Davis Philip, A.R. Upgren, K.A. Janes), L. Davis press, Schenectady, New York, p. 441
Kutner, M.L., Machnik, D.E., Tucker, K.D., Dickman, R.L. 1980, ApJ 237, 734
Leinert, C., Richichi, A., Haas, M. 1997, A&A 318, 472
Levato, A. 1975, A&AS 19, 91
Levreault, R.M. 1988, ApJS 67, 283
Lopes, D.F., Neto, A.D., de Freitas Pacheco, J.A. 1992, A&A 261, 482
Lutz, T.E., Kelker, D.H. 1973, PASP 85, 573
Lynds, B.T. 1962, ApJS 7, 1
Lynds, B.T. 1965, ApJS 12, 163
Malfait, K., Bogaert, E., Waelkens, C. 1998, A&A 331, 211
Marraco, H.G., Rydgren, A.E. 1981, AJ 86, 62
Martín, E.L. 1993, PASP 105, 277
Mel'nikov, S.Y., Shevchenko, V.S., Grankin, K.N. 1995, Astron. Rep. 39, 42
Oudmaijer, R.D., Drew, J.E. 1997, A&A 318, 198
Oudmaijer, R.D., Groenewegen, M.A.T., Schrijver, H. 1998, MNRAS 294, L41
Palla, F., Stahler, S.W. 1993, ApJ 418, 414
Pérez, M.R., Bopp, B.W., Aufdenberg, J., de Winter, D., van den Ancker, M.E., Grady, C.A., Fekel, F.C. 1997, in preparation
Pérez, M.R., Webb, J.R., Thé, P.S. 1992, A&A 257, 209
Pirzkal, N., Spillar, E.J., Dyck, H.M. 1997, ApJ 481, 392
Pogodin, M.A. 1986, Astrofizika 24, 491
Pogodin, M.A. 1994, A&A 282, 141
Pogodin, M.A. 1997, A&A 317, 185
Praderie, F., Catala, C., Czarny, J., Thé, P.S., Tjin A Djie, H.R.E. 1991, A&AS 89, 91

Racine, R. 1968, AJ 73, 233
Reipurth, B., Pedrosa, A., Lago, M.T.V.T. 1996, A&AS 120, 229
Reipurth, B., Zinnecker, H. 1993, A&A 278, 81
Ringuelet, A.E., Rovira, M., Cidale, L., Sahade, J. 1987, A&A 183, 287
Rogers, C., Heyer, M.H., Dewdney, P.E. 1995, ApJ 442, 694
Sabbadin, F., Hamzaoglu, E. 1981, A&A 94, 25
Schmidt-Kaler, Th. 1982, *"Landölt-Bornstein Catalogue"*, VI/2b
Sharpless, S. 1959, ApJS 4, 257
Shevchenko, V.S., Ibragimov, M.A., Chernysheva, T.L. 1991, SvA 35, 229
Shevchenko, V.S., Yabukov, S.D. 1989, A. Zh. 66, 718
Slettebak, A. 1966, ApJ 145, 121
Sonneborn, G., Grady, C.A., Wu, C.C., Hayes, D.P., Guinan, E.F., Barker, P.K., Henrichs, M.F. 1988, ApJ 325, 784
Sylvester, R.J., Skinner, C.J., Barlow, M.J., Mannings, V. 1996, MNRAS 279, 915
Thé, P.S., de Winter, D., Pérez, M.R. 1994, A&AS 104, 315
Thé, P.S., Molster, F.J. 1994, Ap&SS 212, 125
Thé, P.S., Pérez, M.R., Voshchinnikov, N.V., van den Ancker, M.E. 1996, A&A 314, 233
Thé, P.S., Tjin A Djie, H.R.E. 1978, A&A 62, 439
Timoshenko, L.V. 1985, Astrofizika 22, 51
Tjin A Djie, H.R.E., Thé, P.S., Andersen, J., Nordstrom, B., Finkenzeller, U., Jankovics, I. 1989, A&AS 78, 1
van den Ancker, M.E., Thé, P.S., de Winter, D. 1996, A&A 309, 809 (Chapter 4)
van den Ancker, M.E., Thé, P.S., Feinstein, A., Vázquez, R.A., de Winter, D., Pérez, M.R. 1997, A&AS 123, 63
van Leeuwen, F., Evans, D.W., Grenon, M., Grossmann, V., Mignard, F., Perryman, M.A.C. 1997, A&A 323, L61
Vieira, S.L.A., Cunha, N.C.S. 1994, IAU Inform. Bull. Var. Stars 4090, 1
Wackerling, L.R. 1970, PASP 82, 1357
Waelkens, C., Bogaert, E., Waters, L.B.F.M. 1992, ASP Conf. Ser. 62, 405
Walter, F.M., Skinner, S.L., Boyd, W.T. 1990, PASP 102, 754
Warren, W.H., Hesser, J.E. 1978, ApJS 36, 497
Welty, A.D., Wade, R.A. 1995, AJ 109, 327
Wenzel, W. 1968, IAU Coll. *"Non-periodic Phenomena in Variable Stars"*, Budapest, p. 61
Whitcomb, S.E., Gatley, I., Hildebrand, R.H., Keene, J., Sellgren, K., Werner, M.W. 1981, ApJ 246, 416
Whittet, D.C.B. 1974, MNRAS 168, 371
Whittet, D.C.B., Kirrane, T.M., Kilkenny, D., Oates, A.P., Watson, F.G., King, D.J. 1987, MNRAS 224, 497
Whittet, D.C.B., Prusti, T., Franco, G.A.P., Gerakines, P.A., Kilkenny, D., Larson, K.A., Wesselius, P.R. 1997, A&A 327, 1194
Zuckerman, B. 1994, in *"Circumstellar dust disks and planet formation"*, proc. $10^{\rm th}$ IAP astrophysics meeting, Eds. R. Ferlet & A. Vidal-Madjar, p. 131

Chapter 4

The Remarkable Photometric Behaviour of the Herbig Ae Star V351 Ori

M.E. van den Ancker, P.S. Thé and D. de Winter,
A&A 309, 809 (1996)

Abstract

The photometric behaviour of the irregular variable Herbig Ae star V351 Ori was investigated combining data from the literature with new photometric data in the Strömgren system. It is shown that this enigmatic object changed its photometric behaviour from that of a Herbig Ae star with strong photometric variations, due to extinction by circumstellar dust clouds, to that of an almost non-variable star. Such a behaviour is not unique; it has been found also in the star BN Ori (Shevchenko et al. 1997). This suggests that such transitions must occur quite often during the evolution of intermediate mass HAeBe stars towards the main sequence (MS). However, it is equally probable that before such a star arrives at the MS, it will become strongly variable again after collecting enough dust from its environment.

During the process of V351 Ori's transition from a Herbig Ae star with strong photometric variations to a non-variable one, the maximum brightness in the Strömgren v, b and y magnitudes decreased, whereas that in u increased, causing a strong blueing effect in the colour-magnitude diagrams. It should be noted that this effect happened at a decrease in visual brightness by about $0\overset{\mathrm{m}}{.}2$ magnitude only. It is therefore caused by a different mechanism than that in V351 Ori before the transition and in UX Ori type stars, where the blueing effect occurs at a decrease in V of about $2\overset{\mathrm{m}}{.}5$.

The transition, from a strongly variable star to the state in which V351 Ori is nearly constant at a level equal to that of its maximum brightness before the transition, happened very fast (within 50 days), and went along the interstellar reddening line in the colour-magnitude diagrams. A provisional model to explain V351 Ori's behaviour, in which it is assumed that a temporarily strong accretion of matter onto the star took place, is proposed.

4.1 Introduction

The irregular variable Hα-emission line star V351 Ori = HD 38238 (R.A. = $05^{\rm h}44^{\rm m}18\overset{\rm s}{.}8$; Dec. = +00°08′40″; 2000) was not recognized by Herbig (1960) as a Herbig Ae/Be (HAeBe) object. Finkenzeller & Mundt (1984) also did not include V351 Ori in their catalogue of HAeBes, but Koval'chuk (1985b) and Zajtseva (1986) believe that V351 Ori belongs to the HAeBe group. Accidentally, the star was also not listed in the catalogue of HAeBes by Thé et al. (1994). The brightness of V351 Ori changes from $B = 8\overset{\rm m}{.}3$ to $11\overset{\rm m}{.}6$, as given in Parenago's *General Catalogue of Variable Stars*. The star is located in the direction of the Lynds 1630 dark cloud region, defined by Lynds (1962), and is accompanied by a $13^{\rm th}$ magnitude ($m_{\rm pg}$) star, located 15″ west of it.

Photometric observations of V351 Ori were published by Koval'chuk (1984a) in the Johnson $UBVRI$ system, by Chkhikvadze (1990) in the Strömgren $uvby$ system, and by Kilkenny et al. (1985) in the Strömgren $uvby$, Johnson-Cousins $UBV(RI)_C$ and in the near-IR $JHKL$ systems. From his colour-magnitude diagrams Chkhikvadze (1990) notes the presence of a weak blueing effect. However, such blueing effect had been found previously by Koval'chuk (1985a) more pronouncedly. Kilkenny et al. (1985) did not analyse their observations of V351 Ori. Zajtseva (1986) classified V351 Ori as of spectral type A7 III, and InSa as the type of variability. A flare-like event, strongest in the ultraviolet, observed in the lightcurve of V351 Ori has been reported by Koval'chuk (1984b), without an explanation of its cause.

We present in this chapter the results of our study of the photometric and colour behaviour, and the spectral energy distribution (SED) of V351 Ori. For this purpose we have obtained new photometric observations, which were combined with the data of Koval'chuk (1984a), Chkhikvadze (1990) and of Kilkenny et al. (1985). For a better knowledge of the properties of V351 Ori new visual low and high resolution spectra were obtained as well.

4.2 Observations

4.2.1 Photometry

During the last seven years, V351 Ori was monitored by the ESO "Long Term Photometry of Variables" (LTPV) group, using the Strömgren Automatic Telescope (SAT; former Danish 50 cm telescope) at La Silla. This telescope is equipped with a simultaneous multicolour photometer using the Strömgren $uvby$ system. Any systematic effect due to non-simultaneous measurements at the different passbands are therefore avoided. Because we used a diaphragm with a small diameter (17″), we do not expect any significant contamination of our measurements with the light from the $13^{\rm th}$ magnitude star located 15″ west of V351 Ori. Immediately before and after each programme star measurement two comparison stars (HD 38155 and HD 38203), located close to, and with roughly the same magnitude and colours as V351 Ori, were measured to check whether the observed variations are real. Since parts of these observations were

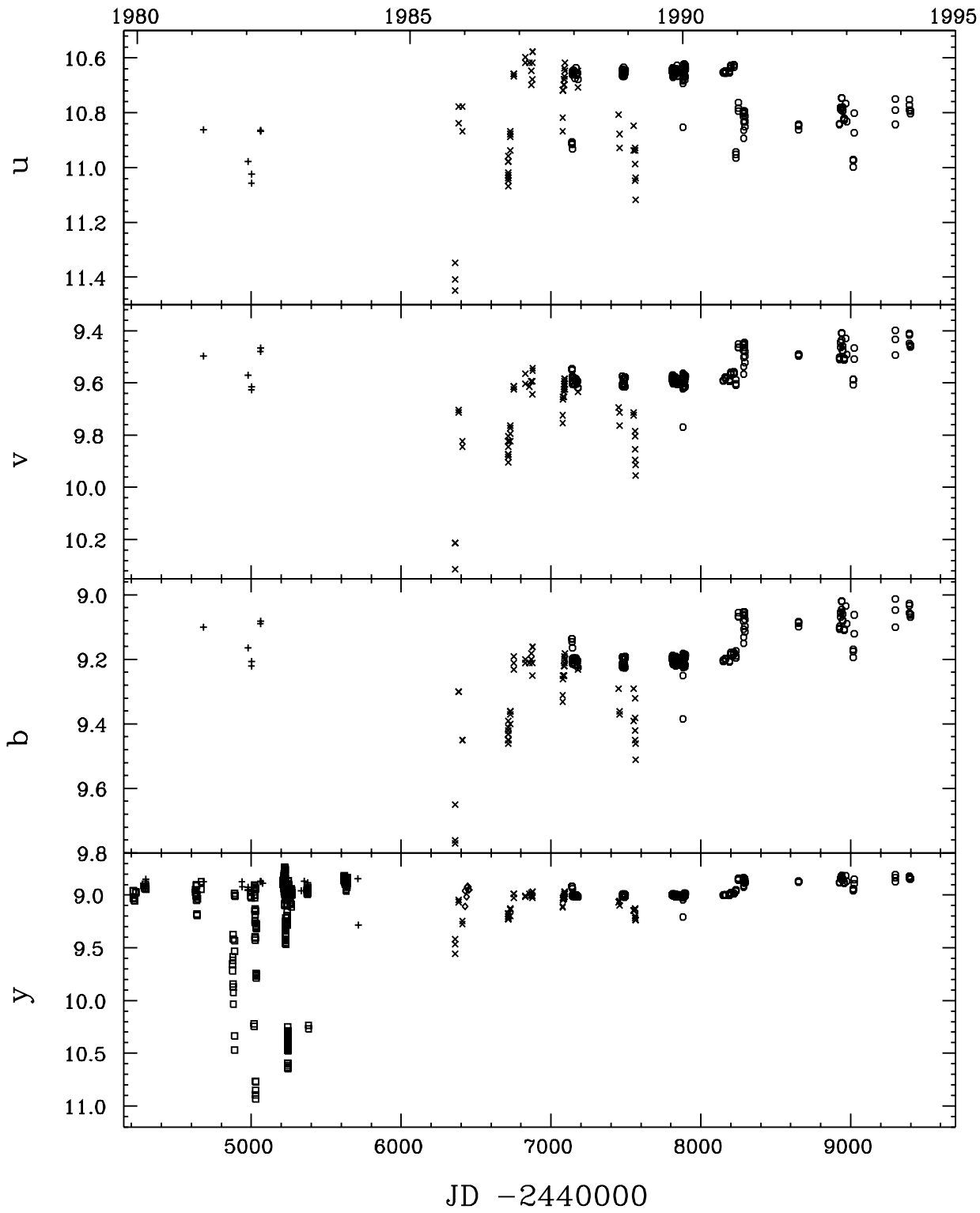

Fig. 4.1. Lightcurves of V351 Ori in the Strömgren u, v, b and y passbands. Squares represent data of Koval'chuk (1984a), plus signs those of Kilkenny et al. (1985), crosses those of Chkhikvadze (1990), diamonds indicate data from Table 4.1 and open circles are data of the ESO LTPV group.

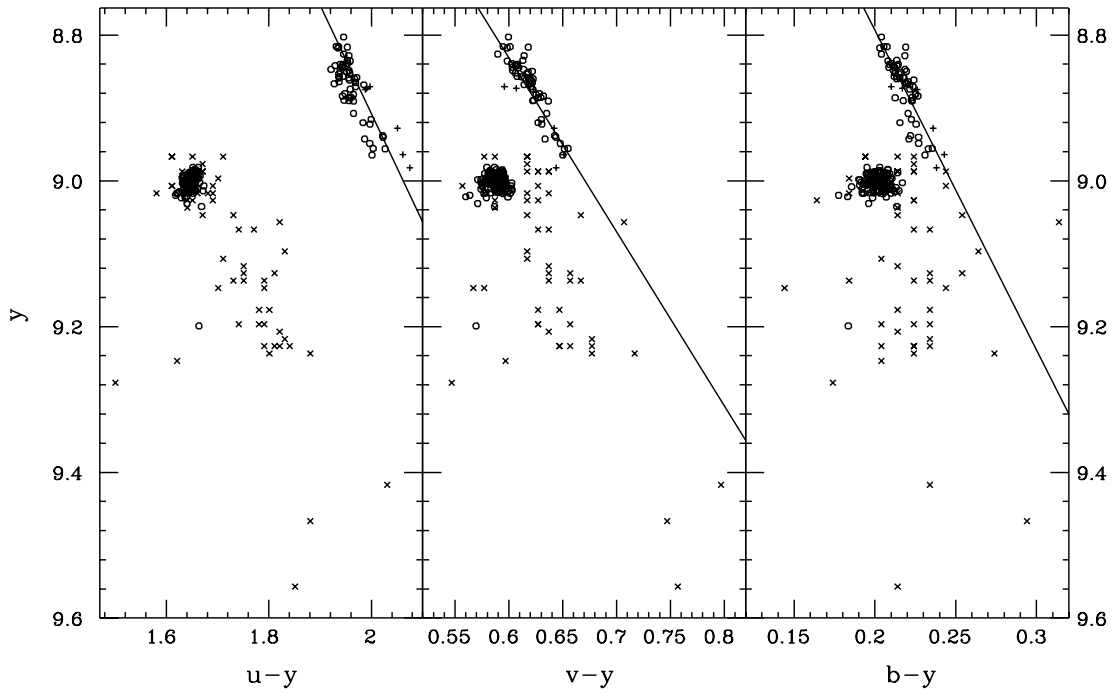

Fig. 4.2. Colour-magnitude diagrams of V351 Ori in the Strömgren $uvby$ system. The symbols have the same meaning as in Fig. 4.1. The solid lines indicate the interstellar reddening direction.

already published by Sterken et al. (1993, 1995), and the other part will appear in a forthcoming publication by the ESO "Long Term Photometry of Variables"-group, they are not listed here.

To achieve the highest accuracy in the corrections for extinction by the earth atmosphere, the measured magnitudes of V351 Ori were corrected, after applying a standard photometric reduction procedure, with the difference between the measured and averaged magnitudes of the comparison stars. The non-variability of the comparison stars was confirmed by comparing the standard deviations in their measurements with those of the other comparison stars in the ESO LTPV programme. Average errors in the in this way obtained new Strömgren photometric data are $0\overset{\mathrm{m}}{.}009$, $0\overset{\mathrm{m}}{.}004$, $0\overset{\mathrm{m}}{.}004$, and $0\overset{\mathrm{m}}{.}005$ for u, v, b and y, respectively.

Additional photometric data of V351 Ori in the Walraven system were obtained in December 1985 and January 1986 using the 90 cm Dutch Light Collector at La Silla. Measuring and reduction procedures have been explained by Lub & Pel (1977). Typical errors in these data are 0.004, 0.003, 0.004, 0.006, and 0.009 for V, $V-B$, $B-U$, $U-W$, and $B-L$, respectively. During these observations the Walraven $WULBV$ intensities were measured simultaneously, thereby avoiding any systematic effects due to non-simultaneous measurements at the different photometric passbands. The resulting new Walraven photometry, measured through a $21\overset{''}{.}5$ diaphragm, is listed in Table 4.1. The last column lists the corresponding V magnitude in the Johnson photometric system, computed using the formula suggested by Brand & Wouterloot (1988).

Table 4.1. New photometry of V351 Ori in the Walraven system

JD −2440000	V	$V-B$	$B-U$	$U-W$	$B-L$	V_J
6425.5682	−0.904	0.180	0.511	0.264	0.243	9.106
6426.7396	−0.845	0.165	0.489	0.234	0.241	8.960
6435.5501	−0.867	0.159	0.497	0.235	0.237	9.015
6439.6571	−0.831	0.156	0.484	0.231	0.237	8.925
6443.6203	−0.828	0.155	0.487	0.221	0.233	8.919
6443.6218	−0.829	0.155	0.482	0.222	0.231	8.922
6450.6728	−0.841	0.158	0.489	0.228	0.234	8.950
6451.6352	−0.842	0.164	0.496	0.231	0.234	8.951

The new Strömgren u, v, b and y magnitudes are plotted against the Julian Date (JD) as open circles in Fig. 4.1. Also shown in this diagram are the Strömgren photometric data by Kilkenny et al. (1985) (+ signs) and Chkhikvadze (1990) (crosses), and the Johnson V data (taken equal to the Strömgren y magnitude) by Koval'chuk (1984a) (open squares) and Kilkenny et al. (1985) (+ signs) and the converted Walraven data from Table 4.1 (diamonds). Colour-magnitude diagrams of the y magnitude vs. the $u-y$, $v-y$ and $b-y$ colours are shown in Fig. 4.2.

In Fig. 4.3 we plotted the Johnson $UBVRI$ data of Koval'chuk (1984b) against the JD using open squares. Also plotted in this diagram (as + signs) are the $UBV(RI)_C$ data in the Johnson/Cousins system by Kilkenny et al. (1985), converted to the Johnson $UBVRI$ system using the transformation formulae of Bessell (1979). Colour-magnitude diagrams of these data as V against $U-B$, $B-V$, $V-R$ and $V-I$ are shown in Fig. 4.4.

4.2.2 Spectroscopy

A single low-resolution CCD spectrum of V351 Ori, covering the wavelength range of 3400 to 6800 Å, was obtained on December 14, 1994 (JD 2449702.1752), using the Boller & Chivens spectrograph mounted on the ESO 1.5 m telescope at La Silla. This new spectrum is shown in Fig. 4.5. A spectrum of the star located 15″ west of V351 Ori was also extracted from this CCD frame. The resulting spectrum (not presented here) shows that this companion star does not have Hα in emission, and is of spectral type late F. Whether this star is physically associated with V351 Ori is not clear.

Two high-resolution (R = 55,000; 0.05 Å/pixel) CCD spectra of V351 Ori, covering the Na I D (5858–5910 Å) and Hα (6536–6591 Å) wavelength ranges were obtained on January 16 (JD 2449733.1197) and January 17, 1995 (JD 2449734.0414), respectively, with the CAT/CES combination at La Silla. These observations were conducted through remote control from ESO Headquarters, Garching bei München, Germany. The new high-resolution spectra are shown in Fig. 4.6. The narrow absorption lines in these

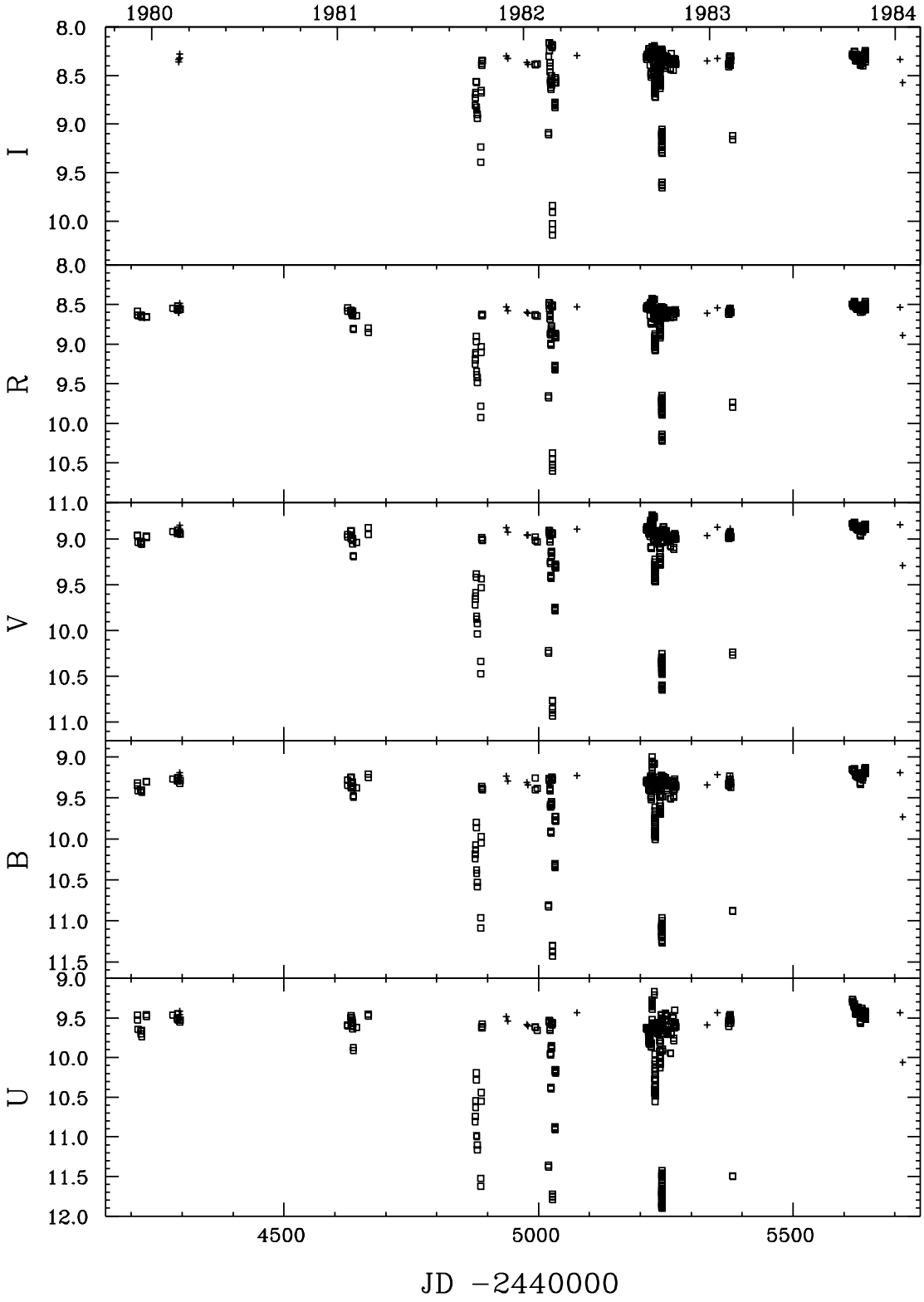

Fig. 4.3. Lightcurves of V351 Ori in the Johnson U, B, V, R and I magnitudes. Squares represent data of Koval'chuk (1984a) and plus signs those of Kilkenny et al. (1985).

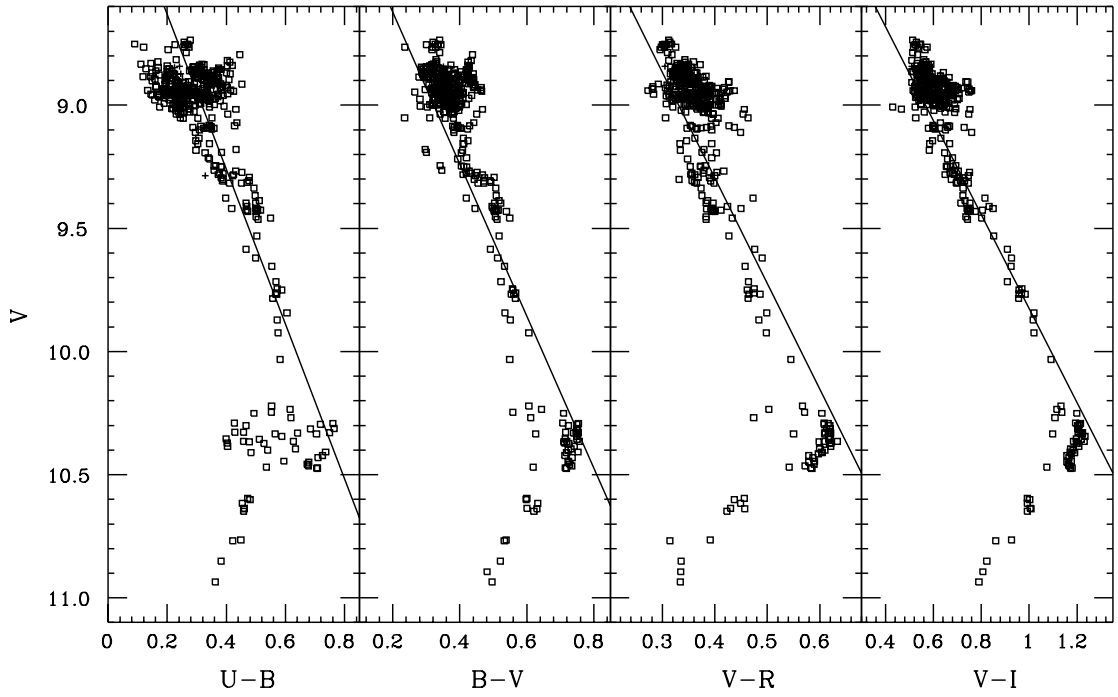

Fig. 4.4. Colour-magnitude diagrams of V351 Ori in the Johnson $UBVRI$ system The plot symbols have the same meaning as in Fig. 4.3. The solid lines indicate the interstellar reddening direction.

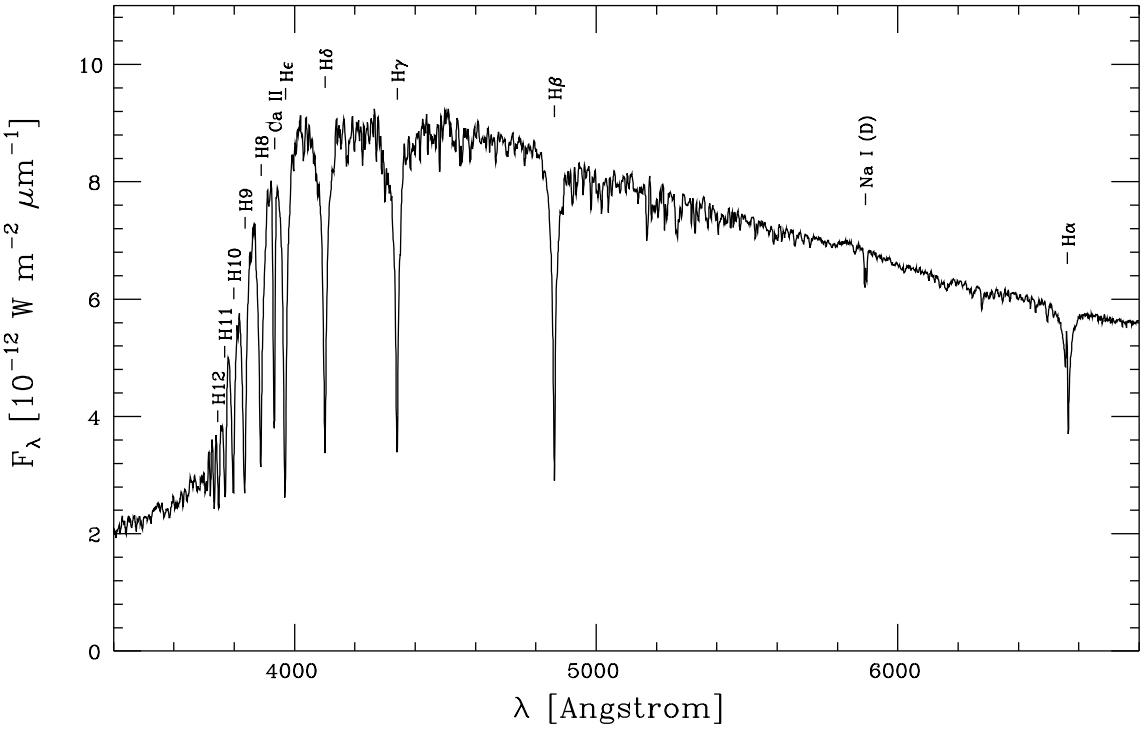

Fig. 4.5. Low resolution optical spectrum of V351 Ori with the most prominent lines identified.

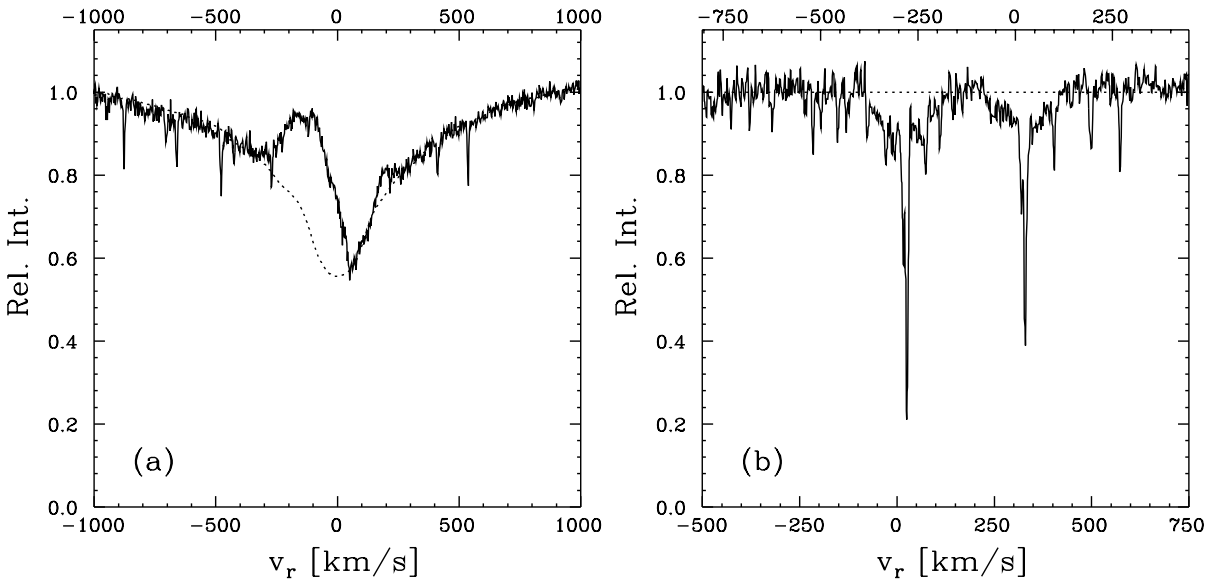

Fig. 4.6. (a) High resolution spectrum of V351 Ori in the Hα region, rebinned to heliocentric velocities. The dotted line indicates the photospheric Hα line of a standard A7 III star; (b) the same for the Na I D region. The dotted line indicates the continuum level.

spectra are due to water vapour in the earth's atmosphere and should therefore be ignored.

4.3 Analysis of the photometric data

When we examine the lightcurves in Figs. 4.1 and 4.3, we notice that V351 Ori has changed its photometric behaviour drastically over the period of 14 years covered by these diagrams. In the period before JD 2446000 the star shows large ($> 2^{\rm m}$) brightness variations in V and y; the maximum visual brightness is $\approx 8\overset{\rm m}{.}8$. When we look at the colour-magnitude diagrams in the Johnson $UBVRI$ system over this period (Fig. 4.4), we notice that for $V < 10\overset{\rm m}{.}0$ there seems to be a linear relation between the V magnitude and the colour-indices, in which the colours become redder as V increases. The slope of this relation is compatible with that of the normal (i.e. $R_V = A_V/E(B-V)$ = 3.1) interstellar extinction law, as derived from the semi-theoretical extinction laws by Steenman & Thé (1991). This suggests that, like in the Herbig Ae star UX Ori (e.g. Grinin et al. 1994), these variations are caused by variable amounts of extinction of the starlight by circumstellar dust particles.

We also notice that there seems to be a fair amount of scatter around $V = 10\overset{\rm m}{.}35$ in Fig. 4.4. This is due to the flare-like event observed by Koval'chuk (1984b). As the stellar brightness decreases even further, we see the blueing effect; with increasing V, the colours now become bluer. Following Grinin (1988), this blueing effect can be explained by assuming the presence of a dust envelope containing sub-μm dust grains around V351 Ori. The radii of these particles are small enough to scatter the blue

photons of the stellar radiation, producing a faint blue emission. The complete colour-magnitude diagram in Fig. 4.4 can now be explained by assuming the passing by of obscuring dust clouds, revolving around the star. Due to the screening by such a dust cloud, the light from the star becomes fainter and redder caused by extinction by the particles in the dust cloud. Below some brightness level, the scattered blue light by the dust envelope dominates, and produces the observed blueing effect.

If we only look at the light-curve in Fig. 4.3 and the colour-magnitude diagrams in Fig. 4.4, we would come to the conclusion that the photometric behaviour of V351 Ori is like that of a typical Herbig Ae star with large photometric variations, such as UX Ori (Grinin et al. 1994). However, in Fig. 4.1 we can see that *V351 Ori changed its photometric behaviour from that of a Herbig Ae star showing large photometric variations to that of a nearly constant one*. This process seems to have started around JD 2446000. Before this date, the star showed large ($> 2^{\rm m}$) variations in y with a maximum brightness of $\approx 8\overset{\rm m}{.}8$ in this passband. Between JD 2446000 and JD 2448200, V351 Ori only varied by several tenths of a magnitude in y, and the star's maximum visual brightness dims by $0\overset{\rm m}{.}16$ to $y \approx 9\overset{\rm m}{.}0$. Between JD 2448200 and JD 2448250, the maximum brightness of V351 Ori rapidly increases to $y \approx 8\overset{\rm m}{.}84$, equal to its level before JD 2446000. After JD 2448250, the variations in brightness nearly vanished.

The same trend as in y can also be observed at the b and v passbands, although the decrease in the maximum brightness mentioned above is at b less than in y and in v lesser again. This creates a small blueing effect when we plot the y vs. $b-y$ and y vs. $v-y$ colour-magnitude diagrams (Fig. 4.2). However, in the plot of y vs. $u-y$ shown in the same figure, we notice a very large and very unusual blueing effect. This is caused by the fact that in the u lightcurve the maximum brightness in the period between JD $\approx$ 2446000 and JD $\approx$ 2448200 increased, whereas it decreased in the y, b and v passbands. It should be stressed here that above observational facts are exhibited not only by our LTPV data, but also by part of those of Chkhikvadze (1990), meaning that these facts are real, not due to systematic errors in the LTPV data.

Finally, it is of interest to note that the relation between brightness increase and colour for the transition period from JD 2448200 to JD 2448250, displayed in Fig. 4.2, goes along lines with a slope compatible with that of the normal (i.e. R_V = 3.1) interstellar extinction law, such as derived from the semi-theoretical extinction laws by Steenman & Thé (1991). This suggest that the dimming and reddening is related to the variable extinction by circumstellar dust.

4.4 The unusual blueing effect of V351 Ori

From new observations in recent years it appears more and more evident that HAeBe stars are surrounded by disks. The outer, cooler part of these disks are inhabited by dust grains, which very often are forming clumps; they are also indicated as dust clouds. These clouds are revolving in Keplerian orbits around the star, and if the inclination angle of the disk is large enough (i.e. the disk is oriented nearly edge on), they are able to screen the star, causing the observed irregular brightness variations.

When a dust cloud obscures the central star, it is possible that the central star is obscured to such an extent that we can measure its light scattered by the small dust particles. Therefore, after the star first becomes redder, when it is obscured, it will become bluer again as it dims further. This is what is called the blueing effect (e.g. Bibo & Thé 1990, 1991). Such a situation is found, for instance, in the star UX Ori (Grinin et al. 1994). The irregular variations in brightness are often named Algol type variations, because at a deep minimum the star can decrease in brightness by more than $2\overset{\mathrm{m}}{.}5$, similar to eclipsing binaries like Algol.

Considering the irregular variation of the light of V351 Ori (see Figs. 4.1 and 4.3) and the blueing effect in its colour-magnitude diagram before JD 2446000 (Fig. 4.4), we believe that the circumstellar disk of this star is oriented nearly edge on. Inspection of the colour-magnitude diagram after JD 2446000 (Fig. 4.2) shows that these also exhibit a blueing effect. However, not during deep minima (like in Fig. 4.4), but with a Δy of only $0\overset{\mathrm{m}}{.}2$ (Fig. 4.2). Furthermore, this blueing effect seems to have a much stronger colour-dependence in $u - y$, than in both $v - y$ and $b - y$, which is also not observed in UX Ori-type systems. Since we will not yet be able to observe scattered radiation with such a small decrease in brightness this unusual blueing effect must be caused by another mechanism than that for the blueing effect with a ΔV of $1\overset{\mathrm{m}}{.}7$ in Fig. 4.4, which can be explained by the same mechanism as suggested for UX Ori.

It is of interest to consider in the discussion of the blueing effect also the peculiar results by Koval'chuk (1984b), who observed a flare-like event lasting less than 2 hours and with a magnitude of $0\overset{\mathrm{m}}{.}4$ in the U band in V351 Ori. Unfortunately his data were obtained in a period when we and Chkhikvadze have not made any observations. For this reason we are not able to make comparisons. The flare-like event Koval'chuk had found occurs in a state of very low stellar brightness, around $V = 10\overset{\mathrm{m}}{.}35$. Since the increase in brightness was the strongest in U, this event creates also a blueing effect in the colour-magnitude diagrams, which is responsible for most of the scatter in the data points around $V = 10\overset{\mathrm{m}}{.}35$ in Fig. 4.4. Although it is striking that this flare-like event occurs at a brightness equal to the turning-point in Fig. 4.4, it does not seem likely that this event is caused by the scattering of the radiation of the central star by dust grains. What the true reason is, is very difficult to understand.

The unusual blueing effect we have observed in V351 Ori (Fig. 4.2) lasts very long, more than 6 years. However, these observations were not done continuously. Therefore, a possibility remains that in between this interval, the star had returned to its normal situation once or more often. It should also be noted that contrary to the flare-like event observed by Koval'chuk (1984b), the blueing effect starts at a higher brightness ($V \approx 9\overset{\mathrm{m}}{.}0$). Therefore, we believe that we are not dealing with the same mechanism causing the flare event observed by Koval'chuk (1984b).

4.5 The spectral type from photometric data

A rough estimate of the spectral type of V351 Ori was made from the broad-band photometry by Kilkenny et al. (1985), obtained near maximum brightness. Using the

intrinsic two colour $(B-V)_0$ versus $(U-B)_0$ diagram for main sequence stars (Schmidt-Kaler 1982), we determined the intrinsic colours $(B-V)_0$ and $(U-B)_0$, assuming a reddening direction of $E(U-B)/E(B-V)$ = 0.72, corresponding to that of a normal (i.e. R_V = 3.1) extinction law. From these intrinsic colours we derive the colour excesses $E(B-V)$ and $E(U-B)$, as well as the spectral types, using the catalogue of Schmidt-Kaler (1982). Since the intrinsic $(B-V)_0$ versus $(U-B)_0$ two colour diagram for stars of different luminosity classes is nearly identical, for the range of spectral types considered here, this method can not be used to determine the luminosity class. The resulting possible spectral types are A0, corresponding to $E(B-V) = 0\overset{\text{m}}{.}37$, and A6, corresponding to $E(B-V) = 0\overset{\text{m}}{.}17$.

4.6 The visual spectra

In the low resolution spectrum of V351 Ori (Fig. 4.5) we recognise that of an A6 or A7 weak emission-line star. The spectrum is dominated by the Balmer lines, with Hβ to H 14 in absorption, whereas Hα is apparently filled in by an emission component. Other features of this spectrum include strong Ca II H (blended with Hε) and K and Na I D absorption lines, as well as numerous weaker metallic absorption lines. Our spectral type of A6/7 agrees well with the spectral type of A7 III obtained by Zajtseva (1986), which we will adopt in our further discussion.

From the high-resolution Hα spectrum of V351 Ori (Fig. 4.6a) we notice that the Hα emission has a very strong reversed P Cygni profile, indicating accretion of matter towards the star. When we compare the Hα profile of V351 Ori with that of a standard A7 III star (the dotted line in Fig. 4.6a), we notice that there are extra emission components at -88 ± 6 km s^{-1} and +190 $\pm$ 6 km s^{-1}. Their equivalent widths are -1.90 ± 0.05 Å and -0.05 ± 0.02 Å, respectively.

In the high-resolution spectrum of the Na I D region of V351 Ori (Fig. 4.6b) we see that the sodium lines consist of a strong and narrow component, superimposed on a much broader ($\Delta v \approx 100$ km s^{-1}) and weaker component. The equivalent widths of the narrow components are 0.67 $\pm$ 0.03 Å for the 5890.2 Å D_1 line and 0.71 $\pm$ 0.03 Å for the 5896.3 Å D_2 line. These are too large to be accounted for by the interstellar sodium lines alone. Therefore, the narrow components must consist of a blend of the interstellar and circumstellar lines. Another indication of the blended nature of these lines is that at our resolving power a double peaked absorption profile is just visible inside these sharp components. The difference in velocity between these two absorption components, presumably the interstellar line and the sharp circumstellar component, is 12 $\pm$ 4 km s^{-1}. The weak and broad component in the sodium lines could very well be due to Na I in the cooler outer parts of an accretion disk around V351 Ori. As can be expected for a late A type star, the He I 5876 Å absorption line (not shown in Fig. 4.6b) is absent in V351 Ori.

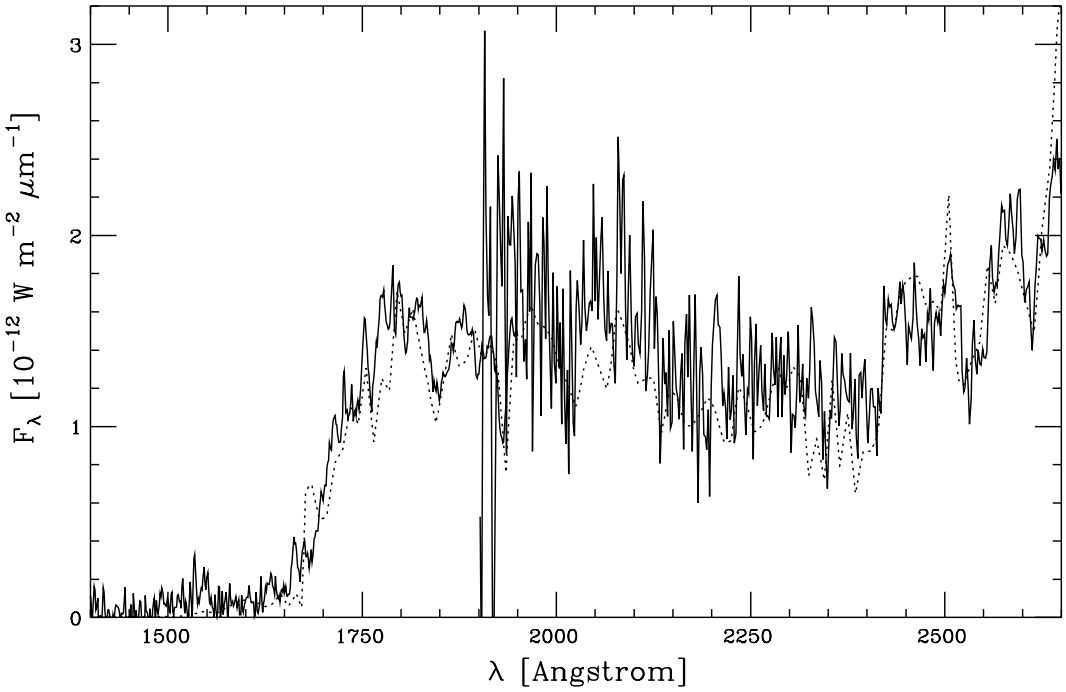

Fig. 4.7. The ultraviolet spectra of V351 Ori. The dotted line indicates the reddened Kurucz (1991) model with $T_{\rm eff}$ = 7650 K and $\log g$ = 3.6.

4.7 The ultraviolet spectra

In connection with their study of the UV-excess in HAeBe stars, Blondel & Tjin A Djie (1994) took two low-dispersion IUE spectra (SWP 29678 and LWP 9520) of V351 Ori in Nov. 1986 (JD 2446749.2602 and JD 2446749.2248, respectively). These are displayed in Fig. 4.7. Since the region longward of 2600 Å is severely underexposed in the LWP image, this part of the spectrum is not shown here. The brightness of V351 Ori when these exposures were made was measured by IUE in the Fine Error Sensor (FES). Using the calibration given by Barylak (1989), which takes the sensitivity decrease of the FES into account, we obtain a V magnitude of $9\overset{\rm m}{.}08 \pm 0\overset{\rm m}{.}05$ from the FES counts when these exposures were made. This implies that at the time of the IUE measurements V351 Ori was near its maximum brightness during the period between JD 2446000 and JD 2448200.

Also shown in Fig. 4.7 is the Kurucz (1991) model with $T_{\rm eff}$ = 7650 K, and $\log g$ = 3.6 (corresponding to a spectral type of A7 III), reddened with the normal interstellar extinction curve by Steenman & Thé (1991), employing a colour excess of $E(B-V)$ = $0\overset{\rm m}{.}16$, derived from the photometry by Kilkenny et al. (1985) and the adopted spectral type of A7 III. From the comparison of the observed IUE spectra with the reddened Kurucz model, it is clear that no UV-excess is visible in the region shortward of 1700 Å.

From this lack of UV-excess shortward of 1700 Å, Blondel & Tjin A Djie (1994) concluded that a possible accretion disk of V351 Ori is oriented in such a way that the hot boundary layer is not visible. Therefore, it will not contribute in the ultraviolet spec-

tral region. If this is indeed the case the observed ultraviolet spectral region will be influenced by possible scattering of radiation of the central star by small grains only. However, in the previous and next sections we find no evidence that accretion is occurring through a disk, eliminating the need for the existence of such a boundary layer.

4.8 The spectral energy distribution

The extinction-free spectral energy distribution (SED) of V351 Ori, taken near maximum brightness, was analyzed by comparing it with the Kurucz (1991) theoretical SED model with $T_{\rm eff}$ = 7650 K, and $\log g$ = 3.6, corresponding to a spectral type of A7 III. The main source of the photometry used in the construction of the SED are the simultaneous $UBVRI$ and $JHKL$ photometric observations by Kilkenny et al. (1985). This photometry was supplemented with the Walraven data from Table 4.1, the Strömgren $uvby$ data from the LTPV programme as well as far-infrared data from Gezari et al. (1993) and the IRAS point source catalogue (second edition). The ultraviolet data consists of the two IUE low-resolution spectra rebinned to the resolution of the Kurucz (1991) models, again omitting data beyond 2600 Å. From the photometry by Kilkenny et al. (1985) and the adopted spectral type of A7 III we derived a colour excess of $E(B-V) = 0\overset{\rm m}{.}16$. The resulting observed (squares) and extinction corrected (circles) SEDs of V351 Ori are shown in Fig. 4.8.

The method used to analyze the SED is explained by Steenman & Thé (1989). With this method it is possible to correct for anomalous extinction characterized by the ratio of total to selective extinction R_V. An R_V-value for a star can be obtained, by fitting its extinction-free SED, until, by trial and error, a best fit is reached, according to the χ^2-test. This fitting procedure is applied only up to 1.3 μm (J-pass band), because beyond this wavelength the SED could be influenced by thermal emission of circumstellar dust grains. Furthermore, our SED fitting procedure differs from the one employed by Steenman & Thé (1989) by the use of the new extinction laws by Steenman & Thé (1991), and the application of the new Kurucz (1991) models. Furthermore, fluxes were integrated over the response curve of the photometric band, instead of using monochromatic fluxes. The resulting value of R_V does not differ significantly from the one usually found for interstellar extinction (R_V = 3.1). As can be seen from Fig. 4.8, the quality of the fit, with R_V = 3.1, to the Kurucz model is very good in the ultraviolet and the optical wavelength ranges, with a large amount of excess radiation above photospheric levels in the infrared.

From the SED, we also computed the stellar luminosity using the following formula:

$$\frac{L_\star}{d^2} = 4\pi \int_0^\infty F_{\lambda,Kurucz} \mathrm{d}\lambda, \tag{4.1}$$

with d the distance towards the star, and $F_{\lambda,Kurucz}$ the Kurucz model, fitted to the extinction-corrected SED. If we adopt a distance towards V351 Ori of 400 $\pm$ 80 pc, as determined from the parallactic component of proper motions of stars in the Ori T3 association by Artyukhina (1959), $L_\star$ = 50 $\pm$ 14 $L_\odot$. This stellar luminosity agrees

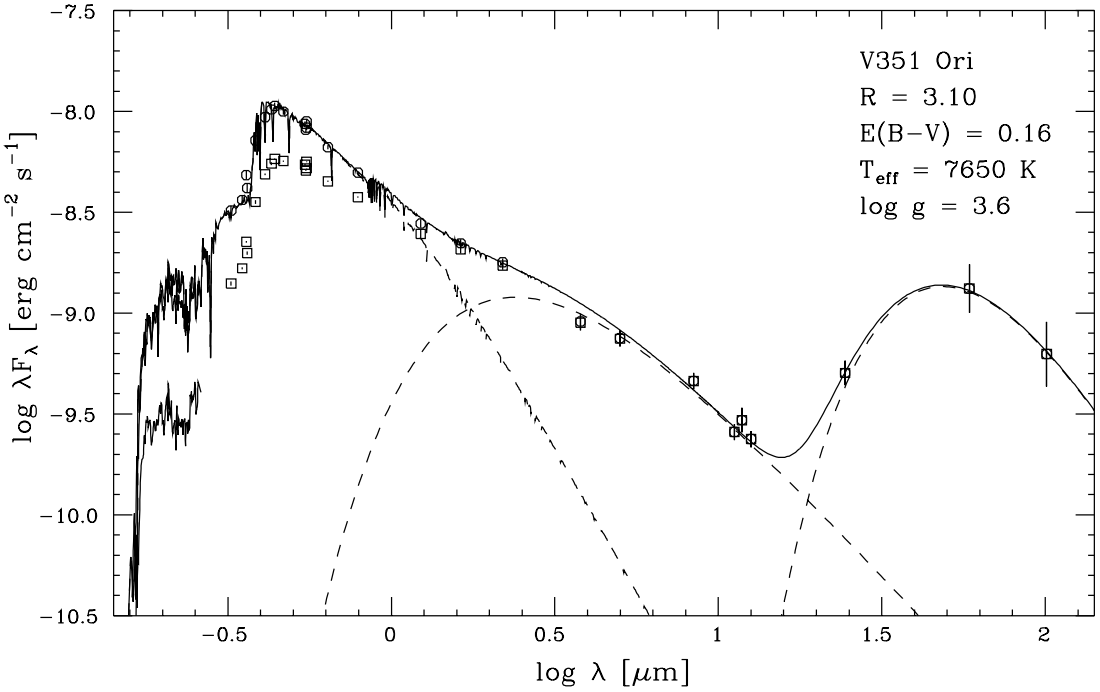

Fig. 4.8. Observed (squares) and extinction-corrected (circles) SEDs for V351 Ori. The leftmost solid lines indicate the observed and extinction corrected IUE spectra. Also shown are the Kurucz model (left dashed line), the disk model (middle dashed line) and the 76 K Planckian (right dashed line) fitted to the infrared excess and the total model (solid line), fitted to the extinction-free SED.

well with the the luminosity of a A7 III star in Schmidt-Kaler (1982), thereby again confirming the spectral classification of this star by Zajtseva (1986).

The fact that the SED in the near infrared can be approximated by a straight line indicates the presence of an extended disk or dust shell around the star, whereas the strong bump in the far-infrared suggests the presence of an additional cooler component. We modelled this SED using a simple disk model (van den Ancker et al. 1997), but with an additional 76 K dust shell, radiating as a black-body. For an assumed range of inclination angles of the system between 15° and 80°, the inner disk radius (at a temperature of 2400 K) is at a distance 0.08–0.19 AU from the central star. The outer disk radius is poorly constrained, but extends at least to 6–14 AU for this grid of models. If we assume that the material in the additional 76 K dust shell is in thermal equilibrium, the distance of this shell to the central star can be computed using the procedure outlined by de Winter & Thé (1990), resulting in a value of 970 AU.

By integrating over the model fitted to the infrared excess, we also computed the luminosities of the disk and the dust shell, 10 $\pm$ 3 and 9 $\pm$ 3 $L_\odot$, or 21 and 18% of the stellar luminosity, respectively. The sum of these two contributions is equal to the amount of stellar luminosity absorbed by dust in the blue and ultraviolet (30 $L_\odot$), computed by taking the difference between the luminosities of the Kurucz model fitted to the extinction-corrected SED and a version of this model reddened with R_V = 3.1 and

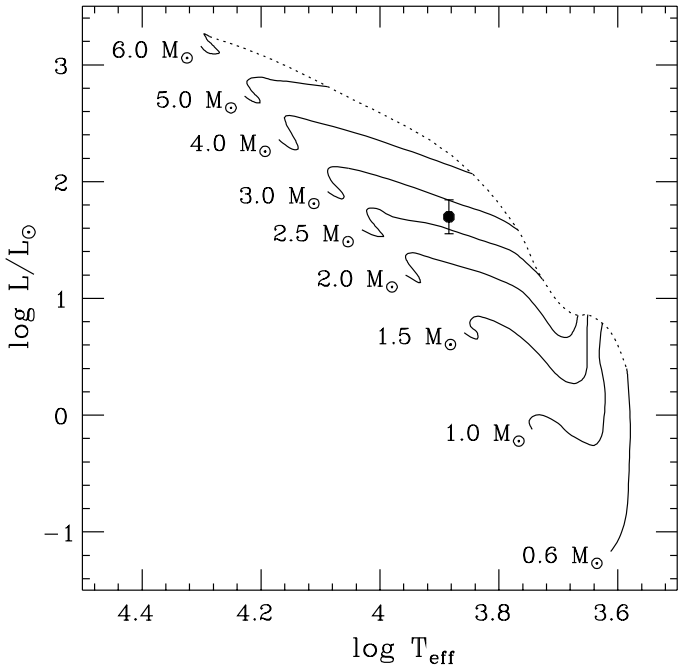

Fig. 4.9. Position of V351 Ori in the Hertzsprung-Russell diagram. Also shown are the theoretical Pre-main sequence evolutionary tracks and the birthline by Palla & Stahler (1993).

$E(B-V) = 0\overset{\text{m}}{.}16$. This shows that dust clouds may indeed be sufficient to explain the observed infrared excess and photometric variations of V351 Ori.

It is important to stress that all infrared observations of V351 Ori were made during the period in which the star still showed photometric variations. Therefore, we do not know whether the infrared excess shown in Fig. 4.8 is still the same today, or that it has changed along with the star's photometric behaviour. New infrared photometric observations of V351 Ori are needed to clarify this issue.

4.9 Position in the HR-diagram

Using the stellar luminosity of 50 $\pm$ 14 $L_\odot$ computed in the last section, we were also able to obtain the position of V351 Ori in the Hertzsprung-Russell diagram. The resulting HR diagram, in which the Pre-Main Sequence evolutionary tracks by Palla & Stahler (1993) are also plotted, is shown in Fig. 4.9. The dotted line in this diagram is the so-called "birthline", where a star becomes visible for the first time during its evolution towards the main sequence. From Fig. 4.9 we note that V351 Ori is located between the main sequence and the birthline, at the evolutionary track of a star with a mass between 2.5 and 3.0 $M_\odot$. According to the isochrones by Palla & Stahler (1993), the age of a star at the position in the HR-diagram indicated in Fig. 4.9 would be 1–2 $\times$ 10^6 year.

4.10 Discussion and conclusions

The photometric behaviour of V351 Ori may play a key rôle in understanding the pre-main sequence evolution of intermediate-mass stars. In this chapter we have shown that this object changed from a Herbig Ae star with strong photometric variations to a almost non-variable one. Such a change had previously only been observed in the Herbig Ae star BN Ori around 1947 (Shevchenko et al. 1997). This behaviour and other properties of V351 Ori deserve special attention in the study of the evolution of Herbig Ae stars towards the main sequence.

A first conclusion that can be drawn from the fact that we have actually been able to observe such transitions in the relative short period these stars have been observed systematically, is, that such transitions from Herbig Ae stars with strong photometric variations to almost non-variable ones must occur quite often during the evolution of intermediate-mass HAeBe stars towards the main sequence (MS). We should realise, however, that it is equally probable that before such a star reach the MS, it will become strongly variable again, after collecting enough dust from its environment.

During the process of V351 Ori's transition from a Herbig Ae star with strong photometric variations to a non-variable one, the maximum brightness in the Strömgren v, b and y magnitudes decreased, whereas the maximum brightness in u increased, causing a strong blueing effect in the colour-magnitude diagrams. The change from this transition period to the state in which V351 Ori is nearly constant, at a brightness level equal to that of its maximum brightness before the transition period, happened very fast (within 50 days), and went along the interstellar reddening line in the colour-magnitude diagrams. These facts may give us a clue to the mechanisms responsible for the peculiar behaviour of this star.

Since before JD 2446000 the photometric variations of V351 Ori were caused by dust clouds revolving in Keplerian orbits around the star, it seems that around this date some event started which either destroyed the dust in these clouds, or moved the dust clouds from our line of sight. This event continued until JD 2448200, after which the star rapidly became nearly constant in brightness. So far, we can only speculate about the cause of this event. It could be that it is correlated with a temporarily strong accretion of dust onto the star. Such an event will be accompanied by shock-fronts which creates an extremely hot gaseous disk near the equatorial plane close to the star. This hot optically thick gaseous disk blocked part of the visual and blue light of the star, causing a visual brightness decrease of about $0\overset{\mathrm{m}}{.}2$. At the same time, this hot object radiates ultraviolet energy superposed on that of the central star. This is causing the increase of the ultraviolet brightness of the star. When the accretion of dust stops, the visual and blue stellar light regain their maximum brightness, whereas the ultraviolet contribution of the hot disk disappears, and the ultraviolet brightness drops. The ROSAT mission flew in the same period in which this extremely hot gaseous disk was presumably present close to V351 Ori; it should be observable in X-rays. Unfortunately no ROSAT observations of the field containing V351 Ori were made.

At present it is very important to observe V351 Ori in the near infrared. If the dust clouds close to the star are indeed accreted onto the central star, we should expect a

clear decrease of the infrared excess in the SED of this star. Further monitoring of V351 Ori remains necessary to see whether the dust clouds around this very interesting object start to re-occur, in which case the star will become strongly variable once more.

Acknowledgements. This chapter is based on observations obtained at the European Southern Observatory, La Silla, Chile, and on data collected in the ESO long-term photometry of variables programme. We would like to thank Dr. N. Voshchinnikov for interesting discussions about the extinction properties of this star and for providing us with Koval'chuk's photometric 1984 data, which are not available in our library. We would also like to thank Dr. T. Preibisch for checking the ROSAT archives for V351 Ori data.

References

Artyukhina, N.M. 1959, SvA 3, 808
Barylak, M. 1989, IUE ESA Newsletter 33, 20
Bessell, M.S. 1979, PASP 91, 589
Bibo, E.A., Thé, P.S. 1990, A&A 236, 155
Bibo, E.A., Thé, P.S. 1991, A&AS 89, 319
Blondel, P.F.C., Tjin A Djie, H.R.E. 1994, ASP Conf. Ser. 62, 211
Brand, J., Wouterloot, J.G.A. 1988, A&AS 75, 117
Chkhikvadze, J.N. 1990, Bull. Abastumani Astroph. Obs. 68, 43
de Winter, D., Thé, P.S. 1990, Ap&SS 166, 99
Finkenzeller, U., Mundt, R. 1984, A&A 55, 109
Gezari, D.Y., Schmitz, M., Pitts, P.S., Mead, J.M. 1993, *"Catalog of Infrared Observations"*, third edition, NASA reference publication No. 1294
Grinin, V.P. 1988, SvA 14, L27
Grinin, V.P., Thé, P.S., de Winter, D., Giampapa, M., Rostopchina, A.N., Tambovtseva, L.V., van den Ancker, M.E. 1994, A&A 292, 165
Herbig, G.H. 1960, ApJS 4, 337
Kilkenny, D., Whittet, D.C.B., Davies, J.K., Evans, A., Bode, M.F., Robson, E.I., Banfield, R.M. 1985, SAAO Circ. 9, 55
Koval'chuk, G.U. 1984a, Glavnaya Astronomicheskaya Observatoriya, UDK 520.823.054 - 524.338.5
Koval'chuk, G.U. 1984b, IAU Inf. Bull. Var. Stars No. 2482
Koval'chuk, G.U. 1985a, Kinem. Fizika Nebesn. Tel. 1, 25
Koval'chuk, G.U. 1985b, Kinem. Fizika Nebesn. Tel. 1, 30
Kurucz, R.L. 1991, in *"Stellar atmospheres–Beyond classical models"* (eds. A.G. Davis Philip, A.R. Upgren, K.A. Janes), L. Davis press, Schenectady, New York, p. 441
Lynds, B.T. 1962, ApJS 7, 1
Lub, J., Pel, J.W. 1977, A&A 54, 137
Palla, F., Stahler, S.W. 1993, ApJ 418, 414
Schmidt-Kaler, Th. 1982, Landolt Börnstein Catalogue, Vol VI/2b
Shevchenko, V.S., Ezhkova, O., Tjin A Djie, H.R.E., van den Ancker, M.E., Blondel, P.F.C., de Winter, D. 1997, A&AS 124, 33
Steenman, H., Thé, P.S. 1991, Ap&SS 184, 9
Sterken, C., Manfroid, J., Anton, K. et al. 1993, *"Second Catalogue of stars measured in the Long-Term Photometry of Variables Project"*, European Southern Observatory Scientific Report No.

12
Sterken, C., Manfroid, J., Beele, D. et al. 1995, *"Fourth Catalogue of stars measured in the Long-Term Photometry of Variables Project"*, European Southern Observatory Scientific Report No. 16
Steenman, H., Thé, P.S. 1989, Ap&SS 159, 189
Thé, P.S., de Winter, D., Pérez, M. 1994, A&AS 104, 315
van den Ancker, M.E., Thé, P.S., Feinstein, A., Vázquez, R.A., de Winter, D., Pérez, M.R. 1997, A&AS 123, 63
Zajtseva, G.V. 1986, Astrofizika 25, 471

Note added in proof The Hipparcos results discussed in Chapter 3 show that V351 Ori has remained constant until the end of the Hipparcos mission in 1993. After the current chapter was published, new $JHKLM$ aperture photometry of V351 Ori was obtained on Sept. 14–16, 1997 (JD 2449975.424–2449979.374), at the South African Astronomical Observatory. The resulting magitudes were not significantly different from those obtained by Kilkenny et al. (1985), showing that the total amount of warm dust has not changed. However, new spectroscopic observations by Gray & Corbally (1998, AJ 116, 2530) have shown V351 Ori to be slightly metal depleted, suggesting a relation of the phenomena discussed in this chapter with those observed in λ Bootis stars.

Chapter 5

Circumstellar Dust in the Herbig Ae Systems AB Aur and HD 163296

M.E. van den Ancker, J. Bouwman, P.R. Wesselius, L.B.F.M. Waters, S.M. Dougherty and E.F. van Dishoeck, A&A, submitted (1999)

Abstract

Using both the Short- and Long-wavelength Spectrometers on board the Infrared Space Observatory (ISO), we have obtained infrared spectra of the Herbig Ae systems AB Aur and HD 163296. In addition, we obtained ground-based *N* band images of HD 163296. Our results can be summarized as follows: (1) The main dust components in AB Aur are amorphous silicates, iron oxide and PAHs; (2) The circumstellar dust in HD 163296 consists of amorphous silicates, iron oxide, water ice and a small fraction of crystalline silicates; (3) The infrared fluxes of HD 163296 are dominated by solid state features; (4) The colour temperature of the underlying continuum is much cooler in HD 163296 than in AB Aur, pointing to the existence of a population of very large (mm sized) dust grains in HD 163296; (5) The composition and degree of crystallization of circumstellar dust are poorly correlated with the age of the central star. The processes of crystallization and grain growth are also not necessarily coupled. This means that either the evolution of circumstellar dust in protoplanetary disks happens very rapidly (within a few Myr), or that this evolution is governed by factors other than stellar mass and age.

5.1 Introduction

Herbig Ae/Be stars are intermediate-mass pre-main sequence stars surrounded by disks of gas and dust which might be the site of on-going planet formation (see Waters & Waelkens 1998 for a recent review). AB Aur (A0Ve) and HD 163296 (A3Ve) belong to the best studied Herbig stars and are sometimes considered prototypical for the

Table 5.1. Astrophysical parameters of programme stars

	AB Aur	Ref.	HD 163296	Ref.
α (2000)	04 55 45.79	(1)	17 56 21.26	(1)
δ (2000)	+30 33 05.5	(1)	$-$21 57 19.5	(1)
d [pc]	144^{+23}_{-17}	(2)	122^{+17}_{-13}	(2)
Sp. Type	A0Ve+sh	(3)	A3Ve	(8)
V [$^{\rm m}$]	7.03–7.09†	(2)	6.82–6.89	(2)
$E(B-V)$ [$^{\rm m}$]	0.16±0.02	(4)	0.04±0.02	(4)
$T_{\rm eff}$ [K]	9500^{+500}_{-300}	(2)	8700^{+200}_{-300}	(4)
$L_\star$ [$L_\odot$]	47±12	(2)	26±5	(4)
$R_\star$ [$R_\odot$]	2.5±0.5	(4)	2.2±0.2	(4)
$M_\star$ [$M_\odot$]	2.4±0.2	(2)	2.0±0.2	(4)
log(Age) [yr]	6.3±0.2	(2)	6.6±0.2	(4)
Hα	P Cygni	(5)	Double-peaked	(9)
$v \sin i$ [km s^{-1}]	80±5	(5)	120±1	(10)
rot. period [$^{\rm h}$]	32±3	(6)	35±5	(11)
i [$^\circ$]	76	(7)	58	(7)
P.A. [$^\circ$]	$+79^{+2}_{-3}$	(7)	$+126^{+2}_{-3}$	(7)

†However, older photographic measurements (Gaposchkin 1952) show values up to $m_{pg} = 8.4$ for AB Aur.

References: (1) Hipparcos Catalogue; (2) Chapter 3; (3) Böhm & Catala (1993); (4) This chapter; (5) Böhm & Catala (1995); (6) Böhm et al. (1996); (7) Mannings & Sargent (1997); (8) Gray & Corbally (1998); (9) Pogodin (1994); (10) Halbedel (1996); (11) Catala et al. (1989).

entire class. As early as 1933, Merrill & Burwell remarked upon the similarity of both systems, which was confirmed by numerous subsequent authors. Apart from the fact that the stellar mass, effective temperature and age of AB Aur and HD 163296 are nearly identical (Table 3.1), the similarity between the two systems also extends to their circumstellar environment: both AB Aur and HD 163296 are examples of relatively isolated star formation, and are not hindered by confusion with other sources (Henning et al. 1998; Di Francesco et al. 1998).

Both AB Aur and HD 163296 show a rich, variable, emission-line spectrum from the ultraviolet to the optical. With a few exceptions, most noticeably the observed [O I] emission, these lines have been successfully modelled as arising in an inhomogeneous stellar wind (Catala et al. 1989; Böhm et al. 1996; Bouret et al. 1997). Infall of material has been detected in both HD 163296 and AB Aur through monitoring of UV and optical absorption and emission lines (Grady et al. 1996, 1999). In the infrared, both stars are among the sources with the strongest 10 μm silicate feature in emission (Cohen 1980; Sitko 1981; Sorrell 1990). Neither star shows the 3.29 μm UIR emission band present toward many Herbig Ae/Be stars (Brooke et al. 1993). Basic astrophysical parameters of both stars are listed in Table 5.1.

There is strong evidence for the presence of a circumstellar disk in both AB Aur and HD 163296. Bjorkman et al. (1995) detected a 90° flip of the polarization angle between the optical and the ultraviolet in HD 163296, which they interpreted as evidence for a flattened, disk-like structure. Mannings & Sargent (1997) resolved the gaseous disks surrounding AB Aur and HD 163296 using CO millimeter wave aperture synthesis imaging. Using continuum measurements at 1.3 mm, the same authors also resolved the circumstellar dust disk of HD 163296. The AB Aur dust disk has also been resolved in the infrared, and shows a surprisingly strong dependence of disk diameter on wavelength, ranging from 0.″0065 (0.94 AU) at 2.2 μm (Millan-Gabet et al. 1999), through 0.″24 (35 AU) at 11.7 μm to 0.″49 (70 AU) at 17.9 μm (Marsh et al. 1995).

In this chapter we present new infrared spectra of AB Aur and HD 163296 obtained with the Short- and Long Wavelength Spectrometers on board the *Infrared Space Observatory* (ISO). We will discuss these spectra and their implications for the evolution of dust in Herbig systems. In a subsequent paper (Bouwman et al. 1999), we will describe a model for the circumstellar dust disks of AB Aur and HD 163296 and apply it to these data.

5.2 Observations

ISO Short Wavelength (2.4–45 μm) Spectrometer (SWS; de Graauw et al. 1996) and Long Wavelength (43–197 μm) Spectrometer (LWS; Clegg et al. 1996) full grating scans of AB Aur were obtained in ISO revolutions 680 (at JD 2450717.747) and 835 (JD 2450872.380), respectively. An SWS full grating scan of HD 163296 was made in revolution 329 (JD 2450367.398). Observing times were 3666 seconds for the SWS and 2741 seconds for the LWS observations. Data were reduced in a standard fashion using calibration files corresponding to OLP version 7.0 (SWS) or 6.0 (LWS), after which they

were corrected for remaining fringing and glitches. To increase the S/N in the final spectra, statistical outliers were removed and the detectors were aligned, after which the spectra were rebinned. The resulting spectra are shown in Fig. 5.1.

N-band (10.1 μm) images of HD 163296 were obtained on July 25, 1997 (at JD 2450654.608) using TIMMI on the ESO 3.6m telescope at La Silla. Total integration time was 65 minutes. The pixel size was $0\farcs336$, with a total field of view of $21\farcs5 \times 21\farcs5$. After a standard reduction procedure, the HD 163296 image was indistinguishable from that of the standard star η Sgr. After deconvolution of the HD 163296 image with that of η Sgr, the resulting stellar image stretched across 2 pixels. We conclude that the bulk of the 10 μm flux of HD 163296 comes from an area less than $0\farcs7$ (90 AU at 122 pc) in diameter.

5.3 Contents of spectra

The infrared spectra of AB Aur and HD 163296 (Fig. 5.1) show big differences: whereas AB Aur shows the cool, strong continuum expected for a Herbig star, for HD 163296 the continuum appears to be so weak that the entire SWS spectrum is dominated by solid-state emission features. The IRAS fluxes also plotted in Fig. 5.1 suggest that an underlying continuum in HD 163296 is present, but peaks longward of 100 μm and therefore is much cooler than the $\approx$40 K continuum in AB Aur.

Both AB Aur and HD 163296 show a strong 9.7 μm amorphous silicate feature together with a broad emission complex ranging from 14 to 38 μm. The emissivities for various dust components in the spectra are included in Fig. 5.1. In the HD 163296 spectrum the broad emission complex ranging from 14 to 38 μm is too broad and too intense to be solely attributed to the 19 μm feature due to the O–Si–O bending mode. We tentatively attribute this feature to a blend of silicates and iron oxide. Lab spectra of FeO also show a strongly rising emissivity in the short-wavelength range of the SWS (Henning et al. 1995). When folded with a $\approx$ 800 K blackbody, this naturally produces a broad emission feature peaking around 3 microns, which is present in both stars.

The large degree of redundancy in the SWS data makes it possible to assess the reality of weak spectral features which at first glance may appear to be lost in the noise. Each part of the spectrum was scanned twice by twelve detectors, so by checking whether a particular feature is seen in all detectors and in both scan directions, it is possible to disentangle real features from noise. The features identified in this way are listed in Table 5.2. AB Aur clearly shows the familiar 6.2 and 7.7 and possibly also the 8.6 and 11.2 μm UIR bands usually attributed to emission by polycyclic aromatic hydrocarbons (PAHs), as well as a new UIR band at 15.9 μm. The 3.29 μm UIR band is absent.

The HD 163296 spectrum shows a number of small emission features at wavelengths corresponding to those of crystalline olivines. ($(Mg_xFe_{1-x})_2SiO_4$). In addition to this, HD 163296 shows emission from the 44 μm H_2O ice feature. The relative location of the IRAS 60 μm measurement in comparison to the SWS spectrum suggests that the long-wavelength H_2O ice feature around 69 μm as well as the broad unidentified

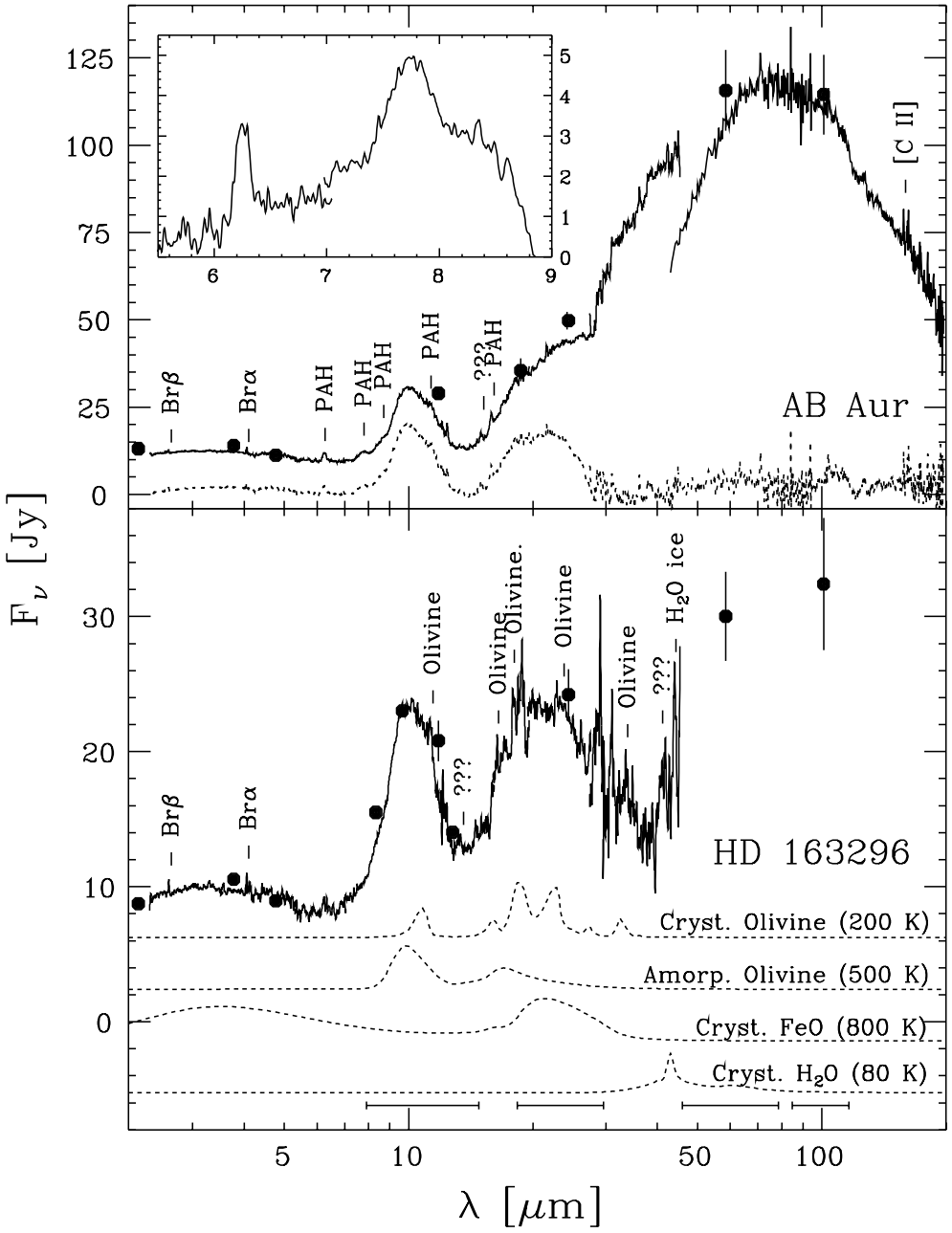

Fig. 5.1. ISO spectra of AB Aur (top) and HD 163296 (bottom) with the main features identified. The solid dots indicate ground-based and IRAS photometry (Berrilli et al. 1987, 1992; Hillenbrand et al. 1992; Weaver & Jones 1992). The dashed line in the top plot is the AB Aur spectrum after subtracting a spline fit to the continuum. Also shown (dashed lines at bottom) are the emissivities at a given temperature of the various dust components in the spectra. The bars at the bottom of the plot show the IRAS 12, 25, 60 and 100 μm passbands (FWHM). The inset in the AB Aur plot shows the UIR bands in the 5.5–9.0 μm region after subtracting a pseudo-continuum.

Table 5.2. Contents of spectra

Feature	FeO	PAH	PAH	PAH	PAH	Si-O	PAH		PAH	O-Si-O	FeO
λ [μm]	[3]	[3.3]	[6.2]	[7.7]	[8.6]	[9.7]	[11.2]	[15.0]	[15.9]	[19]	[23]
AB Aur	√	–	√	√	√	√	√:	√:	√	√	√
HD 163296	√	√:	√:	–	–	√	–	–	–	√	√

Feature	Oliv.		Oliv.	Oliv.	Pyr.?	Oliv.	Oliv.	Oliv.		H_2O ice
λ [μm]	[11.3]	[13.4]	[16.3]	[17.8]	[18.2]	[23.5]	[31.3]	[33.5]	[40.7]	[43.8]
AB Aur	–	–	–	–	–	–	√:	√:	√:	–
HD 163296	√	√	√	√	√	√	√	√	√	√

feature longward of 100 μm, observed in HD 100546 and HD 142527 (Malfait et al. 1998 and in preparation), might also be very prominent in HD 163296. PAHs are very weak or absent in HD 163296.

In addition to the solid-state features, both AB Aur and HD 163296 also contain a number of H I recombination lines at shorter wavelengths. All lines from the Bracket and Pfund included in the SWS wavelength range series are present, while the higher H I series are not detected, possibly due to the combined effect of a lower instrumental sensitivity and a higher background in this part of the spectrum. These recombination line data will be discussed in more detail in a forthcoming paper.

The LWS spectrum of AB Aur is relatively smooth and featureless. The only line that is clearly visible in the spectrum is the [C II] line at 157.7 μm. The strength of this line (8.6×10^{-16} W m^{-2}) is compatible with it originating in the background rather than being circumstellar. As can be seen from Fig. 5.1, there is a $\approx$25% difference in the flux scales between the AB Aur SWS and LWS spectra in the overlapping region. Although within the formal errors of the absolute flux calibration for SWS and LWS, this discrepancy is larger than that found in other sources. The difference cannot be attributed to the different aperture sizes ($33'' \times 20''$ for SWS versus a circular $80''$ FWHM for LWS), and confusion with extended emission, since then the LWS spectrum would have to have a higher flux level than the SWS spectrum. It is interesting to note that in the time interval between the SWS and LWS measurements, AB Aur did show an optical photometric event which could have also affected the infrared brightness (van den Ancker et al. 1999 and references therein), so the difference in flux between SWS and LWS might in fact be due to real variability. In Fig. 5.1 we also plotted the IRAS fluxes of AB Aur. Although compatible with both spectra, the IRAS 60 μm flux agrees better with the SWS spectrum, so we rather arbitrarily choose to adopt the SWS flux calibration for the region around 45 μm.

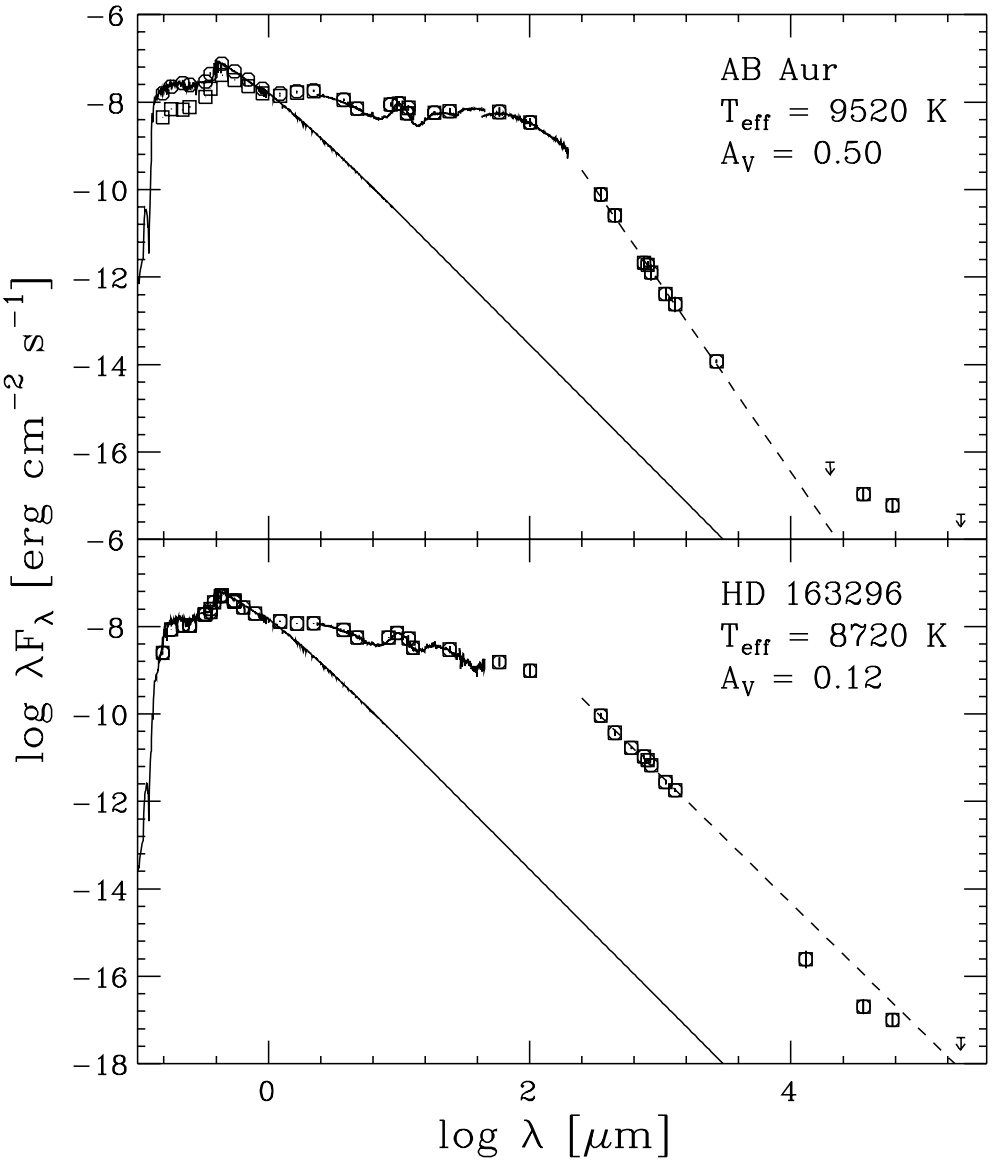

Fig. 5.2. Spectral energy distributions of AB Aur (top) and HD 163296 (bottom). Open squares and circles indicate observed and extinction corrected fluxes from literature (Wesselius et al. 1982; Thé et al. 1985; Strom et al. 1972; Cohen & Schwartz 1976; Berrilli et al. 1987, 1992; Hillenbrand et al. 1992; Weaver & Jones 1992; Mannings 1994; Güdel et al. 1989; Brown et al. 1993; Skinner et al. 1993). The solid lines show Kurucz models for the stellar photospheres of AB Aur and HD 163296. The dashed lines show linear fits to the submm data points for comparison with the slope of the Rayleigh-Jeans tail of the Kurucz model.

5.4 Spectral energy distributions

Spectral Energy Distributions (SEDs) of AB Aur and HD 163296 were constructed from literature data as well as our new ISO spectra and newly obtained VLA photometry for HD 163296 (van den Ancker et al., in preparation) and are shown in Fig. 5.2. All the submm fluxes in these SEDs refer to single-dish measurements. As can be seen from Fig. 5.2, the SED can be naturally decomposed in three parts: the optical wavelength range, where the total system flux is dominated by the stellar photosphere, the infrared to submm, where emission originates from the circumstellar dust disk, and the radio, where free-free emission from the stellar wind becomes dominant.

The difference in behaviour of the dust component in HD 163296 and AB Aur is striking: after a nearly flat energy distribution in the infrared, the sub-mm and mm fluxes of AB Aur drop rapidly ($\lambda F_\lambda \propto \lambda^{-4.3}$), indicative of the dust becoming optically thin at these wavelengths, whereas toward HD 163296 the slope of the sub-mm to mm fluxes ($\propto \lambda^{-2.9}$) is within errors equal to that of the Rayleigh-Jeans tail of a black body ($\propto \lambda^{-3}$). The new radio points at 1.3, 3.6 and 6 cm for HD 163296 do not follow the simple power-law dependence expected if these were solely due to free-free radiation. This demonstrates that even at wavelengths as long as 1.3 cm, a significant fraction of the system flux is due to circumstellar dust. The 3.6 and 6 cm fluxes are probably dominated by free-free emission.

The energy distribution of a circumstellar dust disk is governed by its temperature profile, the density distribution and the dust properties (chemical composition and size distribution). Since the circumstellar disks of AB Aur and HD 163296 stars are expected to be passive (Waters & Waelkens 1998) and the properties of the central stars are nearly identical, the temperature profile in the disks are expected to be similar as well. One possibility to explain the different sub-mm to mm slope for AB Aur and HD 163296 could be a much flatter density distribution for HD 163296. However, with a standard sub-mm dust emissivity (β = 2) the inferred dust mass for HD 163296 would become implausibly large. A better explanation may be that the dust properties of AB Aur and HD 163296 are different, a fact already concluded independently from the ISO spectra. To be able to radiate efficiently, dust particles must have a size similar to (or larger than) the wavelength, pointing to the existence of a population of mm- to cm-sized cold dust grains in the circumstellar environment of HD 163296, whereas those in AB Aur must be micron-sized. The ISO spectrum of HD 163296 also contains warm ($\approx$ 800 K) dust, suggesting a significant lack of emission from dust of intermediate temperatures.

5.5 Discussion and conclusions

We have shown that the main difference between the AB Aur and HD 163296 systems is that HD 163296 contains a population of very large (mm to cm-sized), cold, partially crystalline, dust grains, which is absent in AB Aur. AB Aur contains a population of small dust grains (PAHs), which is absent in HD 163296. In view of the fact that the stellar parameters are nearly identical except for stellar rotation, these differences are

remarkable. This must mean that either the evolution of the dust composition in protoplanetary disks happens within the error in the age determination of both systems (2^{+2}_{-1} Myr for AB Aur vs. 4^{+4}_{-2} Myr for HD 163296; Chapter 3), or that the evolution of the dust is dominated by external factors such as initial cloud size and angular momentum.

We have also shown that in AB Aur and HD 163296 iron oxide is a constituent of the circumstellar dust mixture and can also be responsible for the observed excess emission near 3 μm. Since the near-infrared excess exhibited by our programme stars is by no means unusual for a Herbig Ae/Be star, this means that the same applies for the entire group of Herbig stars. Therefore the results of models attributing this near infrared excess emission to very hot dust from an actively accreting disk (e.g. Hillenbrand et al. 1992) must be regarded with some caution. The case of HD 163296 demonstrates that infrared broad-band photometry can be completely dominated by emission from solid-state features, which must also be taken into account in any future modelling of the energy distributions of Herbig stars.

The detection of PAHs in AB Aur shows that ground-based surveys (e.g. Brooke et al. 1993) have underestimated the fraction of Herbig stars containing PAHs. The case of HD 163296 shows that the fraction of Herbig stars showing PAH emission will not go up to 100%, so models depending on the presence of very small dust grains to explain the observed near-infrared excess in Herbig Ae/Be stars (Natta et al. 1993; Natta & Krügel 1995) will not be successful in all cases. We believe iron oxide to be a more plausible explanation for this near-infrared excess.

It is difficult to attribute the absence of the 3.29 μm feature in AB Aur to an unusual temperature of the PAHs. Since the 6.2 and 7.7 μm C–C stretches are strong, while the bands due to C–H bonds are weak or absent, a more promising possibility seems a very low hydrogen covering factor of the PAHs in AB Aur or the presence of a population of large ($>$ 100 C atoms) PAHs (Schutte et al. 1993). If the new 15.9 μm UIR band in AB Aur is also caused by PAHs, this suggests that it is also due to a C–C bond.

To gain more insight in the evolution of dust in protoplanetary disks, it is useful to compare the spectra presented here to those of other Herbig Ae stars. Except for the absence of crystalline material, the AB Aur spectrum and energy distribution are nearly identical to those of its older counterpart HD 100546 (Malfait et al. 1998). In the case of AB Aur (2.5 $M_\odot$), any possible crystallization of circumstellar dust must therefore occur at a stellar age older than 2×10^6 years. The differences between HD 100546 and HD 163296 are larger: the crystalline dust in HD 100546 is much more prominent than that in HD 163296 and the population of large cold dust grains seen in HD 163296 is absent in HD 100546.

As these cases of AB Aur, HD 163296 and HD 100546 demonstrate, the age of the central star and the degree of crystallization do not show a one to one correspondence, but the processes of grain growth and crystallization in protoplanetary disks are also not necessarily coupled. Studying a larger sample of Herbig Ae/Be stars might shed more light on what causes this large observed diversity in dust properties in systems which appear very similar in other aspects.

Acknowledgements. This chapter is based on observations with ISO, an ESA project with instruments funded by ESA Member States (especially the PI countries: France, Germany, the

Netherlands and the United Kingdom) and with the participation of ISAS and NASA and on observations collected at the European Southern Observatory, La Silla, Chile. The authors would like to thank the SWS IDT for their help with the SWS observations and Norman Trams and Michelle Creech-Eakman for their help with the LWS observations. Koen Malfait and Xander Tielens are gratefully acknowledged for reading of the manuscript of this chapter prior to publication.

References

Berrilli, F., Corciulo, G., Ingrosso, G., Lorenzetti, D., Nisini, B., Strafella, F. 1993, ApJ 398, 254
Berrilli, F., Lorenzetti, D., Saraceno, P., Strafella, F. 1987, MNRAS 228, 833
Bjorkman, K.S. et al. 1995, BAAS 27, 1319
Böhm, T., Catala, C. 1993, A&AS 101, 629
Böhm, T., Catala, C. 1995, A&A 301, 155
Böhm, T., Catala, C., Donati, J.F. et al. 1996, A&AS 120, 431
Bouret, J.C., Catala, C., Simon, T. 1997, A&A 328, 606
Brooke, T.Y., Tokunaga, A.T., Strom, S.E. 1993, AJ 106, 656
Brown, D.A., Pérez, M.R., Yusef-Zadeh, F. 1993, AJ 106, 2000
Catala, C., Simon, T., Praderie, F., Talavera, A., Thé, P.S., Tjin A Djie, H.R.E. 1989, A&A 221, 273
Clegg, P.E., Ade, P.A.R. et al. 1996, A&A 315, L38
Cohen, M. 1980, MNRAS 191, 499
Cohen, M., Schwartz, R.D. 1976, MNRAS 174, 137
de Graauw, Th., Haser, L.N. et al. 1996, A&A 315, L49
Di Francesco, J., Evans, N.J., Harvey, P.M., Mundy, L.G., Butner, H.M. 1998, ApJ 509, 324
Grady, C.A., Pérez, M.R., Talavera, A. et al. 1996, A&AS 120, 157
Grady, C.A., Pérez, M.R., Bjorkman, K.S., Massa, D. 1999, ApJ 511, 925
Gray, R.O., Corbally, C.J. 1998, AJ 116, 2530
Güdel, M., Benz, A.O., Catala, C., Praderie, F. 1989, A&A 217, L9
Halbedel, E.M. 1996, PASP 108, 833
Henning, Th., Begemann, B., Mutschke, H., Dorschner, J. 1995, A&AS 112, 143
Henning, Th., Burkert, A., Launhardt, R., Leinert, C., Stecklum, B. 1998, A&A 336, 565
Henning, Th., Burkert, A. et al. 1998, A&A 336, 565
Hillenbrand, L.A., Strom, S.E., Vrba, F.J., Keene, J. 1992, ApJ 397, 613
Malfait, K., Waelkens, C., Waters, L.B.F.M., Vandenbussche, B. et al. 1998, A&A 332, L25
Mannings, V. 1994, MNRAS 271, 587
Mannings, V., Sargent, A.I. 1997, ApJ 490, 792
Marsh, K.A, van Cleve, J.E., Mahoney, M.J., Hayward, T.L., Houck, J.R. 1995, ApJ 451, 777
Merrill, P.W., Burwell, C.G. 1933, ApJ 78, 87
Millan-Gabet, R., Schloerb, F.P., Traub, W.A., Malbet, F., Berger, J.P., Bregman, J.D. 1999, ApJ 513, L131
Natta, A., Krügel, E. 1995, A&A 302, 849
Natta, A., Prusti, T., Krügel, E. 1993, A&A 275, 527
Pogodin, M.A. 1994, A&A 282, 141
Schutte, W.A., Tielens, A.G.G.M., Allamandola, L.J. 1993, ApJ 415, 397
Sitko, M.L. 1981, ApJ 247, 1024
Skinner, S.L., Brown, A., Stewart, A.T. 1993, ApJS 87, 217

Sorrell, W.H. 1990, ApJ 361, 150
Strom, S.E., Strom, K.E., Yost, J., Carrasco, L., Grasdalen, G. 1972, ApJ 173, 353
Thé, P.S., Felenbok, P., Cuypers, H., Tjin A Djie, H.R.E. 1985, A&A 149, 429
van den Ancker, M.E., Volp, A.W., Pérez, M.R., de Winter, D. 1999, Inf. Bull. Var. Stars 4704, 1
Waters, L.B.F.M., Waelkens, C. 1998, ARA&A 36, 233
Weaver, W.B., Jones, G. 1992, ApJS 78, 239
Wesselius, P.R., van Duinen, R.J., de Jonge, A.R.W., Aalders, J.W.G. et al. 1982, A&AS 49, 427

Chapter 6

Submillimeter Mapping of the R CrA Region

M.E. van den Ancker and G. Sandell,
A&A, to be submitted (1999)

Abstract

We present new 450, 800 and 850 μm maps of the R CrA region obtained with UKT14 as well as the newly installed Submillimeter Common User Bolometer Array (SCUBA) at the JCMT. We show that in addition to the previously known population of class I and II young stellar objects (YSOs), the region also contains at least two and possibly as many as six sofar unknown Class 0 sources. This brings the density of known YSOs in the region to similar values to that found in other star forming regions. From the multitude of Class 0 sources in the region we conclude that either these cannot be unambiguously identified with protostars or that the protostellar evolutionary phase must last much longer than predicted by current evolutionary theories. In addition to this, we show that the two newly detected YSOs are the most likely candidates for the driving sources of the Herbig-Haro objects in the region.

6.1 Introduction

At a distance of 130 pc (Marraco & Rydgren 1981), the Corona Australis cloud is one of the closest regions of active star formation. Superimposed on an elongated system of dark clouds, several more compact bright nebulae are visible, which are thought to be the location of recent star formation. At the heart of condensation A one finds the bright nebula NGC 6729. The Herbig Ae star R CrA is located at the apex of this cometary nebula, whereas another Herbig star, T CrA, is located in the tail. Apart from these two massive, optically visible, young stellar objects (YSOs), it also contains a population of about 20 more embedded YSOs, clustered around R CrA (Knacke et al. 1973; Taylor & Storey 1984; Wilking et al. 1997).

An elongated nebulous structure, apparently associated with R CrA, has been interpreted by Ward-Thompson et al. (1985) as being due to two jets, probably emanating from this star. The same authors also report the presence of a jet associated with T CrA. Ward-Thompson et al. (1985) interpreted these jets as being collimated by a small inner circumstellar disk focussing the CO outflow. An alternative explanation is given by Canto et al. (1986), who suggest that there is only one structure with its plane visible in the North-South direction. The optical jet is then explained as light emitted or reflected by the southern edge of the eastern cavity.

The dynamics of the gas in the molecular cloud is complicated. Levreault (1988) mapped the region in ^{12}CO J=2–1 and pointed out that his results can be best understood as arising from the superposition of two separate bipolar molecular outflows; a strong compact one, arising from the neighbourhood of the R CrA cluster, in the East-West direction and a more extended one, apparently centered on the source HH100-IR, at a position angle of 30°. More recent observations in several sub-mm molecular transitions by Harju et al. (1993) and Anderson et al. (1997) showed that the driving source of the East-Western outflow is not the Herbig star R CrA, as was originally proposed by Levreault, but the infrared source IRS7. They also discovered a dense, rotating molecular disk around this embedded YSO. The rotation axis of this molecular disk is not well aligned with the bipolar molecular outflow, but shows a remarkable coincidence with a string of Herbig-Haro (HH) objects discovered by Hartigan & Graham (1987). They suggested that IRS7 is the driving source for these as well as the powerful shock seen in SiO (J=2–1, v=0) emission.

In the 6 cm VLA map of the R CrA region obtained by Brown (1987), IRS7 shows an extended structure with two point-like sources situated symmetrically on both sides of the object. He proposed that the continuum radio emission may be due to shock-excited inner portions of a thick accretion disk surrounding a YSO with a strong stellar wind. This interpretation was recently rejected by Wilking et al. (1997), who showed that at 10 μm the source is offset from its near-infrared position and can be identified as scattered light from the heavily embedded western radio-source, IRS7A. The nature of the western radio-source, IRS7B, remains unclear.

Henning et al. (1994) and Saraceno et al. (1996) mapped the central region of the R CrA cloud at 1.3 mm. They showed IRS7 to be the strongest submillimeter source and remarked upon the similarity of this embedded ($A_V > 35^{\rm m}$; Taylor & Storey 1984) object to the well-known YSO L1551-IRS5. Considering the proximity of IRS7 to the Herbig Ae/Be star R CrA, this means that published far-infrared and submillimeter fluxes of R CrA in literature (Wilking et al. 1985; Natta et al. 1993; Mannings 1994) must at least partly be attributed to this source rather than the Herbig star. Models describing the distribution or composition of the circumstellar material assuming R CrA is the only contributing source (Natta et al. 1993; Pezzuto et al. 1997) must therefore be used with caution.

In this chapter we present new maps of the R CrA region at 450, 800 and 850 microns and show that it also contains a population of embedded protostars which are the most likely candidates for the driving sources of the Herbig-Haro objects.

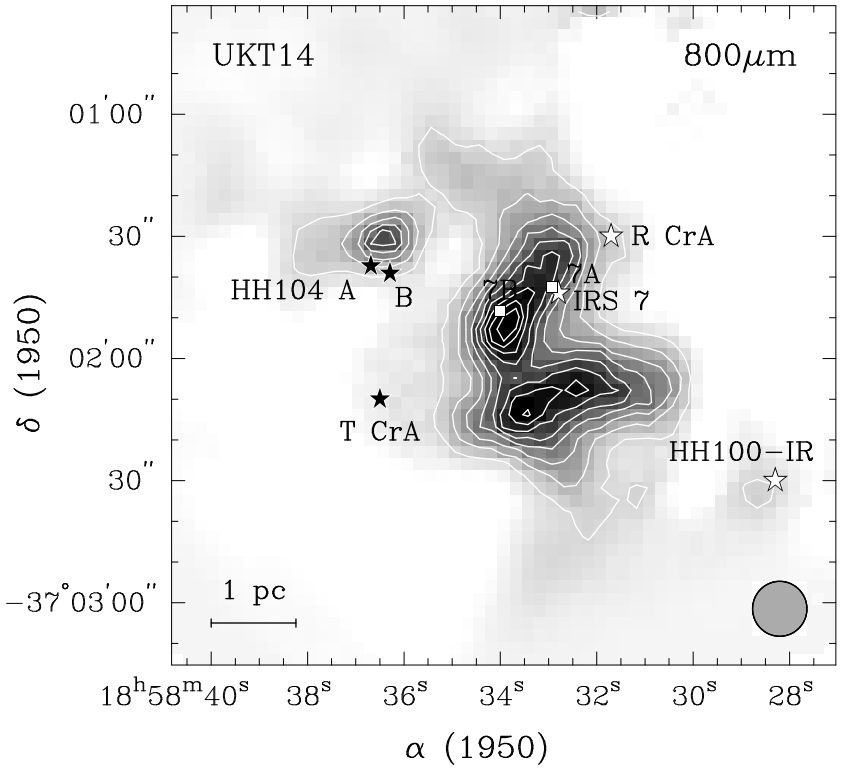

Fig. 6.1. UKT14 850 μm continuum map of the R CrA region. Contours are overplotted at intervals of 0.03 mJy beam^{-1}, starting at a level of 0.03 mJy beam^{-1}. Prominent infrared and radio sources in the region are indicated by stars and squares, respectively. The circle at the bottom right corner illustrates the beam size.

6.2 Observations

The central part of the R CrA region was mapped at 800 μm using the UKT14 Common User Bolometer (Duncan et al. 1990) on the 15 m James Clerk Maxwell Telescope (JCMT) on Mauna Kea, Hawaii, during several periods from 1988 to 1990. Simultaneous 450 and 850 μm maps of the region were obtained in August 1997 with the Submillimeter Common User Bolometer Array (SCUBA) on the same telescope. For the UKT14 data the mapping was performed by scanning the telescope continuously in azimuth, while the SCUBA maps were obtained by jiggling the JCMT's secondary mirror to 64 points to completely sample the 2.′3 hexagonal field of view. Beam sizes (half-power beam width) for these observations were 8.5, 13.5 and 14.″7 for the 450, 800 and 850 μm data, respectively. Sky variations were cancelled out by chopping the secondary by 36 (UKT14) and 120 (SCUBA) arcseconds in azimuth as well as by nodding the telescope. For the SCUBA data, residuals of the remaining emission from the earth's atmosphere were taken out by subtracting an interpolation of the signal of several bolometers at the edge of the array. Since in the region under consideration even these are expected to contain signal from the more extended dark cloud, the average level of the subtracted signal was later added again into the final image. After a standard data reduction process, the resolution of the UKT14 map was enhanced by

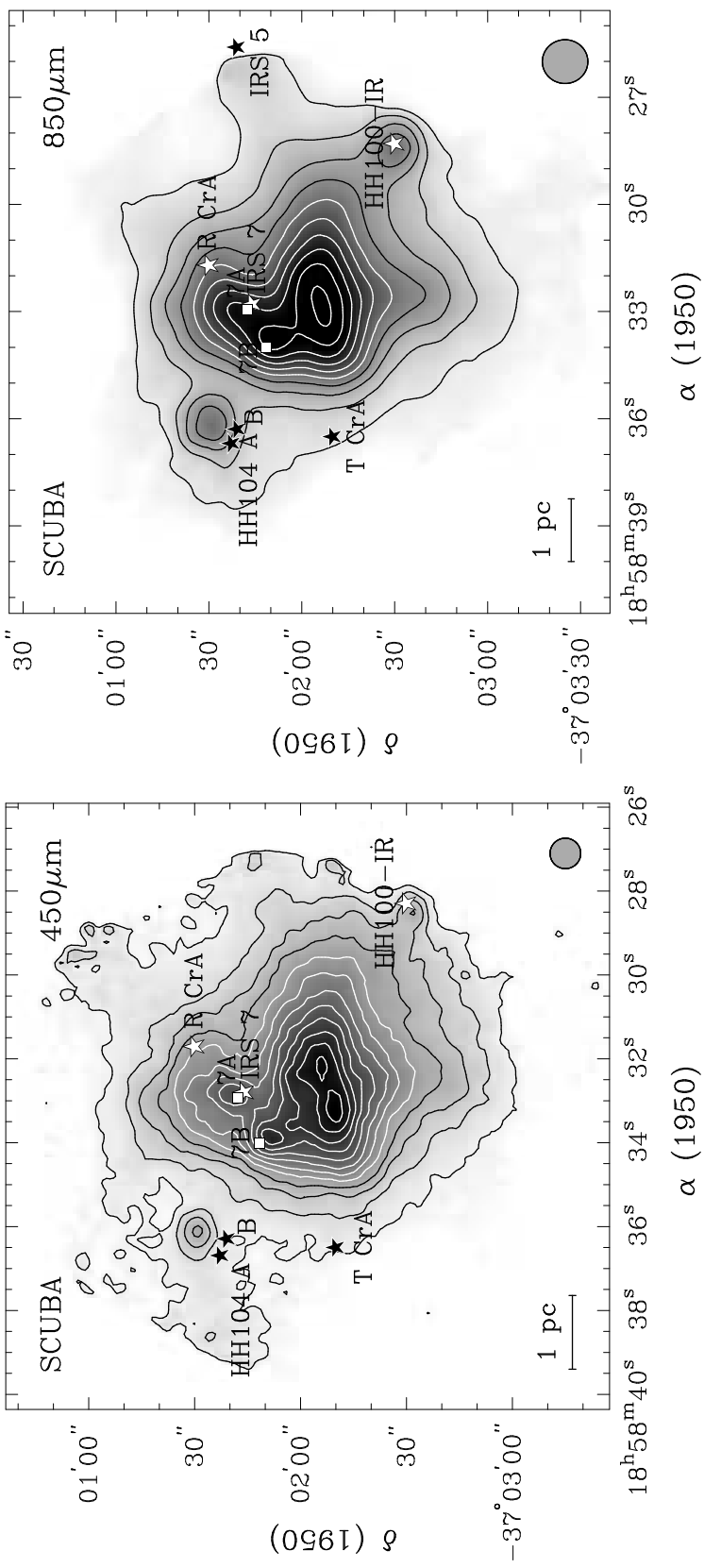

Fig. 6.2. SCUBA 450 (left) and 850 (right) μm maps of the R CrA region. Contours are overplotted at intervals of 1.2 mJy beam^{-1}, starting at a level of 1.3 mJy beam^{-1} for the 450 μm map, and at intervals of 0.3 mJy beam^{-1} starting at 0.3 mJy beam^{-1} for the 850 μm data. Prominent infrared and radio sources in the region as well as beam sizes are again shown.

Table 6.1. Positions and photometry of point-like sources

No.	R.A. (B1950.0)	Decl. (B1950.0)	$S_{sc}(450)$ [mJy]	$S_{sc}(850)$ [mJy]	$S_{ukt}(800)$ [mJy]
1	18 58 28.5	−37 02 32	6.6	1.1	–
2	18 58 32.2	−37 02 07	4.6	–	0.8
3	18 58 32.8	−37 01 41	6.7	1.3	0.9
4	18 58 33.2	−37 02 10	5.2	–	1.5
5	18 58 33.9	−37 01 52	5.5	0.9	0.8
6	18 58 36.1	−37 01 31	7.1	1.3	1.5

deconvolving it using a maximum entropy technique.

Flux calibration of the final maps was achieved by observing the planets Mars and Uranus as well as sources from the list of secondary submm calibrators by Sandell (1994). The accuracy of the absolute flux calibration in the final images is expected to be better than 15% at 800 and 850 μm and approximately 30% for the 450 μm data. The positioning of the telescope was checked by observing standard pointing sources before and after each observation and is accurate up to 2″. Fluxes and positions of point-like sources in the region were determined by fitting two-dimensional Gaussians to the reduced maps and computing the total flux from these. This procedure gave an uncertainty in the measurements, mainly due to the correction for the extended background emission, of around 20%, bringing the total error of the point source fluxes to $\approx$ 25% for 800 and 850 μm and 40% for 450 μm. Resulting positions and fluxes are listed in Table 6.1.

Comparing the fluxes in Table 6.1 with submm aperture photometry of the region in literature it can be easily seen that some authors have considerably overestimated the fluxes coming from the two optically brightest stars, R and T CrA because of poor subtracting of emission from the surrounding nebula. In fact, there is hardly any enhanced continuum flux at the position of these stars in our maps. We conclude that the intrinsic submm flux of these objects must be smaller than 4.5 mJy at 450 and 1.1 mJy at 850 μm.

6.3 Discussion and conclusions

The positions of several known near-infrared and radio-sources are overplotted in Figs. 6.1 and 6.2. The continuum emission at both 450 and 850 μm is dominated by the central region, which appears to be resolved into at least four compact sources, superimposed on a large extended structure, in the 450 μm SCUBA map. Because of the crowded region, these four sources cannot be unambiguously identified with near-infrared sources. Although the positional agreement isn't perfect, we tentatively identify the two most northern compact sources in the core with radio sources 7A and

B from the paper by Brown (1987).

In the 850 μm SCUBA map an extension of the central nebulosity to the west, extending to the edge of the image can be seen. It seems likely that this is due to the source IRS 5, located just outside our 850 μm map, which is also visible in the VLA maps of the R CrA region by Brown (1987) and in the 1.3 mm map of Henning et al. (1994). IRS 5 is one of the few objects in the region to possess an infrared reflection nebula (Castelaz & Hackwell 1987) and was also classified as an infrared excess source by Wilking et al. (1997). Suters et al. (1996) found this source to show variable continuum emission at 6 cm. The reason for this variability remains unclear.

In addition to the sources in the core, there are two point-like sources at the edge and just outside the extended emission. One of these is roughly (offset $< 10''$) coincident with the location of HH-100 IR. The other one is located near the Herbig-Haro objects HH-104 A and B (Hartigan & Graham 1987; Graham 1993). Both these submm sources do not seem to have a near-infrared counterpart and can be identified with Class 0 sources in the classification scheme devised by Lada (1987) and André et al. (1993). Our north-eastern submm source is not present in the radio- and submm continuum maps of the region by Brown (1987), Suters et al. (1996), Henning et al. (1994) and Saraceno et al. (1996). The fact that it is present in both the UKT14 and SCUBA data convinces us that this source is most definitely real and must have escaped detection in the previous surveys because these were either less sensitive (radio) or had less spatial resolution (submm) than ours. The inclusion of the new Class 0 sources in counts of the stellar density in the cluster (Wilking et al. 1997) brings the resulting numbers well in agreement with other embedded clusters such as NGC 2024, NGC 2068 and 2071 in Orion and the BD+40°4124 group.

It is striking that our two isolated point-like submm sources both have several Herbig-Haro (HH) objects in their vicinity. Furthermore, the north-eastern one is located close to HH-104 A and B, the only HH objects in the region not located in the string of Herbig-Haro objects discovered by Hartigan & Graham (1987). Our south-western object is located exactly in the middle of this linear structure. This brings us to suggest that our two Class 0 sources are in fact the driving sources behind the HH objects in the region.

The distribution of sources in Figs. 6.1 and 6.2 is intriguing: The two sources located outside the central nebulosity show that star formation has already advanced past the central core to the outer regions. Since there are four submillimeter sources in the central part of the region and only two in the outer parts, it seems safe to assume that some of these are located in the core of the molecular cloud rather than in the outer parts and seen projected onto the core. From their positions in the Hertzsprung-Russell diagram we conclude that the two optically visible stars, R and T CrA, must have formed at least 1.5×10^5 years ago. Therefore, the star formation process in this 5 pc diameter cloud core must have been going on over this entire period, and possibly longer, since there may be older less massive stars in the region which are still embedded because the pre-main sequence contraction is much slower for low-mass stars.

According to theoretical evolutionary models (Shu et al. 1987; Adams et al. 1987;

Fletcher & Stahler 1994), the protostellar phase (defined as the phase in which a central object has yet to accrete the bulk of its initial stellar mass from its surroundings) is supposed to be shortlived. During this evolutionary phase accretion rates, and hence bolometric luminosities, should be very high ($\sim 10^{-5}$ $M_\odot$ yr^{-1}) and the source should show strong outflow activity. Given the predicted relative timescales of a YSO as a protostar and as an "embedded YSO", protostars are expected to form a very small ($\lesssim 1\%$) fraction of the population of any given cluster. In the past some authors have identified the Class 0 sources as good candidates for protostars. Yet we see at least two and possibly as much of six Class 0 sources in our field, on a population with about 20 Class I and two Class II sources. This must either mean that Class 0 sources cannot be unambiguously identified with protostars, but consist mainly of Class I sources seen through large amounts of extinction, or that the protostellar phase must last much longer (and accretion rates and hence luminosities must be lower) than predicted by current evolutionary models. Further measurements to determine the exact energy distribution of our submm sources can distinguish between these two possibilities.

Acknowledgements. This chapter is based on data obtained with the James Clerk Maxwell Telescope (JCMT), Mauna Kea, Hawaii. The JCMT is operated by the Joint Astronomy Centre on behalf of the UK Particle Physics and Astronomy Research Council, the Netherlands Organization for Scientific Research and the National Research Council of Canada.

References

Adams, F.C., Lada, C.J., Shu, F.H. 1987, ApJ 312, 788
Anderson, I.M., Harju, J., Knee, L.B.G., Haikala, L.K. 1997, A&A 321, 575
André, P., Ward-Thompson, D., Barsony, M. 1993, ApJ 406, 122
Brown, A. 1987, ApJ 322, L31
Canto, J., Sarmiento, A., Rodriguez, L.F. 1986, Rev. Mex. Astron. Astrofis. 13, 107
Castelaz, M.W., Hackwell, J.A. 1987, ApJ 314, 317
Duncan, W.D., Robson, E.I., Ade, P.A.R., Griffin, M.J., Sandell, G. 1990, MNRAS 243, 126
Fletcher, A.B., Stahler, S.W. 1994, ApJ 435, 329
Graham, J.A. 1993, PASP 105, 561
Harju, J., Haikala, L.K., Mattila, K., Mauersberger, R., Booth, R.S., Nordh, H.L. 1993, A&A 278, 569
Hartigan, P., Graham, J.A. 1987, AJ 93, 913
Henning, Th., Launhardt, R., Steinacker, J., Thamm, E. 1994, A&A 291, 546
Knacke, R.F., Strom, K.M., Strom, S.E., Young, E., Kunkel, W. 1973, ApJ 179, 847
Lada, C.J. 1987, IAU Symposium 115: *"Star Forming Regions"*, p. 1
Levreault, R.M. 1988, ApJS 67, 283
Mannings, V. 1994, MNRAS 271, 587
Marraco, H.G., Rydgren, A.E. 1981, AJ 86, 62
Natta, A., Palla, F., Butner, H.M., Evans, N.J., Harvey, P.M. 1993, ApJ 405, 674
Pezzuto, S., Strafella, F., Lorenzetti, D. 1997, ApJ 485, 290
Sandell, G. 1994, MNRAS 271, 75
Saraceno, P., André, P., Ceccarelli, C., Griffin, M., Molinari, S. 1996, A&A 309, 827
Shu, F.H., Adams, F.C., Lizano, S. 1987, Ann. Rev. Astron. Astrophys. 25, 23

Suters, M., Stewart, R.T., Brown, A., Zealey, W. 1996, AJ 111, 320
Taylor, K.N.R., Storey, J.W.V. 1984, MNRAS 209, 5p
Ward-Thompson, D., Warren-Smith, R.F., Scarrott, S.M., Wolstencroft, R.D. 1985, MNRAS 215, 537
Wilking, B.A., Harvey, P.M., Joy, M., Hyland, A.R., Jones, T.J. 1985, ApJ 293, 165
Wilking, B.A., McCaughrean, M.J., Burton, M.G., Giblin, T., Rayner, J.T., Zinnecker, H. 1997, AJ 114, 2029

Chapter 7

ISO Spectroscopy of the Young Bipolar Nebulae S106 and Cep A East

M.E. van den Ancker, A.G.G.M. Tielens and P.R. Wesselius,
A&A, to be submitted (1999)

Abstract

We present the results of ISO SWS and LWS grating scans towards the embedded Young Stellar Objects (YSOs) S106 IR and Cep A East. Emission from the pure rotational lines of H_2 and the infrared fine structure lines of [C II], [O I], [S I], [Si II] and [Fe II], as well as absorption bands due to H_2O, CO and CO_2 ice were detected toward Cep A. In S106 we detected emission lines of H_2, CO, H I, and a number of ionized species including Fe, O, N, C, Si, S, Ne and Ar. S106 also shows many of the infrared PAH bands in emission. Excitation temperatures and masses were derived from the low-lying pure rotational levels of H_2 and are 490 and 740 K and 0.08 and 0.007 $M_\odot$ of H_2 for S106 and Cep A, respectively. Since both objects are expected to have several solar masses of molecular hydrogen in their environment, we conclude that in both cases the bulk of the H_2 is cooler than a few hundred Kelvins. Excitation temperatures and line ratios were compared with those predicted by theoretical models for PDRs and dissociative and non-dissociative shocks. The [S I] 25.2 μm/[Si II] 34.8 μm ratio is a particularly useful shock versus PDR discriminant and we conclude that S106 IR is dominated by PDR emission while Cep A East has a large shock component. The [O I] 145.5 μm/[C II] 157.7 μm ratio is sensitive to density and we conclude that the density in the S106 PDR is about 10^5–10^6 cm^{-3}. The density of the pre-shock gas in Cep A is similar: about 10^6 cm^{-3}.

7.1 Introduction

The infrared emission-line spectrum of Young Stellar Objects (YSOs) is dominated by the interaction of the central object with the remnants of the clouds from which it

formed. The intense UV radiation generated by accretion as well as by the central star itself causes dissociation of molecular material close to the YSO and ionizes much of the atomic material, giving rise to typical nebular and recombination lines. The strong stellar wind, often collimated into a bipolar outflow, will cause a shock wave as it hits the surrounding molecular cloud. The post-shock gas is warmed sufficiently to emit strong molecular and ionic lines. In this chapter we will study the infrared emission-line spectra of two massive YSOs, S106 IR and Cep A, and compare the observed lines with those predicted by theoretical models for photodissociation regions and shocks.

Neutral clouds irradiated by far-ultraviolet (FUV) photons are known as photodissociation regions (PDRs). In these regions, heating of the gas occurs by collisions with electrons, photoelectrically ejected from grain surfaces. Cooling of the gas occurs mainly through emission in atomic fine-structure and molecular lines, reaching intensities that should be easily observable in a wide range of astronomical objects. The gas in the surface regions of these PDRs reaches temperatures of typically 500 K (e.g. Tielens & Hollenbach 1985), making it possible to collisionally excite the low-lying pure rotational levels of molecular hydrogen, provided that the region has a sufficient density and incident FUV flux. Since the lowest ro-vibrational lines of H_2 have energy levels of the order of 5000 K, these low-lying pure rotational H_2 lines, hard to observe from the ground, are the only reliable probe of the physical conditions of the dominant species.

The physical situation in shock waves is quite distinct. Here the molecular gas is compressed by a supersonic wave moving into the gas and consequently heated. Shocks are usually divided into two distinct categories: J- or Jump-shocks, and C- or Continuous-shocks. In J-shocks viscous heating of the neutrals occurs in a thin shock front in which radiative cooling is insignificant, while the post-shock gas is heated to several times 10^4 degrees (e.g. Hollenbach & McKee 1989), dissociating all molecular material. In J-shocks the physical conditions (density, temperature) change from their pre- to post-shock values within one mean free path, causing an apparent discontinuity. Cooling of the post-shock gas occurs through atomic fine-structure lines as well as through re-formation of molecules.

C-shocks are magnetized, non-dissociative shocks in which ions and the magnetic field are compressed ahead of the shock front and are able to heat the neutral gas to a few thousand degrees. In C-shocks the physical conditions change more gradually from their pre- to post-shock values and cooling is mainly through radiation from molecular material (e.g. Kaufman & Neufeld 1996). If the temperatures in a C-shock become sufficiently high to start to dissociate molecules, the cooling through the molecular lines diminishes, and the shock temperature increases until it turns into a J-shock. Shocks with a shock velocity larger than 40 km s^{-1} are usually J-shocks, whereas slower shocks are usually of C-type (Chernoff et al. 1982).

The bipolar nebula S106 is one of the most studied H II regions in our galaxy. The exciting source of the region is a very young massive stellar object, known as either IRS4 in the terminology of Gehrz et al. (1982) or IRS3 following Pipher et al. (1976). Around this central source, Hodapp & Rayner (1991) found a cluster of about 160 stars, embedded in the molecular cloud surrounding S106. Observed radio emission and H I

recombination lines from the region have been suggested to arise in a strong ($\dot{M} \approx 2 \times 10^{-5}$ $M_\odot$ yr^{-1}), fast (≈ 200 km s^{-1}), stellar wind, driving a shock into the surrounding extended molecular cloud (Hippelein & Münch 1981). A dark lane, largely devoid of any optical or infrared emission, separates the two lobes of the H II region. This dark lane has been quoted many times as a prime example of a large (30″) circumstellar disk, consisting of cool gas and dust, seen nearly edge-on (Bieging 1984; Mezger et al. 1987). However, Loushin et al. (1990) showed this structure to be an expanding ring of molecular material rather than a protoplanetary disk. Near-infrared ro-vibrational emission of H_2 is seen to arise just outside the H II region, suggesting an origin in a PDR (Hayashi et al. 1990).

Cep A is another well-known site of recent star formation. It contains a luminous (2.5×10^4 $L_\odot$; Evans et al. 1981) far-infrared source, as well as several fainter infrared sources. The core of the Cep A region remains obscured at optical and infrared wavelengths due to massive amounts of extinction, and is the source of an energetic, complex molecular outflow (Bally & Lane 1982). Radio-observations show that it contains two strings of about 13 ultracompact H II regions, arranged in a Y-shape (Hughes 1988). The source IRS 6a (Lenzen et al. 1984), located in the infrared nebula to the east of the core, is the dominant source of the eastern lobe at 20 μm (Ellis et al. 1990), but polarization measurements show that the nebula is illuminated by the compact radio source HW-2 (Hughes & Wouterloot 1984), located $\sim 5''$ south of IRS 6a (Casement & McLean 1996). The fact that it is not visible at 20 μm implies an extremely large extinction towards HW-2. H_2 emission occurs in both the eastern and western parts of the nebula (Doyon & Nadeau 1988). Hartigan et al. (1996) showed that the molecular emission to the east appears as a regular jet, whereas that to the west concentrates in shells, which they proposed to arise in wakes from bow shocks surrounding Herbig-Haro objects in the region. ISO observations of the western part of the region were discussed by Wright et al. (1996), who modelled the observed infrared fine structure lines as arising in a planar J-shock with shock velocity 70–80 km s^{-1}. The same authors modelled the observed molecular hydrogen emission as arising in a combination of several C-shocks. This multitude of shocks in the region agrees with the explanation of Narayanan & Walker (1996), who reported the presence of multiple episodes of outflow activity from the region. Recently, Goetz et al. (1998) presented strong evidence for this scenario through near-infrared H_2 and [Fe II] images of Cep A East showing several distinct regions containing shocks.

In this chapter we will present new *Infrared Space Observatory* (ISO; Kessler et al. 1996) data on infrared fine-structure and molecular emission lines from the central region of S106, centered on IRS4, and the eastern part of Cep A, centered on IRS 6a. We will show that this emission can be well explained as arising in the combination of a PDR and a H II region in the case of S106, whereas this emission seems to be shock-excited in the case of Cep A.

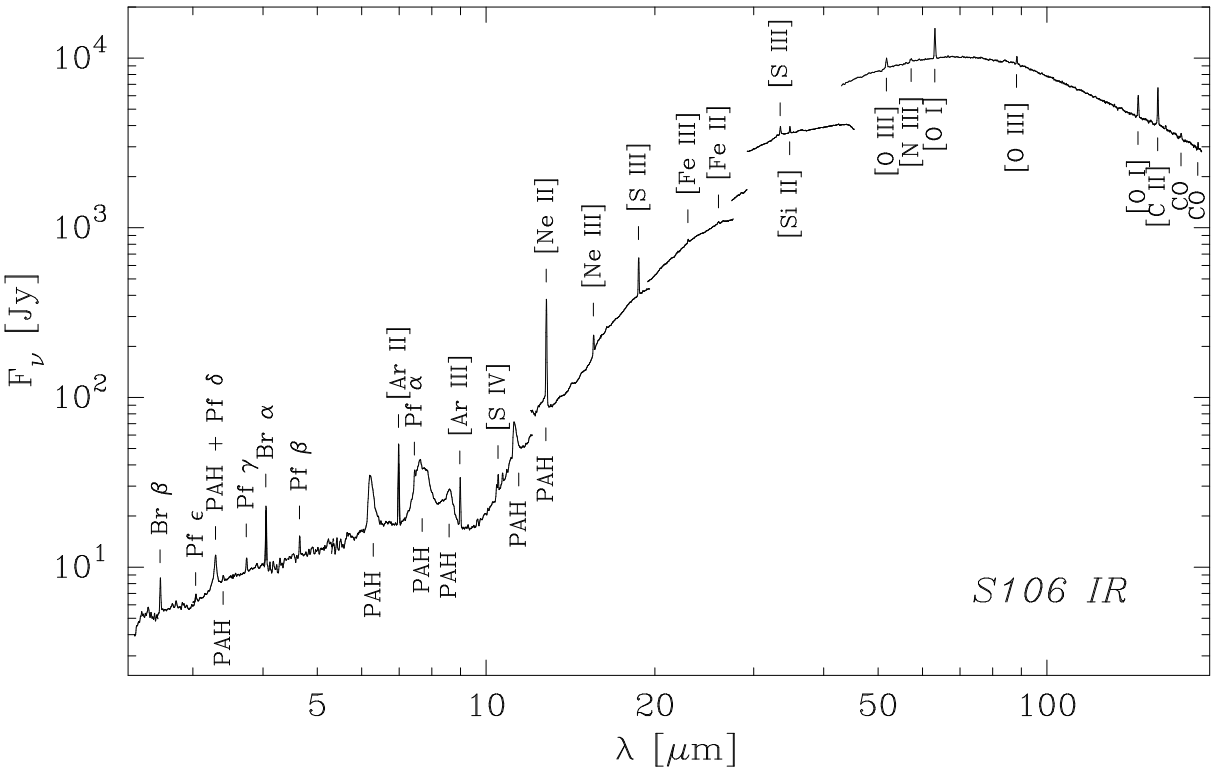

Fig. 7.1. Combined SWS/LWS full grating spectrum for S106 IR with the most prominent features identified.

7.2 Observations

ISO Short Wavelength (2.4–45 μm) Spectrometer (SWS; de Graauw et al. 1996) full grating scans ("AOT S01") of S106 IR and Cep A East were obtained in ISO revolutions 335 (JD 2450373.740) and 843 (JD 2450880.050), respectively. Each of these observations took 2124 seconds of observing time. In addition to this, deeper SWS grating scans on selected molecular and fine transition lines in the two objects ("AOT S02") were obtained in revolutions 134 (at JD 2450172.705; S106), 220 (JD 2450258.463; Cep A) and 566 (JD 2450603.706; Cep A). In revolutions 558 (JD 2450596.103) and 580 (JD 2450617.838), scans at the full SWS grating resolution ("AOT S06") covering the wavelength ranges of 3.0–3.5, 4.0–6.8, 7.0–7.6 and 12.1–16.5 μm were obtained for S106 as well. ISO Long Wavelength (43–197 μm) Spectrometer (LWS; Clegg et al. 1996) grating scans ("AOT L01") of S106 IR and Cep A East were obtained in revolutions 134 (JD 2450172.726) and 566 (JD 2450603.681), respectively. Data were reduced in a standard fashion using calibration files corresponding to OLP version 7.0, after which they were corrected for remaining fringing and glitches. To increase the S/N in the final spectra, the detectors were aligned and statistical outliers were removed, after which the spectra were rebinned to a lower spectral resolution. Since both spectrometers on board ISO use entrance apertures that are smaller than the beam size, a wavelength dependent correction has to be applied to the standard flux calibration when observing extended sources. We determined these correction factors by convolving K-band images of S106

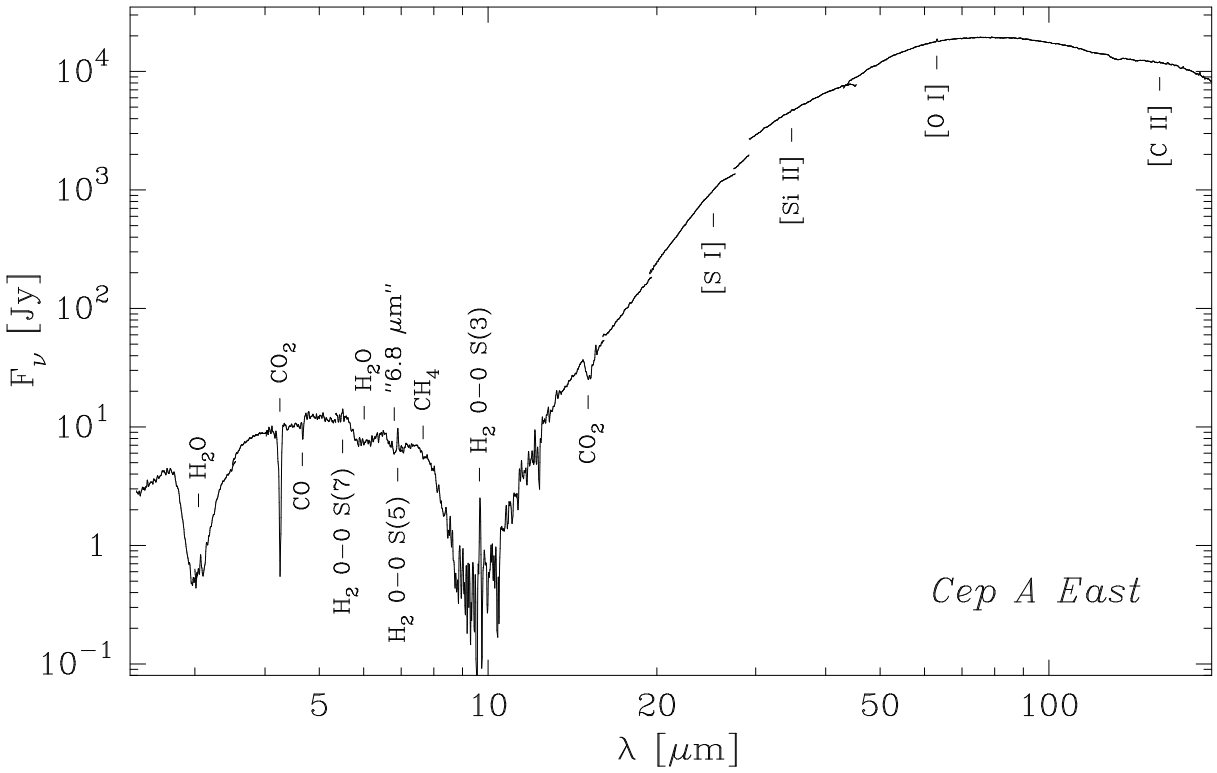

Fig. 7.2. Same as Fig. 7.1 for Cep A East.

and Cep A East (Hodapp & Rayner 1991; Hodapp 1994), shown in Figs. 7.5 and 7.6, with the beam profile and applied these to the data before further analysis. The maximum correction to the flux was 8% in the region around 40 μm. If the sources are more extended at the longer wavelengths or in specific lines than the K-band images we employed in estimating the diffraction losses, we will have underestimated the flux. The maximum error this could introduce in the flux calibration is ≈15%.

Figures 7.1 and 7.2 show the resulting SWS and LWS full grating scans for S106 IR and Cep A East. Scanned lines and measured line fluxes or upper limits to the line flux are listed in Table 7.1. Extinction-corrected surface brightnesses, assuming a beam filling factor of unity, are also listed in this table. Plots of all detected lines, rebinned to a resolution $\lambda/\Delta\lambda$ of 1500 with an oversampling factor of four (SWS), or to a resolution of 500 (LWS), are given in Figs. 7.3 and 7.4.

The SWS spectra shown in Figs. 7.1 and 7.2 consist of twelve different grating scans, each covering a small wavelength region, which were joined to form one single spectrum. Because of the variation of the diffraction limit of the telescope with wavelength, different SWS bands use apertures of different sizes. For a source that is not point-like, one may therefore see a discontinuity in flux at the wavelengths where such a change in aperture occurs. This effect can indeed be seen in both the S106 and Cep A spectra. The relative discontinuities in S106 are close to the maximum possible values, indicating that the source is extended across the entire SWS aperture at the longer wavelengths (33″× 20″). In Cep A the discontinuities are smaller, pointing to a smaller size

Table 7.1. Observed and extinction-corrected line fluxes and model predictions (in 10^{-15} W m^{-2}).

Line	λ	Beam	S106 IR				Cep A East			
	[μm]	[10^{-8} sr]	AOT	Observed	Ext. corr.	Model	AOT	Observed	Ext. Corr.	Model
H_2 0–0 S(0)	28.2188	1.64	S02	$<$ 1.58	$<$ 1.67	0.03	S02	$<$ 3.62	$<$ 3.69	0.03
H_2 0–0 S(1)	17.0348	1.15	S02	0.58±0.18	0.75±0.23	0.98	S02	0.27±0.10	0.28±0.11	0.54
H_2 0–0 S(2)	12.2786	1.15	S02	1.18±0.49	1.61±0.66	0.97	S02	1.27±0.64	1.33±0.67	1.32
H_2 0–0 S(3)	9.6649	0.85	S02	1.19±0.52	2.55±1.11	2.01	S02	0.90±0.38	1.01±0.43	1.31
H_2 0–0 S(4)	8.0251	0.85	S02	0.82±0.29	1.05±0.37	0.76	S02	1.33±0.33	1.38±0.34	1.02
H_2 0–0 S(5)	6.9095	0.85	S02	1.47±0.73	1.69±0.85	0.82	S02	2.42±0.43	2.47±0.43	2.98
H_2 0–0 S(6)	6.1086	0.85	S02	$<$ 1.60	$<$ 1.89	0.04	S02	0.84±0.32	0.86±0.32	0.20
H_2 0–0 S(7)	5.5112	0.85	S02	0.94±0.47	1.13±0.56	0.02	S02	2.48±0.62	2.55±0.63	0.08
H_2 0–0 S(8)	5.0531	0.85	S06	$<$ 0.29	$<$ 0.36	0.00	S02	0.46±0.13	0.48±0.13	0.01
H_2 0–0 S(9)	4.6946	0.85	S02	$<$ 0.57	$<$ 0.73	0.00	S02	$<$ 1.17	$<$ 1.21	0.00
H_2 0–0 S(10)	4.4099	0.85	S02	$<$ 0.48	$<$ 0.62	0.00	S02	0.98±0.49	1.02±0.51	0.00
H_2 0–0 S(11)	4.1813	0.85	S02	$<$ 0.77	$<$ 1.03	0.00	S02	$<$ 0.64	$<$ 0.67	0.00
H_2 0–0 S(12)	3.9960	0.85	S02	$<$ 0.28	$<$ 0.38	0.00	S02	$<$ 0.78	$<$ 0.82	0.00
H_2 1–0 O(5)	3.2350	0.85	S06	0.30±0.05	0.46±0.07	0.00	S01	$<$ 0.74	$<$ 0.79	0.00
H I H7α	19.0624	1.15	S02	0.89±0.30	1.18±0.40	–	S02	$<$ 0.28	$<$ 0.29	–
H I H7β	11.3090	0.85	S02	0.83±0.32	1.29±0.50	–	S01	$<$ 1.05	$<$ 1.12	–
H I H7γ	8.7603	0.85	S02	0.92±0.30	1.57±0.50	–	S01	$<$ 0.70	$<$ 0.76	–
H I H7ε	6.7720	0.85	S06	0.87±0.43	1.01±0.50	–	S01	$<$ 3.67	$<$ 3.75	–
H I H7 13	6.2919	0.85	S06	$<$ 3.25	$<$ 3.80	–	S01	$<$ 3.05	$<$ 3.12	–
H I H7 14	5.9568	0.85	S06	0.54±0.17	0.64±0.20	–	S01	$<$ 4.28	$<$ 4.39	–
H I Huα	12.3719	1.15	S06	4.69±1.31	6.33±1.77	–	S01	$<$ 6.30	$<$ 6.58	–
H I Huβ + H7δ	7.5083	0.85	S02	4.99±1.74	5.79±2.01	–	S02	$<$ 1.37	$<$ 1.40	–
H I Huγ	5.9082	0.85	S06	3.08±0.52	3.67±0.62	–	S01	$<$ 2.94	$<$ 3.01	–
H I Huδ	5.1287	0.85	S06	2.60±0.41	3.20±0.51	–	S01	$<$ 1.91	$<$ 1.96	–
H I Huε	4.6725	0.85	S06	0.87±0.26	1.10±0.33	–	S01	$<$ 6.53	$<$ 6.76	–
H I Hu 12	4.3765	0.85	S06	1.08±0.33	1.40±0.43	–	S01	$<$ 2.01	$<$ 2.09	–
H I Hu 13	4.1708	0.85	S06	1.54±0.51	2.05±0.67	–	S01	$<$ 9.77	$<$ 10.2	–
H I Hu 14	4.0210	0.85	S02	0.97±0.10	1.32±0.14	–	S01	$<$ 1.45	$<$ 1.51	–
H I Pfα	7.4600	0.85	S02	14.6±3.6	16.8±4.2		S02	$<$ 0.30	$<$ 0.31	–
H I Pfβ	4.6539	0.85	S02	9.21±1.18	11.7±1.5	–	S01	$<$ 4.93	$<$ 5.11	–
H I Pfγ	3.7406	0.85	S02	5.60±0.58	7.90±0.82	–	S01	$<$ 1.45	$<$ 1.52	–
H I Pfδ	3.2970	0.85	S02	3.45±0.28	5.32±0.43	–	S01	$<$ 0.72	$<$ 0.76	–
H I Pfε	3.0393	0.85	S06	2.87±0.36	4.76±0.60	–	S01	$<$ 0.65	$<$ 0.70	–
H I Brα	4.0523	0.85	S02	44.6±3.7	60.4±5.0	–	S02	$<$ 1.42	$<$ 1.48	–
H I Brβ	2.6259	0.85	S01	16.9±1.2	32.7±2.3	–	S02	$<$ 1.09	$<$ 1.20	–

Table 7.1. (Continued)

Line	λ	Beam	S106 IR				Cep A East			
	[μm]	[10^{-8} sr]	AOT	Observed	Ext. corr.	Model	AOT	Observed	Ext. Corr.	Model
CO J=14–13	185.999	12.2	L01	118.4±39.5	119.0±39.7	128.0	L01	28.3±2.0	28.3±2.0	29.1
CO J=15–14	173.631	12.2	L01	191.3±63.8	192.5±64.2	149.9	L01	28.3±2.0	28.3±2.0	26.5
CO J=16–15	162.812	11.6	L01	96.4±32.1	97.0±32.3	122.5	L01	21.1±1.5	21.1±1.5	22.7
CO J=17–16	153.267	11.6	L01	99.8±33.3	100.5±33.5	98.4	L01	$<$ 33.3	$<$ 33.4	19.7
He I ($^3D_1$–$^3F_0$)	4.0373	0.85	S02	1.42±0.28	1.93±0.38	–	S02	$<$ 2.05	$<$ 2.15	–
He I ($^3S_1$–$^3P_0$)	4.2954	0.85	S06	6.43±0.85	8.45±1.12	–	S01	$<$ 6.91	$<$ 7.19	–
[Ca IV] ($^2P_{3/2}$–$^2P_{1/2}$)	3.2067	0.85	S06	0.26±0.05	0.40±0.08	0.00	S01	$<$ 0.68	$<$ 0.72	0.00
[Fe I] ($^5D_4$–$^5D_3$)	24.0424	1.15	S02	$<$ 1.01	$<$ 1.22	0.05	S02	$<$ 1.19	$<$ 1.23	–
[Fe I] ($^5D_3$–$^5D_2$)	34.7135	2.01	S02	$<$ 5.99	$<$ 6.64	0.02	S02	$<$ 4.74	$<$ 4.81	–
[Fe II] ($^6D_{9/2}$–$^4F_{9/2}$)	5.3403	0.85	S06	3.04±0.60	3.69±0.73	–	S01	$<$ 4.14	$<$ 4.26	–
[Fe II] ($^4F_{9/2}$–$^4F_{7/2}$)	17.9363	1.15	S02	0.89±0.26	1.19±0.35	0.97	S02	0.24±0.06	0.25±0.07	0.23
[Fe II] ($^6D_{9/2}$–$^6D_{7/2}$)	25.9882	1.15	S02	5.27±1.10	6.20±1.29	3.37	S02	0.64±0.21	0.66±0.21	0.98
[Fe II] ($^6D_{7/2}$–$^6D_{5/2}$)	35.3491	2.01	S02	4.94±2.47	5.46±2.73	1.21	S02	$<$ 4.01	$<$ 4.07	0.40
[Fe III] ($^5D_4$–$^5D_3$)	22.9250	1.15	S01	19.2±3.9	23.5±4.7	28.0	S01	$<$ 22.7	$<$ 23.4	0.00
[Ni II] ($^2D_{5/2}$–$^2D_{3/2}$)	6.6360	0.85	S06	1.88±0.42	2.19±0.49	1.32	S01	$<$ 3.04	$<$ 3.11	1.43
[Ni III] ($^3F_4$–$^3F_3$)	7.349	0.85	S06	1.33±0.35	1.53±0.41	1.05	S01	$<$ 0.66	$<$ 0.67	0.00
[Ar II] ($^2P_{3/2}$–$^2P_{1/2}$)	6.9853	0.85	S01	64.4±9.7	74.2±11.2	74.2	S01	$<$ 1.19	$<$ 1.22	–
[Ar III] ($^3P_2$–$^3P_1$)	8.9914	0.85	S01	24.0±6.0	44.3±11.1	44.5	S01	$<$ 1.11	$<$ 1.22	0.00
[Ne II] ($^2P_{3/2}$–$^2P_{1/2}$)	12.8135	1.15	S06	239.6±60.1	309.3±77.5	320.2	S01	$<$ 2.80	$<$ 2.91	2.67
[Ne III] ($^3P_2$–$^3P_1$)	15.5551	1.15	S06	31.4±7.9	39.3±9.9	31.7	S01	7.87±2.01	8.13±2.17	0.00
[S I] ($^3P_2$–$^3P_1$)	25.2490	1.15	S02	$<$ 2.96	$<$ 3.52	0.05	S02	0.70±0.21	0.72±0.22	0.82
[S III] ($^3P_1$–$^3P_2$)	18.7130	1.15	S01	169.4±34.0	225.3±45.2	243.1	S01	$<$ 2.80	$<$ 2.92	0.00
[S III] ($^3P_0$–$^3P_1$)	33.4810	2.01	S01	132.9±19.3	148.2±21.5	155.5	S01	$<$ 39.2	$<$ 39.9	0.00
[S IV] ($^2P_{1/2}$–$^2P_{3/2}$)	10.5105	0.85	S01	7.33±1.85	13.47±3.40	14.6	S01	$<$ 1.07	$<$ 1.16	0.00
[Si II] ($^2P_{1/2}$–$^2P_{3/2}$)	34.8152	2.01	S02	152.3±59.2	168.7±65.6	116.9	S02	5.86±0.22	5.94±0.23	4.21
[N III] ($^2P_{1/2}$–$^2P_{3/2}$)	57.34	15.7	L01	98.7±19.8	103.4±20.8	88.4	L01	$<$ 81.0	$<$ 81.6	0.00
[O I] ($^3P_2$–$^3P_1$)	63.1850	16.3	L01	1125±114	1172±118	1131	L01	201.9±11.1	203.1±14.2	116.1
[O I] ($^3P_1$–$^3P_0$)	145.535	8.82	L01	288.8±29.0	291.2±29.2	320.6	L01	14.4±1.8	14.4±1.8	2.49
[O III] ($^3P_1$–$^3P_2$)	51.8145	15.7	L01	381.4±42.8	403.8±45.3	388.5	L01	$<$ 80.9	$<$ 81.5	0.00
[O III] ($^3P_0$–$^3P_1$)	88.3562	14.8	L01	124.9±15.1	127.5±15.4	112.9	L01	$<$ 50.3	$<$ 50.5	0.00
[C II] ($^2P_{1/2}$–$^2P_{3/2}$)	157.741	11.6	L01	157.2±15.9	158.3±16.0	140.3	L01	16.3±2.0	16.4±2.0	2.66

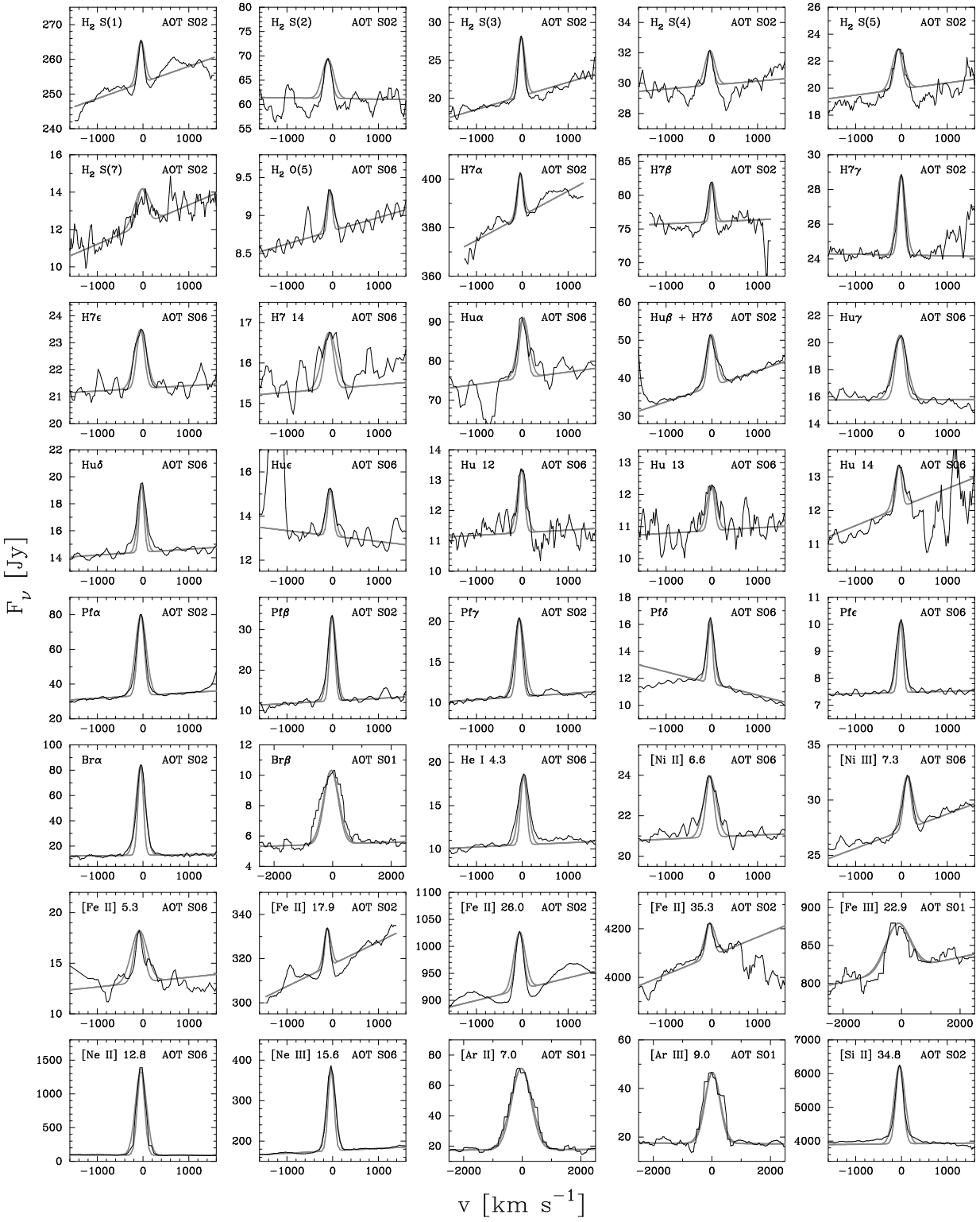

Fig. 7.3. Detected lines in S106 IR. The velocities are heliocentric. The grey lines indicate the instrumental profiles for a point source and an extended source filling the entire aperture.

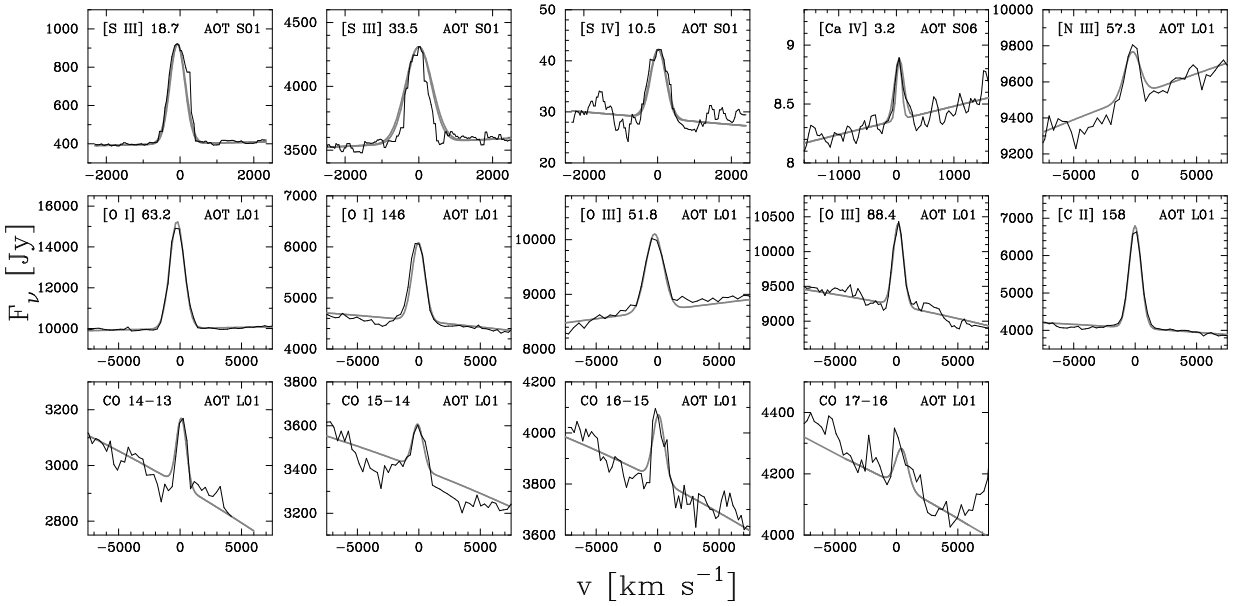

Fig. 7.3. (Continued)

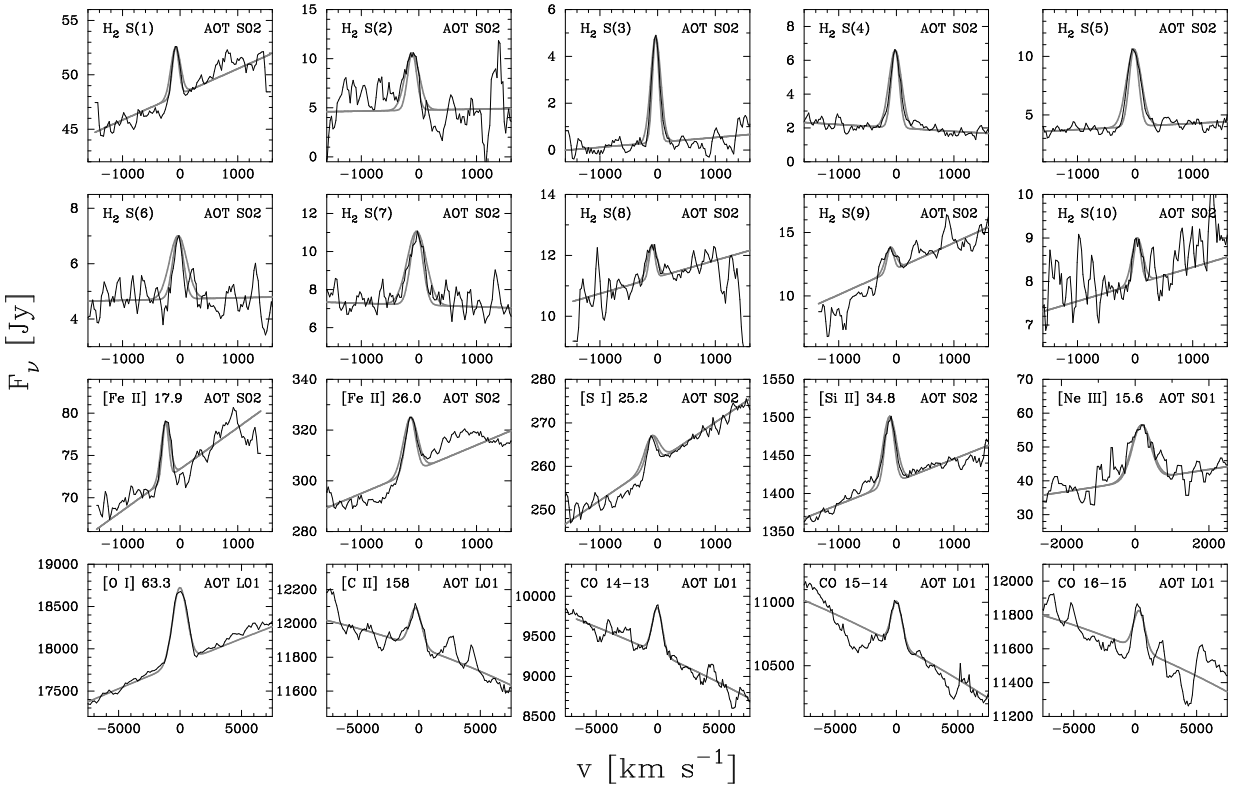

Fig. 7.4. Same as Fig. 7.3 for Cep A East.

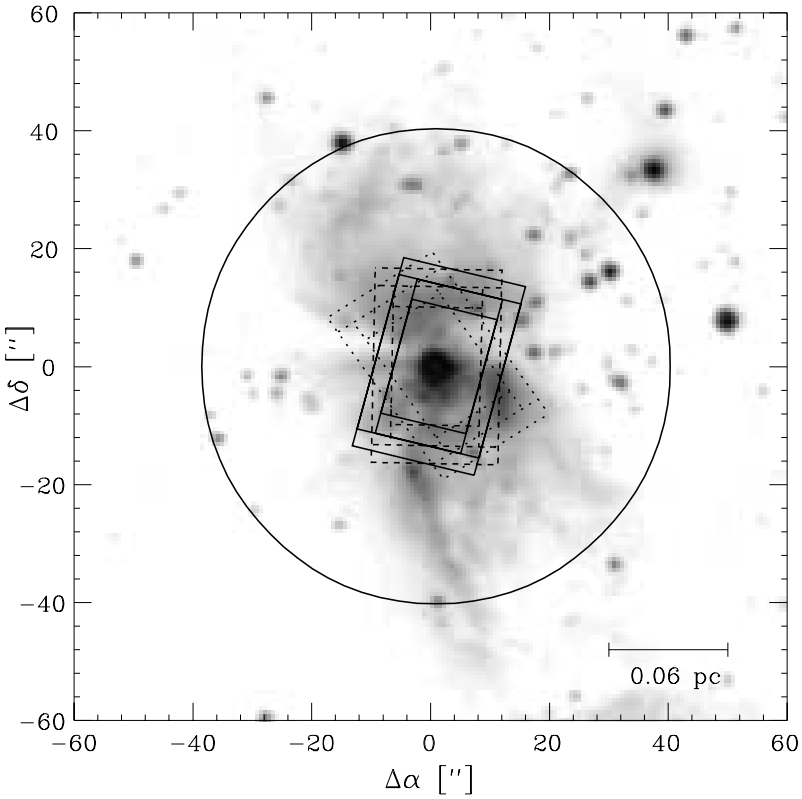

Fig. 7.5. SWS AOT S01 (solid rectangles), AOT S02 (dashed rectangles), AOT S06 (dotted rectangles) and LWS (solid circle; beam average FWHM) aperture positions for our measurements of S106 superimposed on a K′-band image of the region. The rectangles indicate the apertures (in increasing size) for SWS bands 1A–2C (2.4–12.0 μm), 3A–3D (12.0–27.5 μm), 3E (27.5–29.5 μm) and 4 (29.5–40.5 μm).

of the far-infrared source.

Since both grating spectrometers on board ISO use apertures that are fairly large compared to the separation of sources in most star forming regions, some caution is appropriate in interpreting such measurements. We created a plot with the positions of the SWS apertures, overlaid on K-band images of the observed regions (Hodapp & Rayner 1991; Hodapp 1994), shown in Figs. 7.5 and 7.6. As can be seen from these figures, only one strong, albeit extended, near-infrared source is included in each aperture.

7.3 Solid-state features

The SWS spectrum of S106 (Fig. 7.1) consists of a relatively smooth continuum, with numerous strong emission lines superimposed. The familiar UIR bands at 3.3, 3.4, 6.2, 7.6, 7.8, 8.6 and 11.3 μm, usually attributed to polycyclic aromatic hydrocarbons (PAHs), are present in emission and strong. The absorption band around 3.0 μm due to the O–H stretch mode of H_2O ice is present, as well as the familiar 9.7 μm absorption feature due to the Si–O stretching mode in amorphous silicates. Since extinction in

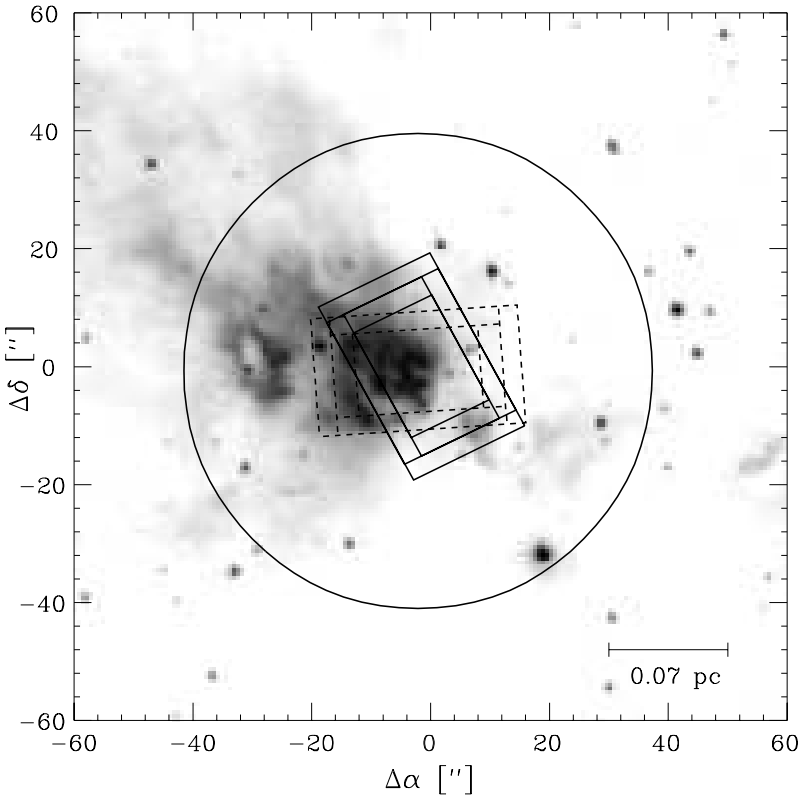

Fig. 7.6. Same as Fig. 7.5 for Cep A East.

the continuum surrounding the 9.7 μm feature is small compared to the extinction within this feature, the extinction A_λ at wavelength λ across a non-saturated 9.7 μm feature can simply be obtained from the relation $A_\lambda = -2.5 \log(I/I_0)$. Using an average interstellar extinction law which includes the silicate feature (Fluks et al. 1994), we can then convert these values of A_λ to a visual extinction, resulting in a value of A_V = 13$^{\rm m}$.7 toward S106 IR. This value is in excellent agreement with that of 13$^{\rm m}$.4 $\pm$ 2.7, derived towards stars in the S106 embedded cluster (Hodapp & Rayner 1991). It is also in agreement with the extinction of A_V = 12$^{\rm m}$ towards the northern lobe of the S106 nebula (Felli et al. 1984). It is somewhat larger than that towards the southern lobe (A_V = 8$^{\rm m}$; Felli et al. 1984) and much smaller than that towards the central source (A_V = 21$^{\rm m}$; Eiroa et al. 1979), suggesting than the main source of the detected continuum emission is the northern lobe of S106.

For Cep A East the SWS spectrum (Fig. 7.2) is dominated by absorption bands from a variety of ices. The O–H bend and stretch modes of H_2O at 3.0 and 6.0 μm are strong, as are the 4.27 μm ^{12}C=O stretch and the 15.3 μm O=C=O bending mode of CO_2. The ^{12}C=O stretch of CO at 4.67 μm is clearly detected. The absorption band around 7.7 μm, attributed to solid CH_4 (Boogert et al. 1996, 1997) is present as well. The unidentified absorption feature around 6.8 μm, also observed toward NGC 7538 IRS9 and RAFGL 7009S (Schutte et al. 1996; d'Hendecourt et al. 1996) is also present in Cep A. The 9.7 μm amorphous silicate feature consists of a very deep, saturated, absorption. From the

Table 7.2. Column densities of solid state absorption features towards S106 and Cep A.

Species	λ	A_m	Cep A East		S106 IR	
	[μm]	[cm molec^{-1}]	$\int \tau(\nu)d\nu$ [cm^{-1}]	N [cm^{-2}]	$\int \tau(\nu)d\nu$ [cm^{-1}]	N [cm^{-2}]
H_2O	3.0	2.0×10^{-16}	1051	5.3×10^{18}	10.1	5.1×10^{16}
H_2O	6.0	1.2×10^{-17}	60	5.0×10^{18}	< 4.9	$< 4.1 \times 10^{17}$
CO	4.67	1.1×10^{-17}	3.8	3.5×10^{17}	< 1.9	$< 1.7 \times 10^{17}$
CO_2	4.26	7.6×10^{-17}	58	7.6×10^{17}	< 6.4	$< 8.4 \times 10^{16}$
CO_2	15.2	1.1×10^{-17}	9.2	8.4×10^{17}	< 1.5	$< 1.3 \times 10^{17}$
CH_4	7.67	7.3×10^{-18}	1.7	2.3×10^{17}	< 2.8	$< 3.9 \times 10^{17}$
Silicate	9.7	1.2×10^{-16}	965	8.0×10^{18}	106	8.8×10^{17}

non-saturated wings of this feature we can again derive a visual extinction, resulting in a value of A_V = 270$^{\rm m}$ for Cep A East. This value is within the range of A_V = 75–1000$^{\rm m}$ extinction for the central source and nebula reported by Lenzen et al. (1984). PAHs appear absent in Cep A East.

From the integrated optical depth $\int \tau(\nu)d\nu$ of a non-saturated absorption feature we can compute a column density N using an intrinsic band strength A_m. For H_2O, CO, CO_2 and CH_4 ices, values of A_m were measured by Gerakines et al. (1995) and Boogert et al. (1997). For silicates, A_m is taken from Tielens & Allamandola (1987), based on the lab measurements by Day (1979). Integrated optical depth and column density values are listed in Table 7.2. The derived abundances of 100:6:15 for H_2O:CO:CO_2 are within the range of values observed in other lines of sight (Whittet et al. 1996; d'Hendecourt et al. 1996).

7.4 Molecular hydrogen emission

From the H_2 line fluxes $I(J)$ listed in Table 7.1 it is possible to calculate the apparent column densities of molecular hydrogen in the upper J levels, averaged over the SWS beam, $N(J)$, using $N(J) = \frac{4\pi I(J)}{A}\frac{\lambda}{hc}$, with λ the wavelength, h Planck's constant and c the speed of light. The transition probabilities A were taken from Turner et al. (1977). Line fluxes were corrected for extinction using the average interstellar extinction law by Fluks et al. (1994). For S106 IR we adopted the value of A_V = 13$^{\rm m}$.7 derived in the previous section. The fact that the 0–0 S(3) line of H_2, with a wavelength near the center of the 9.7 μm amorphous silicate feature, was detected in Cep A indicates that it cannot suffer from the same extinction as the continuum; the H_2 emission must originate in a spatially separate region from the continuum. Therefore we adopt a much smaller value of A_V = 2$^{\rm m}$, expected to be a reasonable value for an origin in either a shock or PDR, for the emission lines observed toward Cep A East.

A useful representation of the H_2 data is to plot the log of $N(\mathrm{J})/\mathrm{g}$, the apparent

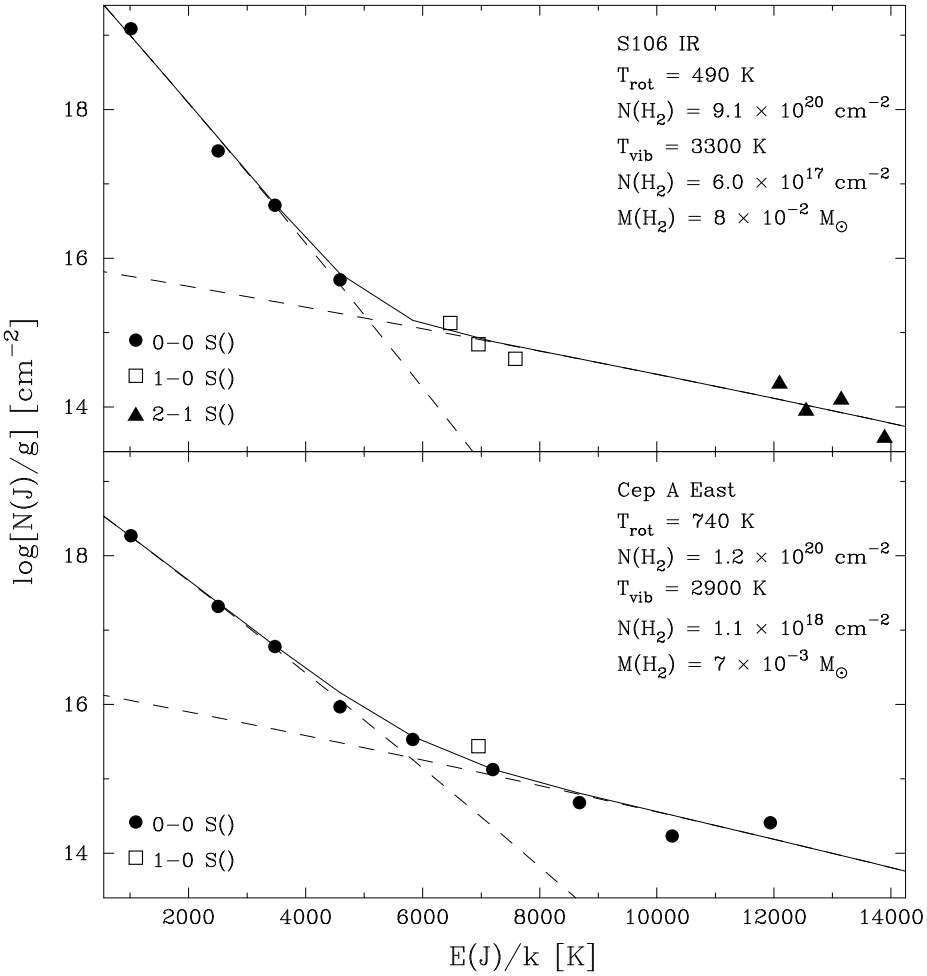

Fig. 7.7. H_2 excitation diagram for S106 (top) and Cep A East (bottom). ISO observations of pure rotational lines are indicated by the circles. Triangles and squares indicate ground-based measurements of ro-vibrational lines from literature. The dashed lines give the Boltzmann distribution fits to the low-lying pure rotational lines and all lines with upper level energies above 5000 K. The solid line shows the sum of both contributions.

column density for a given J upper level divided by the statistical weight, versus the energy of the upper level, taken from Dabrowski (1984). These plots are shown in Fig. 7.7. Also plotted in these figures are several measurements of H_2 ro-vibrational lines in S106 and Cep A from literature (Tanaka et al. 1989; Longmore et al. 1986; Bally & Lane 1982). Although these measurements were taken at the same positions on the sky as ours, the beam sizes used were different and hence one may expect to see systematic differences in the derived specific intensities if the source of H_2 radiation is more extended than the beam size. In fact only the S106 measurements by Longmore et al. (1986), taken with the smallest beam diameter, 12″, differ systematically from the other measurements, indicating that the extent of the H_2 emitting region in S106 is probably somewhat larger than their beam size. This agrees well with the H_2 1–0 S(1) image of the region by Hayashi et al. (1990). In Fig. 7.7 the Longmore et al.

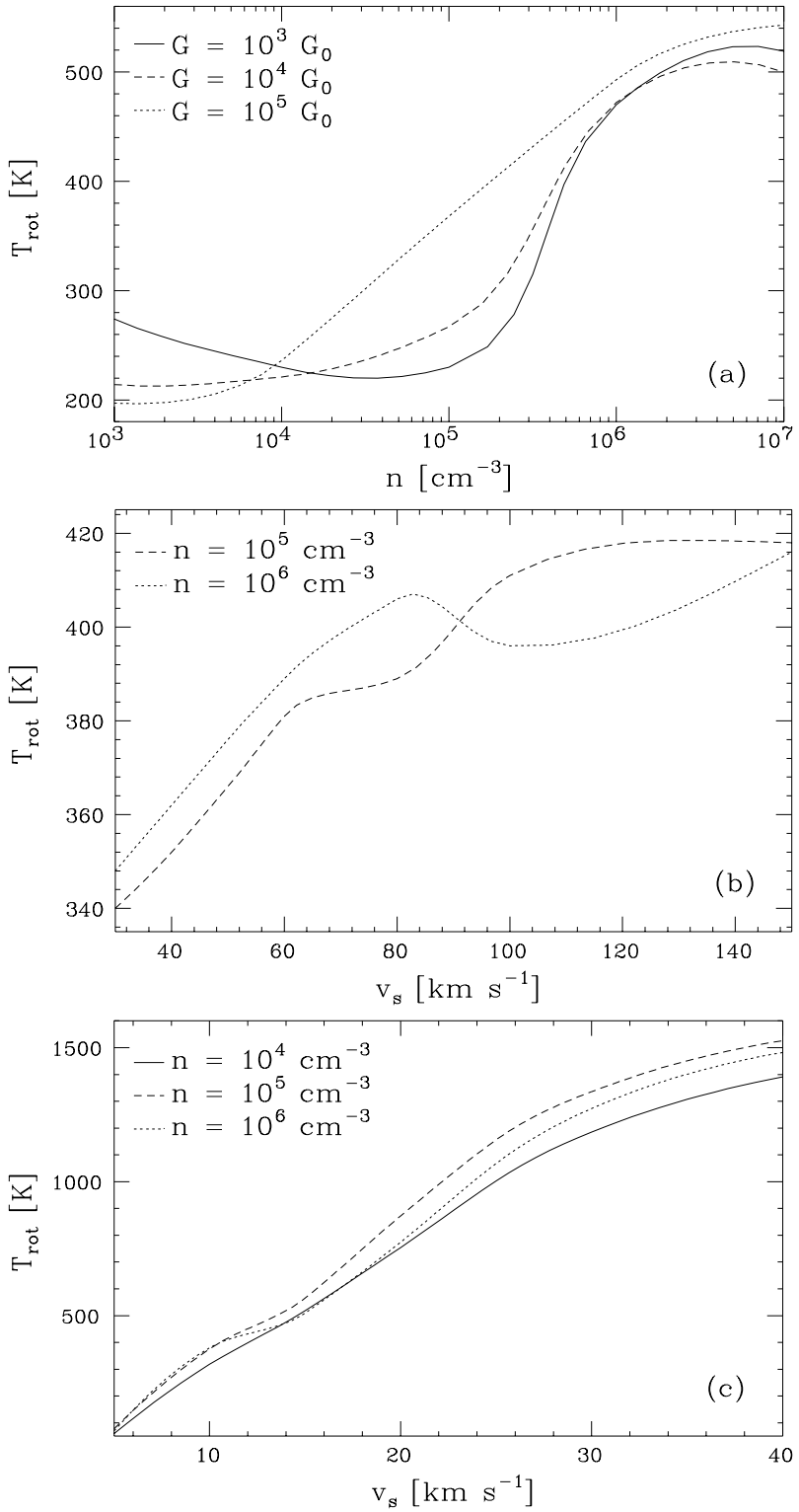

Fig. 7.8. Theoretical relation between a) $T_{\rm rot}(H_2)$ and n for PDR models, b) $T_{\rm rot}(H_2)$ and v_s for J-shock models, and c) $T_{\rm rot}(H_2)$ and v_s for C-shock models.

measurements of S106 were scaled to the Tanaka et al. (1989) data.

The statistical weight g used in Fig. 7.7 is a combination of the rotational and nuclear spin components. We have assumed the high temperature equilibrium relative abundances of 3:1 for the ortho and para forms of H_2 (Burton et al. 1992). For a Boltzmann distribution, the slope of this plot is inversely proportional to the excitation temperature, while the intercept is a measure of the total column density of warm gas. Since the A coefficients for the H_2 lines are quite small, these lines are optically thin and the excitation temperature will be close to the kinetic temperature of the gas.

Using the formula by Parmar et al. (1991) and the rotational constants by Dabrowski (1984) to fit our data points in the low-lying pure rotational levels to a Boltzmann distribution, we arrive at values of 490 K and 9×10^{20} cm^{-2} and 740 K and 1×10^{20} cm^{-2} for S106 IR and Cep A East, respectively. Using the distances to S106 and Cep A of 1200 and 690 pc (Rayner 1994; Mel'nikov et al. 1995), this corresponds to total molecular hydrogen masses of 0.08 and 0.007 $M_\odot$ within the SWS beam. Using the alternative distance estimate towards S106 of 600 pc (Staude et al. 1982) would decrease the S106 H_2 mass to 0.04 $M_\odot$. The fitted Boltzmann distributions are shown as the leftmost dashed lines in Fig. 7.7. The fact that the points for the ortho and para form of H_2 lie on the same line proves that our assumption on their relative abundances is correct.

As can be seen from Fig. 7.7, both the pure-rotational and ro-vibrational lines of H_2 with upper level energies higher than 5000 K deviate significantly from the leftmost dashed line. In both cases a Boltzmann distribution was fitted to these lines as well, shown as the rightmost dashed line in both figures. In the case of S106, the relative location of the 1–0 and 2–1 S(1)-lines in Fig. 7.7 are indicative of fluorescent excitation through UV pumping (Draine & Bertoldi 1996; Black & van Dishoeck 1997). The fitted Boltzmann distribution to the higher energy levels has thus no physical meaning, but may still be useful to provide a simple parametrization of the relative population of the energy levels. In the case of Cep A, the lines may indicate the presence of a smaller column (10^{18} cm^{-2}) of hot (a few 1000 K) molecular hydrogen, in addition to the large column of warm gas.

Employing predictions of H_2 emission from PDR, J-shock and C-shock models by Burton et al. (1992), Hollenbach & McKee (1989) and Kaufman & Neufeld (1996), we determined the excitation temperature $T_{\rm rot}$ from the low-lying pure rotational levels from these models as a function of density n and either incident FUV flux G (in units of the average interstellar FUV field $G_0 = 1.2 \times 10^{-4}$ erg cm^{-2} s^{-1} sr^{-1}; Habing 1968) or shock velocity v_s in an identical way as was done for the observations. The resulting relations between $T_{\rm rot}$ and n or v_s are shown in Fig. 7.8. As can be seen from these plots, the PDR and J-shock models predict a fairly small (200–540 K) range of resulting excitation temperatures, whereas in the C-shocks this range is much larger (100–1500 K). Furthermore, we see that in the model predictions for shocks the resulting $T_{\rm rot}$ does not depend much on density, whereas for PDRs it does not depend much on G, suggesting that once the mechanism of the H_2 emission is established, it can be used to constrain v_s or n in a straightforward way.

Comparing the excitation temperatures of 490 and 740 K for S106 and Cep A with those plotted in Fig. 7.8, we note that for S106 this falls well within the range of PDR-

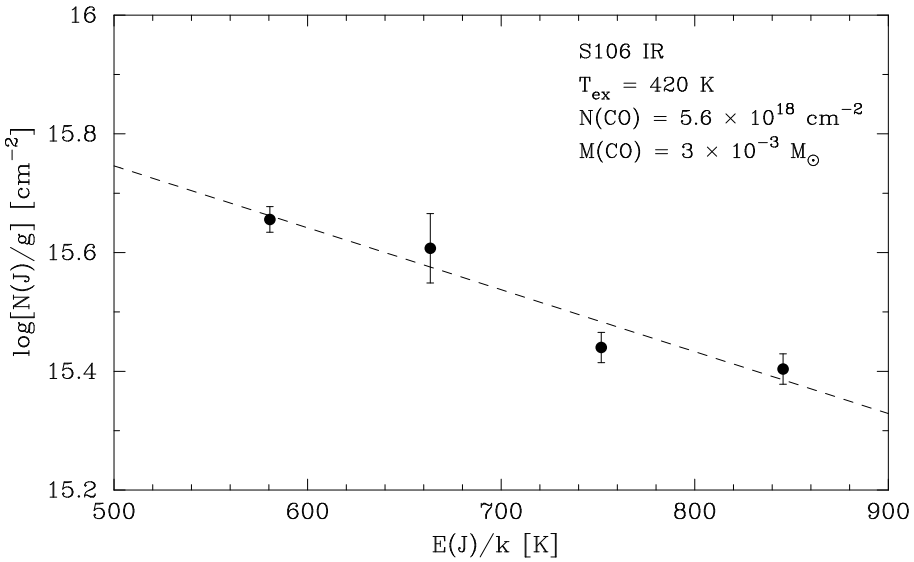

Fig. 7.9. CO excitation diagram for S106. The dashed line gives the fit of the Boltzmann distribution to the data points.

and C-shock model predictions, but are too high compared to the ones expected from J-shocks. The observed bright PAH emission features (Fig. 7.1) and the atomic fine-structure line spectrum (Sect. 7.5) point towards a PDR origin for the H_2 emission in S106. The higher temperature for Cep A can only be reproduced by the C-shock models. Therefore we tentatively conclude that a dense ($\geq 10^6$ cm^{-3}) PDR seems to be the best candidate to explain the observed H_2 emission in S106 IR and a slow ($\approx$ 20 km s^{-1}) non-dissociative shock can explain the observed warm column of H_2 in Cep A East. Since the regions we're looking at probably only fill part of the SWS beam, the absolute intensity of the H_2 emission listed in Table 7.1 can also be reproduced by these same models by varying the beam filling factor.

7.5 Carbon-monoxide emission lines

In S106 IR, several ro-vibrational emission lines due to gas-phase CO were detected in the long-wavelength part of the LWS (Fig. 7.3). Similar to what was done for the H_2 emission in the previous section, we constructed a CO excitation diagram for S106, using molecular data from Kirby-Docken & Liu (1978). It is shown in Fig. 7.9. The temperature and column of CO resulting from the Boltzmann fit to this excitation diagram are 420 K and 5.6×10^{18} cm^{-2}.

The CO excitation temperature of 420 K is somewhat lower than that found from the H_2 lines, in agreement with what is expected from a PDR, in which the CO emission arises in deeper embedded regions than the H_2. We conclude that a PDR is the most likely candidate for the source of the gas-phase CO emission in S106.

The observed CO lines have critical densities of around 10^6 cm^{-3}. Therefore the observation of these lines in S106 also implies densities of this order of magnitude or

higher in the originating region. Assuming that these densities would exist in the entire S106 PDR would be implausible. If these CO lines do indeed arise in the large-scale environment of S106, the PDR must therefore have a clumpy structure (e.g. Burton et al. 1990). An alternative explanation of the presence of these lines, would be to identify the originating region with the surface of the extended disk-like structure surrounding S106 which could act like a PDR. With the present data-set we cannot make a distinction between these two possibilities.

7.6 Fine structure lines

Important constraints on the physical conditions in the line emitting region come from the observed fine structure lines. As a first step towards identifying the mechanism responsible for the observed emission we can look at the mere presence of certain lines. The observed lines with high ionization potentials in S106, such as [O III], [Ar III], [Ne III], [Ni III], [Fe III] and [S IV] can only originate in the H II region surrounding S106. The PAH emission as well as the molecular lines observed towards S106 are indicative of the presence of a PDR as well. This PDR might contribute to the observed [Fe II], [Ni II], [Si II], [O I] and [C II] emission. We thus need to model the fine-structure lines in S106 IR as arising in the combination of an H II model and a PDR.

We have used the photo-ionization code CLOUDY (version 90.04; Ferland 1996) to generate model predictions for line strengths for the H II region surrounding S106 IR, assuming a spherical geometry and constant hydrogen density throughout the region. We generated a grid of models in which the input spectrum, taken from Kurucz (1991) models for a stellar photosphere, and the electron density in the H II region were varied. The total luminosity of the model was fixed to the total bolometric luminosity of S106 of 4.2×10^4 $L_\odot$. The line ratios of the observed [O III] and [S III] fine structure lines are expected to depend mainly on density, and hardly on the temperature. Their behaviour in our H II region model as well as the observed line ratios in S106 are shown in Fig. 7.10. From the fact that both line ratios agree on the thus obtained value for the electron density in the H II region, 1.3–2.5 $\times$ 10^3 cm^{-3}, we conclude that our assumption of a constant density is reasonable. Several other lines ratios ([Ar II]/[Ar III], [Ne II]/[Ne III] and [S III]/[S IV]) depend mainly on the effective temperature of the star and do not depend on density much. Their behaviour in the CLOUDY models for S106 are shown in Fig. 7.10 as well. From these plots, it can be seen that the source of ionizing photons should have a temperature between 37,000 and 40,000 K, corresponding to a spectral type of O6–O8. However, not all observed line ratios yield the same temperature for the central star. Most likely this is due to the fact that the Kurucz models used for the input spectrum do not include the opacity shortward of the He II ionization limit due to the stellar wind, which is expected to be strong in the case of S106. The true temperature for the central source is therefore expected to be around the lower range of temperatures deduced from the Kurucz synthetic photospheres, i.e. around 37,000 K. For illustrative purposes, we also show the ratio of [O I] 63.2 μm/[O III] 51.8 μm for our model H II region, showing that virtually all the atomic

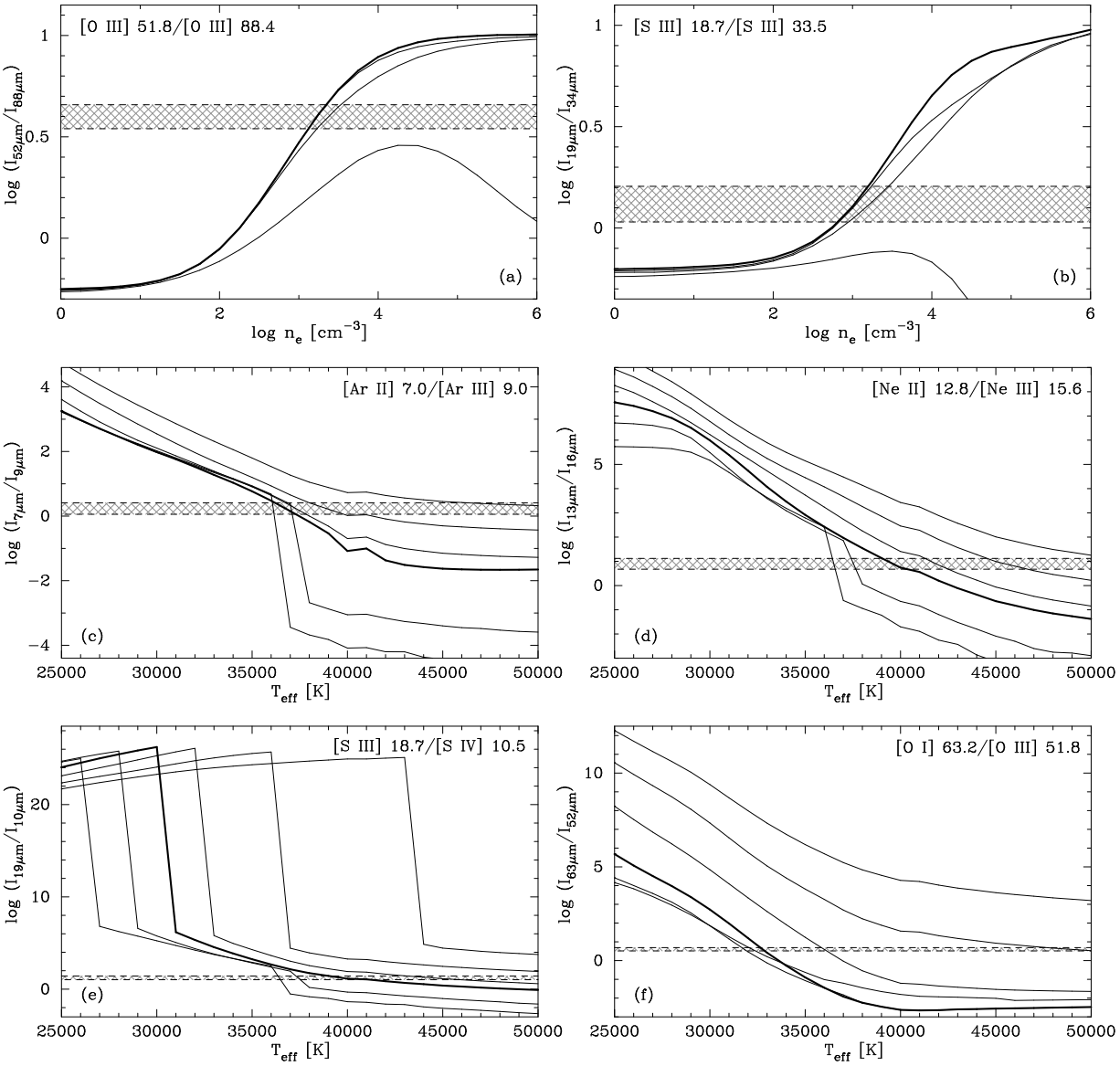

Fig. 7.10. CLOUDY model predictions for various emission line ratios from the S106 H II region as function of electron density n_e and temperature of the ionizing star. The hatched regions between the dashed lines show the error interval of the observed ratios in S106 IR. The solid lines show the computed ratios for log n_e = 1.0–6.0, or $T_{\rm eff}$ = 15,000–50,000 K. The heavy curves indicate the lines with log n_e = 3.0 or $T_{\rm eff}$ = 40,000 K (best fit). (a) Behaviour of the [O III] 51.8 μm/[O III] 88.4 μm line flux ratio. (b) The same for the [S III] 18.7 μm/[S III] 33.5 μm ratio. (c) Same for the [Ar II] 7.0 μm/[Ar III] 9.0 μm ratio. (d) Same for the [Ne II] 12.8 μm/[Ne III] 15.6 μm ratio. (e) Same for the [S III] 18.7 μm/[S IV] 10.5 μm ratio. (f) Same for the [O I] 63.2 μm/[O III] 51.8 μm ratio.

oxygen will be in the form of [O III] and that we can thus safely attribute all of the observed [O I] emission to the PDR.

To be able to explain the observed intensity of 1.3×10^{-2} erg s^{-1} cm^{-1} sr^{-1} for the [Si II] line at 34.8 μm in S106, the Tielens & Hollenbach (1985) PDR models require a density higher than $\approx 10^5$ cm^{-3} and $G \geq 10^5$ G$_0$. This regime can also reproduce the observed ratios of [Si II] and the [Fe II] and [O I] lines, although to reproduce both the exact strength of the [Si II] emission and the relative strength to that to the [Fe II] lines requires a [Fe II] depletion of $\approx 30\%$ higher than the one assumed in the Tielens & Hollenbach models. An alternative explanation could be that the PDR doesn't fill the SWS aperture at 35 micrometer ($33'' \times 20''$) completely, increasing the surface brightness of all lines. The predicted intensities of [S I] and [Fe I] are sufficiently low to be undetectable, in agreement with the observations.

Towards Cep A East, only fine structure lines that can be produced in shocks were observed. In contrast to both C- and J-shocks, PDRs do not produce significant quantities of [S I] emission (Tielens & Hollenbach 1985). Therefore this line must be completely due to one or more shocks. C-shocks only contain trace fractions of ions and hence cannot explain the observed [Fe II], [Si II] and [C II] emission. Hence the simplest hypothesis would be to try to explain the observed fine-structure lines in Cep A in terms of a J-shock model. To explain the [S I] surface brightness of 1.0×10^{-3} erg s^{-1} cm^{-2} sr^{-1} requires a moderately dense (10^4–10^5 cm^{-3}) pre-shock gas. If the shock does not fill the ISO beam completely, as is expected, this number will go up. The absence of [Fe I] emission does indicate that we are dealing with higher (10^5–10^6 cm^{-3}) densities, so line ratios seem to provide more reliable constraints in this case. However, the aperture sizes for lines measured at different wavelengths are also different in some cases, making this method only reliably applicable to line ratios measured in identical SWS or LWS apertures. Therefore the ratio of [Fe II] 26.0 μm to [S I] 25.2 μm might provide the most reliable indicator of physical conditions in the shock. To reproduce the observed value of 0.26 with the Hollenbach & McKee (1989) J-shock models requires either moderately dense (10^5 cm^{-3}) gas with a low (30 km s^{-1}) shock velocity or a high (10^6 cm^{-3}) density with a faster (≈ 60 km s^{-1}) shock. To have the predicted [Fe I] emission sufficiently low to explain our non-detections of those, the moderately dense, slow J-shock model is required. This regime also reproduces the relative [Si II] strength.

As was discussed in the previous section, one or multiple J-shocks cannot reproduce the observed H_2 emission (although a contribution to this can be expected). The success of the J-shock model in explaining the observed fine-structure lines and the absence of PAH emission in Cep A East (Fig. 7.2; see also the discussion by Hodapp & Eiroa 1989), excluding the possibility of a significant contribution from a PDR, leads us to pose that a combination of one or more J- and C-shocks must be responsible for the observed emission in Cep A. The presence of more than one type of shock in the region could be linked to the reported multiple episodes of outflow activity from the embedded source (Narayanan & Walker 1996). In the presence of both a J- and a C-shock, the [Si II] and [Fe II] emission would originate completely in the J-shock, whereas both the C- and the J-shock would contribute to the observed [S I] and H_2 spectra. With the

J-shock parameters derived from the fine-structure lines, an additional C-shock component with a shock-velocity of about 20 km s^{-1} is required to reproduce the observed pure rotational H_2 emission. The observed hot column of H_2 in Cep A may then be due to formation pumping (the effect that H_2 gets re-formed with non-zero energy in the post-shock gas after being dissociated in the shock front) in the J-shock. To have the ro-vibrational lines of comparable intensity as the rotational lines (through collisional excitation) requires pre-shock densities of the order of 10^6 cm^{-3}. For both S106 IR and Cep A, predicted lines strengths of the best fit models are also listed in Table 7.1.

7.7 Discussion and conclusions

It is interesting to compare the derived results for the emission from the eastern lobe of Cep A with the results by Wright et al. (1996), obtained using the same instrument, for the western part of this same nebula. They derived a $T_{\rm rot}$ of 700 $\pm$ 30 K for the H_2 lines with upper level energies up to 7000 K, and a temperature range up to 11,000 K for the higher upper level energies. They explained this H_2 emission as arising from a combination of at least two C-shocks with different pre-shock density, shock velocity and covering factor. In addition to this, they also reported emission from [Ne II], [S I] and [Si II], which they explained as arising in a planar J-shock with pre-shock density of 10^3–10^4 cm^{-3} and shock velocity 70–80 km s^{-1}. Qualitatively, the detected lines in the eastern and western part of the nebula are well in agreement, suggesting a common origin. The main difference between the observed lines seems to be that they are much more intense in the western part of Cep A, indicating that the densities there are a factor of 100 higher than those obtained for the eastern lobe, but the shock velocities are comparable in both parts of the nebula. The similarity between these two parts of Cep A are in agreement with a scenario in which the driving source of the molecular outflow, HW-2, went through multiple episodes of outflow activity, as suggested by Narayanan & Walker (1996). In this scenario, the J-shock component could be due to the most recent period of enhanced mass loss, whereas one or more C-shocks could be due to older generations of outflows. Alternatively, the stellar wind material could produce a (fast) J-shock while the surrounding molecular cloud might be swept up by a slower C-shock.

In section 7.6 we concluded that the atomic fine-structure lines toward S106 could be well explained as arising in a dense (10^5–10^6 cm^{-3}) PDR, with a high ($\geq 10^5$ G_0) incident FUV flux. In section 7.6 we also showed that the central source in S106 is of spectral type O6–O8, with a total luminosity of 4.2 $\times$ 10^4 $L_\odot$. From a Kurucz (1991) model for a stellar photosphere with $T_{\rm eff}$ = 37,000 K and $\log g$ = 4.0, we compute that such a star emits a total FUV (6–13.6 eV) flux of 3.6 $\times$ 10^{36} erg s^{-1} sr^{-1}. To dilute this stellar FUV field to a value of 10^5–10^6 G_0, the PDR must be at a location 3–10 $\times$ 10^3 AU away from the central star, corresponding to a projected distance of 5–17″. This projected distance is independent of the assumed distance towards S106. It is within the range allowed by the SWS entrance apertures and is compatible with an origin in the $\approx 30''$ diameter region of H_2 emission in the H_2 1–0 S(1) image of S106 by Hayashi et

al. (1990). We conclude that the central O6–O8 star of S106 is the most likely candidate for the source of the FUV radiation field reaching the PDR.

The differences between the environment of these two massive embedded YSOs, S106 and Cep A, are remarkable. In S106 the stellar wind and UV radiation of the exciting source have cleared and excited a sufficiently large region to create strong PDR emission, whereas in the case of Cep A, the central source is still heavily embedded and we only observe the interaction of its outflow with its surroundings. Possibly this difference between these two sources is a reflection of their different evolutionary status, with Cep A being the younger of the two. In due time, Cep A could clear its immediate surroundings, ionize the hydrogen, and evolve into a bipolar nebula quite similar to S106. The question of how long this process takes is one which we cannot answer with the current two examples.

Acknowledgements. This chapter is based on observations with ISO, an ESA project with instruments funded by ESA Member States (especially the PI countries: France, Germany, the Netherlands and the United Kingdom) and with the participation of ISAS and NASA. The authors would like to thank John Rayner and Klaus-Werner Hodapp for providing us with the K-band images of S106 and Cep A shown in Fig. 7.5. Peter van Hoof is kindly acknowledged for providing us with a copy of the CLOUDY computer code.

References

Bally, J., Lane, A.J. 1982, ApJ 257, 612
Bieging, J.H. 1984, ApJ 286, 591
Black, F.H., van Dishoeck. E.F. 1987, ApJ 322, 412
Boogert, A.C.A., Schutte, W.A., Tielens, A.G.G.M. et al., 1996, A&A 315, L377
Boogert, A.C.A., Schutte, W.A., Helmich, F.P. et al, 1997, A&A 317, 929
Burton, M.G., Hollenbach, D.J., Tielens, A.G.G.M. 1990, ApJ 365, 620
Burton, M.G., Hollenbach, D.J., Tielens, A.G.G.M. 1992, ApJ 399, 563
Casement, L.S., McLean, I.S. 1996, ApJ 462, 797
Chernoff, D.F., Hollenbach, D.J., McKee, C.F. 1982, ApJ 259, L97
Clegg, P.E. et al. 1996, A&A 315, L38
Dabrowski, I. 1984, Canadian J. Phys. 62, 1639
Day, K.L. 1979, ApJ 234, 158
de Graauw, Th., Haser, L.N., Beintema, D.A., Roelfsema, P.R. et al. 1996, A&A 315, L49
d'Hendecourt, L., Jourdain de Muizon, M., Dartois, A., Breitfellner, M., Ehrenfreund, P., Benit, J., Boulanger, F., Puget, J.L., Habing, H.J. 1996, A&A 315, L365
Doyon, R., Nadeau, D. 1988, ApJ 334, 883
Draine, B.T., Bertoldi, F. 1996, ApJ 468, 269
Eiroa, C., Elsässer, H., Lahulla, J.F. 1979, A&A 74, 89
Ellis, H.B., Lester, D.F., Harvey, P.M., Joy, M., Telesco, C.M., Decher, R., Werner, M.W. 1990, ApJ 365, 287
Evans, N.J., Becklin, E.E., Beichman, C., Gatley, I., Hildebrand, R.H., Keene, J., Slovak, M.H., Werner, M.W., Whitcomb, S.E. 1981, ApJ 244, 115
Felli, M., Simon, M., Fischer, J., Hamann, F. 1985, A&A 145, 305
Ferland, G.J. 1996, Univ. of Kentucky Physics Department Internal Report

Fluks, M.A., Plez, B., Thé, P.S., de Winter, D., Westerlund, B.E., Steenman, H.C. 1994, A&AS 105, 311
Gehrz, R.D., Grasdalen, G.L., Castelaz, M., Gullixson, C., Mozurkewich, D., Hackwell, J.A. 1982, ApJ 254, 550
Gerakines, P.A., Schutte, W.A., Greenberg, J.M., van Dishoeck, E.F. 1995, A&A 296, 810
Goetz, J.A., Pipher, J.L., Forrest, W.J., Watson, D.M., Raines, S.N., Woodward, C.E., Greenhouse, M.A., Smith, H.A., Hughes, V.A., Fischer, J. 1998, ApJ 504, 359
Habing, H.J. 1968, Bull. Astron. Inst. Netherlands 19, 421
Hartigan, P., Carpenter, J.M., Dougados, C., Skrutskie, M.F. 1996, AJ 111, 1278
Hayashi, S.S., Hasegawa, T., Tanaka, M., Hayashi, M., Aspin, C., McLean, I.S., Brand, P.W.J.L., Gatley, I. 1990, ApJ 354, 242
Hippelein, H., Münch, G. 1981, A&A 99, 248
Hodapp, K.W. 1994, ApJS 94, 615
Hodapp, K.W., Eiroa, C. 1989, AJ 97, 166
Hodapp, K.W., Rayner, J. 1991, AJ 102, 1108
Hollenbach, D.J., McKee, C.F. 1989, ApJ 342, 306
Hughes, V.A. 1988, ApJ 383, 280
Hughes, V.A., Wouterloot, J.G.A. 1984, ApJ 276, 204
Kaufman, M.J., Neufeld, D.A. 1996, ApJ 456, 611
Kessler, M.F., Steinz, J.A., Anderegg, M.E., Clavel, J., Drechsel, G., Estaria, P., Faelker, J., Riedinger, J.R., Robson, A., Taylor, B.G., Ximénez de Ferrán, S. 1996, A&A 315, L27
Kirby-Docken, K., Liu, B. 1978, ApJS 36, 359
Kurucz, R.L. 1991, in *"Stellar atmospheres–Beyond classical models"* (eds. A.G. Davis Philip, A.R. Upgren, K.A. Janes), L. Davis press, Schenectady, New York, p. 441
Lenzen, R., Hodapp, K.W., Solf, J. 1984, A&A 137, 202
Longmore, A.J., Robson, E.I., Jameson, R.F. 1986, MNRAS 221, 589
Loushin, R., Crutcher, R.M., Bieging, J.H. 1990, ApJ 362, L67
Mel'nikov, S.Y., Shevchenko, V.S., Grankin, K.N. 1995, Astron. Rep. 39, 42
Mezger, P.G., Chini, R., Kreysa, E., Wink, J. 1987, A&A 182, 127
Narayanan, G., Walker, C.F. 1996, ApJ 466, 844
Parmar, P.S., Lacy, J.H., Achtermann, J.M. 1991, ApJ 372, L25
Pipher, J.L., Sharpless, S., Savedoff, M.P., Kerridge, S.K., Krassner, J., Schurmann, S., Soifer, B.T., Merrill, K.M. 1976, A&A 51, 255
Rayner, J. 1994, in *"Infrared Astronomy with Arrays: The next generation"*, ed. I.S. McLean (Dordrecht: Kluwer), 185
Schutte, W.A., Tielens, A.G.G.M., Whittet, D.C.B., Boogert, A.C.A., Ehrenfreund, P., de Graauw, Th., Prusti, T., van Dishoeck, E.F., Wesselius, P.R. 1996, A&A 315, L333
Staude, H.J., Lenzen, R., Dyck, H.M., Schmidt, G.D. 1982, ApJ 255, 95
Tanaka, M., Hasegawa, T., Hayashi, S.S., Brand, P.W.J.L., Gatley, I. 1989, ApJ 336, 207
Tielens, A.G.G.M., Allamandola, L.J. 1987, in *"Interstellar Processes"*, eds. D.J. Hollenbach & H.A. Thronson Jr. (Dordrecht: Reidel), p. 397
Tielens, A.G.G.M., Hollenbach, D.J. 1985, ApJ 291, 722
Turner, J., Kirby-Docken, K., Dalgarno, A. 1977, ApJS 35, 281
Whittet, D.C.B., Schutte, W.A., Tielens, A.G.G.M. et al. 1996, A&A 315, L357
Wright, C.M., Drapatz, S., Timmermann, R., van der Werf, P.P., Katterloher, R., de Graauw, Th. 1996, A&A 315, L301

Chapter 8

Star Formation in the BD+40°4124 Group: A View From ISO

M.E. van den Ancker, P.R. Wesselius and A.G.G.M. Tielens,
A&A, submitted (1999)

Abstract

We present the results of ISO SWS and LWS grating scans towards the three brightest members of the BD+40°4124 group in the infrared: BD+40°4124 (B2Ve), LkHα 224 (A7e) and the embedded source LkHα 225. Emission from the pure rotational lines of H_2, from rotational and ro-vibrational transitions of CO, from PAHs, from H I recombination lines and from the infrared fine structure lines of [Fe II], [Si II], [S I], [O I], [O III] and [C II] was detected. These emission lines arise in the combination of a low-density ($\approx 10^2$ cm^{-3}) H II region with a clumpy PDR in the case of BD+40°4124. The lower transitions of the infrared H I lines observed in BD+40°4124 are optically thick; most likely they arise in either a dense wind or a circumstellar disk. This same region is also responsible for the optical H I lines and the radio continuum emission. In the lines of sight towards LkHα 224 and LkHα 225, the observed emission lines arise in a non-dissociative shock produced by a slow ($\approx$ 20 km s^{-1}) outflow arising from LkHα 225. Toward LkHα 225 we also observe a dissociative shock, presumably located closer to the outflow source than the non-dissociative shock. In the line of sight towards LkHα 225 we observed absorption features due to solid water ice and amorphous silicates, and due to gas-phase H_2O, CO and CO_2. No solid CO_2 was detected towards LkHα 225, making this the first line of sight where the bulk of the CO_2 is in the gas-phase.

8.1 Introduction

The BD+40°4124 region consists of a few tens of very young stars associated with the probable Herbig Ae/Be stars BD+40°4124 (= V1685 Cyg), LkHα 224 (= V1686 Cyg)

and LkHα 225 (= V1318 Cyg), all of which have infrared excesses (Strom et al. 1972a; Hillenbrand et al. 1992). Together with NGC 6910, NGC 6914, the BD+41°3731 region and IC 1318, it is part of the giant star forming region 2 Cyg, at a distance of about 1 kpc (Shevchenko et al. 1991). The stars in the BD+40°4124 region are significantly younger (ages less than 1 million years) than those in the surrounding OB associations, with the low- and the high-mass stars having formed nearly simultaneously, leading some authors to suggest that star formation in this association might have been induced by the propagation of an external shock wave into the cloud core (Shevchenko et al. 1991; Hillenbrand et al. 1992). The IRAS and AFGL surveys showed a powerful infrared source within the BD+40°4124 group, but the positional uncertainty did not allow to assign the flux to one of the individual objects in the region. More recent submm continuum maps of the region (Aspin et al. 1994; Di Francesco et al. 1997; Henning et al. 1998) clearly peak on LkHα 225, suggesting that it is also dominant in the far-infrared and may be identified with IRAS 20187+4111 (AFGL 2557).

Aspin et al. (1994) have shown LkHα 225 to be a triple system oriented north-south. The most northern and southern components, separated by 5″, appear stellar and are photometrically variable at optical and near-infrared wavelengths. The middle component exhibits strong [S II] emission, suggesting it is a nebulous knot of shock-excited material, not unlike many Herbig-Haro objects (Magakyan & Movseyan 1997). Whereas BD+40°4124 dominates the association in the optical, the southern component of LkHα 225 is brightest in the mid-infrared (Aspin et al. 1994). A K-band spectrum of LkHα 225-South by the same authors shows strong ro-vibrational emission lines of molecular hydrogen. Aspin et al. (1994) estimate the total luminosity of this object to be $\approx 1600\ L_\odot$, which places it in the luminosity range of the Herbig Ae/Be stars.

Palla et al. (1994) obtained near infrared, CO, $C^{18}O$, CS, and H_2O maser observations of the group. Their high resolution VLA data show that a H_2O maser source is clearly associated with LkHα 225-South. Moreover, a density concentration in the molecular cloud (as evidenced by CS J=5–4 emission) and a CO outflow are both associated with LkHα 225. In their model, LkHα 225 is at the center of a dense molecular core of mass $\approx 280\ M_\odot$, while BD+40°4124 lies near the periphery. Continuum radio emission has been detected from BD+40°4124 and a source 42″ to the east of BD+40°4124 (Skinner et al. 1993).

The infrared emission-line spectrum of young stellar objects (YSOs) such as those in the BD+40°4124 group is dominated by the interaction of the central object with the remnants of the cloud from which it formed. If a young stellar object produces intense UV radiation, either due to accretion or because of a high temperature of the central star, an H II region will develop, producing a rich ionic emission line spectrum. At the edge of the H II region, a so-called photodissociation or photon-dominated region (PDR) will be created, in which neutral gas is heated by the photoelectric ejection of electrons from grain surfaces in a strong UV field. Cooling of this neutral gas occurs mainly through emission in atomic fine-structure and molecular lines, allowing us to probe the physical conditions in the PDR through the study of its infrared emission-line spectrum. If the YSO has a strong, often collimated, outflow, it will cause a shock wave as the outflow hits the surrounding molecular cloud, heating the gas. In case

the shock has a velocity smaller than ≈ 40 km s^{-1}, it will not dissociate the molecular material and mainly cool through infrared molecular transitions. Because the physical conditions from the pre-shock gas to the post-shock gas change gradually within such a non-dissociative shock, they are often called C(ontinuous)-shocks. For higher shock velocities, the molecules will be dissociated and cooling in the shock occurs mainly through atomic and ionic emission lines. In such a shock, the physical conditions from the pre- to the post-shock gas will change within one mean free path and therefore they are usually termed J(ump)-shocks. In the post-shock gas of a J-shock, molecules will re-form and cool down the gas further. Therefore a dissociative shock will produce an infrared spectrum consisting of a combination of ionic and molecular emission lines.

In this chapter we present *Infrared Space Observatory* (ISO; Kessler et al. 1996) spectroscopic data obtained at the positions of BD+40°4124, LkHα 224 and LkHα 225. Some of the H_2 lines included in this data-set were already analyzed in a previous *letter* (Wesselius et al. 1996). Here we will re-analyze an extended set of H_2 data using the latest ISO calibrations, in combination with new data on infrared fine-structure lines, gas-phase molecular absorption bands and solid-state emission features in the BD+40°4124 group. We will show that the infrared emission lines arise from the combination of a H II region and a PDR at the position of BD+40°4124, from a non-dissociative shock at the position of LkHα 224, and from the combination of a non-dissociative and a dissociative shock at the position of LkHα 225. We will also discuss the unusual absorption-line spectrum seen in the line of sight towards LkHα 225 and briefly discuss its implications for the physical and chemical evolution of hot cores.

8.2 Observations

We obtained ISO Short Wavelength (2.4–45 μm) Spectrometer (SWS; de Graauw et al. 1996a) and Long Wavelength (43–197 μm) Spectrometer (LWS; Clegg et al. 1996) grating scans at the positions of BD+40°4124, LkHα 224 and LkHα 225. For all three positions, both SWS scans covering the entire SWS wavelength range ("AOT 01") and much deeper scans covering small wavelength regions around particularly useful diagnostic lines ("AOT 02") were obtained. For LWS only scans covering the entire wavelength region were obtained. A full log of the observations is given in Table 8.1.

Data were reduced in a standard fashion using calibration files corresponding to ISO off-line processing software (OLP) version 7.0, after which they were corrected for remaining fringing and glitches. To increase the S/N in the final spectra, the detectors were aligned and statistical outliers were removed, after which the spectra were rebinned to a lower spectral resolution. Figure 8.1 shows the resulting ISO spectra. Plots of all detected lines, rebinned to a resolution $\lambda/\Delta\lambda$ of 2000 with an oversampling factor of four (SWS), or averaged across scans (LWS), are presented in Figs. 8.2–8.4. Line fluxes for detected lines and upper limits (total flux for line with peak flux 3σ) for the most significant undetected lines are listed in Table 8.2.

For BD+40°4124 and LkHα 224, all detected lines appear at their rest wavelength within the accuracy of the ISO spectrometers. For LkHα 225, all lines in the SWS spec-

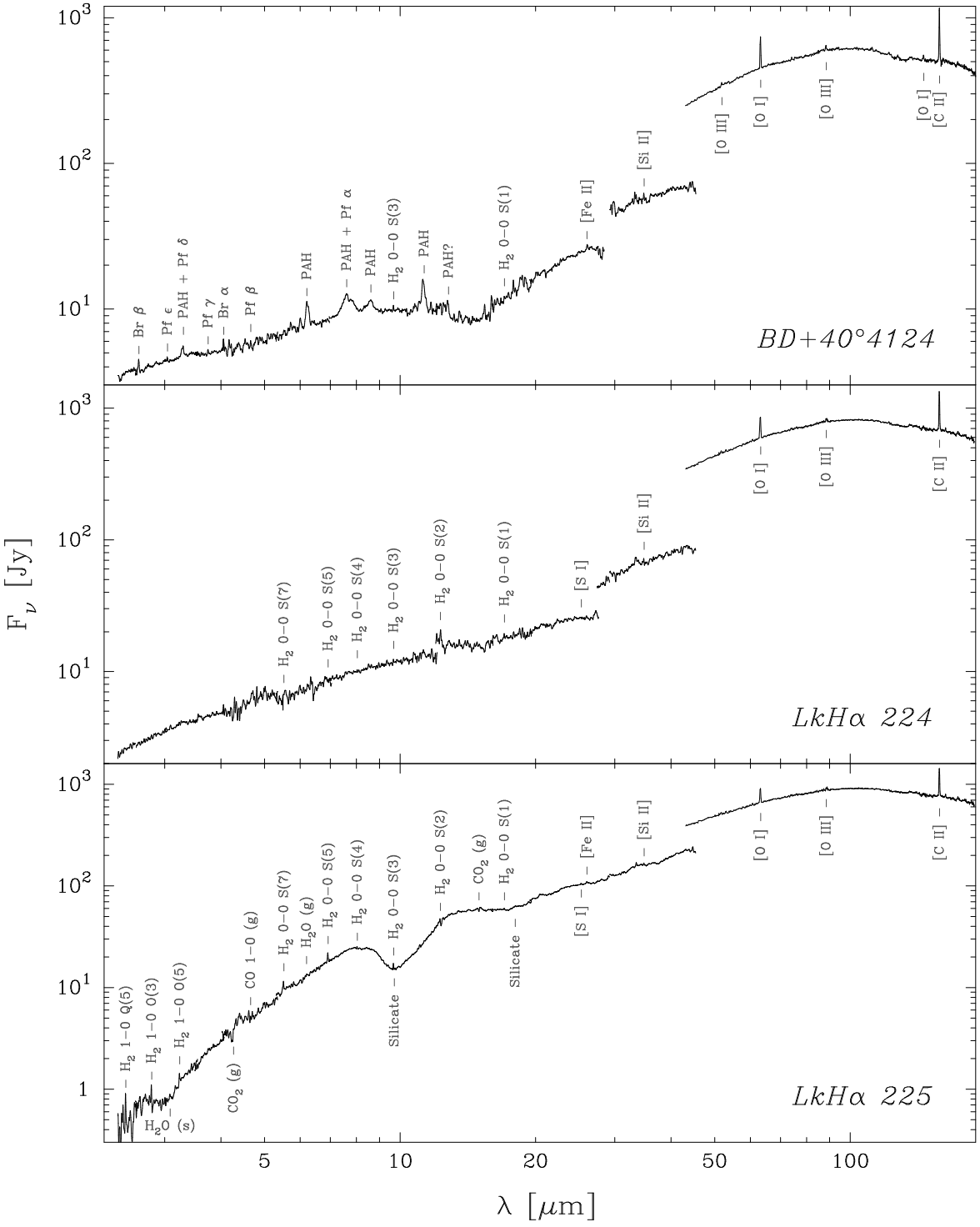

Fig. 8.1. Combined SWS/LWS full grating spectra of (from top to bottom) BD+40°4124, LkHα 224 and LkHα 225 with the most prominent features identified.

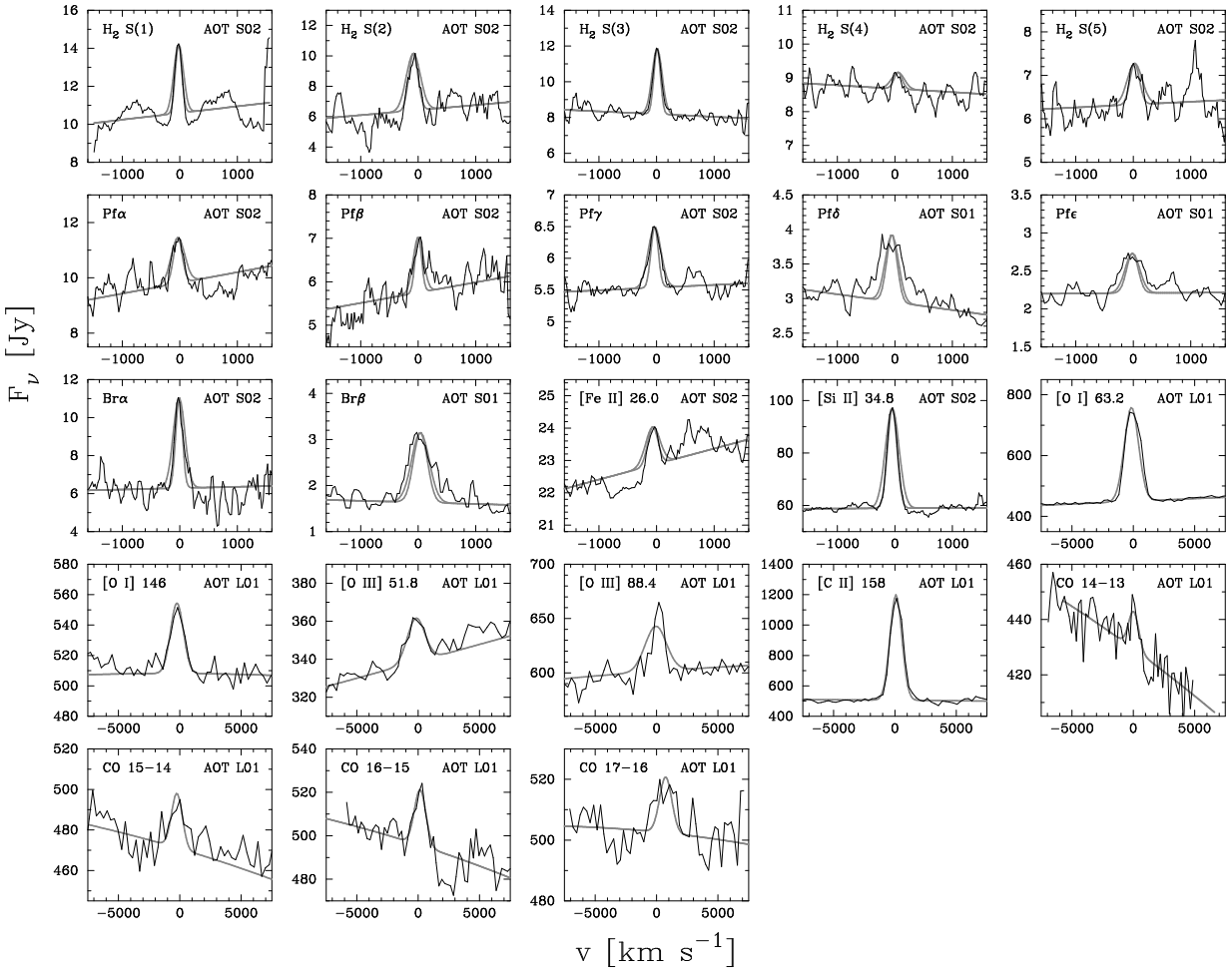

Fig. 8.2. Detected lines in BD+40°4124, rebinned to heliocentric velocities. The grey lines show the instrumental profiles for a point source and an extended source filling the entire aperture.

tra are systematically shifted by ≈ -100 km s^{-1}. This could either be a reflection of the real spatial velocity of LkHα 225 or be caused by a slight offset between our pointing, based on the optical position of the source, and the position of the infrared source. For all three sources, the lines are unresolved, indicating that the velocity dispersion is smaller than a few hundred km s^{-1}

For each complete spectral scan, the SWS actually makes twelve different grating scans, each covering a small wavelength region ("SWS band"), and with its own optical path. They are joined to form one single spectrum (Fig. 8.1). Because of the variation of the diffraction limit of the telescope with wavelength, different SWS bands use apertures of different sizes. For a source that is not point-like, one may therefore see a discontinuity in flux at the wavelengths where such a change in aperture occurs. This effect can indeed be seen in some of our spectra, indicating the presence of extended far-infrared emission throughout the region.

Since both grating spectrometers on board ISO use apertures that are fairly large

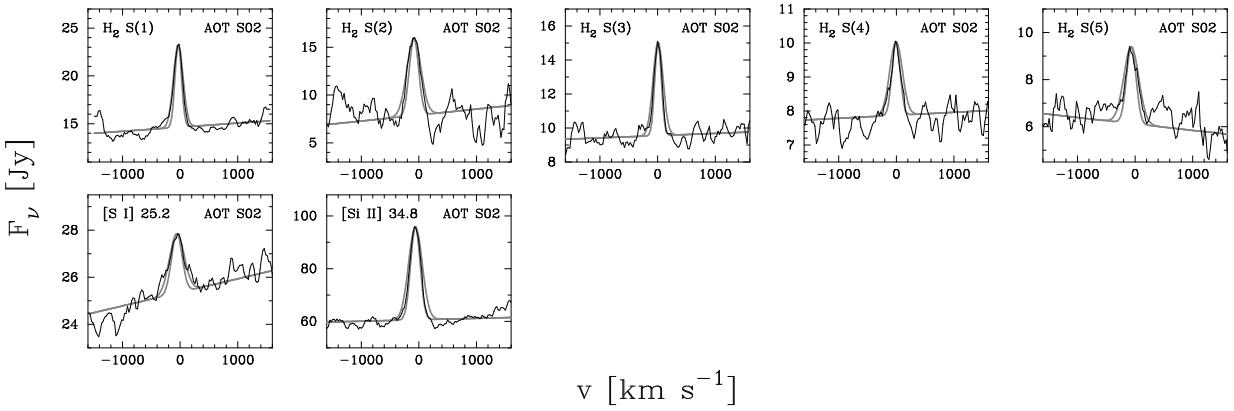

Fig. 8.3. Same as Fig. 8.2 for LkHα 224.

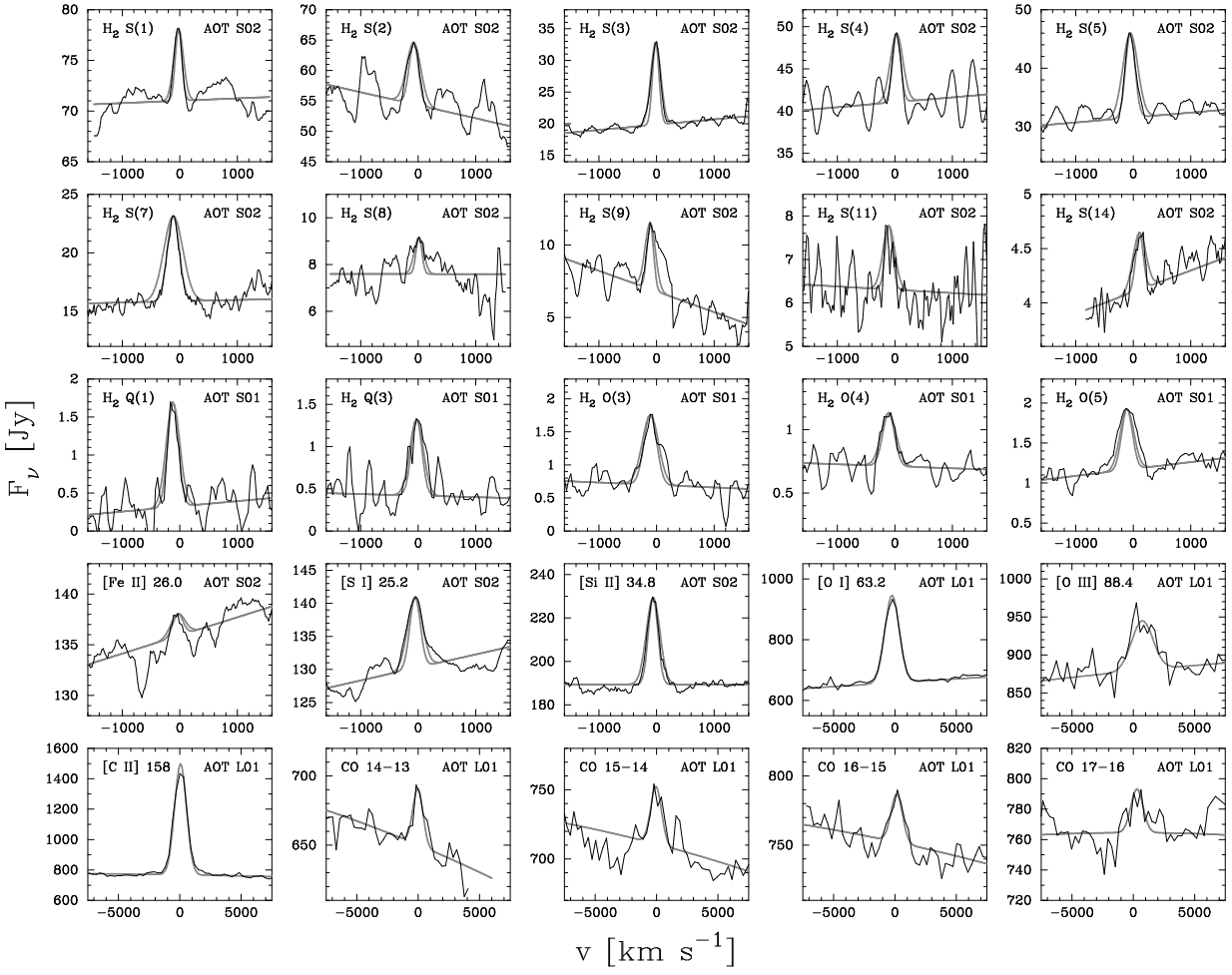

Fig. 8.4. Same as Fig. 8.2 for LkHα 225.

Table 8.1. Log of ISO observations in the BD+40°4124 region.

Object	AOT	Rev.	Date	JD−2450000
BD+40°4124	SWS 02	142	07/04/1996	181.037
	SWS 02	159	24/04/1996	197.635
	SWS 01	355	05/11/1996	393.283
	LWS 01	768	23/12/1997	805.525
LkHα 224	SWS 02	142	07/04/1996	180.960
	SWS 01	858	22/03/1998	894.920
LkHα 225	SWS 02	142	07/04/1996	180.996
	SWS 02	355	05/11/1996	393.306
	SWS 01	858	22/03/1998	894.889
	LWS 01	142	07/04/1996	181.017

compared to the separation of sources in most star forming regions, some caution is appropriate in interpreting such measurements. We created a plot with the positions of the SWS apertures, overlaid on a K′-band image of the region (Hillenbrand et al. 1995), shown in Fig. 8.5. As can be seen from this figure, only one strong near-infrared source is included in the BD+40°4124 and LkHα 224 measurements, whereas the LkHα 225 measurement only includes the question-mark shaped infrared nebula formed by the point-like objects LkHα 225-North and LkHα 225-South and the bridging nebula LkHα 225-Middle. ISO-LWS has a beam that is larger (61–83″ FWHM) than the separation of the objects studied here. Therefore the LWS measurements of BD+40°4124 and LkHα 225 partly cover the same region. The LWS spectrum of LkHα 224 shown in Fig. 8.1 is a weighted average of these spectra.

Accuracies of the absolute flux calibration in the SWS spectra range from 7% in the short-wavelength (< 4.10 μm) part to $\approx 30\%$ in the long wavelength (> 29 μm) part (Leech et al. 1997). The LWS absolute flux calibration is expected to be accurate at the 7% level (Trams et al. 1997). Note that the applied flux calibration is based on the assumption that we are looking at a point source. For an extended source, the diffraction losses will be underestimated and in particular at the long-wavelength part of the LWS, these corrections will exceed the quoted uncertainty.

8.3 Spectral energy distributions

A Spectral Energy Distribution (SED) for BD+40°4124 was constructed by combining UV, optical, infrared, submm and radio data of BD+40°4124 from literature (Wesselius et al. 1982; Strom et al. 1972a; Terranegra et al. 1994; Hillenbrand et al. 1992, 1995; Cohen 1972; Lorenzetti et al. 1983; Di Francesco et al. 1997; Corcoran & Ray 1998; Skinner et al. 1993; Bertout & Thum 1982) with our new ISO spectra (Fig. 8.6a). As can be seen from this plot, the optical to submm photometry forms a smooth curve. At radio

Table 8.2. Observed and extinction-corrected line fluxes and model predictions (in 10^{-15} W m^{-2}) for programme stars.

Line	λ	Beam	AOT	BD+40°4124			LkHα 224			LkHα 225		
	[μm]	[10^{-8} sr]		Observed	Ext. corr.	Model	Observed	Ext. Corr.	Model	Observed	Ext. Corr.	Model
H_2 0–0 S(0)	28.2188	1.64	S02	$<$ 0.66	$<$ 0.68	0.02	$<$ 0.95	$<$ 0.98	0.03	$<$ 1.38	$<$ 1.63	0.04
H_2 0–0 S(1)	17.0348	1.15	S02	0.54±0.18	0.57±0.19	0.54	1.01±0.33	1.07±0.35	1.04	0.78±0.26	1.05±0.35	1.34
H_2 0–0 S(2)	12.2786	1.15	S02	0.71±0.23	0.76±0.25	0.46	1.27±0.42	1.36±0.45	1.13	2.18±0.93	3.08±1.31	1.79
H_2 0–0 S(3)	9.6649	0.85	S02	0.77±0.24	0.91±0.28	0.90	1.55±0.31	1.60±0.37	2.06	2.80±0.73	6.59±1.73	5.47
H_2 0–0 S(4)	8.0251	0.85	S02	0.10±0.05	0.11±0.05	0.16	0.69±0.23	0.73±0.24	0.79	1.71±0.46	2.27±0.60	2.29
H_2 0–0 S(5)	6.9095	0.85	S02	0.25±0.11	0.25±0.12	0.13	1.17±0.25	1.21±0.26	0.99	4.03±0.63	4.73±0.74	4.32
H_2 0–0 S(6)	6.1086	0.85	S02	$<$ 0.80	$<$ 0.83	0.01	$<$ 0.63	$<$ 0.65	0.08	$<$ 2.56	$<$ 3.08	0.56
H_2 0–0 S(7)	5.5112	0.85	S02	$<$ 0.81	$<$ 0.84	0.00	$<$ 1.30	$<$ 1.35	0.04	3.51±0.79	4.33±0.97	0.45
H_2 0–0 S(8)	5.0531	0.85	S01	$<$ 1.83	$<$ 1.92	0.00	$<$ 3.55	$<$ 3.72	0.00	0.81±0.40	1.03±0.51	0.06
H_2 0–0 S(9)	4.6946	0.85	S02	$<$ 1.16	$<$ 1.22	0.00	$<$ 2.55	$<$ 2.69	0.00	3.04±1.01	3.97±1.31	0.05
H_2 0–0 S(10)	4.4099	0.85	S02	$<$ 0.42	$<$ 0.44	0.00	$<$ 0.42	$<$ 0.44	0.00	$<$ 0.63	$<$ 0.85	0.00
H_2 0–0 S(11)	4.1813	0.85	S02	$<$ 0.74	$<$ 0.78	0.00	$<$ 1.08	$<$ 1.15	0.00	0.67±0.22	0.93±0.31	0.00
H_2 1–0 Q(1)	2.4066	0.85	S01	$<$ 0.83	$<$ 0.99	0.00	$<$ 1.63	$<$ 1.93	0.00	1.21±0.20	2.98±0.50	2.59
H_2 1–0 Q(2)	2.4134	0.85	S01	$<$ 0.56	$<$ 0.67	0.00	$<$ 1.51	$<$ 1.79	0.00	$<$ 1.45	$<$ 3.53	0.66
H_2 1–0 Q(3)	2.4237	0.85	S01	$<$ 0.81	$<$ 0.97	0.00	$<$ 1.43	$<$ 1.70	0.00	1.36±0.16	3.28±0.39	1.31
H_2 1–0 Q(4)	2.4475	0.85	S01	$<$ 0.52	$<$ 0.61	0.00	$<$ 1.19	$<$ 1.41	0.00	$<$ 1.06	$<$ 2.51	0.22
H_2 1–0 O(2)	2.6269	0.85	S01	$<$ 2.82	$<$ 3.26	0.00	$<$ 1.71	$<$ 1.98	0.00	$<$ 1.07	$<$ 2.28	0.70
H_2 1–0 O(3)	2.8025	0.85	S01	$<$ 0.63	$<$ 0.71	0.00	$<$ 1.17	$<$ 1.33	0.00	1.75±0.15	3.39±0.30	2.45
H_2 1–0 O(4)	3.0039	0.85	S01	$<$ 0.17	$<$ 0.19	0.00	$<$ 0.54	$<$ 0.61	0.00	0.25±0.10	0.44±0.18	0.70
H_2 1–0 O(5)	3.2350	0.85	S01	$<$ 0.27	$<$ 0.30	0.00	$<$ 0.89	$<$ 0.99	0.00	1.00±0.08	1.65±0.14	0.88
H_2 1–0 O(6)	3.5008	0.85	S01	$<$ 0.47	$<$ 0.51	0.00	$<$ 0.72	$<$ 0.79	0.00	$<$ 0.35	$<$ 0.53	0.11
CO J=14–13	185.999	12.2	L01	2.01±0.32	2.01±0.32	2.01	–	–	–	3.58±0.46	3.59±0.46	3.29
CO J=15–14	173.631	12.2	L01	1.95±0.29	1.95±0.29	1.95	–	–	–	2.91±0.39	2.92±0.39	2.85
CO J=16–15	162.812	11.6	L01	1.78±0.31	1.78±0.31	1.85	–	–	–	2.45±0.45	2.46±4.56	2.41
CO J=17–16	153.267	11.6	L01	1.65±0.33	1.65±0.33	1.72	–	–	–	2.01±0.35	2.01±0.36	1.98
H I Pfα	7.4600	0.85	S02	0.46±0.15	0.48±0.16	0.48	$<$ 0.33	$<$ 0.34	–	$<$ 1.18	$<$ 1.38	–
H I Pfβ	4.6539	0.85	S02	0.81±0.29	0.85±0.31	1.21	$<$ 0.87	$<$ 0.92	–	$<$ 1.23	$<$ 1.61	–
H I Pfγ	3.7406	0.85	S02	0.89±0.18	0.96±0.20	1.31	$<$ 0.21	$<$ 0.22	–	$<$ 0.27	$<$ 0.39	–
H I Pfδ	3.2971	0.85	S01	1.38±0.24	1.51±0.25	1.41	$<$ 0.58	$<$ 0.64	–	$<$ 0.29	$<$ 0.46	–
H I Pfε	3.0393	0.85	S01	0.94±0.12	1.05±0.13	1.32	$<$ 0.62	$<$ 0.69	–	$<$ 0.26	$<$ 0.45	–
H I Brα	4.0523	0.85	S02	2.71±0.54	2.90±0.58	2.90	$<$ 1.01	$<$ 1.08	–	$<$ 1.09	$<$ 1.54	–
H I Brβ	2.6259	0.85	S01	3.40±0.30	3.94±0.35	5.05	$<$ 1.70	$<$ 1.96	–	$<$ 1.15	$<$ 2.44	–
[Fe I] ($^5D_4$–$^5D_3$)	24.0423	1.15	S02	$<$ 0.17	$<$ 0.18	0.00	$<$ 0.15	$<$ 0.15	–	$<$ 0.58	$<$ 0.72	0.03
[Fe I] ($^5D_3$–$^5D_2$)	34.7133	2.01	S02	$<$ 0.40	$<$ 0.41	0.00	$<$ 0.49	$<$ 0.50	–	$<$ 1.45	$<$ 1.63	0.01
[Fe II] ($^4F_{9/2}$–$^4F_{7/2}$)	17.9410	1.15	S02	$<$ 0.10	$<$ 0.10	0.00	$<$ 0.19	$<$ 0.20	0.00	$<$ 0.16	$<$ 0.23	0.51
[Fe II] ($^6D_{9/2}$–$^6D_{7/2}$)	25.9882	1.15	S02	0.07±0.03	0.07±0.03	0.07	$<$ 0.22	$<$ 0.23	0.00	0.33±0.17	0.40±0.20	3.27
[Fe II] ($^6D_{7/2}$–$^6D_{5/2}$)	35.3491	2.01	S02	$<$ 0.44	$<$ 0.45	0.01	$<$ 0.77	$<$ 0.79	0.00	$<$ 0.92	$<$ 1.03	0.90
[S I] ($^3P_2$–$^3P_1$)	25.2490	1.15	S02	$<$ 0.14	$<$ 0.14	0.00	0.16±0.05	0.17±0.05	0.16	0.58±0.16	0.70±0.20	0.78
[Si II] ($^2P_{1/2}$–$^2P_{3/2}$)	34.8140	2.01	S02	2.32±0.77	2.37±0.78	2.31	2.42±0.80	2.48±0.82	0.00	3.05±1.01	3.43±1.13	3.06
[O I] ($^3P_2$–$^3P_1$)	63.1840	16.3	L01	70.36±4.95	70.99±4.99	87.8	–	–	–	65.97±4.78	69.03±5.01	58.5
[O I] ($^3P_1$–$^3P_0$)	145.526	8.82	L01	4.15±0.40	4.16±0.40	3.69	–	–	–	$<$ 9.48	$<$ 9.57	0.82
[O III] ($^3P_2$–$^3P_1$)	51.8145	15.7	L01	7.99±1.20	8.09±1.21	8.09	–	–	–	$<$ 12.1	$<$ 12.9	–
[O III] ($^3P_1$–$^3P_0$)	88.3562	14.8	L01	8.31±0.78	8.35±0.78	8.35	–	–	–	8.27±0.94	8.46±0.96	–
[C II] ($^2P_{1/2}$–$^2P_{3/2}$)	157.741	11.6	L01	51.75±3.64	51.83±3.64	51.8	–	–	–	62.54±4.63	63.03±4.67	0.45

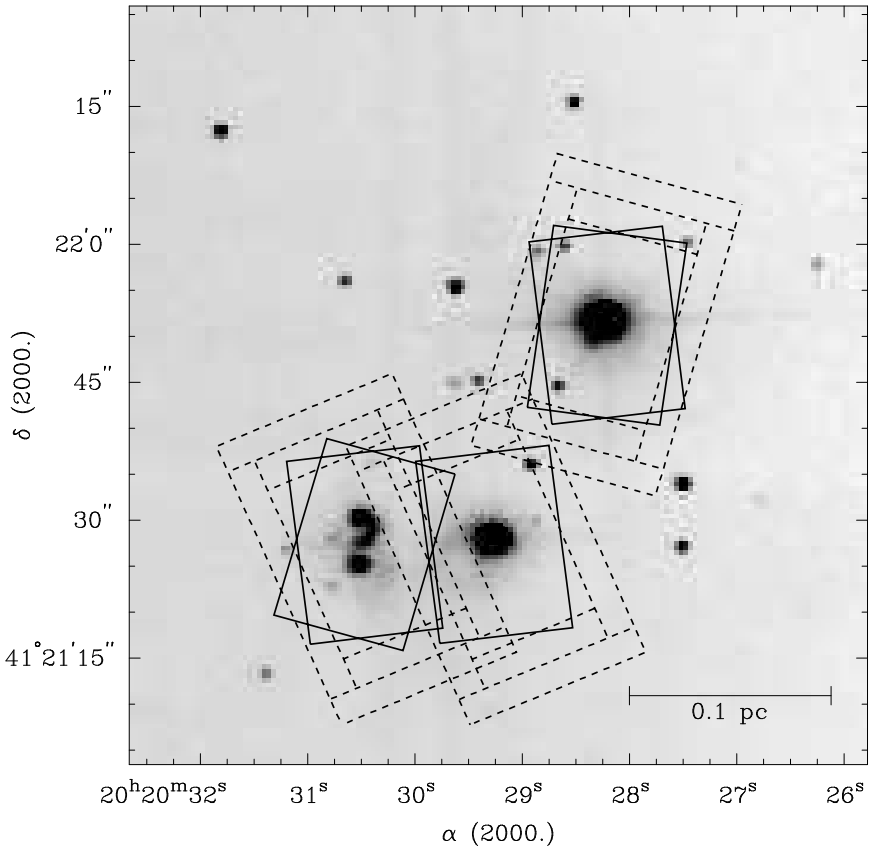

Fig. 8.5. SWS aperture positions for our measurements of (from right to left) BD+40°4124, LkHα 224 and LkHα 225 superimposed on a K′-band image of the region. The rectangles indicate the apertures (in increasing size) for SWS bands 1A–2C (2.4–12.0 μm), 3A–3D (12.0–27.5 μm), 3E (27.5–29.5 μm) and 4 (29.5–40.5 μm). Solid and dashed rectangles give the orientation of the SWS aperture for the AOT S02 and S01 observations, respectively. For clarity, only the smallest aperture is shown for the AOT S02 observations.

wavelengths the slope of the energy distribution appears significantly flatter. We interpret this SED as the sum of three components: continuum emission from the central star in the UV and optical, thermal emission from dust heated by the central star in the infrared to submm and free-free emission from the stellar wind or an H II region at cm wavelengths. The SWS spectrum of BD+40°4124 shows a rising continuum component starting around 13 μm. This component is not present in the infrared photometry by Cohen (1972). This could be due to the smaller aperture size or the chopping throw used for background subtraction by Cohen. We interpret this second dust component, only visible in the ISO data, as diffuse emission throughout the star forming region.

There is general consensus in literature that the spectral type of BD+40°4124 is about B2 Ve+sh (Merrill et al. 1932; Herbig 1960; Strom et al. 1972b; Swings 1981; Finkenzeller 1985; Hillenbrand et al. 1995), corresponding to an effective temperature $T_{\rm eff}$ = 22,000 K and surface gravity $\log g$ = 4.0 (Schmidt-Kaler 1982). With this spectral type and the optical photometry by Strom et al. (1972a) we arrive at a value of $E(B-V)$

= $0\overset{\mathrm{m}}{.}97$ towards the optical star. This value agrees well with the $E(B-V)$ derived from the diffuse interstellar band at 5849 Å (Oudmaijer et al. 1997). With this $E(B-V)$ value and assuming a normal interstellar extinction law (i.e. $R_V = A_V/E(B-V) = 3.1$), we corrected the data for extinction.

A Kurucz (1991) stellar atmosphere model with $T_{\rm eff}$ and $\log g$ corresponding to the star's spectral type (assuming solar abundance) was fitted to the extinction-corrected UV to optical SED. The fit is also shown in Fig. 8.6a. As can be seen from this figure, the SED fit is not perfect in the UV. Possibly a UV excess due to a strong stellar wind is present in BD+40°4124. The fitted Kurucz model was used to compute an apparent stellar luminosity $L/(4\pi d^2)$ for BD+40°4124, which was converted to an absolute stellar luminosity using the BD+40°4124 distance estimate of 1 kpc by Shevchenko et al. (1991). Infrared luminosities were computed by fitting a spline to the infrared to mm data and subtracting the Kurucz model from this fit. The derived values for the optical and infrared luminosity of BD+40°4124 are 6.4×10^3 and 3.1×10^2 $L_\odot$, respectively. These luminosities place the star close to the zero-age main sequence position of a 10 $M_\odot$ star in the Hertzsprung-Russell diagram (HRD).

We followed the same procedure to construct a SED for LkHα 224, combining optical, infrared and submm photometry from literature (Strom et al. 1972a; Shevchenko, personal communication; Hillenbrand et al. 1995; Cohen 1972; Di Francesco et al. 1997) with our new ISO spectra. It is shown in Fig. 8.6b. Since LkHα 224 is strongly variable in the optical, the data used in the SED were selected to be obtained near maximum system brightness, when available. The optical to infrared photometry of LkHα 224 forms a smooth curve in the SED, which we interpret as due to continuum emission from the star in the optical, and thermal emission from dust heated by the central star in the infrared.

There is no agreement in literature on the spectral type of LkHα 224. Wenzel (1980) classified the star spectroscopically as B8e, whereas Hillenbrand et al. (1995) obtained a spectral type of B5 Ve. Corcoran & Ray (1997) derived a spectral type of A0 for LkHα 224, based upon the relative strength of the He I λ4471 and Mg II λ4481 lines. In the optical, LkHα 224 shows large-amplitude photometric variations ($> 3^{\rm m}$) due to variable amounts of circumstellar extinction (Wenzel 1980; Shevchenko et al. 1991, 1993). In the group of Herbig Ae/Be stars, these large-amplitude variations are only observed when the spectral type is A0 or later (Chapter 3). Therefore we favour a later spectral type than B for LkHα 224. The detection of the Ca II H and K lines in absorption (Magakyan & Movseyan 1997) also seems to favour a later spectral type than mid-B. Recent optical spectroscopy of LkHα 224 by de Winter (personal communication) shows strong, variable, P-Cygni type emission in Hα. The higher members of the Balmer series (up to H15) are present and in absorption, together with the Ca II H and K lines. Numerous shell lines are present in the spectrum as well, which could hinder spectral classification solely based upon red spectra. From the available optical spectroscopy, we classify LkHα 224 as A7e+sh, corresponding to $T_{\rm eff}$ = 7850 K. We estimate the uncertainty in this classification to be around 2 subclasses, or 400 K.

With the new spectral type of A7e+sh and the optical photometry by Strom et al. (1972a), we derive an $E(B-V)$ at maximum system brightness for LkHα 224 of $0\overset{\mathrm{m}}{.}96$.

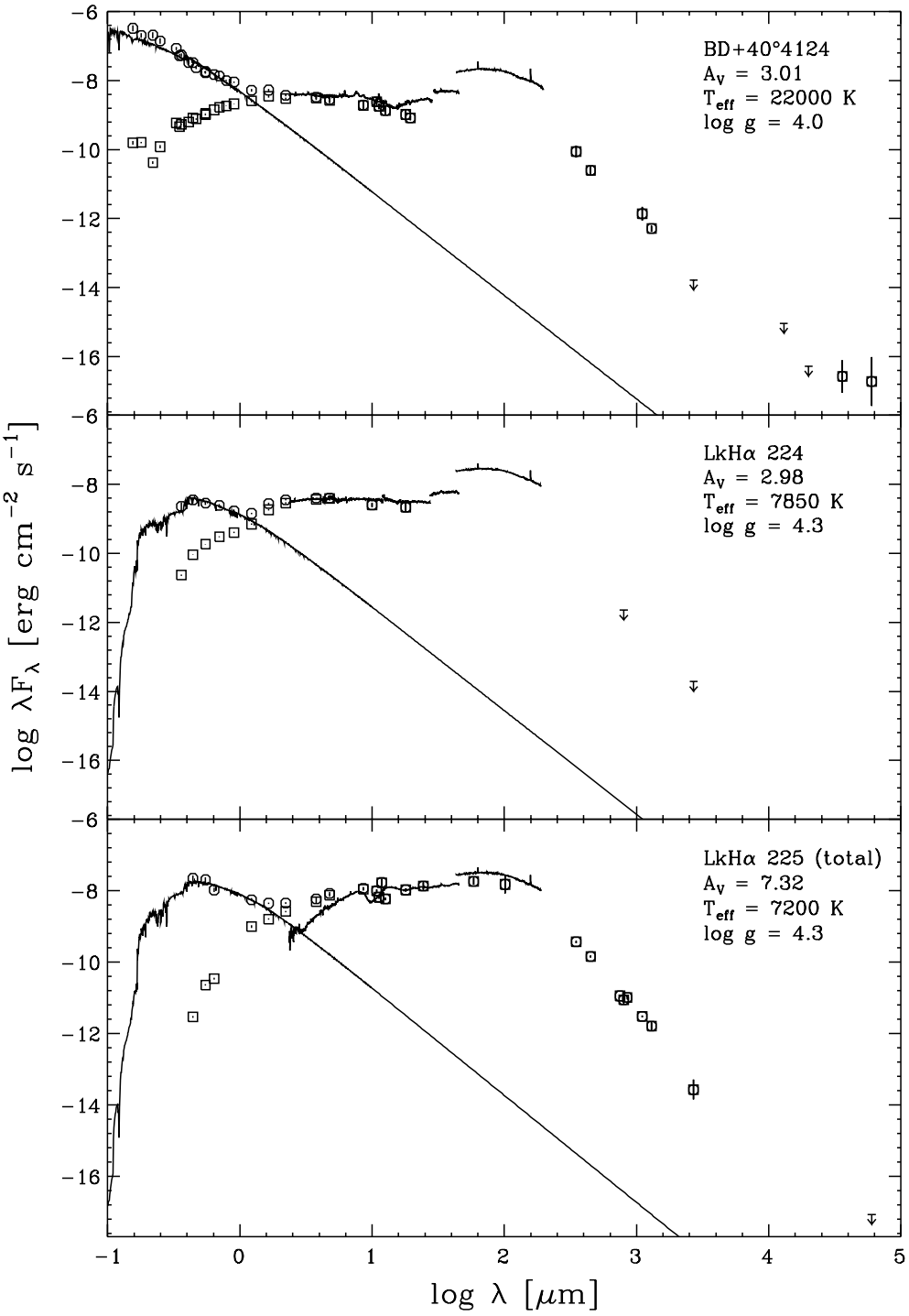

Fig. 8.6. Observed (squares) and extinction-corrected (circles) spectral energy distributions of BD+40°4124 (top), LkHα 224 (middle) and LkHα 225 (bottom). Also shown (lines) are the ISO spectra and a Kurucz model fitted to the extinction-corrected UV to optical photometry for each object.

Again fitting a Kurucz model to the extinction-corrected photometry, we derive values for the optical and infrared luminosity of LkHα 224 of 1.1 $\times$ 10^2 and 2.7 $\times$ 10^2 $L_\odot$, respectively. The good fit of the SED to the Kurucz model with $T_{\rm eff}$ = 7850 K shows that the photometry is consistent with our adopted spectral type of A7e for LkHα 224. Comparing the derived parameters of LkHα 224 with the pre-main sequence evolutionary tracks by Palla & Stahler (1993), we see that it is located in the HRD at the location of a 3 $\times$ 10^5 yr old 3.5 $M_\odot$ star. This brings the age of the star in good agreement with those of the low-mass members of the BD+40°4124 group (Hillenbrand et al. 1995).

Again the same procedure as above was followed to construct a SED for LkHα 225 (Fig. 8.6c), combining optical to radio measurements from literature (Shevchenko, personal communication; Hillenbrand et al. 1995; Cohen 1972; Weaver & Jones 1992; Di Francesco et al. 1998; Henning et al. 1998; Cohen et al. 1982) with our ISO data. These data refer to the sum of all components in this object. Since LkHα 225 shows strong variability in the optical and infrared, only data obtained near maximum brightness was used in the SED. Like in BD+40°4124, the SED of LkHα 225 consists of a smooth continuum ranging from the optical to the submm. In view of the knowledge of the nature of LkHα 225 from literature, this SED must be interpreted as the sum of the three components of LkHα 225 in the optical to submm, each consisting of a hot component with circumstellar dust emission. The plotted IRAS fluxes of IRAS 20187+4111 (Weaver & Jones 1992) are smaller than those in the LkHα 225 LWS spectrum. Most likely, this is due to the background subtraction applied on the IRAS data. This could mean that a cool component is present as well throughout the region, covering an area that is larger than the size of the IRAS detectors. In view of submm maps of the region (Aspin et al. 1994; Henning et al. 1998), this seems plausible.

As can be seen in Fig. 8.6c, below 8 μm the flux levels in the SWS spectrum are considerably smaller than those from ground-based photometry at maximum brightness. At longer wavelengths they agree. By extrapolating our ISO SWS spectrum, we deduce that the total K band magnitude of LkHα 225 was about $8\overset{\rm m}{.}3$ at the time of our observation. This is within the range of values present in literature. Above 10 μm, the SWS flux levels are in agreement with ground-based measurements, suggesting that the large-amplitude variability of LkHα 225 is limited to the optical to near-infrared spectral range.

The spectral type of LkHα 225 is very uncertain. Hillenbrand et al. (1995) give a spectroscopic classification of mid A–Fe for both LkHα 225-North and LkHα 225-South, whereas Wenzel (1980) derives a spectral type of G–Ke for the sum of both components. Aspin et al. (1994) suggested the southern component to be of intermediate-mass, based on its high bolometric luminosity. Unlike for BD+40°4124 and LkHα 224, this makes the direct derivation of $E(B-V)$ very uncertain. Adopting $E(B-V)$ = $4\overset{\rm m}{.}97$, corresponding to A_V = $15\overset{\rm m}{.}4$ derived from the silicate feature in the next section, results in an optical slope in the energy distribution that is steeper than the Rayleigh-Jeans tail of a black body. This could be because the extinction at the time of the optical observations was smaller than during the ISO observations. Therefore we used a rather uncertain value of $E(B-V)$ = $2\overset{\rm m}{.}36$, based on the observed $(B-V)$ colour of LkHα

225 and the intrinsic colours of a F0 star, to correct the photometry of LkHα 225 for extinction.

To obtain a rough measure for the total luminosity of LkHα 225, we fitted a Kurucz model with $T_{\rm eff}$ = 7200 K, corresponding to a spectral type of F0, to the extinction-corrected optical photometry. This results in values of 5.9×10^2 and 1.6×10^3 $L_\odot$ for the total optical and infrared luminosities of LkHα 225. We conclude that at least one of the stars in the LkHα 225 system must be a massive (5–7 $M_\odot$) pre-main sequence object in order to explain these luminosities.

8.4 Solid-state features

The ISO full grating scans of BD+40°4124 consist of a relatively smooth continuum, with a number of strong emission lines superimposed. The familiar unidentified infrared (UIR) emission features at 3.3, 6.2, 7.6, 7.8, 8.6 and 11.3 μm, often attributed to polycyclic aromatic hydrocarbons (PAHs), are prominently present. Possibly the 12.7 μm feature also observed in other sources showing strong PAH emission (Beintema et al. 1996) is present as well. No 9.7 μm amorphous silicate feature, either in emission or in absorption, is visible in the BD+40°4124 SWS spectrum. The slight curvature in the ground-based 8–13 μm BD+40°4124 spectrum obtained by Rodgers & Wooden (1997), which they interpreted as a silicate feature in emission, is absent in our SWS data.

The continuum in BD+40°4124 seems to consist of two distinct components, one from 2.4–13 μm and the other from 13–200 μm. In the SWS range, it is well fit by the superposition of two blackbodies of 320 and 100 K. For the LWS spectrum a significant excess at the long-wavelength part remains after the black-body fit. Probably a range in temperatures is present starting from 100 K down to much lower temperatures. The jumps in the spectrum at the positions corresponding to a change in aperture suggest that this component is caused by diffuse emission in the star forming region.

Remarkably, the line flux measured in the 3.3 μm PAH feature of BD+40°4124 (1.1×10^{-14} W m^{-2}) is much larger than the 2.0×10^{-15} W m^{-2} upper limit obtained by Brooke et al. (1993). PAH features also appear absent in the 8–13 μm HIFOGS spectrum shown by Rodgers & Wooden (1997). This could either be an effect of the different aperture size used ($20'' \times 14''$ for SWS versus a $1\farcs4$ circular aperture by Brooke et al.) in case the PAH emission is spatially extended, or be due to time-variability of the PAH emission. If the first explanation is correct, the PAH emission should come from a region with a diameter larger than $3\farcs2$ and hence be easily resolvable with ground-based imaging.

The ISO spectrum of LkHα 224 consists of one single smooth continuum, with a few emission lines superimposed. No solid-state emission or absorption is apparent in the SWS spectrum. Again the slight curvature seen in the HIFOGS 8–13 μm spectrum of LkHα 224 (Rodgers & Wooden 1997) is absent in our SWS data. In view of the fact that most Herbig Ae stars show strong silicate emission in the 10 μm range (e.g. Chapter 5), the absence of the silicate feature is quite remarkable. It means that the dust emission must come from a region which is completely optically thick up to infrared

wavelengths and yet only produce 3 magnitudes of extinction towards the central star in the optical. It is obvious that such a region cannot be spherically symmetric, but must be highly flattened or have a hole through which we can seen the central star relatively unobscured. A dusty circumstellar disk might be the prime candidate for such a region. The absence of silicate emission in LkHα 224 might then be explained by either an intrinsically higher optical depth in its circumstellar disk than those surrounding other Herbig Ae stars, a view supported by its relative youth, or be caused by a nearly edge-on orientation of the circumstellar disk.

The infrared continuum of LkHα 224 cannot be fit by a single blackbody. Rather a sum of blackbodies with a range of temperatures starting at several hundreds Kelvins and continuing to temperatures of a few tens of K are required to fit the spectrum adequately. Again the jumps in the spectrum at the positions corresponding to a change in aperture are present, suggesting that at the longer wavelengths we are looking at diffuse emission in the star forming region. However, the slope of the continuum in LkHα 224 is significantly different from that of the cool component in BD+40°4124. This could either be due to a difference in the maximum temperature or to a difference in temperature gradient of the diffuse component between the two positions.

The SWS spectrum of LkHα 225 looks very different. Again we have a strong, smooth continuum with many emission lines, but now also absorption lines due to gaseous molecular material as well as strong absorption features due to solid-state material are present. The familiar 9.7 μm absorption feature due to the Si–O stretching mode in amorphous silicates is strong. Apart from a 20% difference in the absolute flux levels, the silicate feature looks very similar to what was found by IRAS LRS (Olnon et al. 1986), suggesting that it is constant in time. The integrated optical depth ($\int \tau(\nu) d\nu$) of the 9.7 μm feature in the ISO SWS spectrum is 196 cm^{-1}. The 18 μm feature due to the bending mode of Si–O is also present in absorption with an integrated optical depth of 11 cm^{-1}. The O–H bending mode of water ice at 3.0 is present in absorption as well (156 cm^{-1}).

Using intrinsic band strengths from literature (Tielens & Allamandola 1987; Gerakines et al. 1995), we have converted the integrated optical depths of the 9.7 μm silicate and 3.0 μm H_2O features to column densities. The results are a column of 1.6 $\times$ 10^{18} molecules for the silicates and 7.8 $\times$ 10^{17} molecules for H_2O ice. The 2:1 ratio of these two species is within the range of what is found in other lines of sight (Whittet et al. 1996 and references therein). Curiously, CO_2 ice, which invariably accompanies H_2O ice in all other lines of sight studied by ISO (Whittet et al. 1996; Boogert et al. 1999; Gerakines et al. 1999) is absent in LkHα 225. The derived upper limit on the solid CO_2/H_2O ratio is 0.04, much less than the canonical value of 0.15.

No aperture jumps are visible in the SWS spectrum of LkHα 225. The bulk of the continuum flux must therefore come from an area that is small compared to the smallest SWS aperture (20″$\times$ 14″). The discontinuity between the SWS and LWS spectra shows that although LkHα 225 itself is probably the strongest far-infrared source in the region, the total far-infrared flux of the group is dominated by the diffuse component. Like in LkHα 224, the SWS spectrum of LkHα 225 cannot be fit well with a single blackbody. Again a sum of blackbodies with a range of temperatures starting at

several hundreds and continuing to temperatures of a few tens of K are required to fit the spectrum adequately.

PAHs appear absent in our LkHα 225 SWS spectrum. In view of the claim by Deutsch et al. (1994) that the southern component of LkHα 225 is the strongest UIR emitter in the region, this is remarkable. One possible explanation for this apparent discrepancy could be the large degree of variability ($> 3^{\rm m}$ in K; Allen 1973) of LkHα 225. In this case the component responsible for the PAH emission should have been much fainter than the other component at the time of observation. However, Aspin et al. (1994) showed the southern component to be dominant longward of 3 μm. Comparison of our LkHα 225 spectrum with infrared photometry by previous authors shows that the source was not near minimum brightness at the time of the SWS observation, making the explanation that the southern component of LkHα 225 was faint improbable. The most likely explanation for the apparent discrepancy between our non-detection and the reported UIR emission (Deutsch et al. 1994) might therefore be that the UIR emission within the southern component of LkHα 225 is variable in time. Note that because the gas cooling timescale is much longer than the PAH cooling timescale, if PAH emission has been present within recent years, gas emission from a remnant PDR might be expected in the vicinity of LkHα 225.

Since extinction in the continuum surrounding the 9.7 μm feature is small compared to the extinction within this feature, the extinction A_λ at wavelength λ across a non-saturated 9.7 μm feature can simply be obtained from the relation $A_\lambda = -2.5 \log(I/I_0)$. Using an average interstellar extinction law which includes the silicate feature (Fluks et al. 1994), we can then convert these values of A_λ to a visual extinction, resulting in a value of $A_V = 15\overset{\rm m}{.}4 \pm 0\overset{\rm m}{.}2$ toward LkHα 225. This value is significantly smaller than the $A_V \approx 50^{\rm m}$ obtained from the $C^{18}O$ column density towards LkHα 225 (Palla et al. 1995). Although smaller, our estimate of A_V is still compatible with the value of $25^{\rm m} \pm 9^{\rm m}$derived from the ratio of the 1–0 S(1) and Q(3) lines of H_2 (Aspin et al. 1994).

8.5 Gas-phase molecular absorption lines

In the SWS spectrum of LkHα 225 several absorption bands are present due to a large column of gas-phase CO, CO_2 and H_2O in the line of sight. They are shown in Fig. 8.7. Molecular absorption bands are absent in the BD+40°4124 and LkHα 224 spectra. We compared the observed gas-phase absorption lines to synthetic gas-phase absorption bands computed using molecular constants from the HITRAN 96 database (Rothmann et al. 1996). First the relative population of the different levels within one molecule were computed for an excitation temperature $T_{\rm ex}$. For the relative abundances of the isotopes, values from the HITRAN database were adopted. A Voigt profile was taken for the lines, with a Doppler parameter $b = \frac{c}{2\sqrt{\ln 2}} \frac{\Delta\lambda}{\lambda}$ for the Gaussian component of the Voigt profile and the lifetime of the considered level times $b/4\pi$ for the Lorentz component. The optical depth τ_λ as a function of wavelength was then computed by evaluating the sum of all integrated absorption coefficients, distributed on the Voigt profile. Synthetic absorption spectra were obtained by computing $\exp(-\tau_\lambda)$. This procedure

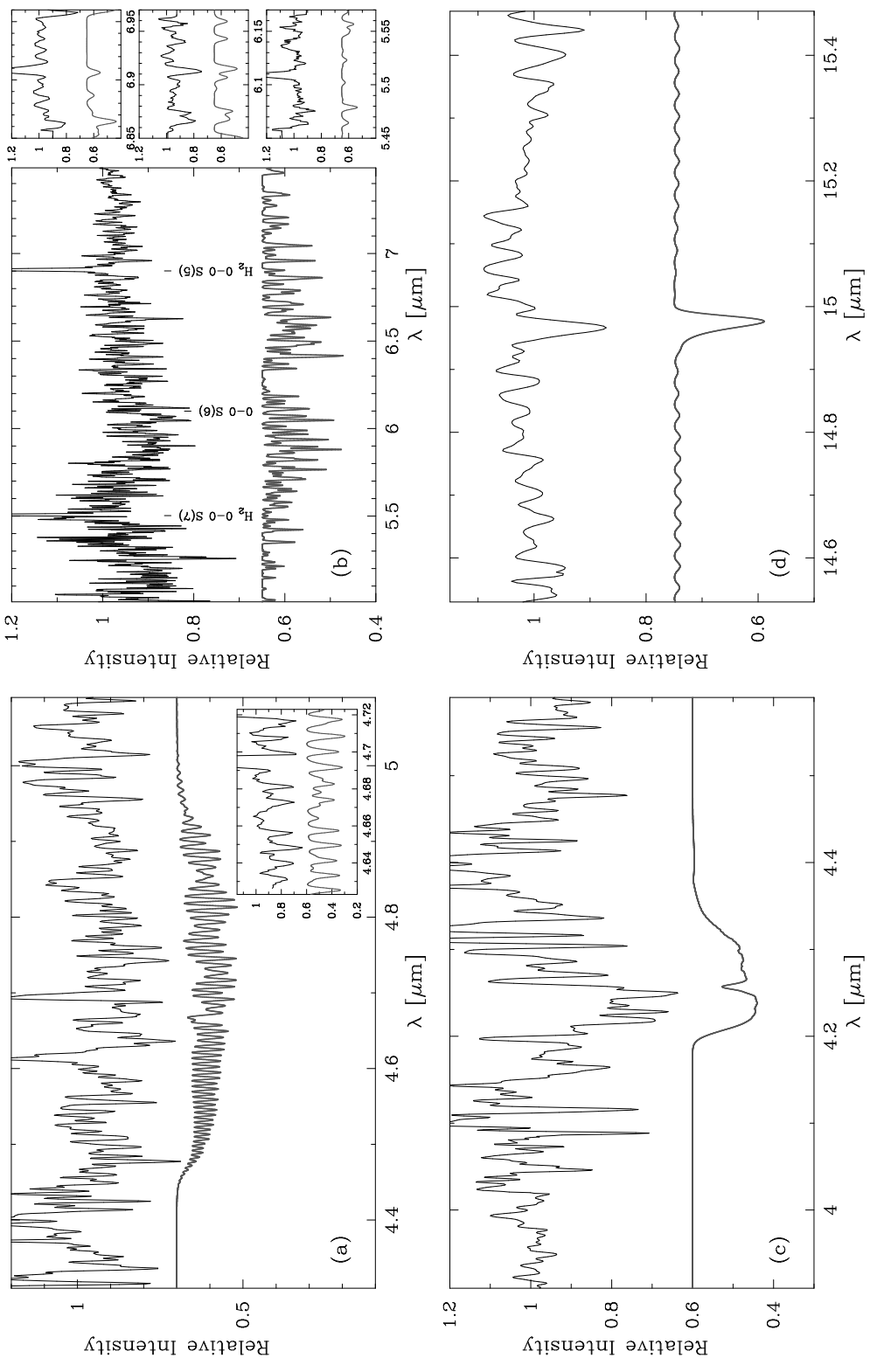

Fig. 8.7. Detected gas-phase molecular absorption bands in LkHα 225 with the continuum normalized to unity (top curves). Also shown (bottom curves) are the best fits of the computed absorption spectra, shifted for clarity. The large plots show the AOT 01 SWS data, whereas the insets show the AOT 02 data containing molecular bands. (a) Observed CO ro-vibrational lines, compared to a $T_{\rm ex}$ = 300 K, b = 5 km s^{-1}, N(CO) = 10^{20} cm^{-2} model. (b) H_2O ν_2 band, with a $T_{\rm ex}$ = 300 K, b = 5 km s^{-1}, $N(H_2O) = 10^{19}$ cm^{-2} model. (c) gas-phase CO_2 ν_3 band, with a $T_{\rm ex}$ = 300 K, b = 5 km s^{-1}, $N(CO_2) = 3 \times 10^{17}$ cm^{-2} model. (d) gas-phase CO_2 ν_2 band, with a $T_{\rm ex}$ = 300 K, b = 5 km s^{-1}, $N(CO_2) = 3 \times 10^{17}$ cm^{-2} model.

for computing absorption spectra is nearly identical to that followed by Helmich et al. (1996) and Dartois et al. (1998). For comparison with the observations, the spectra were convolved with the ISO SWS instrumental profile. For the AOT 02 observations, the instrumental profile is nearly Gaussian with a wavelength-dependent resolving power $R = FWHM/\lambda$ ranging between 1400 and 3000 (Leech et al. 1997). For our AOT 01 observations, the resolution is a factor four lower.

Best fits of the synthetic absorption spectra to the observed CO, CO_2 and H_2O bands are also shown in Fig. 8.7. Because of the relatively low signal to noise in the spectra, the fits for the different absorption bands were not done independently, but $T_{\rm ex}$ and b were required to be the same for all species. This procedure is only valid if the different molecular species are co-spatial. The results of similar fitting procedures in other lines of sight (e.g. van Dishoeck et al. 1996; Dartois et al. 1998; Boogert 1999) suggest that this is the case. Satisfactory fits to the data could be obtained for excitation temperatures of a few 100 K and a Doppler parameter b between 3 and 10 km s^{-1}. The derived column of warm CO_2 is several times 10^{17} cm^{-2}. For H_2O it is about 10^{19} cm^{-2}, whereas the column of gas-phase CO is in the range 10^{19}–10^{21} cm^{-2}.

The derived values of b are much higher than those expected from purely thermal broadening ($0.1290\sqrt{T_{\rm ex}/A}$ km s^{-1}, with A the molecular weight in amu; Spitzer 1978). This must be caused by macroscopic motion within the column of warm gas in our line of sight toward LkHα 225. The fact that our deduced values of b are within the range of those found toward hot cloud cores (Helmich et al. 1996; van Dishoeck & Helmich 1996; Dartois et al. 1998) suggests that it is due to turbulence within the cloud rather than a dispersion in large-scale motion such as infall or rotation.

8.6 Hydrogen recombination lines

The ISO SWS spectrum of BD+40°4124 contains several emission lines of the Pfund and Brackett series of H I. No H I lines were detected in LkHα 224 and LkHα 225. The lines fluxes for BD+40°4124 were corrected for extinction using the value of A_V = 3$^{\rm m}$.0 derived in section 8.3. We combined these data with ground-based measurements of emission lines in the Brackett and Paschen series (Harvey 1984; Hamann & Persson 1992; Rodgers & Wooden 1992) for BD+40°4124 to create plots of the H I line flux ratio as a function of upper level quantum number n (Fig. 8.8). The fact that the values for the Brackett series lie on a continuous curve shows that they are not influenced much by the different beam sizes used, indicating that they must originate in a compact region.

In Fig. 8.8 we also show predicted values for Menzel & Baker (1938) Case B recombination for a range of temperatures from 1000 to 30,000 K and densities from 10^3 to 10^9 cm^{-3}, taken from Storey & Hummer (1995). The fit of the Case B values to the data is poor, indicating that at least the lower lines in the Pfund and Brackett series are not optically thin, as assumed in Case B recombination theory, but have $\tau \gtrsim 1$. An error in our estimate of the extinction towards the line emitting region cannot reconcile our observations with the Case B values. The poor fit of the Case B model predictions to

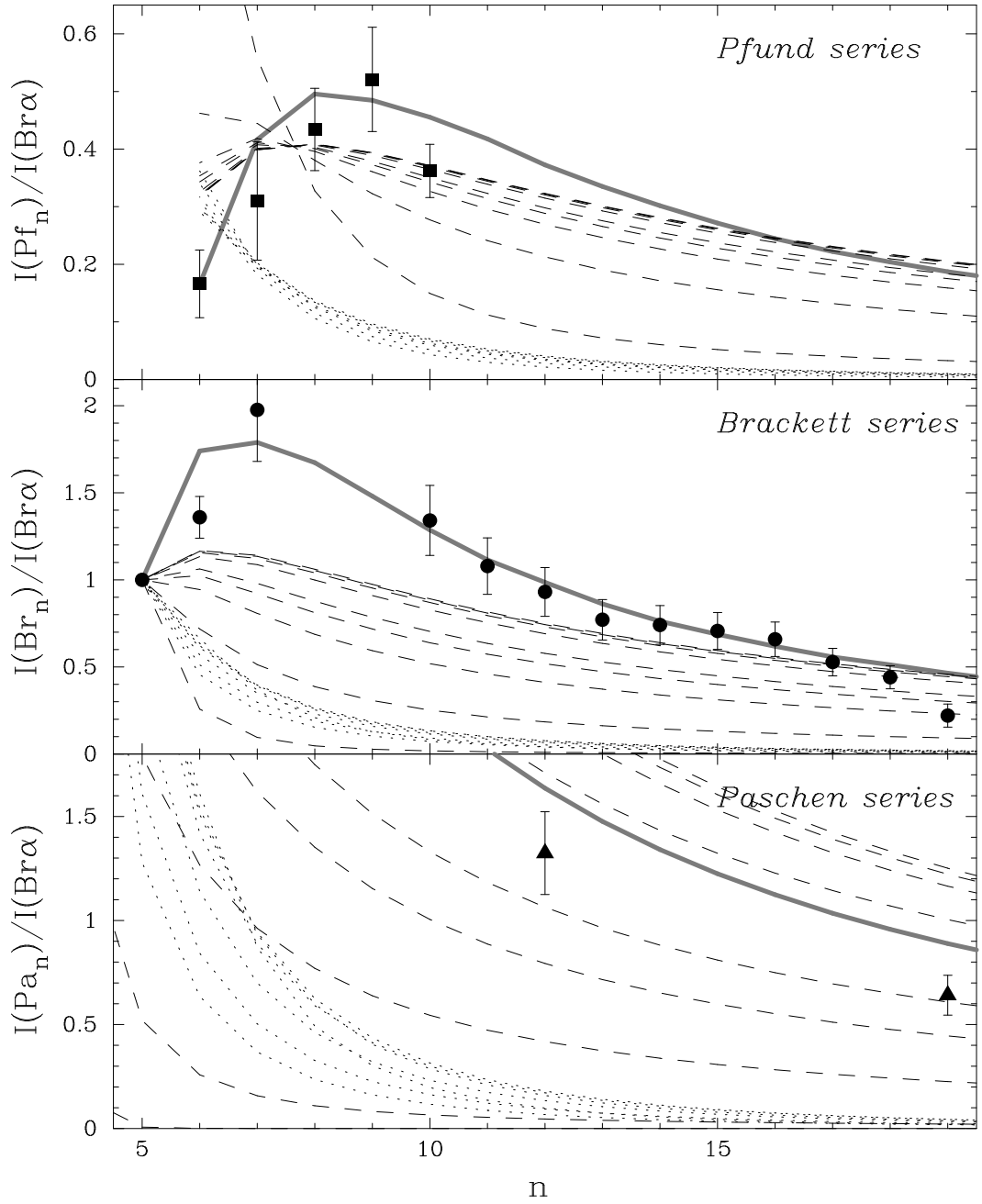

Fig. 8.8. Extinction-corrected H I line flux ratios in BD+40°4124 for (from top to bottom) the Pfund, Brackett and Paschen series. Also shown (dotted lines) are theoretical values for Case B recombination for T = 1000–30,000 K and n = 10^3–10^9 cm^{-3}. The dashed lines give model predictions for an optically thick static slab of gas with temperatures (from bottom to top) between 1000 and 100,000 K. The gray solid line shows the best fit of the LTE fully ionized wind model.

the observed H I line fluxes means that the lines do not originate in the low-density H II region responsible for the [O III] emission (section 8.8).

In the limit that all lines are optically thick, the line flux ratios of a static slab of gas in local thermodynamic equilibrium (LTE) will be dominated by the wings of the line profile. Such a slab of gas will produce line fluxes $I_\lambda \propto B_\lambda(T_e)\ f_{ij}^{2/5}$, with B_λ the Planck function for an electron temperature T_e, and f_{ij} the oscillator strength for the transition (Drake & Ulrich 1980). In Fig. 8.8 we also show these values for a range of electron temperatures between 1000 and 100,000 K. Again this simple model cannot reproduce the observed line flux ratios in BD+40°4124, especially for Pfα/Brα and Brγ/Brα. The most likely explanation for the poor fit is that the lines are more broadened than due to the Stark wings of the line profile, probably due to macroscopic motion of the gas.

The poor fit of both the Case B values and the optically thick static slab model shows that we are not looking at an optically thick static slab of gas, but at an optically thick ionized gas with a significant velocity dispersion. Most likely it originates either in an ionized wind, or in an ionized gaseous disk surrounding BD+40°4124. Without information on the kinematics of the gas, the distinction between these two cases is hard to make. To qualitatively show that such a model can indeed reproduce the observations, we also show in Fig. 8.8 the best fit of a simple LTE model for a totally ionized wind following the treatment of Nisini et al. (1995). This best fit model has a rather high mass loss rate ($\approx 10^{-6}$ M$_\odot$ yr^{-1}), arising from a compact region (≈ 12 R$_\star$) in radius. However, the assumption of LTE will cause this simple model to significantly overestimate the mass loss rate (Bouret & Catala 1998), whereas the assumption that the wind is completely ionized will cause an underestimate of the size of the line emitting region. Therefore the values given here should be approached as lower, respectively upper limits. Also, a model for an ionized gaseous disk surrounding BD+40°4124 may give equally good fits to the data.

If the lower lines in the Pfund and Brackett series are optically thick, the region in which these lines originate should also produce optically thick free-free emission at radio wavelengths. In the simple wind model employed above, the Brα line flux is related to the 6 cm continuum flux by the relation S_ν (mJy) = 1.4 $\times$ 10^{14} $F_{Br\alpha}$ (W m^{-2}) $v_2^{-1/3}$, with v_2 the wind velocity in units of 100 km s^{-1} (Simon et al. 1983). Assuming $v_2 = 1$, this relation yields 0.39 mJy for BD+40°4124, in excellent agreement with the observed 6 cm flux of 0.38 mJy (Skinner et al. 1993). Although highly simplified, this analysis does show that the region responsible for the H I line emission can also produce sufficient amounts of radio continuum emission to account for the observed fluxes and that our interpretation of the radio component in the SED as free-free emission (section 8.3) is correct.

8.7 Molecular hydrogen emission

At all three observed positions in the BD+40°4124 region we detected emission from pure rotational lines of molecular hydrogen. They are listed in Table 8.1 and are shown in Figs. 8.2–8.4. For BD+40°4124 and LkHα 224, 0–0 S(0) to S(5) were detected. For

LkHα 225 pure rotational lines up to S(10) as well as several ro-vibrational lines were detected. It is clear that in LkHα 225 the 0–0 S(6) line escaped detection because of its unfortunate location in the H_2O gas phase ν_2 absorption band (Fig. 8.7b). The line flux of the 0–0 S(5) line may also be slightly ($\approx$ 10%) underestimated because of this. We have detected significantly more lines than the preliminary results reported in the A&A ISO First Results issue (Wesselius et al. 1996), both because of improvements in the SWS data reduction since 1996 and because additional data were obtained. Therefore a new analysis of these H_2 lines is in place.

From the H_2 line fluxes $I(J)$ it is possible to calculate the apparent column densities of molecular hydrogen in the upper J levels, averaged over the SWS beam, $N(J)$, using $N(J) = \frac{4\pi I(J)}{A_{ij}} \frac{\lambda}{hc}$, with λ the wavelength, h Planck's constant and c the speed of light. The transition probabilities A_{ij} were taken from Turner et al. (1977). Line fluxes were corrected for extinction using $I(J) = I_{\rm obs} 10^{A(\lambda)/2.5}$ using the average interstellar extinction law by Fluks et al. (1994). For both BD+40°4124 and LkHα 224 we used A_V = $3\overset{\rm m}{.}0$, valid for the optical stars. For LkHα 225 we used the A_V = $15\overset{\rm m}{.}4$ derived in section 8.4.

A useful representation of the H_2 data is to plot the log of $N(J)/g$, the apparent column density in a given energy level divided by its statistical weight, versus the energy of the upper level. The statistical weight g is the combination of the rotational and nuclear spin components. It is $(2J+1)$ for para-H_2 (odd J) and $(2J+1)$ times the Ortho/Para ratio for ortho-H_2 (even J). We have assumed the high temperature equilibrium relative abundances of 3:1 for the ortho and para forms of H_2 (Burton et al. 1992). The resulting excitation diagrams are shown in Fig. 8.9. For LkHα 225 we also included the measurements of the H_2 ro-vibrational lines by Aspin et al. (1994). For the lines in common, their values differ somewhat with ours, although the line ratios agree. This is probably an effect of their smaller beam size and indicates that in our measurements the beam filling factor is smaller than one. In Fig. 8.9 the values of Aspin et al. were scaled to our measurements.

In case the population of the energy levels is thermal, all apparent column densities should lie on a nearly straight line in the excitation diagram. The slope of this line is inversely proportional to the excitation temperature, while the intercept is a measure of the total column density of warm gas. As can be seen from Fig. 8.9, this is indeed the case in all three stars for the pure rotational lines with an upper level energy up to 5000 K. The fact that the points for ortho and para H_2 lie on the same line proves that our assumption on their relative abundances is correct. We have used the formula for the H_2 column density for a Boltzmann distribution given by Parmar et al. (1991) to fit our data points in the low-lying pure rotational levels, using the rotational constants given by Dabrowski (1984), varying the excitation temperature and column density. The results are shown as the dashed lines in Fig. 8.9.

In Chapter 7, we employed predictions of H_2 emission from PDR, J-shock and C-shock models (Burton et al. 1992; Hollenbach & McKee 1989; Kaufman & Neufeld 1996), to determine the excitation temperature from the low-lying pure rotational levels as a function of density n and either incident FUV flux G (in units of the average interstellar FUV field $G_0 = 1.2 \times 10^{-4}$ erg cm^{-2} s^{-1} sr^{-1}; Habing 1968) or shock velocity

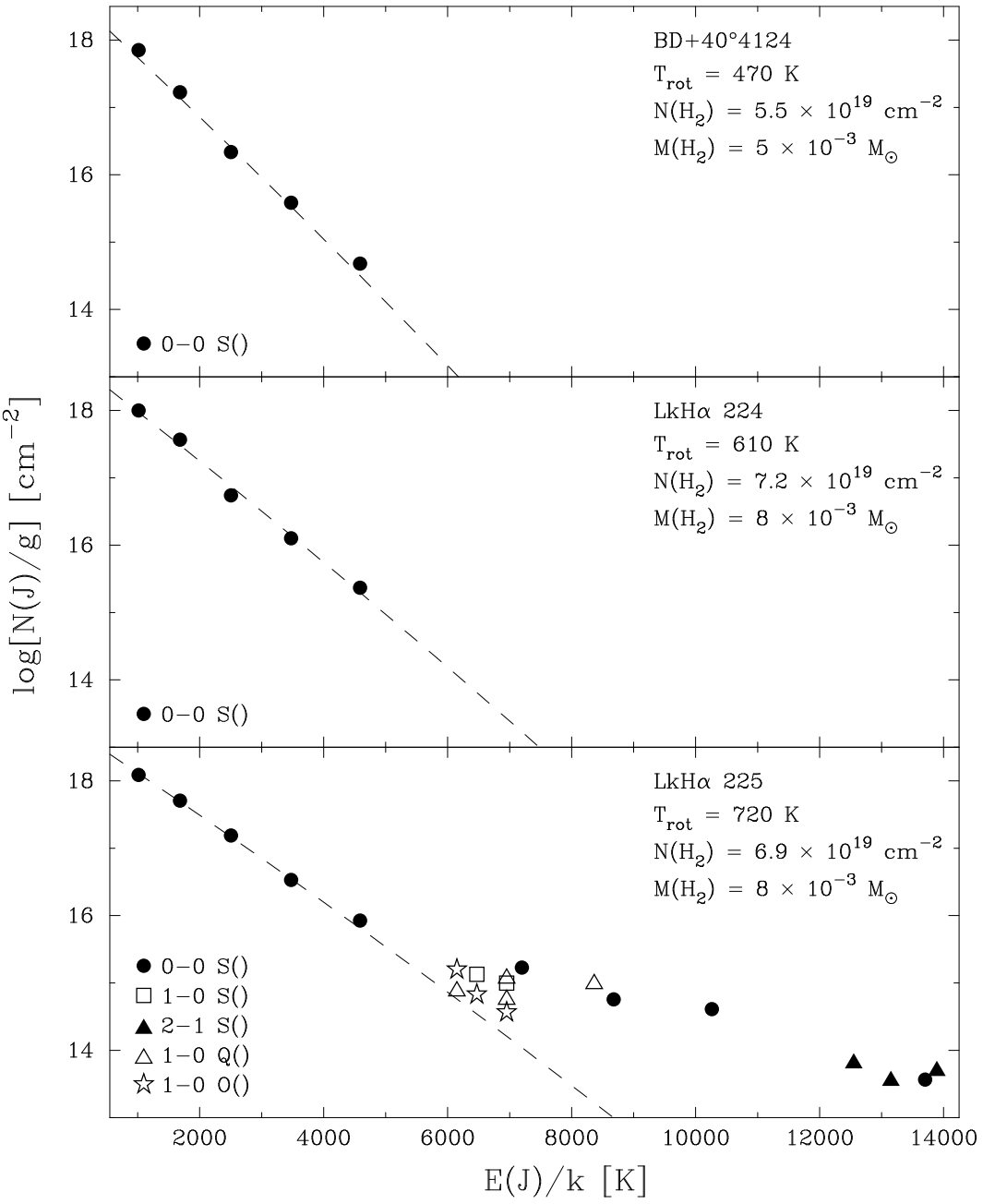

Fig. 8.9. H_2 excitation diagrams for BD+40°4124 (top), LkHα 224 (middle) and LkHα 225 (bottom). ISO observations of pure rotational lines are indicated by the filled dots. Squares, triangles and stars indicate measurements of ro-vibrational lines from the SWS spectra and from Aspin et al. (1994). Formal errors for most measurements are smaller than the plot symbol. The dashed lines gives the Boltzmann distribution fits to the low-lying pure rotational lines.

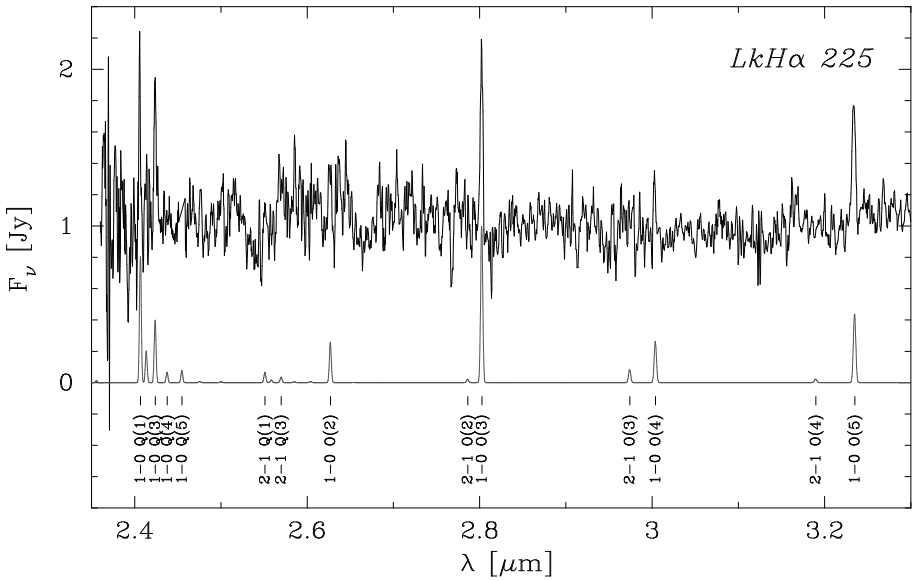

Fig. 8.10. Continuum-subtracted 2.35–3.30 μm SWS spectrum of LkHα 225. Also shown (bottom curve) is a synthetic H_2 spectrum with $T_{\rm exc}$ = 710 K, corrected for an extinction of $A_V = 15\overset{\rm m}{.}4$.

v_s in an identical way as was done for the observations presented here. We arrived at the conclusion that the PDR and J-shock models allow a fairly small (200–540 K) range of excitation temperatures, whereas for C-shocks this range is much larger (100–1500 K). In the model predictions for shocks, $T_{\rm exc}$ does not depend much on density, whereas for PDRs it does not depend much on G. Once the mechanism of the H_2 emission is established, it can therefore be used to constrain v_s or n in a straightforward way.

The values for $T_{\rm exc}$ measured for LkHα 224 and LkHα 225 fall outside the range of $T_{\rm exc}$ values predicted by either PDR or J-shock models. They are similar to the values found in other regions containing shocks (Chapter 7, 9). If the observed pure rotational H_2 emission is indeed due to a planar C-shock, its shock velocity should be around 20 km s^{-1}. In section 8.4 we saw that our BD+40°4124 SWS full grating scan contains strong emission in the PAH bands. This indicates that a PDR is present at that location. If we assume that the observed H_2 emission is entirely due to this PDR, the observed $T_{\rm exc}$ of 470 K points to a rather high ($\gtrsim 5 \times 10^5$) density within the PDR.

For LkHα 225, ro-vibrational as well as pure rotational emission from H_2 was detected (Fig. 8.10). Both the higher pure rotational lines and the ro-vibrational lines significantly deviate from the straight line defined by the lower pure rotational lines in the excitation diagram and do not form a smooth line by themselves, as expected in the case of multiple thermal components. Such a situation can either occur because of fluorescence of H_2 in a strong UV field (Black & van Dishoeck 1987; Draine & Bertoldi 1996), be due to X-ray or EUV heating (Wolfire & Königl 1991; Tiné et al. 1997), or be due to the formation energy of re-formed H_2 in post-shock gas (Shull & Hollenbach 1978). Although the H_2 spectra resulting from the possible formation mechanisms do differ in the relative prominence of transitions with $\Delta v \geq 2$ (Black & van Dishoeck

1987), the distinction between these situations is rather difficult to make with the detected lines in LkHα 225.

By summing all the apparent column densities for the ro-vibrational and higher pure rotational lines we obtain an estimate for the observed total column of non-thermal H_2 in LkHα 225 of 2×10^{16} cm^{-2}, corresponding to 2×10^{-6} M$_\odot$ or 0.3 earth masses within the SWS beam. This value of $N(H_2^*)$ is within the range predicted by UV fluorescence models. However, the absence of PAH emission in LkHα 225 at the time of the ISO observations suggests that there was no strong UV radiation field at that time. Therefore we consider the possibility that the ro-vibrational H_2 emission originates in a shock more likely.

Interestingly, in LkHα 225 we have detected two pairs of lines arising from the same energy level: the 1–0 Q(1) & 1–0 O(3) and the 1–0 Q(3) & 1–0 O(5) lines. For these pairs of lines $N(J)$ must be identical. Therefore they can be used to derive a differential extinction between the two wavelengths of the lines using $A(\lambda_1) - A(\lambda_2) = 2.5 \log\left(\frac{I_2 \lambda_2 A_{ij,1}}{I_1 \lambda_1 A_{ij,2}}\right)$. Using the interstellar extinction curve by Fluks et al. (1994), we can then convert the differential extinction to a value of A_V. The results of this procedure are values for A_V of $60^{\rm m} \pm 20^{\rm m}$ and $40^{\rm m} \pm 20^{\rm m}$ for the 1–0 Q(1) & 1–0 O(3) and 1–0 Q(3) & 1–0 O(5) line pairs, respectively. These extinction values are somewhat larger than the $15\overset{\rm m}{.}4 \pm 0\overset{\rm m}{.}2$ derived from the silicate feature in section 8.4. But they agree well with $A_V \approx 50^{\rm m}$ obtained from the C^{18}O column density towards LkHα 225 (Palla et al. 1995). If the slope of the infrared extinction law is approximately interstellar, the extinction towards the region producing the low-lying pure rotational H_2 lines in LkHα 225 must be smaller than this value though; such a large extinction would cause the extinction-corrected 0–0 S(3) line to deviate significantly from the thermal distribution line in the excitation diagram, since it is located within the 9.7 μm silicate feature in the extinction curve. We conclude that in LkHα 225 either there must be two distinct sources of H_2 emission, a 710 K thermal component suffering little extinction – presumably a C-shock – and a heavily extincted, deeply embedded component – possibly a J-shock, or the slope of the infrared extinction law towards this region must be much steeper than interstellar.

8.8 Carbon-monoxide emission lines

At both the positions of BD+40°4124 and LkHα 225, several emission lines due to gas-phase CO were detected in the long-wavelength part of the LWS spectra (Table 8.2). Similar to what was done for the H_2 emission in the previous section, we constructed CO excitation diagrams, using molecular data from Kirby-Docken & Liu (1978). They are shown in Fig. 8.11. The temperature and column of CO resulting from the Boltzmann fit to these excitation diagrams are 500 K and 8.1×10^{16} cm^{-2} and 300 K and 1.9×10^{17} cm^{-2} for BD+40°4124 and LkHα 225, respectively. We estimate the errors in these fit parameters to be around 50 K in temperature and 50% in CO column.

The observed CO lines have critical densities of around 10^6 cm^{-3}. Therefore the observation of these lines also implies densities of at least this order of magnitude in

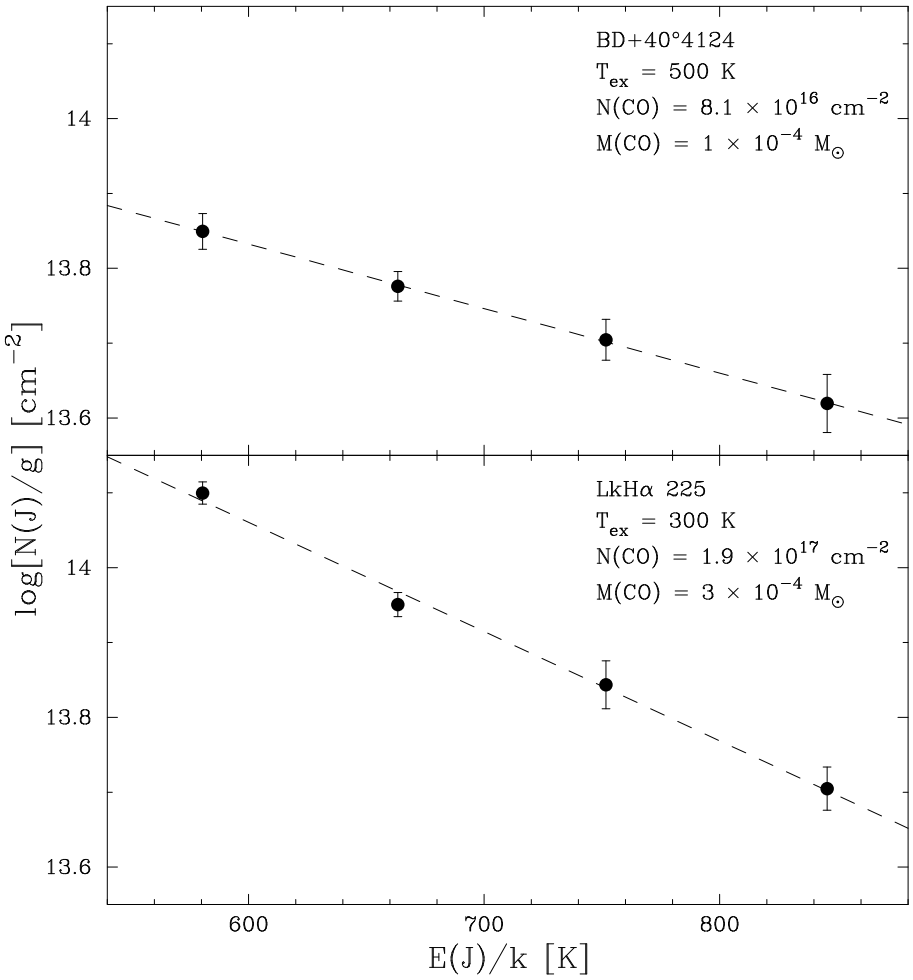

Fig. 8.11. CO excitation diagrams for BD+40°4124 (top) and LkHα 225 (bottom). The dashed lines give the fit of the Boltzmann distribution to the data points.

the originating region. The CO excitation temperature of 500 K found at the position of BD+40°4124 is comparable to that found from the H_2 lines. The CO/H_2 mass fraction of 0.01 is compatible for what one would expect for the warm gas in a PDR. However, assuming that densities of around 10^6 cm^{-3} would exist in the entire BD+40°4124 PDR would be implausible. We therefore conclude that if these CO lines and the H_2 both originate in the large-scale environment of BD+40°4124, the PDR must have a clumpy structure (e.g. Burton et al. 1990).

The CO emission arising from the neighbourhood of LkHα 225 is remarkably different from that seen in H_2: here the excitation temperature of the CO is much lower than that found in H_2. The CO/H_2 mass fraction of 0.03 is also much higher than that found at the position of BD+40°4124. It seems likely that another component than the C-shock responsible for the H_2 emission needs to be invoked to explain the low CO excitation temperature. Again this region must have densities of around 10^6 cm^{-3}. A possible disk or extended envelope around LkHα 225 could have both the temperature and densities required to explain the observed CO spectrum.

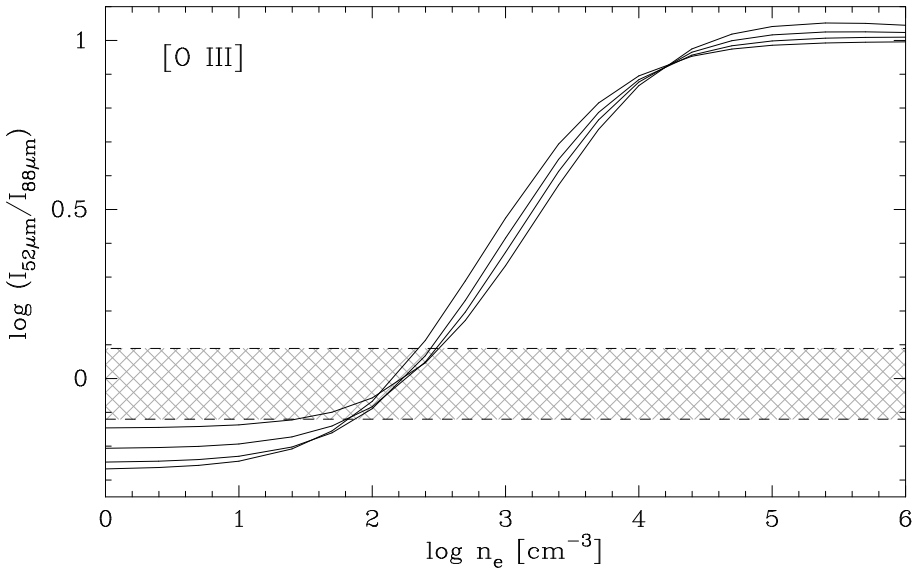

Fig. 8.12. Behaviour of the [O III] 51.8 μm/88.4 μm line flux ratio as a function of electron density n_e (solid lines). The curves for temperatures between 5,000 and 50,000 K (from right to left) are nearly identical. The hatched region between the dashed lines shows the error interval of the observed [O III] ratio in BD+40°4124.

8.9 Atomic fine structure lines

In order to interpret our observations as arising in either a PDR, C-Shock or J-shock, we compare our results with theoretical models of such regions (Tielens & Hollenbach 1985; Hollenbach & McKee 1989; Kaufman & Neufeld 1996). Important constraints come from the observed fine structure lines. The mere presence of certain lines helps us to identify the mechanism responsible for the observed emission. In contrast to both C- and J-shocks, PDRs do not produce significant quantities of [S I] emission (Tielens & Hollenbach 1985). C-shocks only contain trace fractions of ions and hence cannot explain the [Fe II], [Si II] or [C II] emission.

In BD+40°4124 the H_2 lines and the presence of PAH emission strongly suggest the presence of a PDR. No [S I] was detected, so no shock is required to explain the emission from this region. The [Fe II] and [Si II] emission observed at the position of BD+40°4124 may also originate in a PDR. The [O III] emission lines detected by SWS cannot be produced in a PDR. The ratio of the [O III] 52 and 88 μm lines is sensitive to the electron density n_e in the line forming region. It hardly depends on the temperature. We computed the expected ratio for a range of temperatures and densities, in the approximation that we can treat [O III] as a five level ion following the treatment by Aller (1984), using collisional strengths from Aggarwal et al. (1982). The results are shown in Fig. 8.12. We conclude that the [O III] lines observed by LWS are formed in a H II region with n_e = 0.6–2.2 $\times$ 10^2 cm^{-3}. In view of the 22,000 K effective temperature of BD+40°4124, it is surprising that [O III] emission is detected, since simple photo-ionization models predict that for stars with $T_{\rm eff} < 32{,}000$ K most oxygen should remain neutral. Clearly another ionization model must be present here. Possibly the

region also responsible for the H I lines could collisionally ionize the oxygen and we are observing the outer, low-density part of an ionized wind.

Apart from the PDR, a H II region surrounding BD+40°4124 may also contribute significantly to the observed [Fe II] and [Si II] emission. Therefore we have used the photo-ionization code CLOUDY (version 90.04; Ferland 1996) to generate model predictions for line strengths for an H II region surrounding BD+40°4124. A Kurucz (1991) model with parameters appropriate for BD+40°4124 was taken as the input spectrum, and a spherical geometry and a constant electron density of 2×10^2 cm^{-3} throughout the H II region were assumed. According to this model, 30% of the observed [Si II] 34.82 μm flux and 40% of the 25.99 μm [Fe II] flux will originate in the H II region. From comparing the remainder of the fluxes of the atomic fine structure lines to the PDR models of Tielens & Hollenbach (1985), we derive that the PDR should be fairly dense ($\approx 10^4$ cm^{-3}) and have an incident far-UV field of about 10^4 G_0. The extent of this PDR should be around 180 square arcseconds, or about half of the SWS beam.

In view of the observed H_2 spectrum (section 8.7), a C-shock appears the most likely candidate for explaining the observed [S I] emission in LkHα 224. A C-shock with a shock velocity of around 20 km s^{-1} can explain both the H_2 and [S I] emission. However, the density and extent of the region are poorly constrained: the emission may either arise in a dense ($\approx 10^6$ cm^{-3}) region of only a few square arcseconds, or arise in a region of about 10^3–10^4 cm^{-3} with a high beam filling factor. Since it is observed in the largest SWS aperture, the observed [Si II] emission could be due to contamination from LkHα 225 (see Fig. 8.5).

For LkHα 225 the situation appears more complicated. The detection of [S I] clearly shows that a shock must be present in the region. A C-shock can explain the observed thermal H_2 component, with similar parameters as for LkHα 224, but can only explain part of the [S I] emission. The [Fe II] and [Si II] emission could either come from a deeply embedded H II region, a deeply embedded PDR, or a J-shock. In view of necessity to have an additional source of [S I] emission, the most likely candidate might be a J-shock. A J-shock model with $v_s \approx 60$ km s^{-1} and $n \approx 10^4$–10^5 cm^{-3} can indeed reproduce the observed [S I] and [Si II] intensities. However, to reproduce the observed [Fe II] 26.0 μm strength, iron would have to be about eight times more depleted than assumed in the Tielens & Hollenbach PDR models. The observed [C II] 157.7 μm emission at the position of LkHα 225 cannot be explained by shocks. This could very well be due to contamination by the BD+40°4124 PDR or the galactic [C II] background, however.

Fit parameters for the PDR, J-shock and C-shock models used to explain the H_2, CO and fine structure emission lines are listed in Table 8.3. The summed model predictions for the line fluxes are listed in Table 8.2.

8.10 Discussion and conclusions

In the previous sections we have seen that in a small OB association like the BD+40°4124 group, different phenomena contribute to at first glance similar line spectra. The emis-

Table 8.3. Model parameters for the emission line fits.

Object	PDR			C-shock			J-shock		
	n [cm^{-3}]	G [G$_0$]	Ω [10^{-8} sr]	n [cm^{-3}]	v_s [km s^{-1}]	Ω [10^{-8} sr]	n [cm^{-3}]	v_s [km s^{-1}]	Ω [10^{-8} sr]
BD+40°4124	$10^4/10^6$	$10^4/10^5$	0.55/0.05	–	–	–	–	–	–
LkHα 224	–	–	–	$\approx 10^5$	20	≈ 0.10	–	–	–
LkHα 225	–	–	–	$\approx 10^5$	20	≈ 0.20	10^4–10^5	60	0.12

Table 8.4. Comparison of gas-phase and solid-state absorption column densities (in cm^{-2}) towards YSOs.

Object	gas-phase column			solid column			gas/solid ratio			Ref.
	CO	CO_2	H_2O	CO	CO_2	H_2O	CO	CO_2	H_2O	
LkHα 225	10^{19}–10^{21}	1–5 $\times 10^{17}$	0.5–3 $\times 10^{19}$	$< 6 \times 10^{17}$	$< 3 \times 10^{16}$	7.8×10^{17}	> 16	> 3	≈ 13	(1)
T Tau	10^{18}–10^{19}	$< 1 \times 10^{17}$	$< 1 \times 10^{18}$	$< 5 \times 10^{17}$	1.4×10^{17}	5.4×10^{17}	> 20	< 0.7	< 1.9	(2)
AFGL 4176	2×10^{19}	5×10^{15}	2×10^{18}	$< 5 \times 10^{16}$	1.2×10^{17}	9×10^{17}	> 400	≈ 0.04	≈ 2.2	(3,4,5,6)
W33A	4.0×10^{19}	–	1.0×10^{18}	9.0×10^{17}	1.5×10^{18}	2.8×10^{19}	≈ 40	–	≈ 0.04	(3,7,8,9)
AFGL 2136	1.0×10^{19}	1×10^{16}	2×10^{18}	1.8×10^{17}	6.1×10^{17}	5.0×10^{18}	≈ 50	≈ 0.02	≈ 0.4	(3,4,5,6)
RAFGL 7009S	6.1×10^{18}	1.0×10^{17}	$\geq 2 \times 10^{18}$	1.8×10^{18}	2.5×10^{18}	1.1×10^{19}	≈ 3.4	≈ 0.04	≥ 0.18	(10)
Elias 29	$> 1 \times 10^{19}$	–	$> 9 \times 10^{17}$	1.7×10^{17}	6.5×10^{17}	3.0×10^{18}	> 55	–	> 0.3	(9)
AFGL 2591	1.1×10^{19}	1×10^{16}	2×10^{18}	$< 4 \times 10^{16}$	2.7×10^{17}	1.7×10^{18}	> 270	≈ 0.04	≈ 1.1	(3,4,5,6)
NGC 7538 IRS9	1.4×10^{19}	8.0×10^{15}	$< 3 \times 10^{17}$	1.0×10^{18}	1.2×10^{18}	8.0×10^{18}	≈ 14	≈ 0.01	< 0.04	(3,4,5,6)

References: (1) This paper; (2) Chapter 9; (2) Mitchell et al. (1990); (3) van Dishoeck et al. (1996); (4) de Graauw et al. (1996b); (5) van Dishoeck & Helmich (1996); (6) Chiar et al. (1998); (7) Gerakines et al. (1999); (8) Boogert (1999); (9) Dartois et al. (1998).

sion at the position of BD+40°4124 is well reproduced by the combination of a H II region around BD+40°4124 with a PDR. In Section 8.7 we derived values of the far-UV radiation field for its PDR from the observed emission lines. It is useful to compare those values to those expected from the central star to see whether that is a sufficient source of radiation, or another exciting source needs to be invoked. From the Kurucz (1991) model with $T_{\rm eff}$ = 22,000 K and $\log g = 4.0$, fitted to the extinction-corrected UV to optical SED of BD+40°4124 (section 8.3), we compute that BD+40°4124 has a total far-UV (6–13.6 eV) luminosity of 3.2 $\times$ 10^3 $L_\odot$. At a location 5 $\times$ 10^3 AU from the central star, this field will have diluted to the value of 10^5 G_0 obtained from the infrared lines. At the BD+40°4124 distance of 1 kpc, this corresponds to an angular separation of 5″, consistent with the constraints imposed by the SWS aperture. We conclude that BD+40°4124 can indeed be responsible for the incident UV flux upon the PDR observed in that vicinity. Compared to the far-UV luminosity of BD+40°4124, the other two sources only show little UV emission (3 and 6 $L_\odot$ for LkHα 224 and 225, respectively), explaining why we don't observe a PDR at those positions.

For LkHα 224 we showed that the infrared emission-line spectrum could be explained by a single non-dissociative shock. A C-shock with very similar parameters may also be present at the position of LkHα 225. Comparing our ISO SWS aperture positions (Fig. 8.5) with the image of the bipolar outflow centered on LkHα 225 (Palla et al. 1995), we note that this outflow covers both LkHα 224 and LkHα 225. One possible identification for the C-shock in both LkHα 224 and LkHα 225 might therefore be the shock created as the outflow originating from LkHα 225 drives into the surrounding molecular cloud.

Apart from the large-scale C-shock, we have seen that probably a J-shock is present in LkHα 225 as well. This can be naturally identified with the Herbig-Haro knot LkHα 225-M observed in [S II] in the optical (Magakyan & Movseyan 1997). It remains unclear whether the ro-vibrational H_2 lines observed in this object are due to H_2 fluorescence by Lyα photons or to H_2 re-formation in the post-shock gas. Spectroscopy of lines with higher v is required to clarify this.

In the line of sight toward LkHα 225, a large column consisting of warm gas-phase CO, CO_2 and H_2O and solid water ice and silicates was detected. The column of gas-phase water was found to be about 10 times higher that that of water ice. No CO_2 ice was detected toward LkHα 225, demonstrating that the bulk of the CO_2 is in the gas-phase. In Table 8.4 we compare the derived gas/solid ratio for LkHα 225 with those found in the lines of sight towards other young stellar objects. Both the H_2O and CO_2 gas/solid ratios are much higher than those found in other YSOs. For CO_2, the lower limit to the gas/solid is even a factor 100 higher than that found in the source with the previously reported highest ratio! At this point we can only speculate as to why this is the case. One possible explanation could be that the radiation field of BD+40°4124 is heating the outer layers of the LkHα 225 envelope, evaporating the CO_2 ice. If this is the case, BD+40°4124 should be located closer to the observer than LkHα 225, suggesting that LkHα 225 is located at the far side of the "blister" in which the BD+40°4124 group is located. Another explanation could be that the LkHα 225 core itself is unusually warm. Since the abundance of gas-phase water is sensitive to the temperature

(Charnley 1997), this would also explain the high abundance of water vapour in the line of sight toward LkHα 225. Because LkHα 225 is less massive than the luminous objects in which the previous gas/solid ratios have been determined, this high temperature might reflect a more evolved nature of the LkHα 225 core. Future research, such as a temperature determination from gas-phase CO measurements, should be able to distinguish between these possibilities and show whether we have discovered the chemically most evolved hot core known to date, or are looking through a line of sight particularly contaminated by a nearby OB star.

Acknowledgements. This chapter is based on observations with ISO, an ESA project with instruments funded by ESA Member States (especially the PI countries: France, Germany, the Netherlands and the United Kingdom) and with the participation of ISAS and NASA. The authors would like to thank Ewine van Dishoeck for her help in obtaining the BD+40°4124 LWS data and Dolf de Winter for making his optical spectra of LkHα 224 available to us. We thank Adwin Boogert and Issei Yamamura for helpful discussions on the molecular absorption spectra. Lynne Hillenbrand kindly provided the K′-band image of the region shown in Fig. 8.5.

References

Aggarwal, K.M., Baluja, K.L., Tully, J.A. 1982, MNRAS 201, 923
Allen, D.A. 1973, MNRAS 161, 145
Aller, L.H. 1984, *"Physics of Thermal Gaseous Nebulae"*, Dordrecht, Reidel
Aspin, C., Sandell, G., Weintraub, D.A. 1994, A&A 282, L25
Beintema, D.A., van den Ancker, M.E., Molster, F.J. et al. 1996, A&A 315, L369
Bertout, C., Thum, C. 1982, A&A 107, 368
Black, F.H., van Dishoeck. E.F. 1987, ApJ 322, 412
Boogert, A.C.A. 1999, PhD thesis, Groningen University
Boogert, A.C.A., Ehrenfreund, P., Gerakines, P. et al. 1999, A&A, in press
Bouret, J.C., Catala, C. 1998, A&A 340, 163
Brooke, T.Y., Tokunaga, A.T., Strom, S.E. 1993, AJ 106, 656
Burton, M.G., Hollenbach, D.J., Tielens, A.G.G.M. 1990, ApJ 365, 620
Burton, M.G., Hollenbach, D.J., Tielens, A.G.G.M. 1992, ApJ 399, 563
Charnley, S.B. 1997, ApJ 481, 396
Chiar, J.E., Gerakines, P.A., Whittet, D.C.B. et al. 1998, ApJ 498, 716
Cohen, M. 1972, ApJ 173, L61
Cohen, M., Bieging, J.H., Schwartz, P.R. 1982, ApJ 253, 707
Corcoran, M., Ray, T.P. 1996, A&A 321, 189
Corcoran, M., Ray, T.P. 1998, A&A 331, 147
Dabrowski, I. 1984, Canadian J. Phys. 62, 1639
Dartois, E., d'Hendecourt, L., Boulanger, F., Jourdain de Muizon, M., Breitfellner, M., Puget, J.L., Habing, H.J. 1998, A&A 331, 651
de Graauw, Th., Haser, L.N., Beintema, D.A. et al. 1996a, A&A 315, L49
de Graauw, Th., Whittet, D.C.B., Gerakines, P.A. et al. 1996b, A&A 315, L345
Deutsch, L.K., Iyengar, M.A., Hora, J.L., Hoffmann, W.F., Dayal, A., Butner, H.M., Fazio, G.G. 1994, AAS 185, 8416
Di Francesco, J., Evans, N.J., Harvey, P.M., Mundy, L.G., Guilloteau, S., Chandler, C.J. 1997, ApJ

482, 433
Draine, B.T., Bertoldi, F. 1996, ApJ 468, 269
Drake, S.A., Ulrich, R.K. 1980, ApJS 42, 351
Ferland, G.J. 1996, Univ. of Kentucky Physics Department Internal Report
Finkenzeller, U. 1985, A&A 151, 340
Fluks, M.A., Plez, B., Thé, P.S., de Winter, D., Westerlund, B.E., Steenman, H.C. 1994, A&AS 105, 311
Gerakines, P.A., Schutte, W.A., Greenberg, J.M., van Dishoeck, E.F. 1995, A&A 296, 810
Gerakines, P.A., Whittet, D.C.B., Ehrenfreund, P. et al. 1999, ApJ, in press
Habing, H.J. 1968, Bull. Astron. Inst. Netherlands 19, 421
Hamann, F., Persson, S.E. 1992, ApJS 82, 285
Harvey, P.M. 1984, PASP 96, 297
Helmich, F.P., van Dishoeck, E.F., Black, J.H. et al. 1996, A&A 315, L173
Henning, T., Burkert, A., Launhardt, R., Leinert, C., Stecklum, B. 1998, A&A 336, 565
Herbig, G.H. 1960, ApJS 4, 337
Hillenbrand, L.A., Strom, S.E., Vrba, F.J., Keene, J. 1992, ApJ 397, 613
Hillenbrand, L.A., Meyer, M.R., Strom, S.E., Skrutskie, M.F. 1995, AJ 109, 280
Hollenbach, D.J., McKee, C.F. 1989, ApJ 342, 306
Kaufman, M.J., Neufeld, D.A. 1996, ApJ 456, 611
Kessler, M.F., Steinz, J.A., Anderegg, M.E. et al. 1996, A&A 315, L27
Kirby-Docken, K., Liu, B. 1978, ApJS 36, 359
Kurucz, R.L. 1991, in *"Stellar atmospheres–Beyond classical models"* (eds. A.G. Davis Philip, A.R. Upgren, K.A. Janes), L. Davis press, Schenectady, New York, p. 441
Leech, K. et al. 1997, *"SWS Instrument Data Users Manual"*, Issue 3.1, SAI/95-221/Dc
Lorenzetti, D., Saraceno, P., Strafella, F. 1983, ApJ 264, 554
Magakyan, T.Y., Movsesyan, T.A. 1997, Pis'ma Astron. Zh. 23, 764 (Astron. Lett. 23, 666)
Menzel, D.H., Baker, J.G. 1938, ApJ 88, 52
Merrill, P.W., Humason, M.L., Burwell, C.G. 1932, ApJ 76, 156
Mitchell, G.F., Maillard, J.P., Allen, M., Beer, R., Belcourt, K. 1990, ApJ 363, 554
Nisini, B., Milillo, A., Saraceno, P., Vitali, F. 1997, A&A 302, 169
Olnon, F.M., Raimond, E. & IRAS Science Team 1986, A&AS 65, 607
Oudmaijer, R.D., Busfield, G., Drew, J.E. 1997, MNRAS 291, 797
Palla, F., Stahler, S.W. 1993, ApJ 418, 414
Palla, F., Testi, L., Hunter, T.R., Taylor, G.B., Prusti, T., Felli, M., Natta, A., Stanga, R.M. 1995, A&A 293, 521
Parmar, P.S., Lacy, J.H., Achtermann, J.M. 1991, ApJ 372, L25
Rodgers, B., Wooden, D.H. 1997, AAS 191, 4709
Rothmann, L.S., Gamache, R.R., Tipping, R.H. et al. 1996, J. Quant. Spectr. Radiat. Transfer 48, 469
Schmidt-Kaler, Th. 1982, in *"Landolt Börnstein Catalogue"*, Vol VI/2b
Shevchenko, V.S., Ibragimov, M.A., Chernysheva, T.L. 1991, Astron. Zh. 68, 466 (SvA 35, 229)
Shevchenko, V.S., Grankin, K.N., Ibragimov, M.A., Melnikov, S.Y., Yakubov, S.D. 1993, Ap&SS 202, 121
Shull, J.M., Hollenbach, D.J. 1978, ApJ 220, 525
Simon, M., Felli, M., Cassar, L., Fischer, J., Massi, M. 1983, ApJ 266, 623
Skinner, S.L., Brown, A., Stewart, R.T. 1993, ApJS 87, 217
Spitzer, L. 1978, *"Physical Processes in the Interstellar Medium"*, Wiley Interscience, New York

Storey, P.J., Hummer, D.G. 1995, MNRAS 272, 41
Strom, K.M., Strom, S.E., Breger, M., Brooke, A.L., Yost, J., Grasdalen, G., Carrasco, L. 1972a, ApJ 173, L65
Strom, S.E., Strom, K.M., Yost, J., Carrasco, L., Grasdalen, G. 1972b, ApJ 173, 353
Swings, J.P. 1981, A&AS 43, 331
Terranegra, L., Chavarría, C., Diaz, S., Gonzalez-Patino, D. 1994, A&AS 104, 557
Tielens, A.G.G.M., Allamandola, L.J. 1987, in *"Interstellar Processes"*, eds. D.J. Hollenbach & H.A. Thronson Jr. (Dordrecht: Reidel), p. 397
Tielens, A.G.G.M., Hollenbach, D.J. 1985, ApJ 291, 722
Tiné, S., Lepp, S., Gredel, R., Dalgarno, A. 1997, ApJ 481, 282
Trams, N. et al. 1997, *"ISO-LWS Instrument Data Users Manual"*, Issue 5.0, SAI/95-219/Dc
Turner, J., Kirby-Docken, K., Dalgarno, A. 1977, ApJS 35, 281
van Dishoeck, E.F., Helmich, F.P. 1996, A&A 315, L177
van Dishoeck, E.F., Helmich, F.P., de Graauw, Th. et al. 1996, A&A 315, L349
Weaver, W.B., Jones, G. 1992, ApJS 78, 239
Wenzel, W. 1980, Mitt. Ver. Sterne 8, 182
Wesselius, P.R., van den Ancker, M.E., Young, E.T. et al. 1996, A&A 315, L197
Wesselius, P.R., van Duinen, R.J., de Jonge, A.R.W., Aalders, J.W.G., Luinge, W., Wildeman, K.J. 1982, A&AS 49, 427
Whittet, D.C.B., Schutte, W.A., Tielens, A.G.G.M. et al. 1996, A&A 315, L357
Wolfire, M.G., Königl, A. 1991, ApJ 383, 205

Chapter 9

ISO Spectroscopy of Shocked Gas in the Vicinity of T Tau

M.E. van den Ancker, P.R. Wesselius, A.G.G.M. Tielens,
E.F. van Dishoeck and L. Spinoglio, A&A, in press (1999)

Abstract

We present the results of ISO SWS and LWS spectroscopy of the young binary system T Tau. The spectrum shows absorption features due to H_2O ice, CO_2 ice, gas-phase CO and amorphous silicate dust, which we attribute to the envelope of T Tau S. We derive an extinction of $A_V = 17\overset{\mathrm{m}}{.}4 \pm 0\overset{\mathrm{m}}{.}6$ towards this source. Detected emission lines from H I arise in the same region which is also responsible for the optical H I lines of T Tau N. These lines most likely arise in a partially ionized wind. Emission from the infrared fine-structure transitions of [S I], [Ar II], [Ne II], [Fe II], [Si II], [O I] and [C II] was also detected, which we explain as arising in a ≈ 100 km s^{-1} dissociative shock in a fairly dense (5×10^4 cm^{-3}) medium. Pure rotational and ro-vibrational emission from molecular hydrogen was detected as well. We show the H_2 emission lines to be due to two thermal components, of 440 and 1500 K respectively, which we attribute to emission from the dissociative shock also responsible for the atomic fine-structure lines and a much slower (≈ 35 km s^{-1}) non-dissociative shock. The 1500 K component shows clear evidence for fluorescent UV excitation. Additionally, we found indications for the presence of a deeply embedded ($A_V > 40^{\mathrm{m}}$) source of warm H_2 emission. We suggest that this component might be due to a shock, caused by either the outflow from T Tau S or by the infall of matter on the circumstellar disk of T Tau S.

9.1 Introduction

T Tauri (HD 284419) might well be the most studied young stellar object in the sky. It was initially thought of as the prototype of a class of low-mass pre-main sequence stars,

but is now known to be a very unique young binary system. An infrared companion, T Tau S, was discovered 0.″7 south of the optically bright K0–1e T Tauri star T Tau N (Dyck et al. 1982), corresponding to a projected separation of 100 AU at the 140 pc distance of the Taurus-Auriga complex (Kenyon et al. 1994; Wichmann et al. 1998). Reports of a third stellar component in the T Tau system (Nisenson et al. 1985; Maihara & Kataza 1991) remain unconfirmed (Gorham et al. 1992; Stapelfeldt et al. 1998). Whereas T Tau N dominates in the optical and at submm wavelengths, the brightness of the system in the infrared is dominated by T Tau S (Hogerheijde et al. 1997). Both T Tau N and S display irregular photometric variability, possibly connected to variations in the rate of accretion of material onto the stellar surface (Herbst et al. 1986; Ghez et al. 1991). Recent HST imaging failed to detect T Tau S in the V band down to a limiting magnitude of $19\overset{\mathrm{m}}{.}6$, showing that $A_V > 7^{\mathrm{m}}$ towards this source (Stapelfeldt et al. 1998). T Tau N, on the other hand, only suffers little extinction ($A_V = 1\overset{\mathrm{m}}{.}39$; Kenyon & Hartmann 1995). Proper-motion studies (Ghez et al. 1995) as well as the discovery of a bridge of radio emission connecting both components (Schwartz et al. 1986) prove beyond doubt that both stars are physically connected, demonstrating that a significant amount of dust must be present within the binary system itself.

In the last few years, millimeter interferometry has revealed the presence of a circumstellar disk with a total mass of 10^{-2} $M_\odot$ around the optically bright component T Tau N. The presence of a cicumstellar disk around T Tau S is suggested by mid-infrared emission, but the millimeter interferometric data show that its mass is substantially less than that around T Tau N (Hogerheijde et al. 1997; Akeson et al. 1998). Lunar occultation observations of the T Tau system show that these disks must be smaller than 1 AU at 2.2 μm (Simon et al. 1996). In addition to this, an envelope or circumbinary disk of similar mass as the T Tau N disk is required to fit the energy distribution and polarization properties of the system (Weintraub et al. 1992; Whitney & Hartmann 1993; Calvet et al. 1994; Hogerheijde et al. 1997). On larger spatial scales, two nebulae are associated with the T Tau system. A small (≈ 10 ″) cloud, Burnham's nebula (HH 255), is centered on the binary and shows a line spectrum typical of Herbig-Haro objects (Robberto et al. 1995). A spatially separated arc shaped cloud, Hind's nebula (NGC 1555) is located 30″ to the west. Recent maps at 450 and 850 μm have detected a Class I protostar in Hind's nebula, suggesting that star formation in the vicinity of T Tau is more active than previously thought (Weintraub et al. 1999).

The kinematics of molecular material in the vicinity of T Tau have been found to be very complex. Submm observations of CO and HCO^+ (Knapp et al. 1977; Edwards & Snell 1982; Levreault 1988; van Langevelde et al. 1994a; Momose et al. 1996; Schuster et al. 1997; Hogerheijde et al. 1998) suggest that both components of T Tau drive separate bipolar outflows and that at least one of these is directed close to the line of sight. On even larger scales, Reipurth et al. (1997) discovered a giant Herbig-Haro flow (HH 355) with a projected extent of 38 arcminutes (1.55 pc at 140 pc), aligned with the axis of the outflow from T Tau S, which they explained as being due to multiple eruptions of material while the flow axis is precessing. Ray et al. (1997) showed that T Tau S has recently ejected two large lobes of mildly relativistic particles, demonstrating that the emergent picture might be further complicated by significant time-variability in the

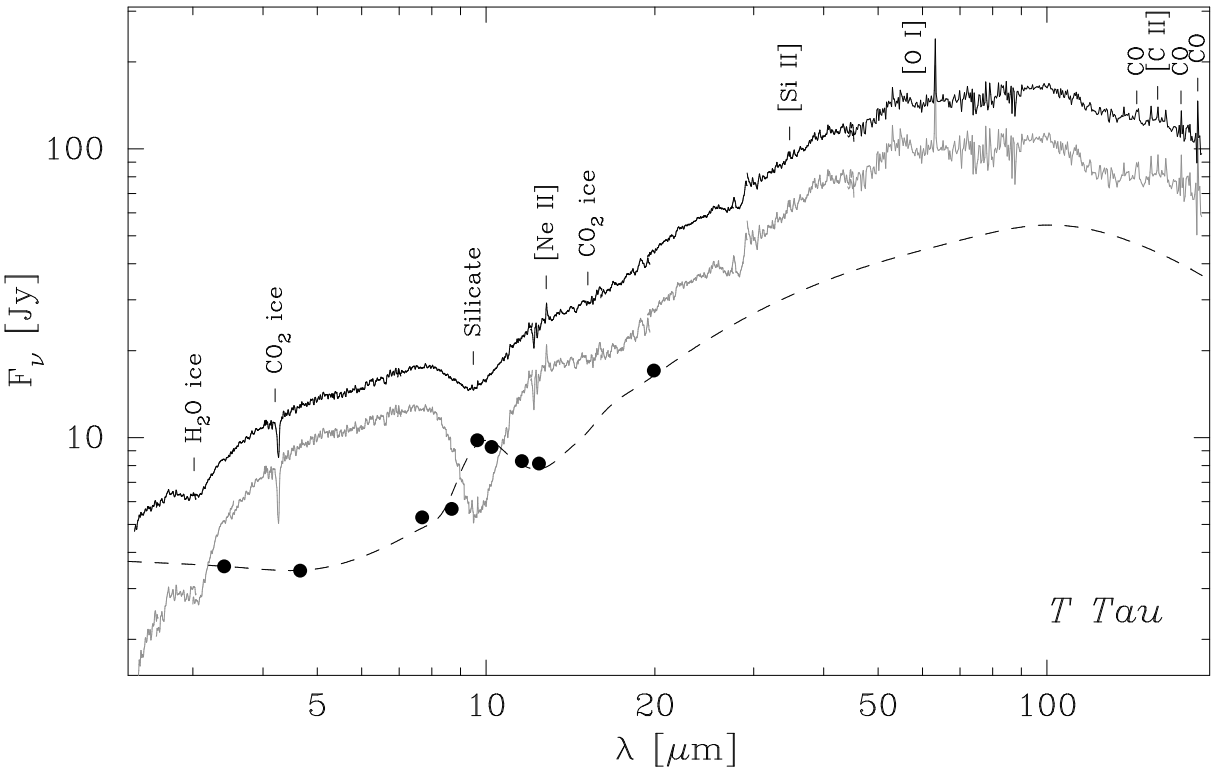

Fig. 9.1. Combined SWS/LWS full grating spectra for T Tau with the most prominent features identified. The apparent dips at 12 and 28 μm as well as the bump around 52 μm are artefacts of the data reduction process. Also shown (dots) is ground-based photometry of T Tau N with a dust shell model fit to these points (dashed line). The grey curve shows the model-subtracted ISO spectra.

outflow rate.

In this chapter we present new *Infrared Space Observatory* (ISO; Kessler et al. 1996) spectroscopy of the T Tau system. In Sections 9.3 and 9.4 we analyze solid-state and gas-phase absorption features and show that these are fairly typical for the envelope of an embedded low-mass young stellar object. In section 9.5 we briefly discuss the infrared H I lines and argue that these have the same origin as the optical lines. In sections 9.6 and 9.7 we will discuss the observed H_2 spectrum and the atomic fine-structure lines, and show that these are due to shocked gas. In the discussion (Sect. 9.8) we will argue that the most likely candidate for a highly embedded molecular shocked gas component is an accretion shock in a circumstellar disk. The presentation of the ISO data on the CO, H_2O and OH emission line spectrum of T Tau is left to a subsequent paper (Spinoglio et al. 1999). We anticipate that the analysis of these data shows that the physical picture outlined here is confirmed.

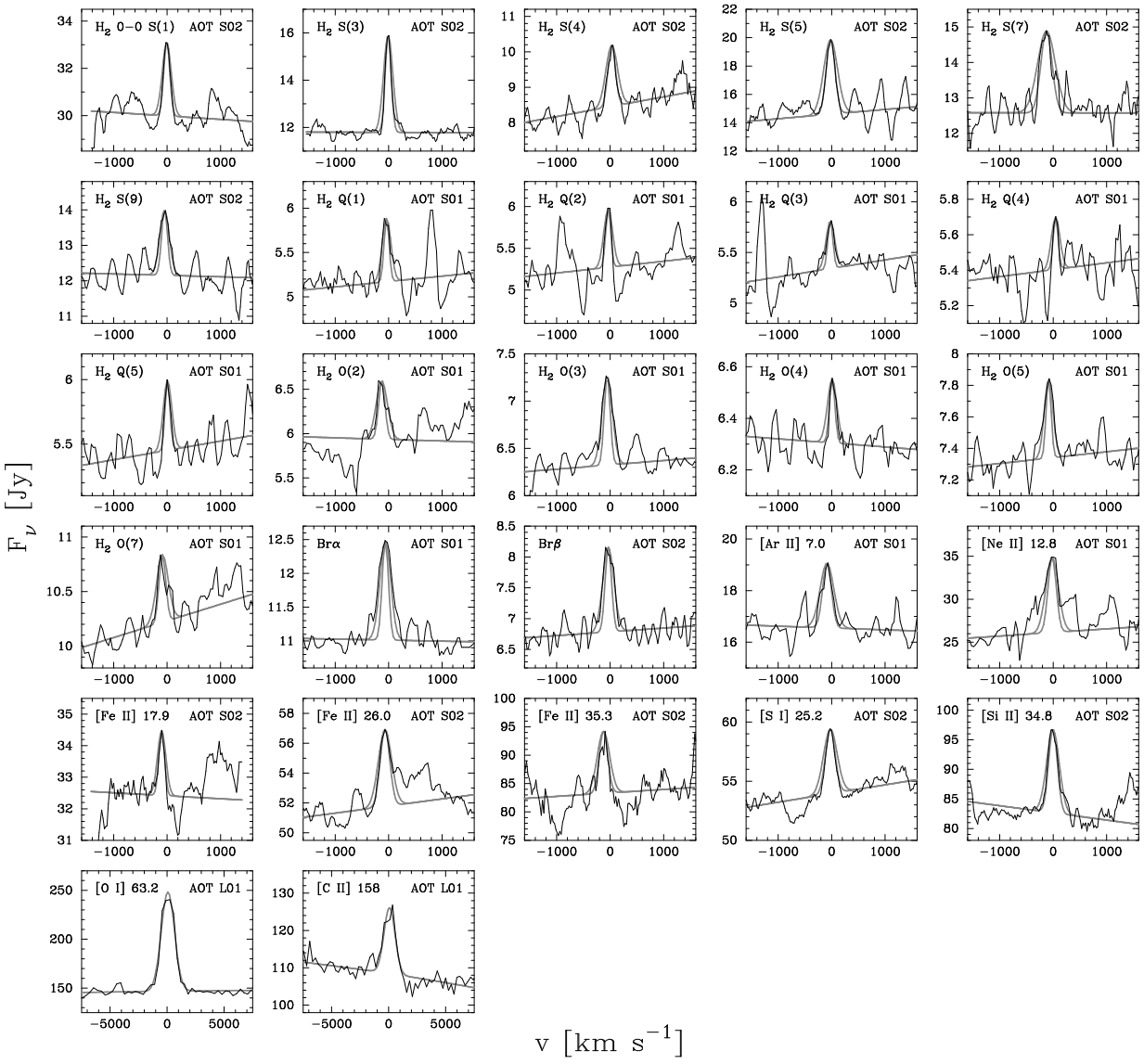

Fig. 9.2. Detected lines in T Tau. The velocities are heliocentric. The grey lines indicate the instrumental profiles for a point source and an extended source filling the entire aperture.

Table 9.1. Observed and extinction-corrected (A_V = 1.$^{\rm m}$39) line fluxes and model predictions (in 10^{-16} W m^{-2}) for T Tau.

Line	λ	Beam	AOT	Observed		Model		
	[μm]	[10^{-8} sr]		Measured	Ext. corr.	J-Shock	C-Shock	Total
H_2 0–0 S(0)	28.2188	1.64	S02	$<$ 4.67	$<$ 4.74	0.06	0.01	0.07
H_2 0–0 S(1)	17.0348	1.15	S02	1.80±0.59	1.85±0.61	1.50	0.35	1.85
H_2 0–0 S(2)	12.2786	1.15	S02	$<$ 9.68	$<$ 9.99	1.10	0.76	1.86
H_2 0–0 S(3)	9.6649	0.85	S02	6.81±1.95	7.36±2.10	1.94	5.26	7.20
H_2 0–0 S(4)	8.0251	0.85	S02	3.17±1.05	3.25±1.07	0.24	3.38	3.62
H_2 0–0 S(5)	6.9095	0.85	S02	13.58±2.63	13.78±2.67	0.14	13.65	13.79
H_2 0–0 S(6)	6.1086	0.85	S02	$<$ 8.07	$<$ 8.21	0.01	4.55	4.56
H_2 0–0 S(7)	5.5112	0.85	S02	11.03±2.63	11.24±2.68	0.00	10.65	10.65
H_2 0–0 S(8)	5.0531	0.85	S02	$<$ 4.52	$<$ 4.62	0.00	2.22	2.22
H_2 0–0 S(9)	4.6946	0.85	S02	2.87±0.95	2.94±0.97	0.00	3.40	3.40
H_2 0–0 S(10)	4.4099	0.85	S02	$<$ 3.13	$<$ 3.21	0.00	0.48	0.48
H_2 0–0 S(11)	4.1813	0.85	S02	$<$ 4.67	$<$ 4.81	0.00	0.51	0.51
H_2 0–0 S(12)	3.9960	0.85	S02	$<$ 2.84	$<$ 2.93	0.00	0.05	0.05
H_2 1–0 Q(1)	2.4066	0.85	S01	5.96±1.97	6.46±2.13	0.00	10.14	10.14
H_2 1–0 Q(2)	2.4134	0.85	S01	1.96±0.65	2.13±0.70	0.00	3.19	3.19
H_2 1–0 Q(3)	2.4237	0.85	S01	4.52±1.20	4.90±1.30	0.00	8.86	8.86
H_2 1–0 Q(4)	2.4475	0.85	S01	0.59±0.21	0.64±0.22	0.00	2.34	2.34
H_2 1–0 Q(5)	2.4547	0.85	S01	1.44±0.48	1.56±0.51	0.00	4.77	4.77
H_2 1–0 Q(6)	2.4755	0.85	S01	$<$ 2.63	$<$ 2.84	0.00	0.94	0.94
H_2 1–0 O(2)	2.6269	0.85	S01	6.20±1.23	6.64±1.31	0.00	2.29	2.29
H_2 1–0 O(3)	2.8025	0.85	S02	9.39±0.99	9.96±1.05	0.00	8.58	8.58
H_2 1–0 O(4)	3.0039	0.85	S02	1.26±0.42	1.33±0.44	0.00	2.46	2.46
H_2 1–0 O(5)	3.2350	0.85	S02	2.87±0.73	3.00±0.77	0.00	4.99	4.99
H_2 1–0 O(6)	3.5008	0.85	S01	$<$ 2.29	$<$ 2.39	0.00	0.92	0.92
H_2 1–0 O(7)	3.8074	0.85	S01	1.32±0.43	1.36±0.45	0.00	1.28	1.28
H I Huα	12.3719	1.15	S01	$<$ 6.23	$<$ 6.42	0.01	–	–
H I Huβ + H7δ	7.5083	0.85	S02	$<$ 3.29	$<$ 3.34	0.00	–	–
H I Pfα	7.4600	0.85	S02	$<$ 3.63	$<$ 3.69	0.03	–	–
H I Pfβ	4.6539	0.85	S02	$<$ 4.90	$<$ 5.03	0.02	–	–
H I Brα	4.0523	0.85	S02	10.97±3.00	11.31±3.09	0.10	–	–
H I Brβ	2.6259	0.85	S02	9.61±1.41	10.29±1.51	0.06	–	–
[Fe I] ($^5D_4$–$^5D_3$)	24.0424	1.15	S02	$<$ 1.83	$<$ 1.87	0.05	–	–
[Fe I] ($^5D_3$–$^5D_2$)	34.7135	2.01	S02	$<$ 1.04	$<$ 1.05	0.02	–	–
[Fe II] ($^4F_{9/2}$–$^4F_{7/2}$)	17.9363	1.15	S02	0.52±0.17	0.53±0.18	0.97	0.00	0.97
[Fe II] ($^6D_{9/2}$–$^6D_{7/2}$)	25.9882	1.15	S02	1.85±0.61	1.88±0.62	3.37	0.00	3.37
[Fe II] ($^6D_{7/2}$–$^6D_{5/2}$)	35.3491	2.01	S02	4.23±1.40	4.28±1.41	1.21	0.00	1.21
[Ni II] ($^2D_{5/2}$–$^2D_{3/2}$)	6.6360	0.85	S01	$<$ 8.15	$<$ 8.27	5.86	0.00	5.86
[Ar II] ($^2P_{3/2}$–$^2P_{1/2}$)	6.9853	0.85	S01	9.38±1.72	9.51±1.75	–	0.00	–
[Ne II] ($^2P_{3/2}$–$^2P_{1/2}$)	12.8135	1.15	S01	28.14±7.15	28.88±7.34	29.36	0.00	29.36
[S I] ($^3P_2$–$^3P_1$)	25.2490	1.15	S02	4.09±1.28	4.16±1.30	2.99	0.31	3.30
[Si II] ($^2P_{1/2}$–$^2P_{3/2}$)	34.8152	2.01	S02	12.59±4.16	12.72±4.20	11.69	0.00	11.69
[O I] ($^3P_2$–$^3P_1$)	63.1850	16.3	L01	230.6±16.1	231.5±16.2	233.2	0.80	234.0
[O I] ($^3P_1$–$^3P_0$)	145.535	8.82	L01	$<$ 14.9	$<$ 14.9	5.00	0.05	5.05
[C II] ($^2P_{1/2}$–$^2P_{3/2}$)	157.741	11.6	L01	10.60±0.74	10.61±0.74	5.22	0.00	5.22

Model parameters:

Component	n [cm^{-3}]	v_s [km s^{-1}]	Ω [10^{-8} sr]
J-shock	5×10^4	100	0.03
C-shock	$\approx 10^5$	35	$\approx$ 0.16

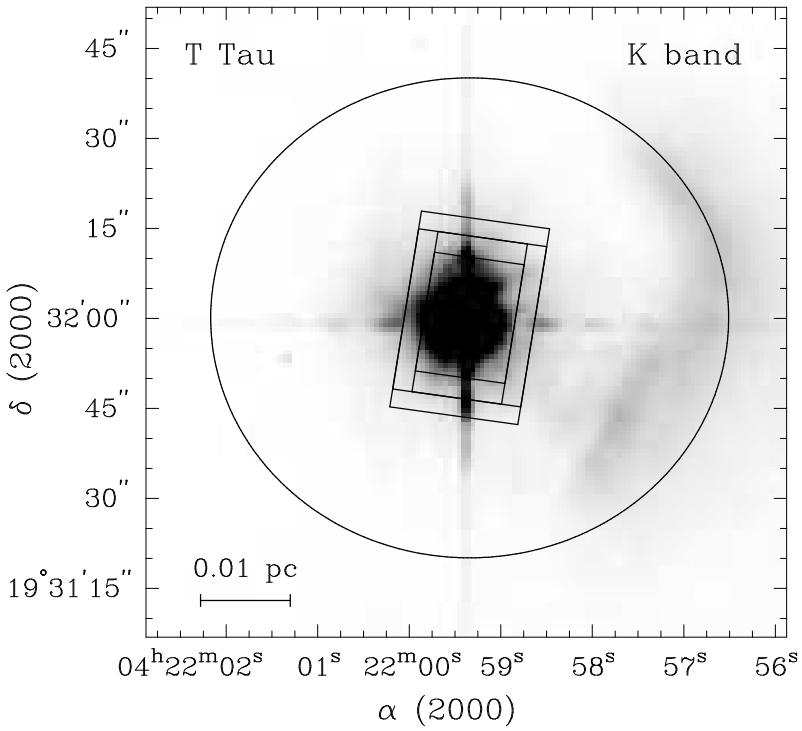

Fig. 9.3. SWS (rectangles) and LWS (circle; beam average FWHM) aperture positions for our measurements of T Tau superimposed on a K′ band image of the region (Hodapp 1994). The orientation of the SWS apertures is nearly identical for the different SWS observations. The rectangles indicate the apertures (in increasing size) for SWS bands 1A–2C (2.4–12.0 μm), 3A–3D (12.0–27.5 μm), 3E (27.5–29.5 μm) and 4 (29.5–40.5 μm).

9.2 Observations

An ISO Short Wavelength (2.4–45 μm) Spectrometer (SWS; de Graauw et al. 1996) full grating scan ("AOT S01", speed 4) of T Tau was obtained in ISO revolution 680 (JD 2450717.411). In addition to this, deeper SWS grating scans on selected molecular and fine structure lines ("AOT S02") were obtained in revolutions 681 and 861 (at JD 2450718.778 and 2450897.973). Besides the SWS results, we present here the results of a relatively fast ISO Long Wavelength (43–197 μm) Spectrometer (LWS; Clegg et al. 1996) full grating scan ("AOT L01", t = 776 s) obtained in revolution 672 (JD 2450709.675), while a deeper LWS spectrum is presented in Spinoglio et al. (1999). In this latter work, LWS off-source measurements on positions 80″ to the North, South, East and West of T Tau were also made, whose results we anticipate here. They show that the [C II] 157.7 μm line was the only one detected in the off-source positions.

Data were reduced in a standard fashion using calibration files corresponding to ISO off-line processing software (OLP) version 7.0, after which they were corrected for remaining fringing and glitches. To increase the S/N in the final spectra, the detectors were aligned and statistical outliers were removed, after which the spectra were

Table 9.2. Line fluxes (in 10^{-16} W m^{-2}) for off-source measurements.

Pos.	α (2000.0)	δ (2000.0)	AOT	λ [μm]	Line	Flux
Off-N	04 21 59.4	+19 33 46.5	L01	157.80	[C II]	7.9±0.9
Off-S	04 21 59.3	+19 20 26.5	L01	157.79	[C II]	8.8±1.3
Off-W	04 22 06.4	+19 32 06.0	L01	157.76	[C II]	8.8±1.1
Off-E	04 21 52.4	+19 32 07.0	L01	157.74	[C II]	9.1±0.9

rebinned to a lower spectral resolution. Figure 9.1 shows the resulting ISO spectra. Accuracies of the absolute flux calibration in the SWS spectra range from 7% in the short-wavelength (< 4.10 μm) part to $\approx 30\%$ in the long wavelength (> 29 μm) part (Leech et al. 1997). The LWS absolute flux calibration is expected to be accurate at the 7% level (Trams et al. 1997). Plots of all detected lines, rebinned to a resolution $\lambda/\Delta\lambda$ of 2000 with an oversampling factor of four (SWS), or with the data averaged (LWS), are presented in Fig. 9.2. Line fluxes for detected lines and upper limits (total flux for line with peak flux 3σ) for the most significant undetected lines on the on-source position are listed in Table 9.1. Detected lines in the off-source LWS spectra are listed in Table 9.2.

For each complete spectral scan, the SWS actually makes twelve different grating scans, each covering a small wavelength region ("SWS band"), and with its own optical path. They are joined to form one single spectrum (Fig. 9.1). Because of the variation of the diffraction limit of the telescope with wavelength, different SWS bands use apertures of different sizes. For a source that is not point-like, one may therefore see a discontinuity in flux at the wavelengths where such a change in aperture occurs. This effect is not seen in the spectra of T Tau, indicating that the bulk of the infrared continuum comes from a region that is small compared to the smallest SWS beam ($14'' \times 20''$). Note that the same does not have to apply to the line emission.

In the course of this chapter we will compare our ISO data of T Tau with measurements by previous authors. To do so accurately, we need to know the relative sizes and orientations of the beams used. Therefore we created a plot of the ISO SWS apertures and LWS average beam size overlaid on a K′-band of the T Tau region (Hodapp 1994), shown in Fig. 9.3. As can be seen from this figure, all SWS apertures include both T Tau N and T Tau S. They do not include Hind's nebula. The LWS beam includes both the central objects of the T Tauri system as well as Hind's nebula. The fact that the fluxes measured by SWS agree well with those measured by LWS in the small region of overlap, suggests that Hind's nebula remains much fainter than the central objects at wavelengths at least up to 45 μm.

Table 9.3. Solid state absorption column densities for T Tau S.

Species	Wavelength [μm]	A_m [cm molec^{-1}]	$\int \tau(\nu) d\nu$ [cm^{-1}]	N [cm^{-2}]
H_2O	3.0	2.0×10^{-16}	109	5.4×10^{17}
H_2O	6.0	1.2×10^{-17}	< 10	$< 8 \times 10^{17}$
CO	4.67	1.1×10^{-17}	< 5	$< 5 \times 10^{17}$
CO_2	4.26	7.6×10^{-17}	12.2	1.6×10^{17}
CO_2	15.2	1.1×10^{-17}	1.2	1.1×10^{17}
CH_4	7.67	7.3×10^{-18}	< 4	$< 5 \times 10^{17}$
Silicate	9.7	1.2×10^{-16}	218	1.8×10^{18}

9.3 Solid-state features

The SWS spectrum of T Tau (Fig. 9.1) consists of a smooth continuum with a number of strong absorption features superposed, in which we recognize the O–H bending mode of water ice around 3 μm, the 4.27 μm C=O stretch and the 15.3 μm O=C=O bend of CO_2 and the familiar 9.7 μm absorption feature due to the Si–O stretching mode in amorphous silicates.

By convolving the SWS spectrum with an L band (3.5 μm) transmission curve, we derive a synthetic L magnitude of $3\overset{\text{m}}{.}4$ for T Tau at the time of the observations. This value is within errors identical to the L' band measurement of Simon et al. (1996) in December 1994. Thus the fading of the infrared brightness of the system after the 1990–1991 flare (Ghez et al. 1991; Kobayashi et al. 1994) appears to have ceased before the system has returned to its pre-outburst magnitude. Synthetic 12, 25, 60 and 100 μm fluxes from the ISO spectra are 1.3–1.5 times those measured by IRAS in 1983. The IRAS LRS spectrum is fainter and redder than the ISO SWS spectrum and does not show a 9.7 μm feature in emission or absorption. The ISO SWS fluxes are about 1.4 times less than those in the November 1993 ground-based 8–13 μm spectroscopy by Hanner et al. (1998), in which the silicate feature also appears stronger.

The spectrum obtained with ISO is the sum of the spectra of T Tau N and S. Although T Tau S is expected to dominate the continuum flux in the thermal infrared, T Tau N might also contribute significantly to the spectrum. In particular, absorption features from T Tau S might appear "filled in" with flux from T Tau N, especially in the 9.7 μm silicate feature, which appears in emission in T Tau N, whereas it is in absorption in the southern component (Ghez et al. 1991; van Cleve et al. 1994; Herbst et al. 1997). While the northern component does show variations in brightness in the optical, all available literature data suggest that the infrared variability is limited to T Tau S. We therefore attempt to isolate the contribution from T Tau S (plus the circumbinary envelope at the longer wavelengths) by subtracting an empirical model for T Tau N, consisting of a sum of blackbodies + emission from amorphous silicate at 500 K

(Dorschner et al. 1995) fitted to ground-based spatially resolved photometry of T Tau N (Ghez et al. 1991; Herbst et al. 1997), from the data. This model and the resulting spectrum of T Tau S are also shown in Fig. 9.1. We note that it is possible to reproduce all existing infrared photometry and spectroscopy of T Tau in the literature by the sum of our empirical model of T Tau N and a multiplicative factor times the spectrum of T Tau S. This means that the infrared variations of T Tau S are not caused by variable circumstellar extinction, but must reflect variations in the intrinsic luminosity of the central source, e.g. by variations in the accretion rate.

From the integrated optical depth $\int \tau(\nu) d\nu$ of a non-saturated absorption feature we can compute a column density N using an intrinsic band strength A_m. For H_2O, CO, CO_2 and CH_4 ices, values of A_m were measured by Gerakines et al. (1995) and Boogert et al. (1997). For silicates, A_m is taken from Tielens & Allamandola (1987). Measured integrated optical depth and column densities for T Tau S of commonly observed ices are listed in Table 9.3. The derived value of 3.4 for the solid H_2O/CO_2 ratio is at the lower range of values observed in the lines of sight towards low-mass YSOs (Whittet et al. 1996; Boogert 1999). Since the line of sight towards T Tau S might actually pass through the outer edge of the T Tau N disk (Hogerheijde et al. 1997), this result may imply that the solid H_2O/CO_2 ratio in the outer disk is similar to those typically found in the envelopes of low-mass YSOs.

Since extinction in the continuum surrounding the 9.7 μm feature is small compared to the extinction within this feature, the extinction A_λ at wavelength λ across a non-saturated 9.7 μm feature can simply be obtained from the relation $A_\lambda = -2.5 \log(I/I_0)$. Using an average interstellar extinction law which includes the silicate feature (Fluks et al. 1994), we can then convert these values of A_λ to a visual extinction, resulting in a value of $A_V = 17\overset{\text{m}}{.}4 \pm 0\overset{\text{m}}{.}6$ toward T Tau S.

9.4 Gas-phase molecular absorption

Shiba et al. (1993) detected shallow absorption features in the spectrum of T Tau at 1.4 and 1.9 μm, which they identified with warm ($\approx$ 2000 K) water vapour. They argue against a photospheric origin because this would be too hot (K type), and hence locate it in the inner disk. We inspected the ISO SWS spectrum for the presence of absorption from the ν_2 band of gas-phase water, readily seen towards other YSOs (Helmich et al. 1996; van Dishoeck & Helmich 1996; Chapter 8). It is not detected in our T Tau spectra. The resulting upper limit for the H_2O gas-phase column is 10^{18} cm^{-2}, incompatible with the strength of the features observed by Shiba et al. If the dips observed by these authors are indeed real and due to water vapour, they must therefore either be strongly variable, or only occur in the inner disk of T Tau N, which dominates at 1.4 and 1.9 μm.

In the AOT S02 ISO SWS spectrum of T Tau, a number of weak absorption lines with maximum depth around 5% of the continuum level can be seen in the 4.7 μm region (Fig. 9.4). These could be due to ro-vibrational lines of gas-phase CO. Although weak, some of the lines (especially the 4.717 μm line, which is also present in the AOT

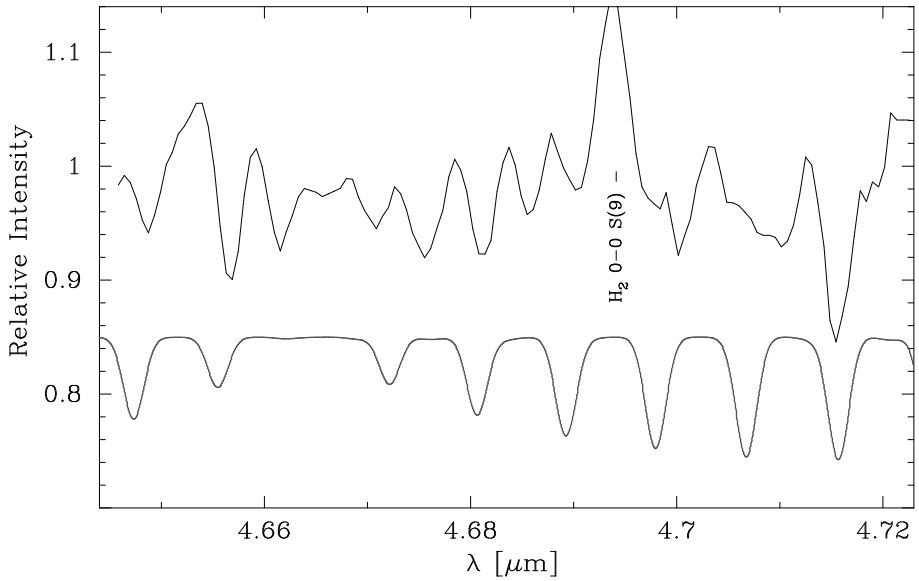

Fig. 9.4. SWS AOT S02 spectrum of T Tau in the 4.7 μm region, with the continuum normalized to unity (top curve). The peak at 4.694 μm is the 0–0 S(9) transition of molecular hydrogen. Also shown (bottom curve) is a synthetic CO spectrum with $T_{\rm ex}$ = 300 K, b = 5 km s^{-1} and N(CO) = 3 $\times$ 10^{18} cm^{-2}, shifted for clarity.

S01 spectrum) appear clearly stronger than the noise level. We therefore consider these absorption features as a tentative detection of gas-phase CO in absorption. Following the procedure outlined in Chapter 8, we compared this spectrum with synthetic gas-phase absorption spectra, computed using molecular constants from the HITRAN 96 database (Rothmann et al. 1996). Assuming a Doppler parameter b of 5 km s^{-1} and excitation temperature of 300 K, typical for those observed towards YSOs (Helmich et al. 1996; van Dishoeck & Helmich 1996; Dartois et al. 1998), we derive a total column of CO gas of 10^{18}–10^{19} cm^{-2} for this line of sight.

9.5 Hydrogen recombination lines

In the ISO SWS spectra of T Tau, the Brα and Brβ lines are present and strong (Table 9.1). No lines from the higher series of H I were detected. The Brα and Brβ line profiles appear broader than those expected for a point source (Fig. 9.2). We deduce an intrinsic FWHM of $\approx$ 300 km s^{-1}, in good agreement with the ground-based Brα profile by Persson et al. (1984). The Brα line flux of 11.0 $\times$ 10^{-16} W m^{-2} measured by SWS in a 20″ $\times$ 14″ aperture is identical to that measured by Evans et al. (1987) in a 3.″5 diameter aperture, suggesting that the infrared H I transitions arise in a compact area. Based on the similarity of their Brα line profile to Hα, Persson et al. (1984) suggested that the infrared hydrogen recombination lines from T Tau arise in the optically visible component, T Tau N, and that any H I lines from T Tau S are obscured by many magnitudes of extinction. This is in agreement with spatially resolved images of the T Tau system, in which the Brγ flux is clearly seen to peak at the position of T Tau N (Herbst

et al. 1996).

We observe a ratio of the Brα/Brβ line flux of 1.1. Case B recombination line theory can only produce a range of 1.4–2.2 for this ratio (Storey & Hummer 1995). This means that these lines are not optically thin, as assumed in Case B, and that optical depth effects play an important rôle in the radiative transfer. Therefore we can rule out a possible origin in an extended low-density region surrounding T Tau for the H I lines. A similar conclusion was already reached from the Brα/Brγ and Brα/Pfγ lines ratios by Evans et al. (1987). We note that the optical Balmer and Paschen lines follow a similar decrement with increasing quantum number n as the infrared recombination lines. This, together with the similarity of the Brα and Hα profiles noted by Persson et al. (1984) brings us to the conclusion that the optical and infrared H I lines have a similar origin; most likely a stellar wind with a mass loss rate of 3.5×10^{-8} $M_\odot$ yr^{-1} (Kuhi 1964; Kenyon & Hartmann 1995).

For an optically thick ionized wind, Simon et al. (1983) derive a simple relation between Brα line flux and free-free radio emission, which for T Tau predicts a flux of 0.17 mJy at 6 cm. Observed 6 cm radio fluxes of T Tau N are a factor of five higher (Ray et al. 1997). One explanation for this discrepancy could be that we would have underestimated the extinction correction for the Brα line. However, if the optical and infrared H I lines indeed come from the same region, this cannot be the case, since this would render the optical lines invisible. We therefore conclude that only part of the radio flux of T Tau N comes from the wind responsible for the H I lines. An additional source of radio emission must be present in the vicinity of T Tau N, possibly similar to the outflow shock model invoked to explain the non-thermal gyrosynchrotron radio emission from T Tau S (Skinner & Brown 1994; Ray et al. 1997).

9.6 Molecular hydrogen emission

One property that distinguishes T Tau from other T Tauri stars is the presence of strong UV and near-IR molecular hydrogen emission in its vicinity (Beckwith et al. 1978; Brown et al. 1981). H_2 emission is present throughout Burnham's nebula, but is dominated by emission close to the central binary (van Langevelde et al. 1994b). The source of the central H_2 emission is controversial: Whereas Herbst et al. (1996) claim that both T Tau N and T Tau S contribute about equally to the 1–0 S(1) flux, the adaptive optics images by Quirrenbach & Zinnecker (1997) seem to indicate that most of this bright H_2 emission arises in the vicinity of T Tau S. H_2 emission is also present in a bright knot 2–3″ northwest of the central stars (Herbst et al 1996, 1997) and in less intense knots and filaments throughout the nebula. Previous authors argue that most of the observed H_2 emission must be collisionally excited, in shocks due to the accretion onto T Tau S and the interaction of a collimated outflow with the surrounding medium. However, a fluorescent emission component seems also to be required. The source of the Lyα radiation required for the fluorescence mechanism remains unclear.

In the SWS spectra of T Tau, we detected pure-rotational (0–0 transitions) emission from H_2 up to S(9) and ro-vibrational (1–0 transitions) lines up to Q(5) and O(7). They

Table 9.4. Extinction determinations from H_2 line flux ratios.

Line ratio	λ_1 [μm]	λ_2 [μm]	$A_{\lambda_1} - A_{\lambda_2}$ [m]	A_V [m]
1–0 Q(1)/1–0 O(3)	2.4066	2.8025	0.67 ± 0.42	41 ± 26
1–0 Q(2)/1–0 O(4)	2.4134	3.0039	-0.19 ± 0.75	-9 ± 34
1–0 Q(3)/1–0 O(5)	2.4237	3.2350	0.13 ± 0.57	5 ± 22
1–0 Q(4)/1–0 O(6)	2.4475	3.5008	< 3.0	< 97
1–0 Q(5)/1–0 O(7)	2.4547	3.8074	1.34 ± 0.75	39 ± 22

are listed in Table 9.1 and shown in Fig. 9.2. All lines appear unbroadened at the SWS resolution, showing that they have a small (< 200 km s^{-1}) velocity dispersion and arise in a region much smaller than the beam size. Interestingly, we have detected four pairs of ro-vibrational lines which share the same upper energy level. The ratios of the fluxes for these lines should only depend upon the ratio of the transition probabilities and on extinction. Using the relation $A(\lambda_1) - A(\lambda_2) = 2.5 \log\left(\frac{I_2 \lambda_2 A_{ij,1}}{I_1 \lambda_1 A_{ij,2}}\right)$, with $A(\lambda)$ the extinction at wavelength λ, I the measured line flux and A_{ij} the Einstein A-coefficient, taken from Turner et al. (1977), we can determine the difference in extinction. We then use the extinction law by Fluks et al. (1994) to convert these to a value of A_V. The results of this procedure are listed in Table 9.4. The 1–0 Q(1)/1–0 O(3) and 1–0 Q(5)/1–0 O(7) line ratios give an extinction of about 40 magnitudes, whereas the 1–0 Q(2)/1–0 O(4) and 1–0 Q(3)/1–0 O(5) line ratios yield much lower values of A_V. Most likely this is because for these ratios the conversion from differential extinction to a value of A_V is erroneous because the 1–0 O(4) and 1–0 O(5) lines are located in the water ice band around 3 microns, prominent in T Tau, which is not included in the Fluks et al. extinction law. However, from the 1–0 Q(3) line flux measured with SWS we compute that a slab of H_2 emitting gas hidden behind the $A_V = 40^{\rm m}$ obtained from the 1–0 Q(1)/1–0 O(3) and 1–0 Q(5)/1–0 O(7) line ratios produces a factor of five less intense 1–0 S(1) radiation than what is observed from the ground. The only way to reconcile these conflicting results is to infer that in fact we are observing ro-vibrational H_2 emission from at least two distinct regions, of which one is heavily embedded ($A_V > 40^{\rm m}$), whereas the other only suffers little extinction. In view of the complex morphology seen in the ground-based 1–0 S(1) images, a scenario with multiple components does not seem unreasonable.

A useful representation of the H_2 data is to plot the log of $N(J)/g$, the apparent column density in a given energy level divided by its statistical weight, versus the energy of the upper level. This plot, in which the data have been corrected for extinction values of $A_V = 1\overset{\rm m}{.}39$ and $40\overset{\rm m}{.}0$ and in which high temperature equilibrium relative abundances of 3:1 for the ortho and para forms of H_2 have been assumed, is shown in Fig. 9.5. For clarity the 1–0 O(4) and O(5) lines, which we were not able to correct for extinction properly, are omitted from this figure. For a purely thermal population of the energy levels, all apparent column densities should lie on a nearly straight line in Fig. 9.5. The slope of this line is inversely proportional to the excitation temperature, while the intercept is a measure of the total column density of warm

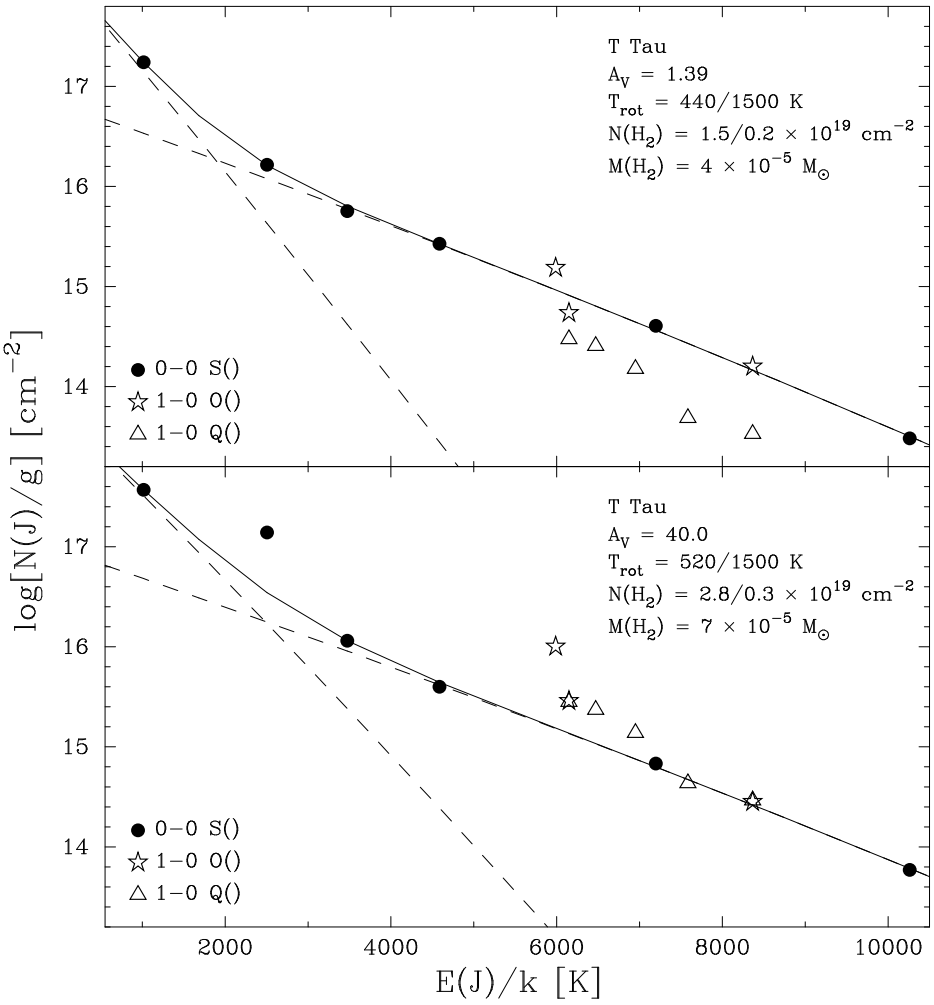

Fig. 9.5. H_2 excitation diagrams for T Tau, with the data corrected for extinction with $A_V = 1\overset{m}{.}39$ (top) and $A_V = 40\overset{m}{.}0$ (bottom). For most measurements, formal errors are about the size of the plot symbol. The dashed lines give the Boltzmann distribution fits to the two components of thermal H_2 emission. The solid line shows the sum of both components.

gas. A higher column of H_2 in the lower energy levels of a certain series than predicted by this straight line may be due to fluorescence by Lyα photons (e.g. Black & van Dishoeck 1987; Draine & Bertoldi 1996). Although this effect might also be expected in T Tau, previous observations failed to distinguish this unambiguously from the shocked component. Careful inspection of Fig. 9.5 shows that in T Tau we have detected two thermal sources of H_2 emission; one responsible for the lines with upper level energy higher than 3000 K and a much cooler component necessary to explain the strong 0–0 S(1) emission. In addition to this, the third component necessary to explain the ground-based near-infrared emission will also contribute to the lines below 3 μm. From Fig. 9.5 it also becomes immediately evident that the 0–0 S(3) line, at a wavelength within the amorphous silicate band, cannot suffer from great amounts of extinction, provided that the obscuring material contains silicates. The deviation of

the apparent column densities of the 1–0 O(2), O(3) and Q(1) lines from the straight line predicted by a purely thermal gas is clear evidence for the presence of the UV fluorescence mechanism.

Following the procedure outlined in Chapter 7 we have fitted a Boltzmann distribution to the two thermal H_2 components, resulting in excitation temperatures of 440 and 1500 K and column densities of 1.5 and 0.2 $\times$ 10^{19} cm^{-2}, respectively. This corresponds to a total H_2 mass of 4 $\times$ 10^{-5} $M_\odot$ or 13 earth masses within the SWS beam. The total molecular cloud mass, as derived from CO observations, is several orders of magnitude larger (Momose et al. 1996; Schuster et al. 1997). Therefore we conclude that an additional H_2 source must be present in the T Tau system, whose emission we have failed to detect because its temperature is much lower than the components we have detected here. This component will also contain the bulk of the H_2 mass. Note that this also implies that the bulk of the gas in the CO outflow must be very cool. This is consistent with the 40 K temperature of the outflow derived from ratios of CO line wings by Hogerheijde et al. (1998).

Warm molecular gas can either occur in a photo-dissociation region (PDR) or can be heated by shocks. A shock can either be a J-shock, sufficiently powerful to dissociate molecules, or be a C-shock, which cools mainly through molecular material. In Chapter 7 we employed predictions of H_2 emission from simple, plane parallel, PDR, J-shock and C-shock models (Burton et al. 1992; Hollenbach & McKee 1989; Kaufman & Neufeld 1996) to determine the excitation temperature from the low-lying pure rotational levels as a function of density n and either incident far-UV flux G or shock velocity v_s in an identical way as was done for the observations presented here. We arrived at the conclusion that the PDR and J-shock models allow a fairly small (200–540 K) range of excitation temperatures, whereas for C-shocks this range is much larger (100–1500 K). In the model predictions for shocks, $T_{\rm exc}$ does not depend much on density, whereas for PDRs it does not depend much on G. Once the mechanism of the H_2 emission is established, it can therefore be used to constrain v_s or n in a straightforward way.

This means that the 1500 K component can only be caused by a C- (i.e. non-dissociative) shock. From the correlation between excitation temperature and shock speed derived in Chapter 7, we derive a shock velocity of $\approx$ 35 km s^{-1} for the C-shock. The density and the extent of the shocked gas are poorly constrained. The total column of the 1500 K H_2 component is compatible with either a small ($<$ 5 square arcseconds) region of high ($\approx$ 10^6 cm^{-3}) density, or with a low-density ($\approx$ 10^4 cm^{-3}) region filling a significant fraction ($\approx$ 100 square arcseconds) of the SWS beam. The 440 K H_2 component falls in the parameter space allowed by either J-shock, C-shock and by PDR models. However, the uncertainty in the 440 K temperature is too large to be able to constrain these models any further. Comparison of the absolute line intensities with those predicted by PDR models (Black & van Dishoeck 1987; Draine & Bertoldi 1996) show that the 440 K component can be explained by photon heating if the PDR is located close to the system. These same PDR models are then also able to reproduce the observed UV fluorescence in a natural way. However, shock models can also produce the 440 K component, although current shock models do not include the physics

necessary to take into account the UV fluorescence mechanism.

9.7 Atomic fine structure lines

In the SWS and LWS spectra of T Tau we detected atomic fine-structure lines due to [Fe II], [Ar II], [Ne II], [S I], [Si II], [O I] and [C II]. All lines appear unbroadened at the SWS resolution, suggesting they have a velocity dispersion smaller than 200 km s^{-1} and arise in a region that is compact compared to the beam size. The [O I] 63 μm line was previously detected in T Tau from KAO observations (Cohen et al. 1988). The LWS line flux agrees with that measured by these authors in a 47″ aperture. In the LWS spectrum of T Tau, a line is present at the position of [O I] 146 μm, but in view of the strength of other CO lines in the spectrum we attribute most of the line flux to CO J=18–17 and only report an upper limit to the [O I] 146 μm line flux in Table 9.1. The deeper LWS spectrum of T Tau (Spinoglio et al. 1999) clearly separates the [O I] 146 μm line from the CO J=18–17 emission and a line flux of 8.2 $\times$ 10^{-16} W m^{-2} is derived.

The observed infrared spectrum of T Tau can either originate in a PDR or in one or more shocks. The detection of strong [S I] 25.3 μm emission in T Tau is important, since it is predicted to be weak in PDRs (e.g. Tielens & Hollenbach 1985). It can only reach observable strengths in shock-excited gas. Also, the absence of PAH emission in the SWS spectrum and the non-detection of [O I] emission in the LWS off-source observations argue against a PDR origin of the emission lines. Therefore our working hypothesis will be that the infrared fine structure lines are dominated by shocked gas. Ionized species like [Fe II], [Ne II], [Ar II] and [Si II] which we detected in T Tau cannot be produced in a C-shock, so we will explain those as arising in a J-shock.

We will try to determine the shock parameters by comparing the line fluxes listed in Table 9.1 with the J-shock models by Hollenbach & McKee (1989). From their Fig. 7 it can readily be seen that the ratios of the [O I] 63.2 μm, [Fe II] 26.0 μm and [S I] 25.3 μm lines constrain the density well, whereas [Ne II] 12.8 μm is particularly sensitive to shock velocity. A χ^2 fit of line fluxes ratios for T Tau to the Hollenbach & McKee J-shock models yielded a best fit shock velocity $v_s \approx 100$ km s^{-1}, and a density $n \approx 5 \times 10^4$ cm^{-3}. We estimate the errors in these fit parameters to be smaller than 20 km s^{-1} in velocity and smaller than 0.5 dex in density. To reproduce the absolute line fluxes, The J-shock needs to have an extent of 11 square arcseconds. This J-shock will also produce H_2 emission with the strength observed for the 440 K component identified in the previous section. Therefore we infer that this H_2 component is also due to the J-shock.

The line fluxes predicted by the Hollenbach & McKee J-shock models for the best fit parameters are also listed in Table 9.1. The fit gives satisfactory results, except for the [C II] 157.7 μm, [O I] 145.5 μm, and the [Fe II] lines. The background-corrected [C II] flux of 2.0 $\times$ 10^{-16} W m^{-2} is only half of that predicted by the J-shock model. However, the emergent [C II] flux is strongly dependent on the shock velocity. A model with v_s = 80 km s^{-1} would be able to reproduce the observed fine-structure spectrum, with the exception of [Ne II], which would then appear too strong. Since these differences are

within the error with which we think we can determine the shock velocity, we do not consider them significant. The deconvolved [O I] 145.5 μm flux of 8.2×10^{-16} W m^{-2} is 1.6 times that predicted by the J-shock model. However, this line appears stronger than model predictions in many regions where it is observed (e.g. Liseau et al. 1999), so the discrepancy might be caused by a poor knowledge of the atomic data and/or an inadequate understanding of the atomic processes of the oxygen atom. The mismatch of the J-shock model to the [Fe II] fluxes might be more worrisome. The Hollenbach & McKee models predict the 26.0 μm line to be the strongest of the three throughout the parameter space, whereas we observe the 35.3 μm line to be significantly stronger. At present this result lacks a satisfactory explanation.

9.8 Discussion and conclusions

From the previous sections a complex picture of the T Tau environment emerges. The ISO spectra presented here show evidence for a dusty disk or envelope, an ionized stellar wind, three distinct sources of H_2 emission, and warm atomic gas in dissociative and non-dissociative shocks. What is the origin of all these phenomena? Literature data show that both T Tau N and T Tau S have a circumstellar disk or envelope containing dust and that a dusty circumbinary envelope is present as well. Clearly the continuum data presented here arise in the superposition of these phenomena, with T Tau N dominating at the shortest wavelengths studied here, T Tau S dominant in most of the spectrum, and a contribution of the circumbinary envelope that increases with wavelength. We have seen that the composition of the circumstellar material is by no means unusual: amorphous silicates, water and carbon-dioxide ice and gaseous CO in fairly typical proportions. We derive an extinction of $17\overset{\mathrm{m}}{.}4 \pm 0\overset{\mathrm{m}}{.}6$ in this dust shell. This result resolves the discrepancy between earlier determinations and the $A_V > 7^{\mathrm{m}}$ from the non-detection of T Tau S in HST images (Stapelfeldt et al. 1998). We also found all infrared data to be consistent with a scenario in which T Tau N is constant and T Tau S shows strong wavelength-independent variations in brightness.

The H I data presented in Section 9.5 point to T Tau N as the sole contributing source to these lines. Because our data on these recombination lines extend further to the infrared than previous studies, this does have implications for the mechanism responsible for the radio emission in T Tau S. A scenario in which the continuum radio flux of T Tau S is due to an ionized wind, of which the H I lines are hidden by many magnitudes of extinction is now definitely ruled out by our non-detection of lines from the Pfund and Humphreys series. The outflow shock model to produce non-thermal gyrosynchrotron radiation (Skinner & Brown 1994; Ray et al. 1997) seems more likely and may also be responsible for part of the T Tau N radio flux.

We have distinguished three sources of H_2 emission in our ISO spectra: A cool ($\sim$ 440 K) component suffering little extinction, and two warmer ($\approx$ 1500 K) components, of which one suffers little extinction and the other probably is heavily extincted ($A_V > 40^{\mathrm{m}}$). The far-infrared CO, H_2O and OH emission from T Tau discussed by Spinoglio et al. (1999) show evidence for similar cool and warm temperature components (although

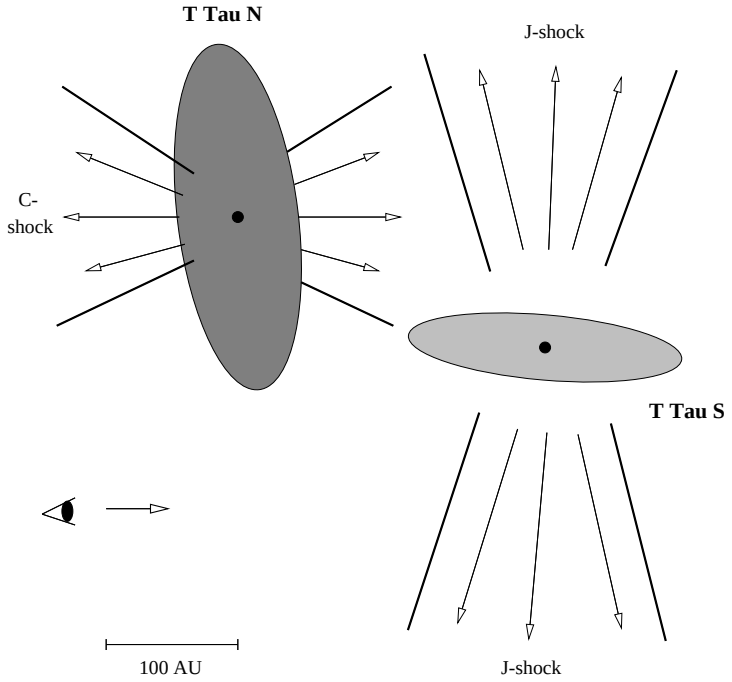

Fig. 9.6. Schematic picture of the T Tau system with probable sources of C-shock (H_2, [S I]) and J-shock (H_2, [S I], [O I], [Fe II], [Ar II], [Ne II], [Si II], [C II]) emission indicated.

OH and H_2O appear overabundant), supporting the picture outlined here. In Sections 9.6 and 9.7 we showed that the cool component can be identified with a dissociative shock or PDR, whereas the non-embedded warm component could be due to a non-dissociative shock. In studying the infrared images by Herbst et al. (1996) we note that the dominant region of [Fe II] 1.64 μm emission is around the H_2 knot T Tau NW. The size of this region is only slightly smaller than the size of 11 square arcseconds required by our J-shock. Therefore we identify T Tau NW as a J-shock in the outflow from T Tau S. Most likely it is a knot in a non-steady outflow, similar to Herbig-Haro objects. The remainder of the shocked ionized emission probably arises from the fainter H_2/[Fe II] knot T Tau SE, which could be a similar knot in the other lobe of the same outflow. The low velocities of these components measured in CO, as well as the morphology and the kinematics of the optical forbidden emission lines suggest that it has an orientation nearly perpendicular ($i \approx 79°$; Solf & Böhm 1999) to our line of sight. It could also drive the giant Herbig-Haro outflow HH 355 (Reipurth et al. 1997).

The location of the C-shock is less clear. Both the "diffuse" and the "west jet" component distinguished by Herbst et al. (1996) have an extent that could produce the required beam filling factor. By comparing the ground-based H_2 imaging results (Herbst et al. 1996; van Langevelde et al. 1994b; Quirrenbach & Zinnecker 1997) with the CO maps of the region by Momose et al. (1996), we note that the "diffuse" component can very well be due to the low-velocity outflow with small ($\approx 10°$) inclination angle, presumably arising in T Tau N. Such an outflow could easily produce a C-shock with a large beam filling factor. Therefore we tentatively identify our C-shock with the "diffuse" component, although some contribution from the "west jet" might also be

present. A schematic picture of the T Tau system in which we have identified the most likely sources of the detected infrared line emission is shown in Fig. 9.6.

A remarkable result is the clear signature of the UV fluorescence mechanism in the ro-vibrational H_2 lines. To explain this, an H_2 containing area that is seeing a fairly high number of Lyα photons needs to be present in the T Tau system. However, the low [C II] flux indicates that this area seems to be heated to lower temperatures than predicted by standard PDR models (e.g. Tielens & Hollenbach 1985). This could for example be due to a depletion of small dust particles in the area, consistent with the absence of PAH emission in the SWS spectrum.

We have also found indications for the presence of H_2 emission from a warm, embedded source. In the T Tauri system, only T Tau S suffers significant amounts of extinction, possibly because the line of sight towards T Tau S passes through the outer edge of the T Tau N disk. Therefore it seems likely that this H_2 component comes from a region in the envelope or disk of T Tau S. An interesting possibility is that we are picking up emission from the shock caused by the impact of circumstellar matter onto the circumstellar disk of T Tau S. If this picture is correct, future H_2 images in e.g. the 1–0 O(5) line should show a morphology that is more concentrated towards T Tau S than the existing 1–0 S(1) data.

The complex situation in the circumstellar environment of T Tau, with multiple outflows and a multitude of shocks, is reminiscent of the situation in the intermediate-mass young stellar object LkHα 225 (Chapter 8). The infrared emission line spectrum of T Tau is also strikingly similar to that of LkHα 225. Interestingly, both LkHα 225 and T Tau are young binary systems containing an optically invisible intermediate-mass component. It could therefore very well be that these properties that make the T Tau system so unique are not so much related to the central sources, but more to the interaction of the circumstellar disks and outflows with the accretion of matter through a circumbinary disk or envelope.

Acknowledgements. This chapter is based on observations with ISO, an ESA project with instruments funded by ESA Member States (especially the PI countries: France, Germany, the Netherlands and the United Kingdom) and with the participation of ISAS and NASA. The authors would like to thank M.R. Hogerheijde for useful discussions on the nature of T Tau. We are also especially grateful to Th. de Graauw for his generous allocation of guaranteed and discretionary time for the ISO-SWS observations presented here.

References

Akeson, R.L., Koerner, D.W., Jensen, E.L.N. 1998, ApJ 505, 358
Beckwith, S., Gatley, I., Matthews, K., Neugebauer, G. 1978, ApJ 223, L41
Black, F.H., van Dishoeck. E.F. 1987, ApJ 322, 412
Boogert, A.C.A. 1999, PhD thesis, Groningen University
Boogert, A.C.A., Schutte, W.A., Helmich, F.P., Tielens, A.G.G.M., Wooden, D.H. 1997, A&A 317, 929
Brown, A., Jordan, C., Millar, T.J., Gondhalekar, P., Wilson, R. 1981, Nature 290, 34
Burton, M.G., Hollenbach, D.J., Tielens, A.G.G.M. 1992, ApJ 399, 563

Calvet, N., Hartmann, L., Kenyon, S.J., Whitney, B.A. 1994, ApJ 434, 330
Clegg, P.E., Ade, P.A.R., Armand, C. et al. 1996, A&A 315, L38
Cohen, M., Hollenbach, D.J., Haas, M.R., Erickson, E.F. 1988, ApJ 329, 863
Dartois, E., d'Hendecourt, L., Boulanger, F., Jourdain de Muizon, M., Breitfellner, M., Puget, J.L., Habing, H.J. 1998, A&A 331, 651
de Graauw, Th., Haser, L.N., Beintema, D.A., Roelfsema, P.R. et al. 1996, A&A 315, L49
Dorschner, J., Begemann, B., Henning, Th., Jäger, C., Mutschke, H. 1995, A&A 300, 503
Draine, B.T., Bertoldi, F. 1996, ApJ 468, 269
Dyck, H.M., Simon, T., Zuckerman, B. 1982, ApJ 255, 103
Edwards, S., Snell, R.L. 1982, ApJ 261, 151
Evans, N.J., Levreault, R.M., Beckwith, S., Skrutskie, M. 1987, ApJ 320, 364
Fluks, M.A., Plez, B., Thé, P.S., de Winter, D., Westerlund, B.E., Steenman, H.C. 1994, A&AS 105, 311
Gerakines, P.A., Schutte, W.A., Greenberg, J.M., van Dishoeck, E.F. 1995, A&A 296, 810
Ghez, A.M., Neugebauer, G., Gorham, P.W., Haniff, C.A., Kulkarni, S.R., Matthews, K., Koresko, C., Beckwith, S. 1991, AJ 102, 2066
Ghez, A.M., Weinberger, A.J., Neugebauer, G., Matthews, K., McCarthy, D.W. 1995, AJ 110, 753
Gorham, P.W., Ghez, A.M., Haniff, C.A., Kulkarni, S.R., Matthews, K., Neugebauer, G. 1992, AJ 103, 953
Hanner, M.S., Brooke, T.Y., Tokunaga, A.T. 1998, ApJ 502, 871
Helmich, F.P., van Dishoeck, E.F., Black, J.H. et al. 1996, A&A 315, L173
Herbst, W., Booth, J.F., Chugainov, P.F. et al. 1986, ApJ 310, L71
Herbst, T.M., Beckwith, S.V.W., Glindemann, A., Tacconi-Garman, L.E., Kroker, H., Krabbe, A. 1996, AJ 111, 2403
Herbst, T.M., Robberto, M., Beckwith, S.V.W. 1997, AJ 114, 744
Hodapp, K.W. 1994, ApJS 94, 615
Hogerheijde, M.R., van Langevelde, H.J., Mundy, L.G., Blake, G.A., van Dishoeck, E.F. 1997, ApJ 490, L99
Hogerheijde, M.R., van Dishoeck, E.F., Blake, G.A., van Langevelde, H.J. 1998, ApJ 502, 315
Hollenbach, D.J., McKee, C.F. 1989, ApJ 342, 306
Kaufman, M.J., Neufeld, D.A. 1996, ApJ 456, 611
Kenyon, S.J., Dobrzycka, D., Hartmann, L. 1994, AJ 108, 1872
Kenyon, S.J., Hartmann, L. 1995, ApJS 101, 117
Kessler, M.F., Steinz, J.A., Anderegg, M.E. et al. 1996, A&A 315, L27
Knapp, G.R., Kuiper, T.B.H., Knapp, S.L., Brown, R.L. 1977, ApJ 214, 78
Kobayashi, N., Nagata, T., Hodapp, K.W., Hora, J.L. 1994, PASJ 46, L183
Kuhi, L.V. 1964, ApJ 140, 1409
Leech, K. et al. 1997, *"SWS Instrument Data Users Manual"*, Issue 3.1, SAI/95-221/Dc
Levreault, R.M. 1988, ApJS 67, 283
Liseau, R., White, G.J., Larsson, B. et al. 1999, A&A 344, 342
Maihara, T., Kataza, H. 1991, A&A 249, 392
Momose, M., Ohashi, N., Kawabe, R., Hayashi, M., Nakano, T. 1996, ApJ 470, 1001
Nisenson, P., Stachnik, R.V., Karovska, M., Noyes, R. 1985, ApJ 297, L17
Persson, S.E., Geballe, T.R., McGregor, P.J., Edwards, S., Lonsdale, C.J. 1984, ApJ 286, 289
Quirrenbach, A., Zinnecker, H. 1997, The Messenger 87, 36
Ray, T.P., Muxlow, T.W.B., Axon, D.J., Brown, A., Corcoran, D., Dyson, J., Mundt, R. 1997, Nature 385, 415

Reipurth, B., Bally, J., Devine, D. 1997, AJ 114, 2708
Robberto, M., Clampin, M., Ligori, S., Paresce, F., Saccà, V., Staude, H.J. 1995, A&A 296, 431
Rothmann, L.S., Gamache, R.R., Tipping, R.H. et al. 1996, J. Quant. Spectr. Radiat. Transfer 48, 469
Schwartz, P.R., Simon, T., Campbell, R. 1986, ApJ 303, 233
Schuster, K.F., Harris, A.I., Russell, A.P.G. 1997, A&A 321, 568
Shiba, H., Sato, S., Yamashita, T., Kobayashi, Y., Takami, H. 1993, ApJS 89, 299
Simon, M., Felli, M., Cassar, L., Fischer, J., Massi, M. 1983, ApJ 266, 623
Simon, M., Longmore, A.J., Shure, M.A., Smillie, A. 1996, ApJ 456, L41
Skinner, S.L., Brown, A. 1994, AJ 107, 1461
Solf, J., Böhm, K.H. 1999, ApJ, in press
Spinoglio, L., Giannini, T., Nisini, B., Pezzuto, S., Saraceno, P., Di Giorgio, A.M., Palla, F., Caux, E., Ceccarelli, C., Lorenzetti, D., Smith, H.A., van den Ancker, M.E., White, G.J. 1999, A&A, submitted
Stapelfeldt, K.R., Burrows, C.J., Krist, J.E. et al. 1998, ApJ 508, 736
Storey, P.J., Hummer, D.G. 1995, MNRAS 272, 41
Tielens, A.G.G.M., Allamandola, L.J. 1987, in *"Interstellar Processes"*, eds. D.J. Hollenbach & H.A. Thronson Jr. (Dordrecht: Reidel), p. 397
Tielens, A.G.G.M., Hollenbach, D.J. 1985, ApJ 291, 722
Trams, N. et al. 1997, *"ISO-LWS Instrument Data Users Manual"*, Issue 5.0, SAI/95-219/Dc
Turner, J., Kirby-Docken, K., Dalgarno, A. 1977, ApJS 35, 281
van Cleve, J.E., Hayward, T.L., Miles, J.W., Gull, G.E., Schoenwald, J., Houck, J.R. 1994, Ap&SS 212, 239
van Dishoeck, E.F., Helmich, F.P. 1996, A&A 315, L177
van Langevelde, H.J., van Dishoeck, E.F., Blake, G.A. 1994a, ApJ 425, L45
van Langevelde, H.J., van Dishoeck, E.F., van der Werf, P.P., Blake, G.A. 1994b, A&A 287, L25
Weintraub, D.A., Kastner, J.H., Zuckerman, B., Gatley, I. 1992, ApJ 391, 784
Weintraub, D.A., Sandell, G., Huard, T.L., Kastner, J.H., van den Ancker, M.E., Waters, L.B.F.M. 1999, ApJ 517, 819
Whitney, B.A., Hartmann, L. 1993, ApJ 402, 605
Whittet, D.C.B., Schutte, W.A., Tielens, A.G.G.M. et al. 1996, A&A 315, L357
Wichmann, R., Bastian, U., Krautter, J., Jankovics, I., Ruciński, S.M. 1998, MNRAS 301, L43

Chapter 10

ISO Spectroscopy of PDRs and Shocks in Star Forming Regions

M.E. van den Ancker, A.G.G.M. Tielens and P.R. Wesselius,
A&A, to be submitted (1999)

Abstract

We present the results of ISO SWS and LWS grating scans of pure rotational lines of H_2, as well as the infrared fine structure lines of [C II], [O I], [S I], [Si II], [Fe I] and [Fe II] towards galactic star forming regions. We find that intense H_2 emission is only observed in the vicinity of stars with spectral type earlier than B4 or in the neighbourhood of embedded YSOs associated with outflows. We interpret these lines as arising in either a photo-dissociation region (PDR) near the early-type stars, or a shock caused by the interaction of an outflow with the surrounding molecular cloud material. Molecular hydrogen excitation temperatures and fine structure line intensities were compared with those predicted by theoretical models for PDRs and dissociative and non-dissociative shocks and to those observed towards regions known to contain PDRs and shocks. It is shown that both shocks and PDRs show a warm and hot component in H_2. The observed temperatures of the warm component appear in general too high to be explained by current dissociative shock models. We find that the mere detection of [S I] 25.2 μm emission with ISO is an unambiguous sign of the presence of shocked gas. Strong [C II] 157.7 μm can only be due to a PDR. An evolutionary scenario is suggested in which the circumstellar material around a young star changes from being heated mechanically by shocks into heated by radiation from the central star through a PDR as the star clears its surroundings.

10.1 Introduction

The infrared emission-line spectrum of Young Stellar Objects (YSOs) is dominated by the interaction of the central object with the remnants of the clouds from which it

formed. The intense UV radiation generated by accretion as well as by the central star itself causes dissociation of molecular material close to the YSO and ionizes much of the atomic material, giving rise to typical nebular and recombination lines. The strong stellar wind, often collimated into a bipolar outflow, will cause a shock wave as it hits the surrounding molecular cloud, heating the post-shock gas sufficiently to cause strong molecular and ionic emission.

Neutral clouds irradiated by far-ultraviolet (FUV) photons are known as photodissociation regions (PDRs; see Hollenbach & Tielens 1999 for a comprehensive review). In these regions, heating of the gas occurs by collisions of photoelectrically ejected electrons from grain surfaces. Cooling of the gas occurs mainly through emission in atomic fine-structure and molecular lines, reaching intensities that should be easily observable in a wide range of astronomical objects. The gas in the surface regions of these PDRs reaches temperatures of typically 500 K (e.g. Tielens & Hollenbach 1985), making it possible to collisionally excite the low-lying pure rotational levels of molecular hydrogen, provided that the region has a sufficient density and incident FUV flux. Since the lowest ro-vibrational lines of H_2 have energy levels of the order of 5000 K, only these low-lying pure rotational H_2 lines, hard to observe from the ground, can reliable probe the physical conditions of the dominant species and thus provide us with detailed information of the physical conditions occurring in the PDR.

The physical situation in shock waves is quite distinct: here the molecular gas is heated by compression of a supersonic wave moving through the gas. Shocks are usually divided into two distinct categories: J- or Jump-shocks, and C- or Continuous-shocks. In the J-shocks viscous heating of the neutrals occurs in a thin shock front in which radiative cooling is insignificant, and the post-shock gas is heated to several times 10^4 degrees (e.g. Hollenbach & McKee 1989), dissociating all molecular material. In these J-shocks, the physical conditions (density, temperature) change from their pre- to post-shock values within one mean free path, causing an apparent discontinuity. Cooling of the post-shock gas occurs trough atomic fine-structure lines.

C-shocks are magnetized, non-dissociative shocks in which ions and the magnetic field are compressed ahead of the shock front and are able to heat the neutral gas (containing only a trace fraction of ions) to a few thousand degrees. In C-shocks the physical conditions change more gradually from their pre- to post-shock values and cooling is mainly through radiation from molecular material (e.g. Kaufman & Neufeld 1996). If the temperatures in a C-shock become sufficiently high to start to dissociate molecules, the cooling through the molecular lines goes down, and the shock temperature increases until it turns into a J-shock. Shocks with a velocity larger than 40 km s^{-1} are usually J-shocks, whereas slower shocks are usually of C-type (Chernoff et al. 1982).

In this chapter we will study the infrared emission-line spectra of a sample of YSOs observed with the *Infrared Space Observatory* (ISO; Kessler et al. 1996). In order to interpret our observations as arising in either a PDR, C-Shock or J-shock, we compare measured line intensities with those predicted by theoretical models of such regions. Since the regions surrounding our target sources are often highly confused, and the applicability of the simplified models to a complex physical situation is by no means sure, we will also compare our new ISO observations with those of relatively clean regions

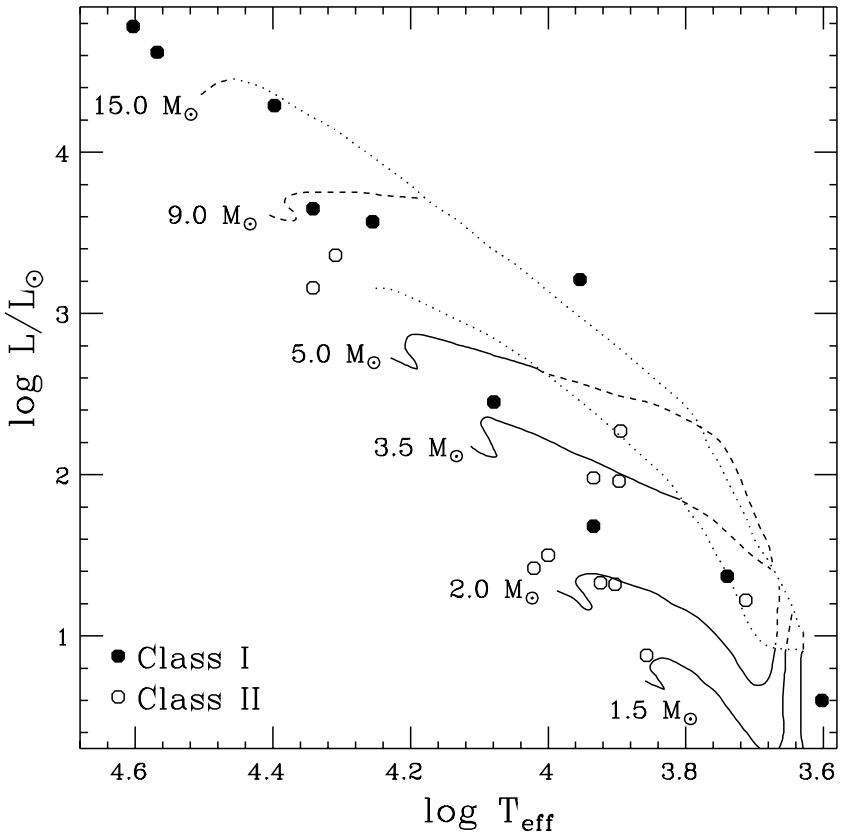

Fig. 10.1. Hertzsprung-Russell diagram for the YSOs included in this study. Filled and open plot symbols indicate Class I and II sources, respectively. Also shown are theoretical PMS evolutionary tracks (solid/dashed lines) and the birthlines for 10^{-4} (upper dotted line) and 10^{-5} $M_\odot$ yr^{-1} (lower dotted line) by Palla & Stahler (1993).

known to contain a shock or a PDR. We will show that the distinction between a shock and a PDR spectrum can be made with relative ease and the infrared lines are a good diagnostic tool for constraining the physical conditions in the material surrounding YSOs.

10.2 Sample selection

Young stellar objects are commonly divided into classes depending on their energy distribution. Class I YSOs are heavily embedded, optically invisible, but usually infrared bright objects. Class II YSOs are already optically visible, but also still show excess infrared emission above photospheric levels due to dust, heated by the central star, in the direct circumstellar environment. Intermediate-mass (2–10 $M_\odot$) Class II YSOs are usually referred to as Herbig stars, whereas their lower mass counterparts are the T Tauri stars. In the remainder of this chapter we will study the infrared emission line spectra in the vicinity of a sample of 10 Class I YSOs and 11 Class II sources. They are listed in Table 10.1. Because of the brightness limitations imposed by the instruments

Table 10.1. Properties of programme stars.

Source	α (2000)	δ (2000)	Region	d [pc]	Ref.	Sp. Type	$T_{\rm eff}$ [K]	Ref.	Outflow	A_V [m]	$\log L/L_\odot$	$M_\star$ [$M_\odot$]	Age [yr]
AFGL 490	03 27 38.6	+58 47 00	Cam OB1	900	(1)	B1–6e	18000	(13)	$\surd$	≈ 31	3.57	≈ 8	–
IRAS03260+3111	03 29 10.4	+31 21 58	NGC 1333	350	(2)		12000	(14)	–	≈ 20	2.45	≈ 4	–
L1489 IRS	04 04 43.0	+26 18 58	L1491	140	(3)	$>$ Ke	4000	(15)	$\surd$	≈ 20	0.60	< 2	–
L1551 IRS5	04 31 34.0	+18 08 04	Tau R2	140	(3)	G–Ke	5500	(15)	$\surd$	≈ 19	1.37	≈ 3	–
IRAS12496−7650	12 53 16.0	−77 07 02	Cha II	180	(4)	Ae	8600	(16)	$\surd$	≈ 14	1.68	≈ 2.5	–
GGD 27-ILL	18 19 12.0	−20 47 31	IC 1318	1700	(5)	B1	25000	(17)	$\surd$	≈ 20	4.29	≈ 14	–
LkHα 225	20 20 30.4	+41 21 27	Cyg R1	1000	(6)	A–Fe	9000	(18)	$\surd$	≈ 15	3.21	≈ 7	–
S106 IRS4	20 27 26.6	+37 22 48	Cyg OB2	1200	(7)	O6–O8e	37000	(19)	–	≈ 14	4.62	≈ 20	–
AFGL 2591	20 29 24.6	+40 11 19	Cyg X	1700	(8)	$<$ O8	40000	(20)	$\surd$	≈ 30	4.78	≈ 25	–
Cep A East	22 56 18.6	+62 02 00	Cep OB3	690	(9)	B:	22000	(20)	$\surd$	≈ 62	3.65	≈ 9	–
Elias 3-1	04 18 40.5	+28 19 17	L1495	140	(3)	A6:e	8000	(21)	–	7.83	1.32	2.0	3×10^6
T Tau	04 21 59.1	+19 32 06	Tau R2	140	(3)	K0–1e	5200	(22)	$\surd$	1.39	1.22	2.5	$< 10^6$
HD 97048	11 08 04.6	−77 39 17	Ced 111	180	(10)	B9.5Ve	10000	(23)	–	1.27	1.50	2.5	$\geq 3 \times 10^6$
HD 97300	11 09 50.6	−76 36 47	Ced 112	190	(10)	B9V	10500	(24)	–	1.33	1.42	2.4	$\geq 3 \times 10^6$
HR 5999	16 08 34.2	−39 06 18	Lupus 3	210	(10)	A5–7IIIe	7900	(25)	–	0.47	1.96	3.2	5×10^5
R CrA	19 01 53.9	−36 57 10	NGC 6729	130	(11)	A1–F7ev	8600	(10)	$\surd$	2.26	1.98	3.0	1×10^6
T CrA	19 01 58.8	−36 57 49	NGC 6729	130	(11)	F0e	7200	(26)	$\surd$	1.64	0.88	1.5	1×10^7
WW Vul	19 25 58.6	+21 12 31	Vul R1	440	(12)	A4IV–Ve	8400	(27)	–	0.96	1.33	2.0	5×10^6
BD+40° 4124	20 20 28.3	+41 21 51	Cyg R1	1000	(6)	B2Ve	22000	(17)	–	3.01	3.16	7.0	$\geq 10^5$
LkHα 224	20 20 29.2	+41 21 27	Cyg R1	1000	(6)	A7e	7900	(28)	–	2.98	2.27	4.0	1×10^5
HD 200775	21 01 36.8	+68 09 49	NGC 7023	430	(10)	B2.5IVe	20400	(29)	$\surd$	1.92	3.36	9.0	2×10^7

References to Table 10.1: (1) Harvey et al. (1979); (2) Herbig & Jones (1983); (3) Kenyon et al. (1994); (4) Whittet et al. (1997); (5) Rodríguez et al. (1980); (6) Shevchenko et al. (1991); (7) Rayner (1994); (8) Dame & Thaddeus (1985); (9) Mel'nikov et al. (1995); (10) Chapter 2; (11) Marraco & Rydgren (1981); (12) Voshchinnikov (1981); (13) Snell et al. (1984); (14) This chapter; (15) Kenyon et al. (1998); (16) Hughes et al. (1991); (17) Yamashita et al. (1987); (18) Hillenbrand et al. (1995); (19) Chapter 7; (20) Lada et al. (1984); (21) Zinnecker & Preibisch (1994); (22) Kenyon & Hartmann (1995); (23) Whittet et al. (1987); (24) Rydgren (1980); (25) Tjin A Djie et al. (1989); (26) Finkenzeller & Mundt (1984); (27) Gray & Corbally (1998); (28) Chapter 8; (29) Rogers et al. (1995).

used, the sample is biased towards infrared bright objects, either because they are inherently anomalously luminous in the infrared or because they are located relatively nearby.

To understand the occurrence of infrared emission lines due to PDRs or shocks in the vicinity of the stars in our sample, it is useful to study their basic properties in a consistent way. We have therefore made new estimates of the bolometric luminosity of each source by constructing spectral energy distributions (SEDs), using ultraviolet to submm data compiled from literature. A fit consisting of the sum of a reddened Kurucz (1991) model for the stellar photosphere and a spline fitted to the excesses in the infrared to submm range, extrapolated to infinity by a blackbody curve, was made to the energy distribution for each source. Total bolometric luminosities were then determined by computing $4\pi d^2 \int F_\lambda \mathrm{d}\lambda$, with d the distance to the source and F_λ the SED fit. The results of this procedure, as well as the distances and effective temperatures used, are listed in Table 10.1. For the extincted sources the resulting values of $L_{\rm bol}$ do not depend on the adopted value of $T_{\rm eff}$.

From the results listed in Table 10.1 we have created the Hertzsprung-Russell diagram (HRD) shown in Fig. 10.1. In this figure, we also have plotted the pre-main sequence evolutionary tracks and the birthline by Palla & Stahler (1993). By comparing the location of a source in the HRD with these computations, we can determine stellar masses and ages for pre-main sequence stars. For single Class II sources the required parameters (luminosity and temperature) can be determined fairly accurately. For the Class I sources, the temperature is usually not well determined, but since the luminosity of an intermediate-mass star stays relatively constant during its contraction to the zero-age main sequence, the evolutionary tracks can still be used to estimate its mass. Resulting stellar masses and ages are also listed in Table 10.1.

10.3 Observations

Using the Short (SWS: 2.4–45 μm; de Graauw et al. 1996) and Long Wavelength (LWS: 43–197 μm; Clegg et al. 1996) Spectrometers on board ISO, we obtained spectroscopy of infrared transitions of H_2, [Fe I], [Fe II], [S I], [Si II], [O I] and [C II] centered on the positions of the 21 young stellar objects listed in Table 10.1. Most of the lines in the SWS wavelength range were scanned with the full grating resolution ("AOT S02"), although in some objects some were taken from lower resolution full grating scans ("AOT S01"). When the latter were available, we also report the flux in the 6.2 μm UIR band in Table 10.3. All lines in the LWS wavelength range were obtained from LWS full grating scans ("AOT L01"). A full log of the ISO observations used in this study is given in Table 10.2.

Data were reduced in a standard fashion using calibration files corresponding to ISO off-line processing software (OLP) version 7.0, after which they were corrected for remaining fringing and glitches. To increase the S/N in the final spectra, detectors were aligned and statistical outliers were removed, after which the spectra were rebinned to a lower spectral resolution (SWS) or simply averaged (LWS).

Table 10.2. Log of ISO observations of programme stars.

Object	AOT	Rev.	Date	JD−2450000
AFGL 490	SWS 02	863	27/03/1998	899.939
	LWS 01	623	31/07/1997	660.879
IRAS03260+3111	SWS 01	659	05/09/1997	696.880
	LWS 01	848	12/03/1998	884.909
L1489 IRS	SWS 02	654	31/08/1997	691.635
L1551 IRS5	SWS 02	668	14/09/1997	705.561
	LWS 01	668	14/09/1997	705.571
IRAS12496−7650	SWS 02	141	06/04/1996	179.909
	LWS 01	115	11/03/1996	153.678
GGD27-ILL	LWS 01	148	13/04/1996	187.161
	SWS 02	149	14/04/1996	187.595
	SWS 01	149	14/04/1996	187.621
LkHα 225	SWS 02	142	07/04/1996	180.996
	SWS 02	355	05/11/1996	393.306
	SWS 01	858	22/03/1998	894.889
	LWS 01	142	07/04/1996	181.017
S106 IRS4	SWS 02	134	30/03/1996	172.705
	LWS 01	134	30/03/1996	172.726
	SWS 01	335	17/10/1996	373.740
AFGL 2591	SWS 02	134	30/03/1996	172.577
	LWS 01	142	07/04/1996	180.737
Cep A East	SWS 02	220	23/06/1996	258.463
	LWS 01	566	04/06/1997	603.681
	SWS 02	566	04/06/1997	603.706
	SWS 01	843	07/03/1998	880.050
Elias 3-1	SWS 02	667	13/09/1997	704.605
T Tau	LWS 01	672	18/09/1997	709.675
	SWS 01	680	25/09/1997	717.411
	SWS 02	681	27/09/1997	718.778
	SWS 02	861	25/03/1998	897.973
HD 97048	SWS 01	141	06/04/1996	179.947
	LWS 01	261	04/08/1996	299.565
HD 97300	SWS 02	141	06/04/1996	179.826
HR 5999	SWS 01	289	01/09/1996	327.627
	SWS 02	289	01/09/1996	327.669
R CrA	LWS 01	495	25/03/1997	533.284
	SWS 02	704	19/10/1997	741.322
	SWS 01	704	19/10/1997	741.353
T CrA	SWS 02	141	06/04/1996	179.738
	SWS 01	689	04/10/1997	726.278
WW Vul	SWS 01	176	11/05/1996	214.507
	SWS 02	176	11/05/1996	214.541
	SWS 02	865	29/03/1998	901.889
BD+40°4124	SWS 02	142	07/04/1996	181.037
	SWS 02	159	24/04/1996	197.635
	SWS 01	355	05/11/1996	393.283
	LWS 01	768	23/12/1997	805.525
LkHα 224	SWS 02	142	07/04/1996	180.960
	SWS 01	858	22/03/1998	894.920
HD 200775	SWS 02	143	08/04/1996	182.108
	SWS 01	339	21/10/1996	377.670
	LWS 01	339	21/10/1996	377.695

Scanned lines and measured line fluxes for the detected lines or upper limits (total flux for line with peak flux 3σ) for the undetected lines are listed in Table 10.3. In a number of sources the H_2 0–0 S(2) line was not detected because of strong fringing of the continuum in this part of the spectrum, either due to the continuum source being spatially extended, or due to the continuum source not being in the center of the beam. The H_2 0–0 S(6) line has a wavelength that puts it the middle of the H_2O ν_2 absorption band, also hindering its detection in some sources (c.f. Chapter 8).

Accuracies of the absolute flux calibration in the SWS spectra range from 7% in the short-wavelength (< 4.10 μm) part to $\approx 30\%$ in the long wavelength (> 29 μm) part (Leech et al. 1997). The LWS absolute flux calibration is expected to be accurate at the 7% level (Trams et al. 1997). The errors listed in Table 10.3 include both the error in the line flux measurement itself and this absolute error. Note that the applied flux calibration is based on the assumption that we are looking at a point source. For an extended source, the diffraction losses will be underestimated and, in particular at the long-wavelength part of the LWS, these corrections will exceed the quoted uncertainty.

10.4 Molecular hydrogen emission

From the H_2 line fluxes $I(J)$ listed in Table 10.3 it is possible to calculate the apparent column densities of molecular hydrogen in the upper J levels, averaged over the SWS beam, $N(J)$, using $N(J) = \frac{4\pi I(J)}{A}\frac{\lambda}{hc}$, with λ the wavelength, h Planck's constant and c the speed of light. The transition probabilities A were taken from Turner et al. (1977). Line fluxes were corrected for extinction using the average interstellar extinction law by Fluks et al. (1994) using the values compiled in Table 10.1.

A useful representation of the H_2 data is then to plot the log of $N(\mathrm{J})/\mathrm{g}$, the apparent column density for a given J upper level divided by the statistical weight, versus the energy of the upper level. The resulting excitation diagrams are shown in Fig. 10.2. For a Boltzmann distribution, the points in Fig. 10.2 should form a nearly straight line. The slope of this line is inversely proportional to the excitation temperature, while the intercept is a measure of the total column density of warm gas. Since the A coefficients for the H_2 lines are quite small, these lines are optically thin and, because the critical densities are low, the excitation temperature will be close to the kinetic temperature of the gas.

The statistical weight g is a combination of the rotational and nuclear spin components. For this, we have assumed the high temperature equilibrium relative abundances of 3:1 for the ortho and para forms of H_2 (Burton et al. 1992a). From Fig. 10.2 it is apparent that for most sources, the H_2 points below 5000 K do indeed form a straight line in the excitation diagram. The fact that the points for ortho and para H_2 lie on the same line proves that our assumption on their relative abundances is correct.

Using the formula by Parmar et al. (1991) and the rotational constants by Dabrowski (1984), we have fitted Boltzmann distributions to the low-lying pure rotational lines. For a number of sources, the pure rotational lines at the higher energy levels can be

Table 10.3. Observed and extinction-corrected line fluxes (in 10^{-16} W m^{-2}).

Line	λ	Beam	AFGL 490		IRAS03260+3111		L1489 IRS		L1551-IRS5		IRAS12496−7650	
	[μm]	[10^{-8} sr]	Obs.	Ext. corr.	Obs.	Ext. Corr.	Obs.	Ext. Corr.	Obs.	Ext. Corr.	Obs.	Ext. Corr.
H_2 0–0 S(0)	28.2188	1.64	$<$ 39.9	$<$ 40.3	$<$ 5.65	$<$ 5.71	$<$ 5.59	$<$ 5.64	$<$ 20.6	$<$ 20.8	$<$ 7.89	$<$ 7.97
H_2 0–0 S(1)	17.0348	1.15	$<$ 16.9	$<$ 17.2	16.6±3.6	16.9±3.6	$<$ 1.07	$<$ 1.09	$<$ 1.94	$<$ 1.97	1.11±0.36	1.13±0.37
H_2 0–0 S(2)	12.2786	1.15	$<$ 52.3	$<$ 53.5	33.0±9.4	33.7±9.7	$<$ 21.1	$<$ 21.7	$<$ 16.2	$<$ 16.6	$<$ 20.1	$<$ 20.5
H_2 0–0 S(3)	9.6649	0.85	3.77±1.24	3.99±1.32	21.7±5.5	22.9±5.8	$<$ 2.03	$<$ 2.15	$<$ 1.97	$<$ 2.08	2.51±0.83	2.70±0.89
H_2 0–0 S(4)	8.0251	0.85	$<$ 15.9	$<$ 16.2	10.2±2.7	10.4±2.8	$<$ 2.81	$<$ 2.87	$<$ 3.04	$<$ 3.10	$<$ 2.96	$<$ 3.02
H_2 0–0 S(5)	6.9095	0.85	9.62±2.43	9.72±2.45	20.1±3.8	20.4±3.8	$<$ 2.75	$<$ 2.78	$<$ 2.77	$<$ 2.80	$<$ 4.96	$<$ 5.01
H_2 0–0 S(6)	6.1086	0.85	$<$ 23.0	$<$ 23.2	$<$ 50.2	$<$ 50.8	–	–	–	–	$<$ 12.0	$<$ 12.1
H_2 0–0 S(7)	5.5112	0.85	$<$ 30.7	$<$ 31.1	$<$ 17.3	$<$ 17.6	$<$ 13.5	$<$ 13.7	$<$ 10.0	$<$ 10.1	$<$ 13.0	$<$ 13.2
H_2 0–0 S(8)	5.0531	0.85	–	–	$<$ 7.70	$<$ 7.82	–	–	–	–	–	–
H_2 0–0 S(9)	4.6946	0.85	$<$ 27.8	$<$ 28.2	$<$ 8.67	$<$ 8.82	–	–	–	–	$<$ 59.4	$<$ 60.5
H_2 0–0 S(10)	4.4099	0.85	$<$ 9.50	$<$ 9.69	$<$ 5.07	$<$ 5.16	–	–	–	–	$<$ 12.8	$<$ 13.1
H_2 0–0 S(11)	4.1813	0.85	$<$ 10.7	$<$ 10.9	$<$ 11.0	$<$ 11.2	–	–	–	–	$<$ 7.56	$<$ 7.72
[Fe I] ($^5D_4$–$^5D_3$)	24.0424	1.15	$<$ 24.2	$<$ 24.6	$<$ 5.06	$<$ 5.13	–	–	–	–	$<$ 1.47	$<$ 1.49
[Fe I] ($^5D_3$–$^5D_2$)	34.7135	2.01	$<$ 7.25	$<$ 7.30	$<$ 12.4	$<$ 12.5	$<$ 5.72	$<$ 5.76	$<$ 7.22	$<$ 7.27	$<$ 4.58	$<$ 4.62
[Fe II] ($^4F_{9/2}$–$^4F_{7/2}$)	17.9363	1.15	$<$ 3.44	$<$ 3.51	$<$ 2.36	$<$ 2.41	–	–	–	–	0.62±0.20	0.63±0.21
[Fe II] ($^6D_{9/2}$–$^6D_{7/2}$)	25.9882	1.15	$<$ 24.3	$<$ 24.6	$<$ 3.31	$<$ 3.35	–	–	–	–	0.75±0.25	0.76±0.25
[Fe II] ($^6D_{7/2}$–$^6D_{5/2}$)	35.3491	2.01	$<$ 7.63	$<$ 7.69	$<$ 7.30	$<$ 7.35	–	–	–	–	$<$ 5.15	$<$ 5.18
[S I] ($^3P_2$–$^3P_1$)	25.2490	1.15	$<$ 9.91	$<$ 10.0	$<$ 6.97	$<$ 7.06	$<$ 2.05	$<$ 2.08	$<$ 8.26	$<$ 8.37	$<$ 2.56	$<$ 2.59
[Si II] ($^2P_{1/2}$–$^2P_{3/2}$)	34.8152	2.01	5.64±1.86	5.68±1.87	27.2±9.0	27.4±9.1	$<$ 7.20	$<$ 7.26	20.1±6.6	20.3±6.7	5.37±1.77	5.41±1.79
[O I] ($^3P_2$–$^3P_1$)	63.1850	16.3	222.0±15.5	222.7±15.6	1083±76	1086±76	–	–	111.2±7.8	111.6±7.8	43.0±3.0	43.1±3.0
[O I] ($^3P_1$–$^3P_0$)	145.535	8.82	26.9±4.6	26.9±4.6	190.8±13.4	190.9±13.4	–	–	$<$ 18.7	$<$ 18.7	3.10±0.80	3.10±0.80
[C II] ($^2P_{1/2}$–$^2P_{3/2}$)	157.741	11.6	62.1±5.5	62.2±5.5	323.1±22.6	323.2±22.6	–	–	$<$ 19.1	$<$ 19.1	4.00±1.00	4.01±1.00
UIR (C–C stretch)	6.22	0.85	–	–	1327±99	1359±102	–	–	–	–	–	–

Table 10.3. (Continued)

Line	λ	Beam	GGD27-ILL		LkHα 225		S106 IRS4		AFGL 2591		Cep A East	
	[μm]	[10^{-8} sr]	Obs.	Ext. corr.	Obs.	Ext. Corr.	Obs.	Ext. Corr.	Obs.	Ext. Corr.	Obs.	Ext. Corr.
H_2 0–0 S(0)	28.2188	1.64	$<$ 12.1	$<$ 12.3	$<$ 13.8	$<$ 14.3	$<$ 15.8	$<$ 16.7	$<$ 124.2	$<$ 125.5	$<$ 36.2	$<$ 36.9
H_2 0–0 S(1)	17.0348	1.15	5.57±1.84	5.68±1.87	7.76±2.56	8.23±2.72	5.76±1.75	7.54±2.29	17.9±4.7	18.3±4.8	2.73±0.90	2.84±0.94
H_2 0–0 S(2)	12.2786	1.15	$<$ 41.5	$<$ 42.5	21.8±7.2	23.3±7.7	11.8±4.9	16.1±6.6	$<$ 189.9	$<$ 194.3	12.7±4.2	13.3±4.4
H_2 0–0 S(3)	9.6649	0.85	5.63±1.86	5.95±1.96	28.0±7.3	33.1±8.7	11.9±3.9	25.5±8.4	13.5±3.7	14.3±3.9	9.02±2.98	10.1±3.3
H_2 0–0 S(4)	8.0251	0.85	3.35±1.10	3.41±1.13	17.1±4.6	18.1±4.8	8.16±2.69	10.5±3.5	$<$ 106.3	$<$ 108.3	13.3±3.3	13.8±3.4
H_2 0–0 S(5)	6.9095	0.85	10.6±2.2	10.7±2.2	40.3±6.3	41.6±6.5	14.7±4.8	16.9±5.6	$<$ 117.4	$<$ 118.7	24.2±4.3	24.7±4.3
H_2 0–0 S(6)	6.1086	0.85	$<$ 6.98	$<$ 7.06	$<$ 25.6	$<$ 26.5	$<$ 16.0	$<$ 18.9	$<$ 214.6	$<$ 217.2	8.41±2.78	8.62±2.84
H_2 0–0 S(7)	5.5112	0.85	$<$ 50.2	$<$ 50.9	35.1±7.9	36.6±8.2	9.36±3.09	11.3±3.7	$<$ 157.5	$<$ 159.6	24.8±6.2	25.5±6.3
H_2 0–0 S(8)	5.0531	0.85	$<$ 9.86	$<$ 10.0	8.14±2.69	8.53±2.81	$<$ 2.95	$<$ 3.64	$<$ 64.4	$<$ 65.4	4.61±1.25	4.75±1.29
H_2 0–0 S(9)	4.6946	0.85	$<$ 10.9	$<$ 11.0	30.4±10.0	32.0±10.6	$<$ 5.75	$<$ 7.28	$<$ 783.4	$<$ 797.1	$<$ 11.7	$<$ 12.1
H_2 0–0 S(10)	4.4099	0.85	$<$ 25.1	$<$ 25.6	$<$ 6.33	$<$ 6.70	$<$ 4.81	$<$ 6.23	$<$ 32.5	$<$ 33.1	9.79±3.23	10.2±3.35
H_2 0–0 S(11)	4.1813	0.85	$<$ 44.4	$<$ 45.3	6.72±2.22	7.15±2.36	$<$ 7.75	$<$ 10.3	$<$ 30.7	$<$ 31.3	$<$ 6.41	$<$ 6.68
[Fe I] ($^5D_4$–$^5D_3$)	24.0424	1.15	$<$ 53.3	$<$ 54.0	$<$ 5.80	$<$ 6.05	$<$ 10.1	$<$ 12.2	$<$ 45.9	$<$ 46.5	$<$ 11.9	$<$ 12.3
[Fe I] ($^5D_3$–$^5D_2$)	34.7135	2.01	$<$ 5.38	$<$ 5.42	$<$ 14.5	$<$ 14.8	$<$ 59.9	$<$ 67.3	$<$ 33.9	$<$ 34.2	$<$ 47.4	$<$ 48.1
[Fe II] ($^4F_{9/2}$–$^4F_{7/2}$)	17.9363	1.15	$<$ 19.0	$<$ 19.4	$<$ 1.64	$<$ 1.74	8.94±2.63	11.9±3.5	$<$ 6.15	$<$ 6.28	2.39±0.65	2.49±0.67
[Fe II] ($^6D_{9/2}$–$^6D_{7/2}$)	25.9882	1.15	$<$ 1.84	$<$ 1.86	3.33±1.10	3.45±1.14	52.7±11.0	62.0±12.9	$<$ 62.1	$<$ 62.8	6.42±2.08	6.58±2.13
[Fe II] ($^6D_{7/2}$–$^6D_{5/2}$)	35.3491	2.01	$<$ 12.7	$<$ 12.8	$<$ 9.22	$<$ 9.43	49.4±16.3	54.6±18.0	$<$ 39.4	$<$ 39.7	$<$ 40.1	$<$ 40.7
[S I] ($^3P_2$–$^3P_1$)	25.2490	1.15	$<$ 3.35	$<$ 3.39	5.75±1.63	5.97±1.69	$<$ 29.6	$<$ 35.2	$<$ 59.8	$<$ 60.6	7.02±2.10	7.20±2.15
[Si II] ($^2P_{1/2}$–$^2P_{3/2}$)	34.8152	2.01	23.1±7.6	23.3±7.7	30.5±10.1	31.2±10.3	1523±251	1687±279	95.2±31.4	95.9±31.7	58.6±4.1	59.4±4.2
[O I] ($^3P_2$–$^3P_1$)	63.1850	16.3	945.7±66.2	948.5±66.4	659.7±47.8	665.5±48.3	11253±1138	11717±1185	782.5±54.8	784.8±54.9	5348±298	5380±299
[O I] ($^3P_1$–$^3P_0$)	145.535	8.82	189.5±17.8	189.6±17.8	$<$ 94.8	$<$ 95.0	2888±290	2912±292	225.7±25.0	225.8±25.0	$<$ 284.4	$<$ 285.0
[C II] ($^2P_{1/2}$–$^2P_{3/2}$)	157.741	11.6	294.6±20.6	294.8±20.6	625.4±46.3	626.3±46.4	1572±159	1583±160	395.3±27.7	395.5±27.7	2245±232	2247±232
UIR (C–C stretch)	6.22	0.85	774±58	792±59	$<$ 307	$<$ 317	2214±166	2267±170	–	–	$<$ 253	$<$ 259

Table 10.3. (Continued)

Line	λ	Beam	Elias3–1		T Tau		HD 97048		HD 97300		HR 5999	
	[μm]	[10^{-8} sr]	Obs.	Ext. corr.	Obs.	Ext. Corr.	Obs.	Ext. Corr.	Obs.	Ext. Corr.	Obs.	Ext. Corr.
H_2 0–0 S(0)	28.2188	1.64	$<$ 4.72	$<$ 5.12	$<$ 4.67	$<$ 4.74	$<$ 5.83	$<$ 5.91	$<$ 2.33	$<$ 2.37	$<$ 4.97	$<$ 5.00
H_2 0–0 S(1)	17.0348	1.15	$<$ 4.10	$<$ 4.78	1.80±0.59	1.85±0.61	$<$ 2.07	$<$ 2.12	–	–	$<$ 1.50	$<$ 1.52
H_2 0–0 S(2)	12.2786	1.15	$<$ 19.9	$<$ 23.7	$<$ 9.68	$<$ 9.99	$<$ 5.40	$<$ 5.56	–	–	$<$ 20.0	$<$ 20.2
H_2 0–0 S(3)	9.6649	0.85	$<$ 2.29	$<$ 3.54	6.81±1.95	7.36±2.10	$<$ 1.83	$<$ 1.97	$<$ 3.06	$<$ 3.29	$<$ 0.59	$<$ 0.61
H_2 0–0 S(4)	8.0251	0.85	$<$ 3.44	$<$ 3.97	3.17±1.05	3.25±1.07	$<$ 2.20	$<$ 2.25	$<$ 2.15	$<$ 2.20	$<$ 4.22	$<$ 4.25
H_2 0–0 S(5)	6.9095	0.85	$<$ 6.26	$<$ 6.79	13.6±2.6	13.8±2.7	$<$ 6.17	$<$ 6.25	$<$ 5.91	$<$ 5.99	$<$ 4.60	$<$ 4.63
H_2 0–0 S(6)	6.1086	0.85	$<$ 9.12	$<$ 10.0	$<$ 8.07	$<$ 8.21	$<$ 10.2	$<$ 10.3	$<$ 9.19	$<$ 9.34	$<$ 10.6	$<$ 10.7
H_2 0–0 S(7)	5.5112	0.85	$<$ 9.66	$<$ 10.7	11.0±2.6	11.2±2.7	$<$ 9.28	$<$ 9.45	$<$ 15.7	$<$ 16.0	$<$ 16.2	$<$ 16.3
H_2 0–0 S(8)	5.0531	0.85	–	–	$<$ 4.52	$<$ 4.62	$<$ 4.53	$<$ 4.62	–	–	$<$ 12.2	$<$ 12.3
H_2 0–0 S(9)	4.6946	0.85	–	–	2.87±0.95	2.94±0.97	$<$ 5.47	$<$ 5.59	–	–	$<$ 15.4	$<$ 15.5
H_2 0–0 S(10)	4.4099	0.85	$<$ 5.66	$<$ 6.56	$<$ 3.13	$<$ 3.21	$<$ 4.99	$<$ 5.11	$<$ 7.06	$<$ 7.24	$<$ 10.7	$<$ 10.8
H_2 0–0 S(11)	4.1813	0.85	$<$ 9.10	$<$ 10.7	$<$ 4.67	$<$ 4.81	$<$ 5.25	$<$ 5.39	$<$ 9.07	$<$ 9.33	$<$ 5.07	$<$ 5.13
[Fe I] ($^5D_4$–$^5D_3$)	24.0424	1.15	$<$ 2.13	$<$ 2.37	$<$ 1.83	$<$ 1.87	$<$ 3.02	$<$ 3.07	$<$ 1.52	$<$ 1.54	$<$ 0.89	$<$ 0.90
[Fe I] ($^5D_3$–$^5D_2$)	34.7135	2.01	$<$ 4.70	$<$ 4.98	$<$ 1.04	$<$ 1.05	$<$ 3.45	$<$ 3.48	$<$ 2.32	$<$ 2.35	$<$ 5.85	$<$ 5.87
[Fe II] ($^4F_{9/2}$–$^4F_{7/2}$)	17.9363	1.15	–	–	0.52±0.17	0.53±0.18	$<$ 1.85	$<$ 1.90	–	–	$<$ 1.43	$<$ 1.44
[Fe II] ($^6D_{9/2}$–$^6D_{7/2}$)	25.9882	1.15	$<$ 2.29	$<$ 2.51	1.85±0.61	1.88±0.62	$<$ 2.86	$<$ 2.90	$<$ 1.41	$<$ 1.43	$<$ 1.26	$<$ 1.27
[Fe II] ($^6D_{7/2}$–$^6D_{5/2}$)	35.3491	2.01	$<$ 3.86	$<$ 4.08	4.23±1.40	4.28±1.41	$<$ 4.98	$<$ 5.03	–	–	$<$ 6.98	$<$ 7.00
[S I] ($^3P_2$–$^3P_1$)	25.2490	1.15	$<$ 2.59	$<$ 2.86	4.09±1.28	4.16±1.30	$<$ 1.80	$<$ 1.83	$<$ 0.70	$<$ 0.71	$<$ 1.24	$<$ 1.25
[Si II] ($^2P_{1/2}$–$^2P_{3/2}$)	34.8152	2.01	$<$ 6.32	$<$ 6.70	12.6±4.2	12.7±4.2	$<$ 3.80	$<$ 3.84	$<$ 2.24	$<$ 2.26	$<$ 2.63	$<$ 2.64
[O I] ($^3P_2$–$^3P_1$)	63.1850	16.3	–	–	234.8±23.5	235.8±23.6	19.0±3.0	19.1±3.0	–	–	–	–
[O I] ($^3P_1$–$^3P_0$)	145.535	8.82	–	–	$<$ 14.9	$<$ 14.9	–	–	–	–	–	–
[C II] ($^2P_{1/2}$–$^2P_{3/2}$)	157.741	11.6	–	–	10.3±1.9	10.3±1.9	7.01±1.04	7.02±1.04	–	–	–	–
UIR (C–C stretch)	6.22	0.85	–	–	$<$ 161	$<$ 164	440±33	446±34	–	–	$<$ 293	$<$ 294

Table 10.3. (Continued)

Line	λ	Beam	R CrA		T CrA		WW Vul		BD+40°4124		LkHα 224		HD 200775	
	[μm]	[10^{-8} sr]	Obs.	Ext. corr.	Obs.	Ext. Corr.	Obs.	Ext. Corr.	Obs.	Ext. Corr.	Obs.	Ext. Corr.	Obs.	Ext. Corr.
H_2 0–0 S(0)	28.2188	1.64	< 11.4	< 11.7	< 6.04	< 6.14	< 1.78	< 1.80	< 6.60	< 6.81	< 9.51	< 9.81	< 6.04	< 6.17
H_2 0–0 S(1)	17.0348	1.15	< 10.7	< 11.2	3.96±1.31	4.09±1.35	< 0.75	< 0.77	5.37±1.77	5.69±1.88	10.1±3.3	10.7±3.5	< 3.24	< 3.37
H_2 0–0 S(2)	12.2786	1.15	< 46.0	< 48.3	5.58±1.68	5.80±1.74	< 9.84	< 10.1	7.12±2.35	7.62±2.51	12.7±4.2	13.6±4.5	< 5.32	< 5.56
H_2 0–0 S(3)	9.6649	0.85	< 6.40	< 7.25	< 2.09	< 2.29	< 0.95	< 1.01	7.74±2.36	9.15±2.79	9.81±3.12	11.6±3.7	< 2.13	< 2.37
H_2 0–0 S(4)	8.0251	0.85	< 20.3	< 21.2	< 3.14	< 3.23	< 4.34	< 4.42	1.02±0.34	1.08±0.36	6.89±2.27	7.28±2.40	< 2.75	< 2.85
H_2 0–0 S(5)	6.9095	0.85	< 28.9	< 29.6	< 4.04	< 4.11	< 1.65	< 1.67	2.45±0.81	2.53±0.83	11.7±2.5	12.1±2.6	< 5.22	< 5.33
H_2 0–0 S(6)	6.1086	0.85	< 19.5	< 20.0	< 20.1	< 20.5	< 5.05	< 5.11	< 7.96	< 8.25	< 6.26	< 6.49	< 7.65	< 7.83
H_2 0–0 S(7)	5.5112	0.85	< 25.9	< 26.7	< 10.7	< 10.9	< 14.7	< 14.9	< 8.10	< 8.44	< 13.0	< 13.5	< 12.2	< 12.6
H_2 0–0 S(8)	5.0531	0.85	< 12.3	< 12.7	< 6.76	< 6.93	< 15.7	< 16.0	< 18.3	< 19.2	< 35.5	< 37.2	< 7.06	< 7.27
H_2 0–0 S(9)	4.6946	0.85	< 17.6	< 18.3	< 4.86	< 5.00	< 15.5	< 15.8	< 11.6	< 12.2	< 25.5	< 26.9	< 17.3	< 17.9
H_2 0–0 S(10)	4.4099	0.85	< 35.2	< 36.8	< 6.10	< 6.29	< 7.37	< 7.50	< 4.17	< 4.41	< 4.15	< 4.40	< 10.3	< 10.7
H_2 0–0 S(11)	4.1813	0.85	< 30.0	< 31.5	< 6.70	< 6.93	< 10.5	< 10.7	< 7.37	< 7.85	< 10.8	< 11.5	< 18.4	< 19.2
[Fe I] ($^5D_4$–$^5D_3$)	24.0424	1.15	< 5.02	< 5.18	< 0.68	< 0.69	< 1.26	< 1.28	< 1.72	< 1.79	< 1.46	< 1.53	< 2.05	< 2.10
[Fe I] ($^5D_3$–$^5D_2$)	34.7135	2.01	< 8.35	< 8.49	< 4.14	< 4.19	< 3.90	< 3.93	< 4.00	< 4.09	< 4.86	< 4.97	< 3.89	< 3.94
[Fe II] ($^4F_{9/2}$–$^4F_{7/2}$)	17.9363	1.15	< 3.96	< 4.15	< 0.89	< 0.92	< 0.85	< 0.86	< 0.97	< 1.03	< 1.86	< 1.98	< 1.10	< 1.15
[Fe II] ($^6D_{9/2}$–$^6D_{7/2}$)	25.9882	1.15	1.33±0.44	1.36±0.45	< 1.14	< 1.17	< 1.10	< 1.12	0.69±0.23	0.71±0.23	< 2.23	< 2.31	< 1.89	< 1.93
[Fe II] ($^6D_{7/2}$–$^6D_{5/2}$)	35.3491	2.01	< 4.76	< 4.84	< 4.07	< 4.12	< 4.19	< 4.22	< 4.40	< 4.50	< 7.70	< 7.86	< 3.81	< 3.87
[S I] ($^3P_2$–$^3P_1$)	25.2490	1.15	6.78±2.05	6.97±2.10	< 0.82	< 0.84	< 0.65	< 0.65	< 1.37	< 1.42	1.60±0.52	1.66±0.54	< 1.26	< 1.29
[Si II] ($^2P_{1/2}$–$^2P_{3/2}$)	34.8152	2.01	9.38±3.09	9.54±3.15	< 3.63	< 3.67	< 2.92	< 2.94	23.2±7.7	23.7±7.8	24.2±8.0	24.8±8.2	19.0±6.3	19.3±6.4
[O I] ($^3P_2$–$^3P_1$)	63.1850	16.3	681.4±47.6	684.9±47.9	–	–	–	–	703.6±49.5	709.9±49.9	–	–	714.4±72.8	718.5±73.2
[O I] ($^3P_1$–$^3P_0$)	145.535	8.82	< 40.0	< 40.1	–	–	–	–	41.5±4.0	41.6±4.0	–	–	297.4±29.8	297.7±29.8
[C II] ($^2P_{1/2}$–$^2P_{3/2}$)	157.741	11.6	35.7±5.5	35.8±5.5	–	–	–	–	517.5±36.4	518.3±36.4	–	–	329.6±33.1	330.0±33.1
UIR (C–C stretch)	6.22	0.85	< 270	< 277	< 106	< 108	< 192	< 194	260±20	269±20	< 135	< 140	< 132	< 135

Table 10.4. Observed (Obs.) and extinction corrected (EC) data for shocks and PDRs from literature. Numbers in brackets indicate the errors in the last digits.

Line	Orion BN/KL				IC 443				RCW 103			
	Obs. [10^{-3} erg s^{-1} cm^{-2} sr^{-1}]	EC	Beam [10^{-8} sr]	Ref.	Obs. [10^{-3} erg s^{-1} cm^{-2} sr^{-1}]	EC	Beam [10^{-8} sr]	Ref.	Obs. [10^{-3} erg s^{-1} cm^{-2} sr^{-1}]	EC	Beam [10^{-8} sr]	Ref.
H_2 0–0 S(1) 17.03 μm	3.3(6)	4.0(7)	0.01	(1)					0.11(3)	0.12(3)	1.15	(13)
H_2 1–0 S(1) 2.122 μm	8.4(8)	18.0(17)	0.06	(2)	0.637(2)	1.172(3)	0.05	(7)	0.386(12)	0.544(17)	0.11	(14)
H_2 2–1 S(1) 2.248 μm	0.85(10)	1.67(20)	0.06	(2)	0.0547(5)	0.0937(9)	0.05	(7)	0.047(10)	0.064(14)	0.11	(14)
[S I] 25.25 μm	3.9(6)	4.4(7)	2.45	(3)					< 0.01	< 0.01	1.15	(13)
[Si II] 34.82 μm	6.1(6)	6.6(6)	3.27	(3)	0.26(3)	0.27(4)	2.01	(8)	1.4(2)	1.4(2)	2.01	(13)
[O I] 63.18 μm	56(20)	58(21)	2.15	(4)	2.26(19)	2.31(19)	2.51	(9)	0.44(5)	0.44(5)	15.3	(13)
[O I] 145.5 μm									0.037(8)	0.037(8)	15.3	(13)
[C II] 157.7 μm	3.9(5)	3.9(5)	7.24	(5)	0.39(8)	0.39(8)	2.61	(10)	0.54(6)	0.54(6)	15.3	(13)
A_V [m]		10.0		(1)		8.0		(11)		4.5		(14)
d [pc]		430		(6)		1500		(12)		6600		(15)

Line	Orion Bar				NGC 2023				S140			
	Obs. [10^{-3} erg s^{-1} cm^{-2} sr^{-1}]	EC	Beam [10^{-8} sr]	Ref.	Obs. [10^{-3} erg s^{-1} cm^{-2} sr^{-1}]	EC	Beam [10^{-8} sr]	Ref.	Obs. [10^{-3} erg s^{-1} cm^{-2} sr^{-1}]	EC	Beam [10^{-8} sr]	Ref.
H_2 0–0 S(1) 17.03 μm	0.110(5)	0.121(6)	0.06	(16)					0.020(6)	0.022(6)	1.15	(24)
H_2 1–0 S(1) 2.122 μm	0.078(13)	0.114(19)	0.15	(17)	0.060(2)	0.067(2)	0.92	(21)	0.16(2)	0.22(3)	0.03	(25)
H_2 2–1 S(1) 2.248 μm	0.008(4)	0.011(6)	0.15	(18)	0.016(2)	0.018(2)	0.92	(21)				
[S I] 25.25 μm	< 0.13	< 0.14	2.45	(10)								
[Si II] 34.82 μm	9.0(5)	9.3(5)	5.51	(19)	0.20(11)	0.20(11)	3.10	(22)	0.030(9)	0.032(9)	2.01	(24)
[O I] 63.18 μm	54(5)	55(5)	2.15	(5)	3.62(10)	3.63(10)	2.61	(22)	0.33(10)	0.33(10)	15.3	(26)
[O I] 145.5 μm	4.2(5)	4.2(5)	6.72	(5)	0.23(4)	0.23(4)	4.42	(22)				
[C II] 157.7 μm	3.4(5)	3.4(5)	7.24	(5)	0.68(4)	0.68(4)	4.22	(22)	0.35(11)	0.35(11)	15.3	(26)
A_V [m]		5.0		(20)		1.4		(23)		4.0		(24)
d [pc]		430		(6)		475		(23)		910		(27)

References to Table 10.4: (1) Parmar et al. (1994); (2) Brand et al. (1988); (3) Haas et al. (1991); (4) Crawford et al. (1986); (5) Stacey et al. (1993); (6) Warren & Hesser (1978); (7) Richter et al. (1995a); (8) Oliva et al. (1999a); (9) Burton et al. (1990b); (10) Haas (1997); (11) van Dishoeck et al. (1993); (12) Burton et al. (1988); (13) Oliva et al. (1999b); (14) Oliva et al. (1990); (15) Leibowitz & Danziger (1983); (16) Parmar et al. (1991); (17) Burton et al. (1990a); (18) Hayashi et al. (1985); (19) Haas et al. (1986); (20) Assumed; (21) Hasegawa et al. (1987); (22) Steiman-Cameron et al. (1997); (23) Jaffe et al. (1990); (24) Timmermann et al. (1996). (25) Carr (1990); (26) Emery et al. (1996); (27) Crampton & Fisher (1974).

seen to deviate strongly from this fit. In these cases, we have attempted to characterize this behaviour by fitting a second Boltzmann distribution to the higher energy level populations. The resulting excitation temperatures and derived column and mass of molecular hydrogen are listed in Table 10.5.

In Fig. 10.2 we also show similar plots for six regions which have been quoted in literature as prime examples of shock- and PDR emission, peak 1 of the shocked H_2 emission in the Orion BN/KL region (Hasegawa et al. 1987; Brand et al. 1988; Parmar et al. 1994), the shock in the old supernova remnant IC 443 (Burton et al. 1989; Richter et al. 1995a, 1995b; Oliva et al. 1999a), the X-ray irradiated shock in the young supernova remnant RCW 103 (Oliva et al. 1990, 1999b), the Orion bar PDR (Burton et al. 1990a; Parmar et al. 1991; Marconi et al. 1998), the NGC 2023 PDR (Hasegawa et al. 1987; Burton et al. 1992b; Steiman-Cameron et al. 1997) and the PDR S140 (Timmermann et al. 1996). The ground-based observations of these regions reveal spatial structure in the derived temperature on a scale which is small compared to the ISO SWS beam. Basic parameters for these regions are listed in Table 10.4. As can be seen from Fig. 10.2, the excitation diagrams of these template regions show in general the warm and hot component also visible in some of our ISO sources. The results of the Boltzmann distribution fits are again given in Table 10.5.

Employing predictions of H_2 emission from PDR, J-shock and C-shock models by Burton et al. (1992a), Hollenbach & McKee (1989) and Kaufman & Neufeld (1996), we determined the excitation temperature $T_{\rm rot}$ from the low-lying (from S(1) to S(5)) pure rotational levels from these models as a function of density n and either incident FUV flux G (in units of the average interstellar FUV field $G_0 = 1.2 \times 10^{-4}$ erg cm^{-2} s^{-1} sr^{-1}; Habing 1968) or shock velocity v_s in an identical way as was done for the observations. For PDRs, the total infrared flux F_{IR} is expected to be directly correlated to G by the relation $G = 0.5\ F_{IR}/\Omega^2$, with Ω the spatial extent of the PDR. We have computed F_{IR} for all our sources by the same procedure as was used to compute the bolometric luminosity in Sect. 10.2, but in this case only use the excess above the reddened Kurucz model to integrate F_λ. From these values of F_{IR} we then computed G, assuming a beam filling factor of one. The resulting G-values, listed in Table 10.6, were used to plot our observations directly in the parameter space of the PDR models (Fig. 10.3). Note that if the extent of the PDR is smaller than the beam size, as might be expected for some sources, our data points in Fig. 10.4 may be shifted along the direction indicated by the arrows. However, for PDRs the resulting $T_{\rm rot}$ does not depend much on G (c.f. Fig. 7.8), so this does not introduce an additional uncertainty in our analysis.

For the shocks such a direct comparison between theory and observation is more cumbersome. We have decided to plot the results of the $T_{\rm rot}$ fits from the J- and C-shock models versus the total flux observed in all lines (Fig. 10.3). Since [O I] 63.2 μm, [C II] 157.7 μm and [Si II] 34.8 μm are expected to be the dominant coolants in the lines we study here, we only plot this quantity in sources where these three lines were measured. It is also given in Table 10.6. For shocks with velocities in excess of 20 km s^{-1}, Lyα is also an important coolant, which we have neglected here. The total luminosity of the cooling in a shock is proportional to nv_s^3, so for the shocks plotted in Fig. 10.3 the ordinate will no longer directly correspond to a single parameter in the models, and

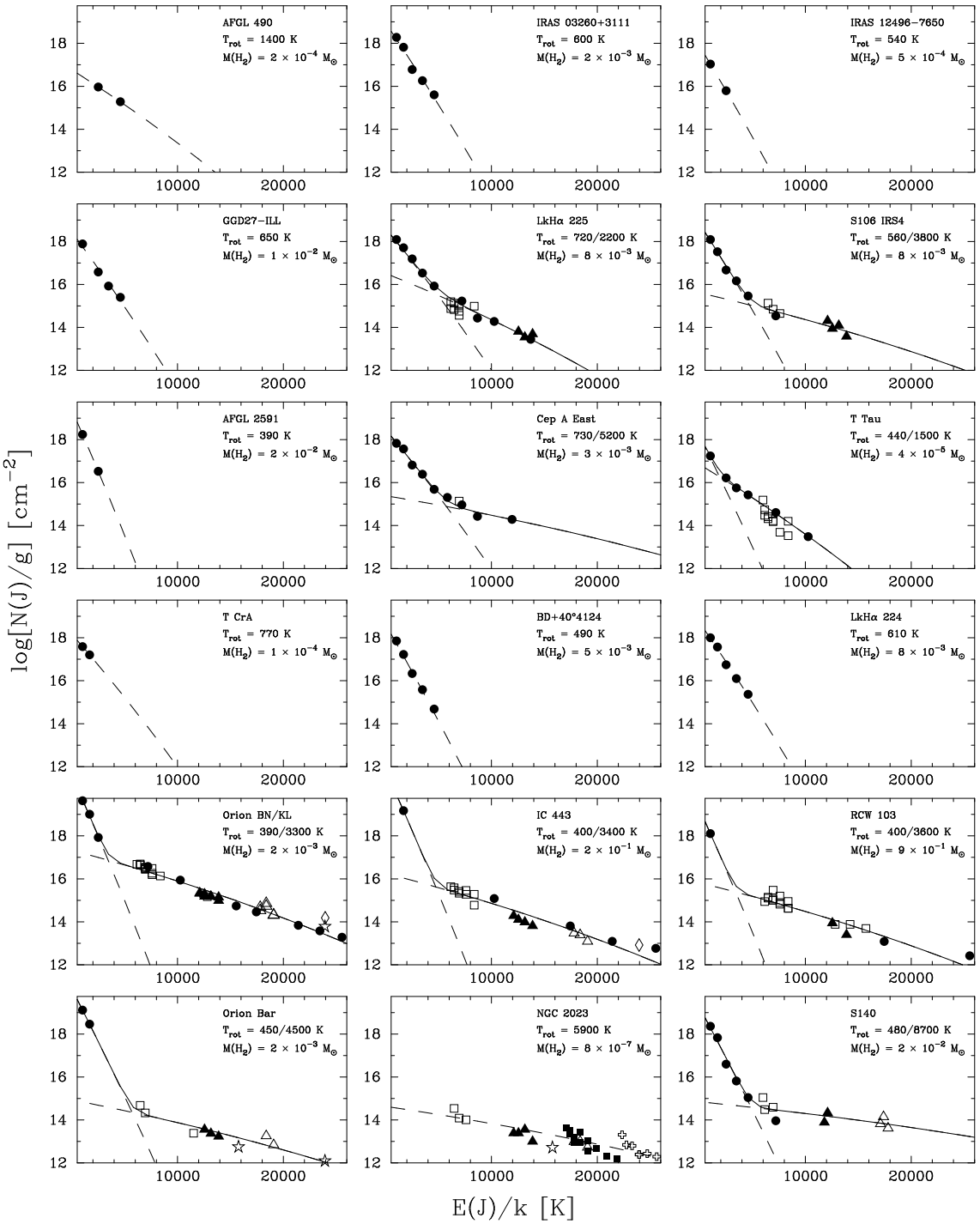

Fig. 10.2. H_2 excitation diagrams for programme and comparison stars. Shown are apparent columns of H_2 in the pure-rotational (0–0) transitions (filled dots), 1–0 transitions (open squares), 2–1 transitions (filled triangles), 2–0 transitions (open stars), 3–2 transitions (open triangles), 3–0 transitions (filled squares), 4–3 transitions (open diamonds), and 4–1 transitions (open crosses). Observational errors are smaller than the size of the plot symbol. The Boltzmann distribution fits are plotted as dashed lines. The solid lines show the sum of both thermal components for each source.

Table 10.5. Results of H_2 Boltzmann distribution fits.

Object	$T_{\rm rot}$ [K]	$N_{\rm rot}$ [cm^{-2}]	$T_{\rm vib}$ [K]	$N_{\rm vib}$ [cm^{-2}]	$M(H_2)$ [M$_\odot$]
AFGL 490	1400	1.9×10^{18}	–	–	2×10^{-4}
IRAS 03260+3111	600	1.2×10^{20}	–	–	2×10^{-3}
IRAS 12496−7650	540	9.1×10^{18}	–	–	5×10^{-4}
GGD 27-ILL	650	4.2×10^{19}	–	–	1×10^{-2}
LkHα 225	720	6.7×10^{19}	2200	1.7×10^{18}	8×10^{-3}
S106 IRS4	560	8.7×10^{19}	3800	3.6×10^{17}	8×10^{-3}
AFGL 2591	390	2.2×10^{20}	–	–	2×10^{-2}
Cep A East	730	5.0×10^{19}	5200	3.0×10^{17}	3×10^{-3}
T Tau	440	1.5×10^{19}	1500	2.1×10^{18}	4×10^{-5}
T CrA	770	2.7×10^{19}	–	–	1×10^{-4}
BD+40°4124	490	4.8×10^{19}	–	–	5×10^{-3}
LkHα 224	610	7.0×10^{19}	–	–	8×10^{-3}
Orion BN/KL	390	6.1×10^{21}	3300	1.7×10^{19}	2×10^{-3}
IC 443	400†	1.0×10^{22}	3400	1.4×10^{18}	2×10^{-1}
RCW 103	400†	1.6×10^{20}	3600	5.5×10^{17}	9×10^{-1}
Orion Bar	450	1.3×10^{21}	4500	9.1×10^{16}	2×10^{-3}
NGC 2023	–	–	5900	6.0×10^{16}	8×10^{-7}
S140	480	1.9×10^{20}	8700	1.4×10^{17}	2×10^{-2}

† Assumed temperature.

instead of the simple lines for the PDRs, we get a grid of models with different shock parameters. We are also left with the additional uncertainty that the shock will likely not fill the entire beam, so our data points must be shifted along a vector indicated in the figures to take this into account.

Comparing the excitation temperature of the template sources listed in Table 10.5 with the ones plotted in Fig. 10.2, we note that for the relatively clean PDRs S140 and the Orion Bar, the derived excitation temperature falls within the range predicted by PDR models. Although the Tielens & Hollenbach (1985) models do not predict a detailed ro-vibrational H_2 spectrum, competing PDR models (e.g. Black & van Dishoeck 1987; Draine & Bertoldi 1996) also show the same hot component which we observe in these PDR template sources. This hot PDR may reflect the combined effects of UV-pumped infrared fluorescence and the presence of a very warm, but thin, surface layer.

The only shock template source for which we were able to derive a reliable $T_{\rm rot}$, Orion BN/KL peak 1, agrees well with the value expected for a J-shock. Note however that all three of our template shock sources also show evidence for a hot H_2 component,

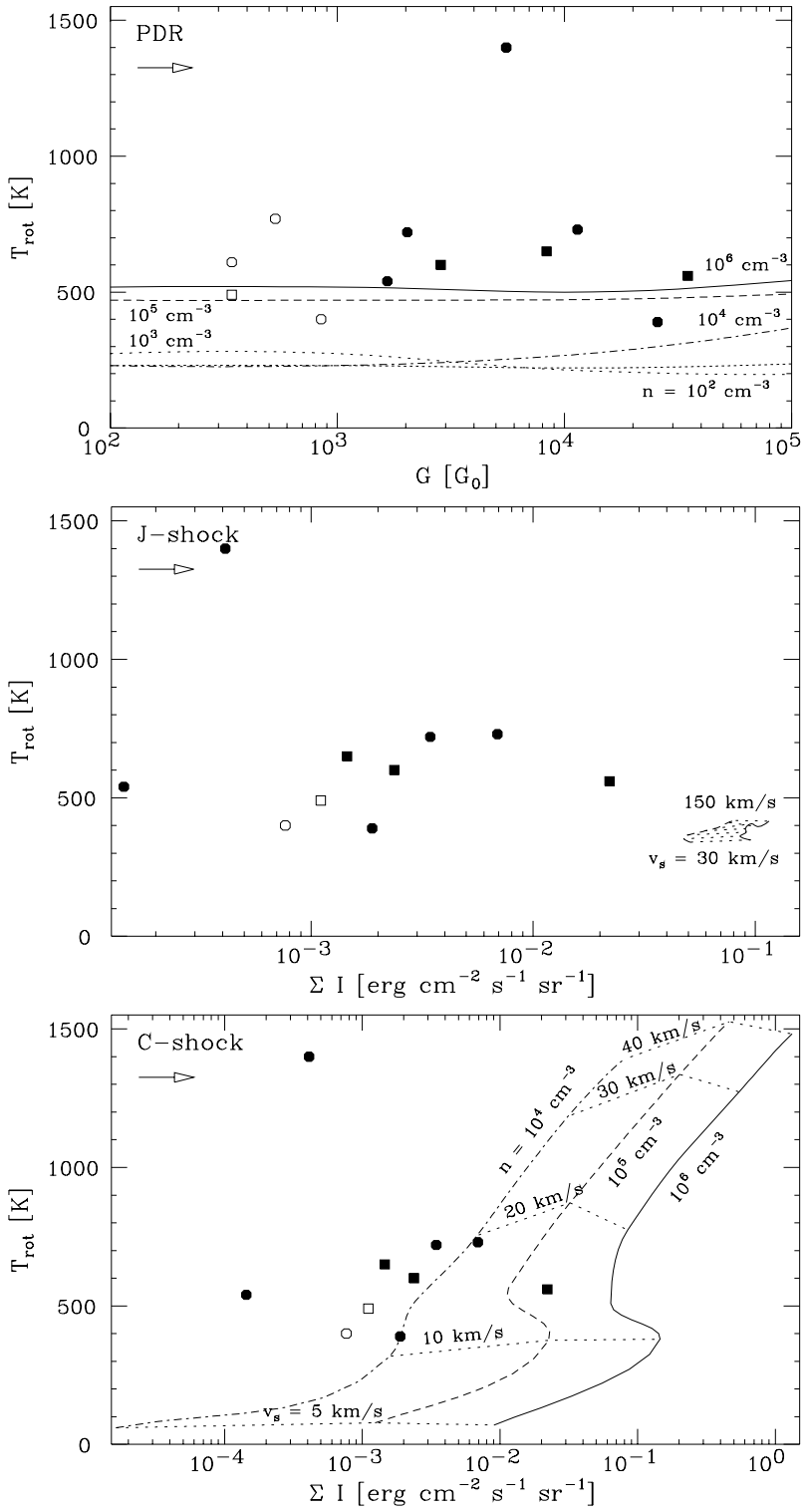

Fig. 10.3. Comparison of observed H_2 rotational temperatures to theoretical relation between continuum fluxes and $T_{\rm rot}$ (PDR models) or summed intensity in all observed lines and $T_{\rm rot}$ (shocks). Sources which show PAH emission are plotted as squares. Plot symbols are filled for Class I sources. The arrows show the direction of beam dilution.

which is not predicted by J-shock models. This probably means that even in these relatively clean template cases, we do not observe a single J-shock, but a combination of one or more J- and C-shocks. Possibly this reflects the presence of shocked clumps of gas where the J-shock corresponds to the region around the point of impact while the C-shock emission originates from oblique shocks further away.

The situation for the programme sources is distinctly less clear-cut. Except for GGD 27-ILL and IRAS 03260+3111, which appear somewhat warmer in pure rotational H_2 than predicted by the models, all sources which show PAH emission and might therefore be expected to be dominated by PDR emission have excitation temperatures within the range predicted by the PDR models. Small differences between observations and the models may reflect the fact that these observations spatially resolve the PDR while the models refer to integrated (i.e. averaged) values. Of the remaining sources, only AFGL 2591 has an excitation temperature compatible with the J-shock models. All are compatible with excitation temperatures expected for C-shocks. However, in the next section we will show that the observed atomic fine-structure spectrum in these sources does require the presence of a J-shock. This could either mean that the H_2 has a stronger C-shock component than the template sources, or that the J-shock models of Hollenbach & McKee (1989) underestimate the temperature in the post-shock gas, where the H_2 emission originates in a J-shock. We will come back to this in the discussion and argue that the latter explanation is more likely.

10.5 Fine structure lines

In order to interpret our observations as arising in either a PDR, a C-Shock or a J-shock, we compare our results with the line fluxes predicted by theoretical models of such regions (Tielens & Hollenbach 1985; Hollenbach & McKee 1989; Kaufman & Neufeld 1996). Since the *Infrared Space Observatory* offers the first possibility to confront the infrared spectrum predicted by these models with a wide range of astronomical objects, and the physics behind these models is still not completely understood, there are significant uncertainties in such a procedure. Therefore we also again compare our results with observations from literature of the template sources containing shocks and PDRs.

In Figs. 10.4–10.6 we have plotted the absolute line intensities predicted either against the G-values computed from the infrared luminosity (PDRs) or against the sum of all observed lines fluxes (shocks), computed in the previous section. Note that since the quantities plotted on both axes of these plots depend on the beam filling factor, the points may be expected to shift along the arrows shown in the plots in case the PDR or shock is smaller than the beam size.

By comparing the predicted line fluxes for the PDR, J-shock and C-shock models with our observations in Figs. 10.4–10.6 we can directly draw several interesting conclusions. The predicted intensity in the [Fe I] and [S I] lines is orders of magnitudes higher in the shock models than in the PDR models, because in the latter nearly all iron and sulfur will be ionized in the heated surface layer of a PDR. [Fe I] was not de-

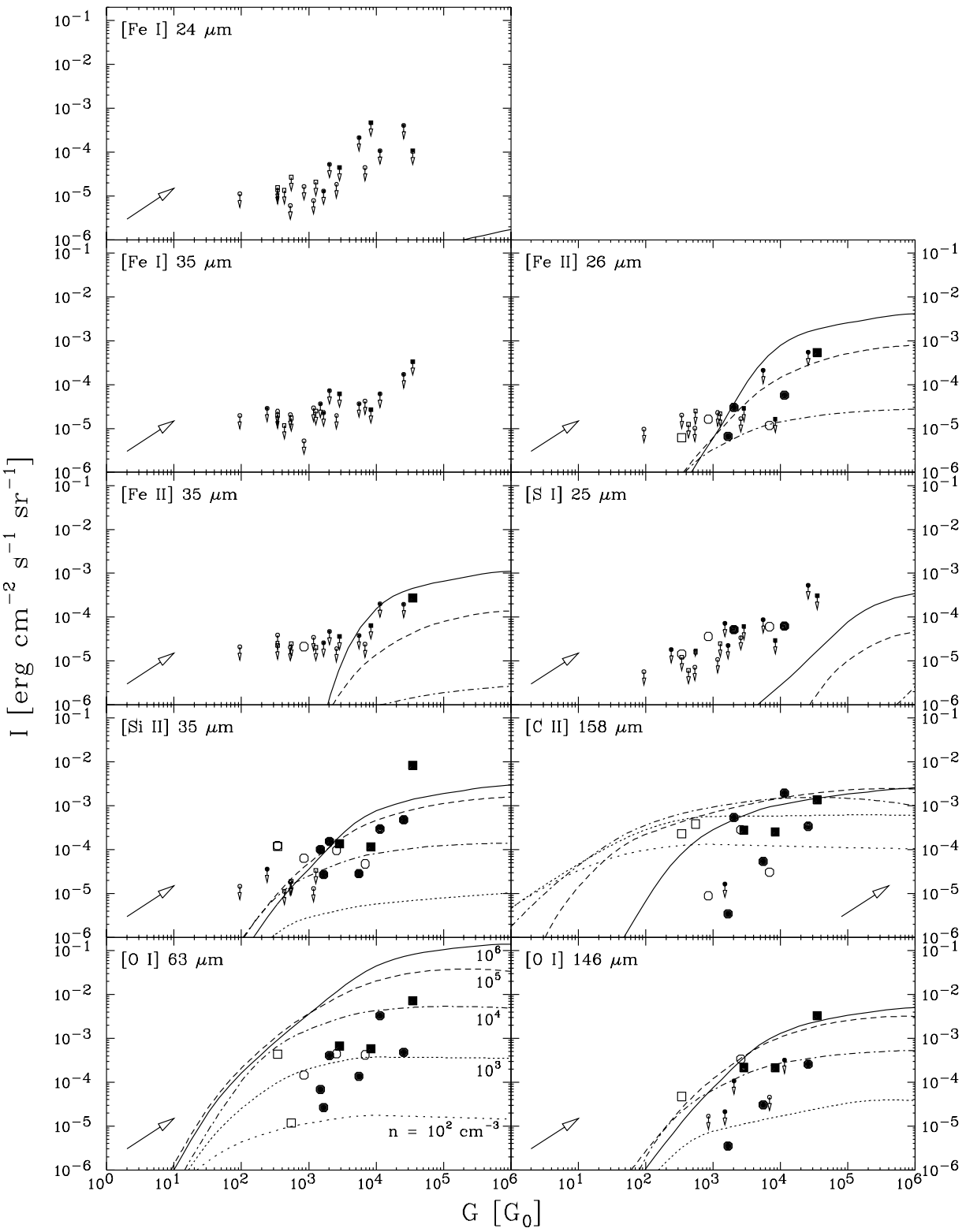

Fig. 10.4. Comparison of observed fine-structure line intensities and continuum flux to the PDR models. Sources which show PAH emission are plotted as squares. The large arrows show the direction of beam dilution.

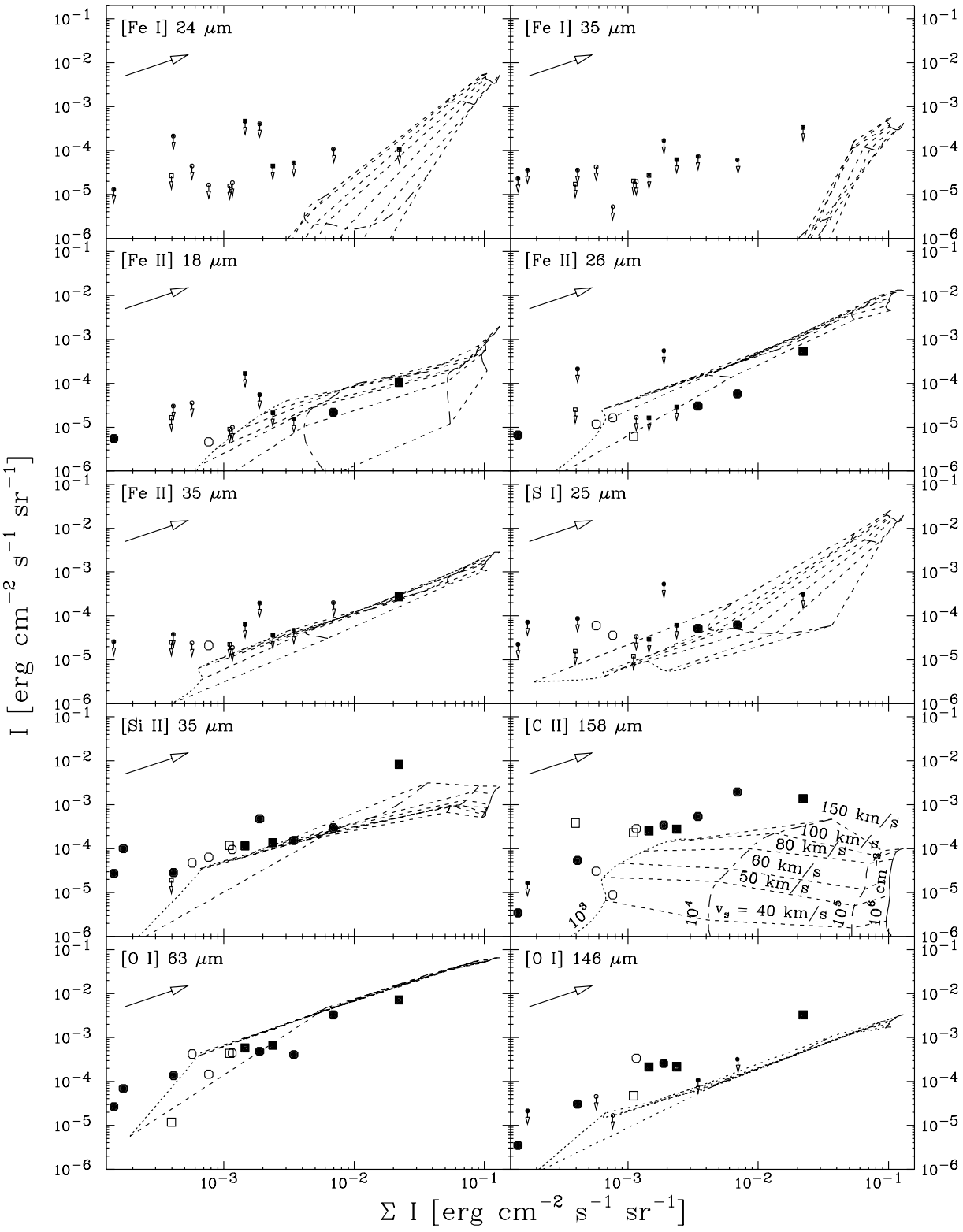

Fig. 10.5. Comparison of observed fine-structure line intensities to the J-shock models. Sources which show PAH emission are again plotted as squares. The large arrows show the direction of beam dilution.

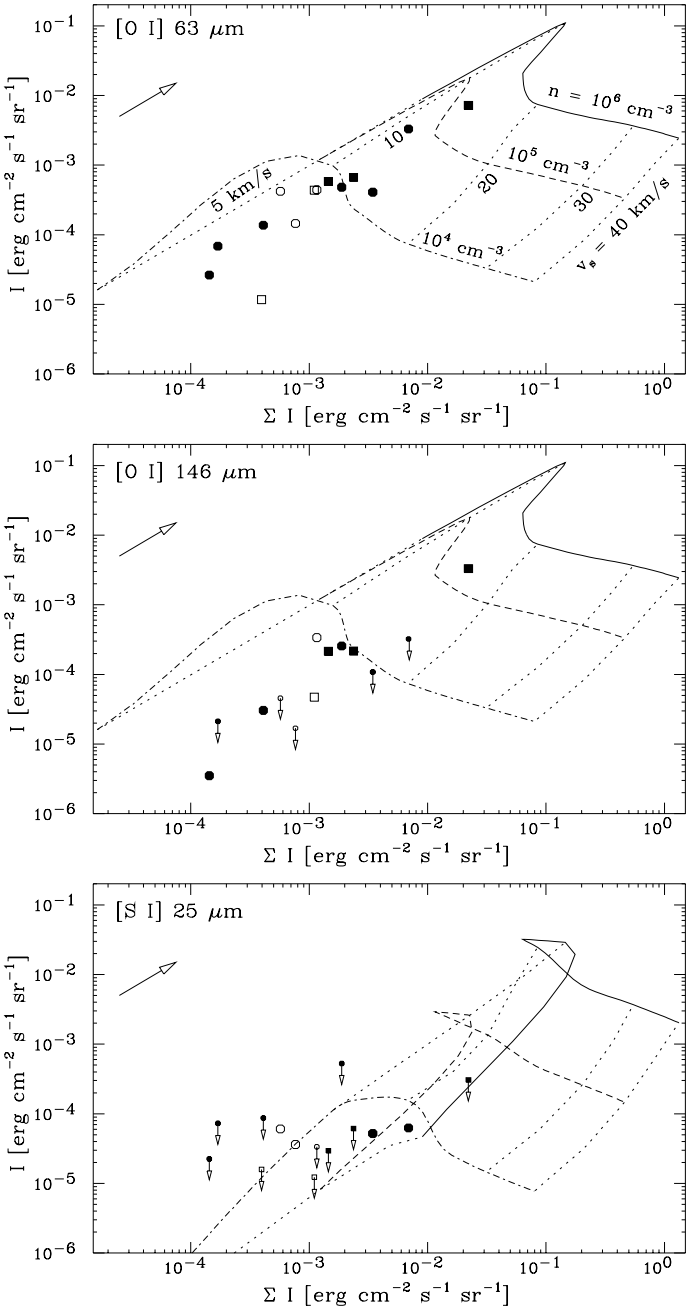

Fig. 10.6. Comparison of observed fine-structure line intensities to the C-shock models. Sources with PAH emission are plotted as squares. The large arrows show the direction of beam dilution.

tected in any source within our sample. However, [S I] 25.3 μm emission was detected for seven sources. Comparing the location of these line fluxes in Fig. 10.4 with the PDR model prediction we see that the observed [S I] fluxes are too high to be compatible with a PDR origin, even for PDRs as dense as 10^6 cm^{-3}. This means that *the detection of [S I] emission with ISO can only mean that a shock is present*. Also note that the detection of [S I] and PAHs appear mutually exclusive in our sample (Table 10.6), suggesting that these may be a fast and relatively straightforward way to distinguish PDRs and shocks.

By definition, C-shocks cannot produce ionized species like [Fe II], [Si II] and [C II]. The last species may still be detected in such regions because it will also reach observable strengths in PDRs illuminated by weak FUV fields (c.f. Fig. 10.4), such as the diffuse galactic background emission ($G \approx 1$). Since the [C II] line fluxes listed in Table 10.3 are not corrected for background emission, the we cannot draw conclusions from just the detection of [C II]. However, the mere detection of [Si II] or [Fe II] means that either a PDR or a J-shock must be present within the ISO-SWS beam. For most sources in which we have detected [Si II] or [Fe II] emission, it can be well explained by either the PDR or the J-shock models (Figs. 10.4–10.5). In only one case, S106 IRS4, is the observed [Si II] 34.8 μ line intensity clearly too strong to be explained by either PDR or J-shock models. However, in Chapter 7 we found that the infrared spectrum of this source is dominated by its associated H II region, which will also contribute to the [Si II] and [Fe II] lines studied here.

Although both the PDR and the J-shock models predict the presence of observable amounts of [C II] emission, the expected line strength in PDRs of moderate to high density ($\leq 10^3$ cm^{-3}) is more than an order of magnitude higher than in J-shocks. Most of the sources with observed [C II] 158 μm emission have strengths that are too high to be explained by the J-shock models. For these sources we can therefore immediately infer that they must be due to a PDR. For the remainder of the sources, the [C II] 158 μm line strength becomes comparable to the one expected for the background, so a direct comparison of those values to J-shock models will yield inconclusive results.

Intense [O I] 63.2 μm emission can be produced by PDRs, as well as J- and C-shocks. The observed [O I] 63.2 μm intensities are all within the range that can be reproduced by the models. The [O I] 145.5 μm line can also be produced by the PDR and C-shock models; the J-shock models predict less [O I] 146 μm emission than is observed. Also, in nearly all the cases we study here, the PDR or C-shock model parameters found from the [O I] 63.2 and 145.5 μm lines do not agree with each other; either the [O I] 63.2 μm line appears too weak, or the [O I] 145.5 μm line appears too strong. Such a discrepancy is not unique to the sources we study here. It has also been observed in spatially resolved PDRs (Liseau et al. 1999), so it cannot be due to the different LWS beam sizes at 63 and 146 microns. One possible explanation would be that [O I] 145.5 μm is blended with the CO J=18–17 line. In view of the strength of other CO lines in our LWS spectra, this line is in general expected to be too weak to dominate the line flux, and thus cannot account for the observed anomaly. Another, more promising, explanation may be that the [O I] 63.2 μm line intensity has been diminished by absorption by cool foreground material. [O I] 63.2 μm absorption has indeed been found in the line

Table 10.6. Results of fine-structure line analysis.

Object	F_{IR}	$G_{\rm av.}$	PAH	$\Sigma\, I$	n [cm^{-3}]							Type
	[W m^{-2}]	[G$_0$]		[erg cm^{-2} s^{-1} sr^{-1}]	H_2	[Fe I]	[Fe II]	[S I]	[Si II]	[O I]	[C II]	
AFGL 490	1.4×10^{-10}	5.5×10^{3}	–	4.1×10^{-4}	–	–	–	–	$\gtrsim 10^{3}$	$\gtrsim 10^{3}$	–	Shock?
IRAS03260+3111	7.4×10^{-11}	2.9×10^{3}	$\surd$	2.4×10^{-3}	$\gtrsim 10^{6}$	–	–	–	$\gtrsim 10^{5}$	$> 10^{3}$	$> 10^{2}$	PDR
L1489 IRS	6.2×10^{-12}	2.4×10^{2}	–	–	–	–	–	–	–			–
L1551 IRS5	3.9×10^{-11}	1.5×10^{3}	–	1.7×10^{-4}	–	–	–	–	$\geq 10^{3}$	$\gtrsim 10^{3}$	–	Shock?
IRAS12496−7650	4.3×10^{-11}	1.7×10^{3}	–	1.4×10^{-4}	–	–	$\geq 10^{2}$	–	$\geq 10^{3}$	$\gtrsim 10^{3}$	–	Shock?
GGD 27-ILL	2.2×10^{-10}	8.3×10^{3}	$\surd$	1.5×10^{-3}	$\gtrsim 10^{6}$	–	–	–	$\geq 10^{4}$	$\gtrsim 10^{3}$	$> 10^{2}$	PDR
LkHα 225	5.3×10^{-11}	2.0×10^{3}	–	3.4×10^{-3}	$\geq 10^{4}$	–	$\gtrsim 10^{4}$	$\geq 10^{4}$	$\geq 10^{4}$	$\gtrsim 10^{4}$	–	Shock
S106 IRS4	9.1×10^{-10}	3.5×10^{4}	$\surd$	2.2×10^{-2}	$\approx 10^{6}$	–	$> 10^{5}$	–	–	$\geq 10^{4}$	$> 10^{3}$	PDR
AFGL 2591	6.7×10^{-10}	2.6×10^{4}	–	1.9×10^{-3}	$\geq 10^{4}$	–	–	–	$> 10^{3}$	$\geq 10^{3}$	$\gtrsim 10^{3}$	PDR?
Cep A East	3.0×10^{-10}	1.1×10^{4}	–	6.9×10^{-3}	$\gtrsim 10^{4}$	–	$\geq 10^{4}$	$\gtrsim 10^{4}$	$\geq 10^{4}$	$\gtrsim 10^{4}$	–	Shock
Elias 3-1	3.3×10^{-11}	1.3×10^{3}	$\surd$	–	–	–	–	–	–			–
T Tau	2.2×10^{-11}	8.5×10^{2}	–	7.7×10^{-4}	$\gtrsim 10^{4}$	–	$\geq 10^{3}$	$\geq 10^{3}$	$\geq 10^{3}$	$\geq 10^{3}$	–	Shock
HD 97048	1.4×10^{-11}	5.5×10^{2}	$\surd$	4.0×10^{-4}	–	–	–	–	–	$\geq 10^{2}$	–	PDR
HD 97300	1.1×10^{-11}	4.3×10^{2}	$\surd$	–	–	–	–	–	–			–
HR 5999	3.0×10^{-11}	1.2×10^{3}	–	–	–	–	–	–	–			–
R CrA	1.8×10^{-10}	6.9×10^{3}	–	5.7×10^{-4}	–	–	$\gtrsim 10^{3}$	$\geq 10^{3}$	$\geq 10^{3}$	$\gtrsim 10^{3}$	–	Shock†
T CrA	1.4×10^{-11}	5.3×10^{2}	–	–	–	–	–	–	–			–
WW Vul	2.5×10^{-12}	9.4×10^{1}	–	–	–	–	–	–	–			–
BD+40°4124	9.0×10^{-12}	3.4×10^{2}	$\surd$	1.1×10^{-3}	$\gtrsim 10^{4}$	–	$\geq 10^{5}$	–	–	$\gtrsim 10^{4}$	$\leq 10^{3}$	PDR
LkHα 224	8.9×10^{-12}	3.4×10^{2}	–	–	–	–	–	–	–			Shock†
HD 200775	6.7×10^{-11}	2.6×10^{3}	–	1.2×10^{-3}	–	–	–	–	$\gtrsim 10^{4}$	$\gtrsim 10^{3}$	$\gtrsim 10^{3}$	PDR

† Probably not connected to optical source.

of sight towards a few sources (Poglitsch et al. 1996; Kraemer et al. 1998), lending credence to the suggestion that this may also be the case in our sources. Note that if this suggestion is correct, this means that the observed [O I] emission in *all* our sources must come from either PDRs or C-shocks, since the [O I] 145.5 μm line fluxes are too high compared to the J-shock models.

10.6 Notes on individual objects

AFGL 490 (IRAS 03236+5836) is a luminous infrared source, powering a strong bipolar CO outflow with an extent of $\approx 100''$ (Lada & Harvey 1981). The central peak in AFGL 490 is believed to be an embedded intermediate-mass YSO and the driving source for the molecular outflow (Minchin et al. 1991; Haas et al. 1992). Ground-based H_2 1–0 S(1) images (Davis et al. 1998) show several knots of shocked molecular gas in the AFGL 490 outflow as well as diffuse H_2 emission, suggesting a composite origin for the emission lines detected with ISO. The temperatures derived from the H_2 0–0 S(3) and S(5) lines can only be explained by a non-dissociative shock. However, the detection of strong [Si II] and [O I] emission show that either a PDR or a fast J-shock must be present as well.

IRAS 03260+3111 was found to be a candidate for a class of objects making the transition between Class I and II YSOs by Magnier et al. (1999). Strong PAH-emission in the SWS spectrum suggests that it has a significant PDR contribution. The lines detected confirm this hypothesis: The [Si II], [O I] and [C II] are strongly suggestive of a PDR origin. The temperature of the H_2 is somewhat higher than that expected for a PDR, but this may be influenced by an apparent discontinuity between the 0–0 S(2) and S(3) lines, where SWS uses apertures of different sizes.

L1489 IRS (IRAS 04016+2610) is a Class I source in an extended molecular gas core in the Taurus star forming region. It powers a low-velocity molecular outflow adjacent to the source (Myers et al. 1988; Hogerheijde et al. 1998) and has been suggested as the powering source of a more extended molecular outflow (Terebey et al. 1989; Moriarty-Schieven et al. 1992). Recent HST NICMOS images of the source reveal a bright near-infrared nebula crossed by a dark lane, interpreted as an optically thick disk seen in silhouette (Padgett et al. 1999). Ground-based images in the H_2 1–0 S(1) line reveal strong H_2 emission from the HH 360a knot in the molecular outflow (Gómez et al. 1997). No emission lines were detected with ISO, suggesting that the shocked material in the region is confined to these small knots.

L1551 IRS5 (IRAS 04287+1801) is one of the best studied embedded YSOs. The bipolar molecular outflow emanating from L1551 IRS5 was the first to be discovered (Snell et al. 1980), and it remains a text-book example of a Class I source. It illuminates the reflection nebula HH 102, and drives both a strong molecular outflow as well as a highly collimated jet, as traced by a number of Herbig-Haro objects with high proper motions (Mundt et al. 1991; Staude & Elsässer 1993). Interferometry of L1551 IRS5 at mm wavelengths (Keene & Masson 1990) reveals the source to consist of two distinct components: an envelope with radius $\approx 12''$ and a compact structure of $\approx 0\farcs3$, presum-

ably an accretion disk of a similar size as the solar system. Diffuse H_2 1–0 S(1) emission in the L1551 region was observed by Yamashita & Tamura (1992), and later shown to have a patchy structure by Davis et al. (1995), which may be due to gas which is shock-heated by the strong wind from IRS5. No compact H_2 knots similar to those observed in the surroundings of other YSOs were found in the large-scale surroundings of L1551 IRS5 (Gómez et al. 1997), suggesting the presence of shocks sufficiently powerful to destroy the dust required to re-form molecular hydrogen in post-shock gas. Only [Si II] and [O I] emission was detected with ISO. In view of the previous discussion it seems likely that this will be shock excited.

IRAS 12496−7650 (DK Cha) is an embedded active young stellar object located in the Chamaeleon II dark cloud. It is associated with a weak molecular outflow (Knee 1992) and possibly drives a collimated jet (Hughes et al. 1991). It is associated with the Herbig-Haro objects HH 52–54, some of which are also included in the ISO beam. If the H_2 ortho-/para-ratio in these objects is smaller than the high-temperature equilibrium value of 3, as suggested by recent ISO spectroscopy of HH 54 (Neufeld et al. 1998), our estimate of the H_2 mass (Table 10.5) will be too low. The ISO [O I]/[C II] ratio suggests a strong shock component to be present in the infrared emission-line spectrum. In view of the detected [Fe II] and [Si II] emission, this shock must be of J-type.

GGD27 (IRAS 18162−2048) is a small reflection nebula containing six point-like infrared sources, interpreted as a small group of massive YSOs (Yamashita et al. 1987; Stecklum et al. 1997). The object GGD 27-ILL (Aspin et al. 1991) is the probable illuminating source of the nebula and might also power the bipolar outflow seen in CO (Yamashita et al. 1995). The emission lines observed with ISO appear dominated by PDR emission rather than trace a shock driven by the outflow. The ISO emission-line spectrum is also indicative of a PDR origin, although the H_2 temperature falls outside the range predicted by the PDR models.

LkHα 225 (IRAS 20187+4111) is an embedded source in the BD+40°4124 region. The source was shown to be a triple system oriented north-south by Aspin et al. (1994). It is associated with a H_2O maser source and drives a CO outflow (Palla et al. 1994). The detection of [S I] emission shows that a shock must be present in the region. In Chapter 8 we studied the ISO spectra of LkHα 225 in more detail and concluded that the emission line spectrum can be well explained as arising in the combination of a C-shock produced by a slow ($\approx$ 20 km s^{-1}) outflow and a J-shock. In addition to this, we found absorption due to solid water ice and to gas-phase H_2O, CO and CO_2 in the line of sight towards LkHα 225, with unusually high gas/solid ratios. The extreme [O I]/[C II] ratio found at the position of LkHα 225 suggest that a PDR might be present throughout the region as well.

S106 IRS4 (IRAS 20255+3712) is a massive young stellar object believed to be the powering source for the well-known bipolar nebula S106. Apart from the central source IRS4 (Gehrz et al. 1982), S106 also contains an embedded cluster of about 160 stars, as well as an expanding ring of molecular material (Hodapp & Rayner 1991; Loushin et al. 1990; Staude & Elsässer 1993). In Chapter 7 we made a more detailed study of the ISO SWS and LWS spectra of S106 and concluded that the emission line spectrum could be well explained as arising from the superposition of an extended H II

region with a density of about 10^3 cm^{-3} surrounding an O6–8 star, and a PDR of much higher density (10^5–10^6 cm^{-3}). Since it is implausible that such densities would exist throughout the PDR, the PDR must be clumpy in nature.

AFGL 2591 (IRAS 20275+4001) is one of the rare examples of a relatively isolated massive young star. Located in the obscured Cygnus X region, it is invisible in the optical, although it is one of the brightest YSOs at infrared to submm wavelengths. It is associated with a powerful bipolar molecular outflow (Lada et al. 1984) and is surrounded by an envelope of which part might be in free fall collapse onto the star (van der Tak et al. 1999). Tamura & Yamashita (1992) discovered a bipolar outflow-like structure extending over 90″ in ro-vibrational H_2 emission, suggesting a shock origin for the spectral lines detected with ISO. This would also explain the absence of PAH emission. The [O I]/[C II] flux ratio is more suggestive of a PDR origin, though.

Cep A East (IRAS 22543+6145) is the eastern lobe of an energetic, complex molecular outflow (Bally & Lane 1982), believed to be powered by the deeply embedded source HW-2 only visible at radio wavelengths (Hughes & Wouterloot 1984). Cep A East is the site of a fast jet, as well as a number of Herbig-Haro like objects, whereas the western lobe of the Cep A outflow contains a number of distinct shells (Hartigan et al. 1996; Goetz et al. 1998). ISO SWS observations of the western lobe were discussed by Wright et al. (1996), who modelled the emission line spectrum as the combination of several C-type shocks with a planar J-shock of 70–80 km s^{-1}. In Chapter 7 we discussed the entire SWS and LWS spectra of Cep A East in detail and concluded that the continuum radiation at near-infrared wavelengths is dominated by emission from the embedded source IRS 6A (Casement & McLean 1996), whereas another, more luminous, component only becomes visible in the far-infrared. We explained the infrared emission line spectrum as the superposition of a 20 km s^{-1} C-shock and a 60 km s^{-1} J-shock arising in a dense (10^6 cm^{-3}) medium.

Elias 3-1 (IRAS 04155+2812) is an embedded luminous object which is believed to be a young Herbig Ae star. It illuminates a cometary-shaped reflection nebula, in which an east-west oriented elongated structure is visible at near-infrared wavelengths, interpreted by Haas et al. (1997) as two lobes of a cone-like structure. One feature that distinguishes Elias 3-1 is that it is one of the only three sources known that shows the 3.43 and 3.53 μm infrared emission bands, as well as the other infrared emission features usually attributed to PAHs (Schutte et al. 1990). No infrared emission lines were detected.

T Tau (IRAS 04190+1924) is a young binary system, consisting of an optically visible K0–1e classical T Tauri star with an embedded (A_V = 17$^{\rm m}\!.$4), more luminous, companion. Both stars are surrounded by a compact nebula as well as spatially separated arc-shaped cloud 30″ to the west. The ISO SWS observations presented here only include the compact nebula, whereas the LWS observations also include the more extended cloud. Both the optically visible and embedded components of the T Tau system drive separate molecular outflows, whereas the embedded source might also power a string of Herbig-Haro objects as far away as 38 arcminutes (1.55 pc) from the source (Edwards & Snell 1982; van Langevelde et al. 1994; Reipurth et al. 1997). In the previous chapter we studied the complete ISO SWS and LWS spectra of T Tau in more detail and came

to the conclusion that the observed molecular and atomic fine structure emission line spectrum can be well explained as arising in the superposition of a C-shock with a speed of ≈ 35 km s^{-1} and a much faster (≈ 100 km s^{-1}) J-shock arising in a fairly dense (5×10^4 cm^{-3}) medium.

HD 97048 (IRAS 11066−7722) is a fairly typical late B-type Herbig Ae/Be star located in the Chamaeleon I dark cloud. Wesselius et al. (1984) discovered the source to have a strong infrared excess, which was interpreted in terms of a flattened shell or disk of dust particles heated by the central star by Thé et al. (1986). One feature that distinguishes HD 97048 is that it is one of the only three sources known that shows the 3.43 and 3.53 μm infrared emission bands, as well as the other infrared emission features usually attributed to PAHs (Schutte et al. 1990). Although extended mid-infrared emission around HD 97048 has been reported from multi-aperture photometry (Prusti et al. 1994), unpublished N band imaging by the authors with the TIMMI instrument at the ESO 3.6 m telescope show the source to be point-like (diameter $< 1''$), suggesting that the extended emission might be limited to the PAH bands. Only weak [O I] and [C II] emission was detected. If we assume that this emission comes from the same region as the PAH emission, it is compatible with an origin in the surface layer of a circumstellar disk surrounding HD 97048, acting as a PDR.

HD 97300 (IRAS 11082−7620) is a B9 star located in the Cha I complex. The absence of Hα emission and infrared excess at wavelengths shortwards of 5 μm suggests that it is a relatively evolved object within the group of Herbig Ae/Be stars (Thé et al. 1986). HD 97300 is located near (or is seen projected on) the reflection nebula Ced 112, in which Siebenmorgen et al. (1998) discovered a ring of PAHs with ISOCAM. No emission lines were detected with SWS.

HR 5999 (IRAS 16052−3858) is one of the best studied Herbig Ae stars. In the visual, it shows irregular large-amplitude photometric variations due to variable amounts of circumstellar extinction (Tjin A Djie et al. 1989; Thé et al. 1996). HR 5999 is located in the pre-main sequence instability strip, and also shows regular pulsations similar to those observed in the evolved δ Scuti stars (Kurtz & Marang 1995; Marconi & Palla 1998). In the infrared, HR 5999 is a fairly isolated point source (Siebenmorgen et al. 1997), suggesting the star has cleared most of its wide stellar environment. This is in agreement with the non-detection of infrared emission lines with ISO.

R CrA is a well studied Herbig Ae star at the apex of a cometary nebula in the Corona Australis cloud. In the visual, it shows strong photometric variations, while its visual absorption line spectrum is also variable, suggesting it may in fact be a composite system (Bibo et al. 1992; Chapter 3). Several strong molecular outflows containing knots of shocked gas have been detected in the vicinity of R CrA, but recent high-resolution continuum and molecular mappings of the region have shown that the driving sources of these are the embedded sources IRS7 and HH100-IR rather than the optical Herbig stars in the region (Harju et al. 1993; Anderson et al. 1997; Chapter 6). The detection of [S I] shows that a shock must be present within the SWS beam. Most likely, this is due to the outflow of IRS7.

T CrA is a late-type Herbig star located in the tail of a cometary nebula in the Corona Australis cloud. It shows strong photometric variations in the visual, prob-

ably due to variable amounts of circumstellar extinction (Bibo et al. 1992). Based on optical spectro-astrometric measurements, Bailey (1998) suggested T CrA to be a binary system. Ward-Thompson et al. (1987) reported the presence of a jet associated with T CrA, but more recent papers suggest that this may in fact be part of the east-west molecular outflow from the source IRS7 in the region around R CrA (Canto et al. 1986; Harju et al. 1993; Anderson et al. 1997). The H_2 emission detected by ISO is suggestive of a C-shock which may be attributed to this same outflow.

WW Vul (IRAS 19238+2106) is a prototypical Herbig Ae star showing large amplitude photometric variations due to variable circumstellar extinction (Friedemann et al. 1993), as well as evidence for the presence of evaporating solid bodies (Grinin et al. 1996). It shows a large infrared excess, indicative of the presence of a dusty circumstellar disk or envelope. WW Vul is located in relative isolation, which is confirmed by our non-detection of infrared emission lines.

BD+40°4124 (V1685 Cyg) is the most massive member of a small cluster of young stars, commonly known as the BD+40°4124 group (Hillenbrand et al. 1992). It is the ionizing source of a low-density ($\approx 10^2$ cm^{-3}) H II region, surrounded by a dense ($> 10^5$ cm^{-3}) PDR (Chapter 8). The lines detected with ISO are indicative of PDR emission. In view of the luminosity of BD+40°4124 and the strong [C II] emission detected at the position of LkHα 225, it seems likely that the PDR is more extended than the ISO beam and may in fact produce observable PDR emission lines throughout the optical reflection nebula.

LkHα 224 (V1686 Cyg) is a fairly typical Herbig Ae star located in the BD+40°4124 region. In the optical it shows large variations in brightness due to variable amounts of circumstellar extinction (Wenzel 1980; Shevchenko et al. 1991). One remarkable aspect about LkHα 224 is the complete absence of a 10 μm silicate feature, either in absorption or emission in its spectrum (Chapter 8). In Chapter 8 we also studied the infrared emission line spectrum of LkHα 224 and concluded that it is most likely due to non-dissociative shock produced by a slow ($\approx$ 20 km s^{-1}) outflow arising from LkHα 225.

HD 200775 is the illuminating star of the well-known reflection nebula NGC 7023 (IRAS 20599+6755). A biconical cavity of $\approx 20''$ diameter surrounds the star, outside of which the nebulosity shows a highly filamentary structure (Rogers et al. 1995; Lemaire et al. 1996; Gerin et al. 1998). Observations with ISOCAM and ISOPHOT revealed the nebulosity to show strong emission bands due to Polycyclic Aromatic Hydrocarbons (Cesarsky et al. 1996; Laureijs et al. 1996). The SWS observations shortward of 12.0 μm only include the central star and the cavity, whereas the SWS data at longer wavelengths as well as the LWS spectrum also cover part of the PDR. The [O I]/[C II] ratio clearly reflects this PDR nature. Fuente et al. (1999) have analyzed ISO SWS observations centered on parts of NGC 7023 and concluded that they arise in a PDR with temperatures in the range 300–700 K, and with an ortho/para ratio of H_2 of 1.5–2. Our observations suggest the PDR to have a density of $\approx 10^5$ cm^{-3}, much higher than the modelling results of the NGC 7023 PDR by Chokshi et al. (1988). Most likely the lines we have detected are dominated by a few of the high density clumps reported by Martini et al. (1997).

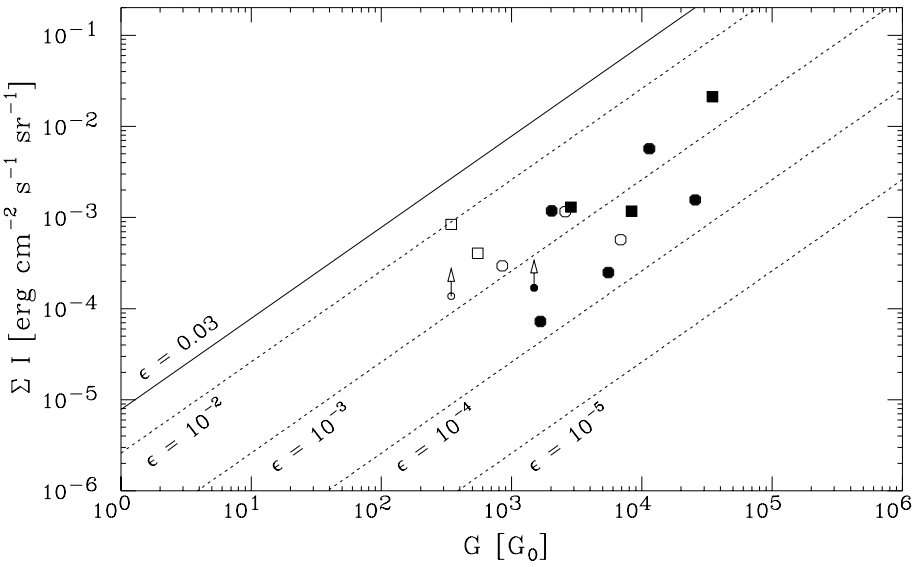

Fig. 10.7. Comparison of the sum the fluxes of all observed lines with G values as derived from the infrared continuum flux. Plots symbols have the same meaning as in Fig. 10.3. Lower limits are shown for objects in which one or two of the major coolants ([O I] 63 μm, [C II] 158 μm, [Si II] 35 μm) were not observed. Also shown are lines of equal ε (ratio of gas heating to far-ultraviolet absorption rate of grains and PAHs).

10.7 Discussion and conclusions

In the previous sections we have seen that based on the observed H_2 and atomic fine-structure lines we can make a distinction between PDRs and shocks with relative ease, and derive the physical properties in the emitting region, provided that key lines like [S I], [O I] and [C II] and the low-lying pure rotational molecular hydrogen lines were detected. The mere presence of [S I] is a sure way to recognize a shock, whereas the [O I] 63.2 μm/[C II] 157.7 μm ratio is able to distinguish PDRs of average to high density from shocks.

An interesting question which we have not yet addressed in the previous sections is whether the heating efficiency assumed in the theoretical models is confirmed by the observations presented here. This efficiency will determine the absolute line fluxes, and could also influence the detailed structure of PDRs and shocks. For PDRs, the model parameter which determines the efficiency is the ratio of gas heating to the far-ultraviolet absorption rate of dust grains and PAHs, ε. On theoretical grounds, it is expected that the maximum allowed value of ε would be 3–5% (Bakes & Tielens 1994). This efficiency decreases when the PAHs are charged up and hence decreases with increasing G (ionization rate) and decreasing n_e (recombination rate; Bakes & Tielens 1998). Since for most sources in our sample the lines which we have detected include the major PDR coolants [O I] 63.2 μm, [C II] 158 μm and [Si II] 34.8 μm we are able to directly derive a value of ε for our PDR sources. For this reason, we we have plotted the summed intensity in all detected lines against the values of G derived from

the infrared continuum flux derived listed in Table 10.6. From this plot (Fig. 10.7), in which we also show lines of constant ε, it can be seen that most of our PDR sources (as identified from the associated PAH emission) have ε of a few times 10^{-3}. This estimate is nearly independent of the beam filling factor. Although somewhat lower than assumed in most PDR models, this value agrees well with those observed towards PDRs in different astrophysical environments (see e.g. Hollenbach & Tielens 1999).

As a final note to this chapter, let us now wonder how to put our main results, that both shocks and PDRs are observed near Class I YSOs, whereas Class II YSOs only show PDR emission, in context. In the previous sections we have seen that the detection of [S I], indicative of shocks, and PAH-emission, indicative of PDR activity, appear mutually exclusive. To illustrate this mutual exclusion of [S I] and the PAH emission and to illustrate its dependence on the evolutionary state of the YSO, we have created plots of the luminosity in the [S I] 25.3 μm line and in the 6.2 μm PAH band, normalized to the bolometric luminosity, against the visual extinction A_V for the sources in our sample (Fig. 10.8). We can see here that the Class I sources for which we have detected [S I] emission, LkHα 225 and Cep A East, are also among the sources with higher values of A_V. However, apparently the mere embeddedness of a source does not guarantee that strong [S I] is present, as evidenced by some of the upper limits plotted in Fig. 10.8. Note that the three Class II sources in whose vicinity we have detected [S I] emission, T Tau, LkHα 224 and R CrA, are all located near Class I sources driving a strong bipolar outflow. We associate the observed [S I] emission in these three sources with the embedded instead of the optical star.

PAH emission was observed in both Class I (IRAS 03260+3111, GGD 27-ILL, S106 IRS4) and Class II (BD+40°4124, HD 97048) sources. The range in fraction of the total luminosity coming out in the 6.2 μm C–C stretch mode does not appear different between the two groups, although the cooler stars in both groups appear to have a higher $L_{\rm PAH}/L_{\rm bol}$ than the hotter stars. The values of A_V used in Fig. 10.8 are those for the associated continuum source; the lines do not necessarily have to suffer from the same amount of extinction. Because a young star is expected to clear its circumstellar environment as it accretes mass, these values of A_V may be taken as a rough indication of evolutionary status. Geometry is however also important in interpreting these results as exemplified by S106 IRS4 where our direct view of the YSO is inhibited by an optically thick circumstellar disk but the gas along the poles is photoionized by the star (Chapter 7).

It is interesting that the most embedded source in our sample, Cep A East, also has the highest [S I] luminosity, and that all Class I sources which show PAH emission are only moderately embedded. This is exactly what one would also expect: as a star has just formed, it is heavily embedded and any PAH emission arising in a PDR close to the star will be completely obscured. As long as the young star accretes matter it will also drive a bipolar outflow, which can power a shock as it interacts with the ambient medium. As this process proceeds, the surroundings of the star are cleared and the UV radiation from the newly formed star can escape to illuminate a PDR. The intensity of the PDR emission is mainly determined by its spatial extent. As the material in the wide circumstellar environment is slowly cleared by the still strong stellar wind and

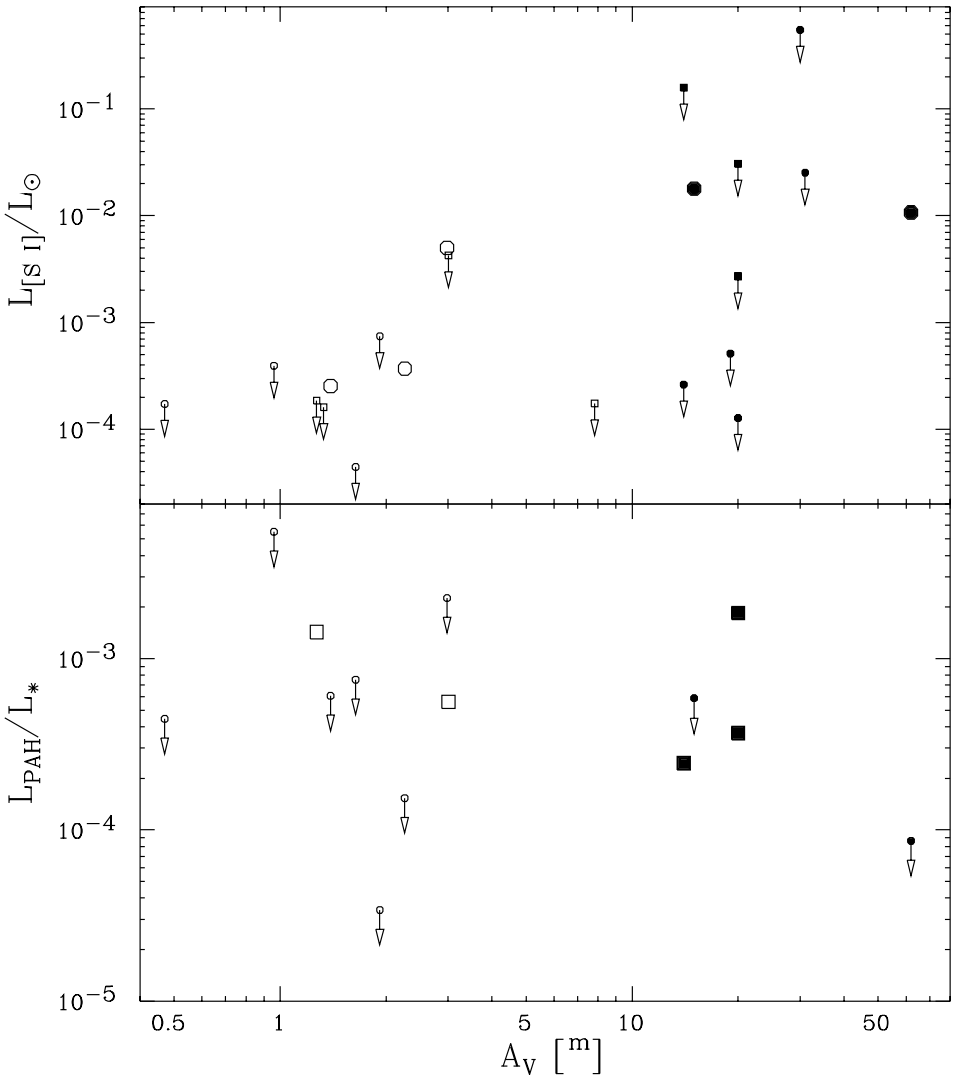

Fig. 10.8. Comparison of flux emitted in [S I] 25.3 μm (top) and 6.2 μm PAH band (bottom) with estimated visual extinction towards the associated source. Plot symbols have the same meaning as in Figs. 10.4–10.6.

the effect of photoevaporation, the extent of the PDR and hence the intensity of the PDR lines will gradually decrease until the only, weak, source of PDR emission will become the surface of a circumstellar disk, acting as a PDR (e.g. the case of HD 97048). With the tools presented in this chapter, the study of such PDRs offers the promise of a fundamental better understanding of the processes occurring in protoplanetary disks when far-infrared spectrographs with higher spatial resolution become available.

Acknowledgements. This chapter is based on observations with ISO, an ESA project with instruments funded by ESA Member States (especially the PI countries: France, Germany, the Netherlands and the United Kingdom) and with the participation of ISAS and NASA. The authors would like to thank the SWS and LWS IDTs for their help with the observations. Drs. David Hollenbach and Michael Kaufman are gratefully acknowledged for shocking discussions. This research has made use of the Simbad data base, operated at CDS, Strasbourg, France.

References

Anderson, I.M., Harju, J., Knee, L.B.G., Haikala, L.K. 1997, A&A 321, 575
Aspin, C., Rayner, J.T., McLean, I.S., Hayashi, S.S. 1990, MNRAS 246, 565
Aspin, C., Sandell, G., Weintraub, D.A. 1994, A&A 282, L25
Bailey, J. 1998, MNRAS 301, 161
Bakes, E.L.O., Tielens, A.G.G.M. 1994, ApJ 427, 822
Bakes, E.L.O., Tielens, A.G.G.M. 1998, ApJ 499, 258
Bally, J., Lane, A.J. 1982, ApJ 257, 612
Bibo, E.A., Thé, P.S., Dawanas, D.N. 1992, A&A 260, 293
Black, F.H., van Dishoeck. E.F. 1987, ApJ 322, 412
Brand, P.W.J.L., Moorhouse, A., Burton, M.G., Geballe, T.R., Bird, M., Wade, R. 1988, ApJ 334, L103
Burton, M.R., Geballe, T.R., Brand, P.W.J.L., Webster, A.S. 1988, MNRAS 231, 617
Burton, M.R., Brand, P.W.J.L., Geballe, T.R., Webster, A.S. 1989, MNRAS 236, 409
Burton, M.R., Geballe, T.R., Brand, P.W.J.L., Moorhouse, A. 1990a, ApJ 352, 625
Burton, M.R., Hollenbach, D.J., Haas, M.R., Erickson, E.F. 1990b, ApJ 355, 197
Burton, M.G., Hollenbach, D.J., Tielens, A.G.G.M. 1992a, ApJ 399, 563
Burton, M.G., Bulmer, M., Moorhouse, A., Geballe, T.R., Brand, P.W.J.L. 1992b, MNRAS 257, 1p
Canto, J., Sarmiento, A., Rodríguez, L.F. 1986, Rev. Mex. Astron. Astrofis. 13, 107
Carr, J.S. 1990, AJ 100, 1244
Casement, L.S., McLean, I.S. 1996, ApJ 462, 797
Cesarsky, D., Lequeux, J., Abergel, A., Perault, M., Palazzi, E., Madden, S., Tran D. 1996, A&A 315, L305
Chernoff, D.F., Hollenbach, D.J., McKee, C.F. 1982, ApJ 259, L97
Chokshi, A., Tielens, A.G.G.M., Werner, M.W., Castelaz, M.W. 1988, ApJ 334, 803
Clegg, P.E. et al. 1996, A&A 315, L38
Crampton, D., Fisher, W.A. 1974, Pub. Dom. Astrophys. Obs. 14, 283
Crawford, M.K., Lugten, J.B., Fitelson, W., Genzel, R., Melnick, G. 1986, ApJ 303, L57
Dabrowski, I. 1984, Canadian J. Phys. 62, 1639
Dame, T.M., Thaddeus, P. 1985, ApJ 297, 751
Davis, C.J., Moriarty-Schieven, G., Eislöffel, J., Hoare, M.G., Ray, T.P. 1998, AJ 115, 1118

Davis, C.J., Mundt, R., Eislöffel, J., Ray, T.P. 1995, AJ 110, 766
de Graauw, Th., Haser, L.N., Beintema, D.A., Roelfsema, P.R. et al. 1996, A&A 315, L49
Draine, B.T., Bertoldi, F. 1996, ApJ 468, 269
Edwards, S., Snell, R.L. 1982, ApJ 261, 151
Emery, R., Aannestad, P., Minchin, N. et al. 1996, A&A 315, L285
Finkenzeller, U., Mundt, R., 1984, A&AS 55, 109
Fluks, M.A., Plez, B., Thé, P.S., de Winter, D., Westerlund, B.E., Steenman, H.C. 1994, A&AS 105, 311
Friedemann, C., Reimann, H.G., Gürtler, J, Tóth, V. 1993, A&A 277, 184
Fuente, A., Martín-Pintado, J., Rodríguez-Fernández, N.J., Rodríguez-Franco, A., de Vicente, P., Kunze, D. 1999, A&A, in press
Gehrz, R.D., Grasdalen, G.L., Castelaz, M., Gullixson, C., Mozurkewich, D., Hackwell, J.A. 1982, ApJ 254, 550
Gerin, M., Phillips, T.G., Keene, J., Betz, A.L., Boreiko, R.T. 1998, ApJ 500, 329
Goetz, J.A., Pipher, J.L., Forrest, W.J. et al. 1998, ApJ 504, 359
Gómez, M., Whitney, B.A., Kenyon, S.J. 1997, AJ 114, 1138
Gray, R.O., Corbally, C.J. 1998, AJ 116, 2530
Grinin, V.P., Kozlova, O.V., Thé, P.S., Rostopchina, A.N. 1996, A&A 309, 470
Haas, M.R., Hollenbach, D.J., Erickson, E.F. 1986, ApJ 301, L57
Haas, M.R., Hollenbach, D.J., Erickson, E.F. 1991, ApJ 374, 555
Haas, M.R. 1997, personal communication
Haas, M.R., Leinert, C., Lenzen, R. 1992, A&A 261, 130
Haas, M.R., Leinert, C., Richichi, A. 1997, A&A 326, 1076
Habing, H.J. 1968, Bull. Astron. Inst. Netherlands 19, 421
Harju, J., Haikala, L.K., Mattila, K., Mauersberger, R., Booth, R.S., Nordh, H.L. 1993, A&A 278, 569
Hartigan, P., Carpenter, J.M., Dougados, C., Skrutskie, M.F. 1996, AJ 111, 1278
Harvey, P.M., Campbell, M.F., Hoffmann, W.F., Thronson, H.A., Gatley, I. 1979, ApJ 229, 990
Hasegawa, T., Gatley, I., Garden, R.P., Brand, P.W.J.L., Ohishi, M., Hayashi, M., Kaifu, N. 1987, ApJ 318, L77
Hayashi, M., Hasegawa, T., Gatley, I., Garden, R.P., Kaifu, N. 1985, MNRAS 215, 31p
Herbig, G.H., Jones, B.F. 1983, AJ 88, 1040
Hillenbrand, L.A., Strom, S.E., Vrba, F.J., Keene, J. 1992, ApJ 397, 613
Hillenbrand, L.A., Meyer, M.R., Strom, S.E., Skrutskie, M.F. 1995, AJ 109, 280
Hodapp, K.W., Rayner, J. 1991, AJ 102, 1108
Hogerheijde, M.R., van Dishoeck, E.F., Blake, G.A., van Langevelde, H.J. 1998, ApJ 502, 315
Hollenbach, D.J., McKee, C.F. 1989, ApJ 342, 306
Hollenbach, D.J., Tielens, A.G.G.M. 1999, Rev. Mod Phys. 71, 173
Hughes, J.D., Hartigan, P., Graham, J.A., Emerson, J.P., Marang, F. 1991, AJ 101, 1013
Hughes, V.A., Wouterloot, J.G.A. 1984, ApJ 276, 204
Jaffe, D.T., Genzel, R., Harris, A.I., Howe, J.E., Stacey, G.J., Stutzki, J. 1990, ApJ 353, 193
Kaufman, M.J., Neufeld, D.A. 1996, ApJ 456, 611
Keene, J., Masson, C.R. 1990, ApJ 355, 635
Kenyon, S.J., Brown, D.I., Tout, C.A., Berlind, P. 1998, AJ 115, 2491
Kenyon, S.J., Dobrzycka, D., Hartmann, L. 1994, AJ 108, 1872
Kenyon, S.J., Hartmann, L. 1995, ApJS 101, 117
Kessler, M.F., Steinz, J.A., Anderegg, M.E. et al. 1996, A&A 315, L27

Knee, L.B.G. 1992, A&A 259, 283
Kraemer, K.E., Jackson, J.M., Lane, A.P. 1998, ApJ 503, 785
Kurtz, D.W., Marang, F. 1995, MNRAS 276, 191
Kurucz, R.L. 1991, in *"Stellar atmospheres–Beyond classical models"* (eds. A.G. Davis Philip, A.R. Upgren, K.A. Janes), L. Davis press, Schenectady, New York, p. 441
Lada, C.J., Harvey, P.N. 1981, ApJ 245, 58
Lada, C.J., Thronson, H.A., Smith, H.A., Schwarz, P.R., Glaccum, W. 1984, ApJ 286, 302
Laureijs, R.J., Acosta-Pulido, J., Abraham, P., Kinkel, U., Klaas, U., Castaneda, H.O., Cornwall, L., Gabriel, C., Heinrichsen, I., Lemke, D., Pelz G., Schulz B., Walker, H.J. 1996, A&A 315, L313
Leech, K. et al. 1997, *"SWS Instrument Data Users Manual"*, Issue 3.1, SAI/95-221/Dc
Leibowitz, E.M., Danziger, I.J. 1983, MNRAS 204, 273
Lemaire, J.L., Field, D., Gerin, M., Leach, S., Pineau des Forêts, G., Rostas, F., Rouan, D. 1996, A&A 308, 895
Liseau, R., White, G.J., Larsson, B. et al. 1999, A&A 344, 342
Loushin, R., Crutcher, R.M., Bieging, J.H. 1990, ApJ 362, L67
Magnier, E.A., Volp, A.W., Laan, K., van den Ancker, M.E., Waters, L.B.F.M. 1999, A&A, to be submitted
Marconi, A., Testi, L., Natta, A., Walmsley, C.M. 1998, A&A 330, 696
Marconi, M., Palla, F. 1998, ApJ 507, L141
Marraco, H.G., Rydgren, A.E. 1981, AJ 86, 62
Martini, P., Sellgren, K., Hora, J.L. 1997, ApJ 484, 296
Mel'nikov, S.Y., Shevchenko, V.S., Grankin, K.N. 1995, Astron. Rep. 39, 42
Minchin, N.R., Hough, J.H., Burton, M.G., Yamashita, T. 1991, MNRAS 251, 522
Moriarty-Schieven, G.H., Wannier, P.G., Tamura, M., Keene, J. 1992, ApJ 400, 260
Mundt, R., Ray, T.P., Raga, A.C. 1991, A&A 252, 740
Myers, P.C., Heyer, M., Snell, R.L., Goldsmith, P.F. 1988, ApJ 324, 907
Neufeld, D.A., Melnick, G.J., Harwitt, M. 1998, ApJ 506, L75
Oliva, E., Moorwood, A.F.M., Danziger, I.J. 1990, A&A 240, 453
Oliva, E., Lutz, D., Drapatz, S., Moorwood, A.F.M. 1999a, A&A 341, L75
Oliva, E., Moorwood, A.F.M., Drapatz, S., Lutz, D., Sturm, E. 1999b, A&A 343, 943
Padgett, D.L., Brandner, W., Stapelfeldt, K.R., Strom, S.E., Terebey, S., Koerner, D. 1999, AJ 117, 1490
Palla, F., Stahler, S.W. 1993, ApJ 418, 414
Palla, F., Testi, L., Hunter, T.R., Taylor, G.B., Prusti, T., Felli, M., Natta, A., Stanga, R.M. 1995, A&A 293, 521
Parmar, P.S., Lacy, J.H., Achtermann, J.M. 1991, ApJ 372, L25
Parmar, P.S., Lacy, J.H., Achtermann, J.M. 1994, ApJ 430, 786
Poglitsch, A., Herrmann, F., Genzel, R., Madden, S.C., Nikola, T., Timmermann, R., Geis, N., Stacey, G.J. 1996, ApJ 462, L43
Prusti, T., Natta, A., Palla, F. 1994, A&A 292, 593
Rayner, J. 1994, in *"Infrared Astronomy with Arrays: The next generation"*, ed. I.S. McLean (Dordrecht: Kluwer), p. 185
Reipurth, B., Bally, J., Devine, D. 1997, AJ 114, 2708
Richter, M.J., Graham, J.R., Wright, G.S. 1995a, ApJ 454, 277
Richter, M.J., Graham, J.R., Wright, G.S., Kelly, D.M., Lacy, J.H. 1995b, ApJ 449, L83
Rodríguez, L.F., Moran, J.M., Ho, P.T.P., Gottlieb, E.W. 1980, ApJ 235, 845

Rogers, C., Heyer, M.H., Dewdney, P.E. 1995, ApJ 442, 694
Rydgren, A.E. 1980, AJ 85, 444
Schutte, W.A., Tielens, A.G.G.M., Allamandola, L.J., Cohen, M., Wooden, D.H. 1990, ApJ 360, 577
Shevchenko, V.S., Ibragimov, M.A., Chernysheva, T.L. 1991, Astron. Zh. 68, 466 (SvA 35, 229)
Siebenmorgen, R., Prusti, T., Krügel, E., Natta, A. 1997, in proc. *"First ISO Workshop on Analytical Spectroscopy"*, eds. A.M. Heras et al., ESA SP-419, p. 229
Siebenmorgen, R., Natta, A., Krügel, E., Prusti, T. 1998, A&A 339, 134
Snell, R.L., Loren, R.B., Plambeck, R.L. 1980, ApJ 239, L17
Snell, R.L., Scoville, N.Z., Sanders, D.B., Erickson, N.R. 1984, ApJ 284, 176
Stacey, G.J., Jaffe, D.T., Geis, N., Genzel, R., Harris, A.L., Poglitsch, A., Stutzki, J., Townes, C.H. 1993, ApJ 404, 219
Staude, H.J., Elsässer, H. 1993, A&A Rev. 5, 165
Stecklum, B., Feldt, M., Richichi, A., Calamai, G., Lagage, P.O. 1997, ApJ 479, 339
Steiman-Cameron, T.Y., Haas, M.R., Tielens, A.G.G.M., Burton, M.G. 1997, ApJ 478, 261
Tamura, M., Yamashita, T. 1992, ApJ 391, 710
Terebey, S., Vogel, S.N., Myers, P.C. 1989, ApJ 340, 472
Thé, P.S., Pérez, M.R., Voshchinnikov, N.V., van den Ancker, M.E. 1996, A&A 314, 233
Thé, P.S., Wesselius, P.R., Tjin A Djie, H.R.E., Steenman, H. 1986, A&A 155, 347
Tielens, A.G.G.M., Hollenbach, D.J. 1985, ApJ 291, 722
Timmermann, R., Bertoldi, F., Wright, C.M., Drapatz, S., Draine, B.T., Haser, L., Sternberg, A. 1996, A&A 315, L281
Tjin A Djie, H.R.E., Thé, P.S., Andersen, J., Nordstrom, B., Finkenzeller, U., Jankovics, I. 1989, A&AS 78, 1
Trams, N. et al. 1997, *"ISO-LWS Instrument Data Users Manual"*, Issue 5.0, SAI/95-219/Dc
Turner, J., Kirby-Docken, K., Dalgarno, A. 1977, ApJS 35, 281
van der Tak, F.F.S., van Dishoeck, E.F., Evans, N.J., Bakker, E.J., Blake, G.A. 1999, ApJ, in press
van Dishoeck, E.F., Jansen, D.J., Phillips, T.G. 1993, A&A 279, 541
van Langevelde, H.J., van Dishoeck, E.F., Blake, G.A. 1994, ApJ 425, L45
Voshchinnikov, N.V. 1981, Astron. Tsirk. 1200, 1
Ward-Thompson, D., Warren-Smith, R.F., Scarrott, S.M., Wolstencroft, R.D. 1985, MNRAS 215, 537
Warren, W.H., Hesser, J.E. 1978, ApJS 36, 497
Wenzel, W. 1980, Mitt. Ver. Sterne 8, 182
Wesselius, P.R., Beintema, D., Olnon, F.M. 1984, ApJ 278, L37
Whittet, D.C.B., Kirrane, T.M., Kilkenny, D., Oates, A.P., Watson, F.G., King, D.J. 1987, MNRAS 224, 497
Whittet, D.C.B., Prusti, T., Franco, G.A.P., Gerakines, P.A., Kilkenny, D., Larson, K.A., Wesselius, P.R. 1997, A&A 327, 1094
Wright, C.M., Drapatz, S., Timmermann, R., van der Werf, P.P., Katterloher, R., de Graauw, Th. 1996, A&A 315, L301
Yamashita, T., Sato, S., Suzuki, S., Hough, H.J., McLean, I., Garden, R., Gatley, I. 1987, A&A 177, 258
Yamashita, T., Murata, Y., Kawabe, R., Kaifu, N., Tamura, M. 1991, ApJ 373, 560
Yamashita, T., Tamura, M. 1992, ApJ 387, L93
Zinnecker, H., Preibisch, Th. 1994, A&A 292, 152

Chapter 11

Conclusions and Outlook

11.1 Introduction

In the previous chapters we recovered several well-known results from literature, as well as made new conclusions as to the intricacies of the star formation process and it implications for planet formation. In this concluding chapter we will briefly recapitulate the main results of this thesis, outline the new questions that these results have produced, and discuss the ways in which these problems may be solved in the future.

11.2 Herbig Ae/Be stars

In Chapters 2–5 we have studied the properties of Herbig Ae/Be stars (HAeBes) using a variety of techniques. In Chapter 2 we have studied the basic stellar properties of a small sample of HAeBes using newly obtained astrometric data from the *Hipparcos* mission, which allowed us, as the first ones, to compute the location of a sample of HAeBes in the Hertzsprung-Russell diagram without making any a priori assumptions about a physical association with a star forming region, as was necessary in all previous studies. The basic conclusion from this study, as well as the more extensive study done in Chapter 3, is that most HAeBes in our sample must indeed be pre-main sequence stars. This is an important basic conclusion, which has entered into most studies of HAeBes implicitly in the past, but is now rigorously proven. However, the sample of stars for which we were able to obtain reliable distance estimates in Chapters 2 and 3 has strong observational biases. Because the nearest site of the formation of massive stars, the Orion complex, is located too far away for the *Hipparcos* mission to yield a reliable parallax for individual stars, we only have a reliable distance estimate for one early B-type star, HD 200775, whose location in the HRD has proven to be somewhat deviant; it appears above the zero-age main sequence whereas such a behaviour would not be expected for a massive young star. With the present data we cannot decide whether this one star in our sample is representative of all Herbig Be stars. The development of a successor to the *Hipparcos* mission which would also be able to observe the parallaxes of the early-type HAeBes out to 2 kpc, such as currently

planned by the European Space Agency, would be a chance opportunity to investigate this question and put the stellar pre-main sequence evolutionary models for massive stars to a rigorous test. For now, we conclude that for masses up to 5 $M_{\odot}$, the basic stellar data and the models agree well.

In Chapters 2–5 we not only studied the Herbig Ae/Be stars themselves, but mainly focussed on the dust in their direct circumstellar environment. In Chapters 3 and 4 we studied this dust through its effect on the light of the central star as it moves in and out of our line of sight. We showed that such an effect can only be seen towards Herbig Ae/Be systems with a central star of spectral type A0 or later, which we explained as being due to the evolutionary effect that Herbig Be stars are not optically visible while still contracting towards the zero-age main sequence. The current view in literature of this effect of variable circumstellar extinction in Herbig Ae stars is that it is caused by patchy dust clouds located in the circumstellar disk. In this view, the presence of variable circumstellar extinction could be interpreted as a sign of seeing the system edge-on. However, in this thesis we have presented several facts that are hard to reconcile with such a scenario. The remarkable photometric behaviour of the Herbig Ae star V351 Ori, discussed in Chapter 4, seems to indicate that a large fraction of all Herbig Ae stars may be alternating between a state in which they do show evidence for variable circumstellar extinction and one in which they do not, whereas the total dust mass in the inner disk, as traced by the near-infrared excess, remains constant. This, as well as the lack of periodicities found in the photometric events and the lack of correlation of the stellar $v \sin i$ with level of photometric variability, discussed in Chapter 3, leads us to question the presence of patchy dust clouds located in a circumstellar disk as the cause of the variable circumstellar extinction. A more viable way of explaining this may be to think of the photometric events as being due to the passage and breaking-up of large comet-like bodies orbiting the system. These comet-like bodies, whose existence was already inferred from gas-phase absorption-line studies, need not be necessarily confined to the equatorial plane of the system and may explain all variable extinction phenomena discussed in this thesis. A study relating these two phenomena of gas-phase and dust absorption in HAeBes is badly needed and should be able to confirm or disprove our suggestion that the two have the same cause, infalling evaporating comet-like bodies, with relative ease.

Although the presence of patchy dust clouds moving in and out of our line of sight might be dubious, there is no question that a dusty circumstellar disk must be present in Herbig Ae/Be systems. This disk will be responsible for the excess emission seen at infrared wavelengths. Probably the central issue in the study of Herbig Ae/Be stars in the years to come will be how this circumstellar disk is transformed into a planetary system. In Chapter 2 we suggested a simple evolutionary scenario in which a gap is opened in the disk due to the formation of a large, possibly planet-like, body, after which the inner disk will gradually be accreted, either on the central star or on planet-like bodies, and only the outer disk will remain. There is no doubt that the formation of a planet will indeed cause the phenomena described above. However, a question which is still open is whether a dip in the spectral energy distribution around 10 μm, as we found for a number of stars in Chapter 2, can be equated to such a gap in the disk

or can also be caused by other phenomena such as optical depth effects on the disk's temperature structure. Further theoretical work on the structure of disks surrounding HAeBes should be able to give the answer to the latter question within the next few years and thus show whether the evolutionary scenario outlined in Chapter 2 remains viable. Observationally, the presence of disk gaps in the sources for which we found energy distribution dips around 10 μm can be tested when infrared instrumentation of higher angular resolution, such as the interferometer on ESO's *Very Large Telescope* (VLT), become available.

In Chapter 5 we looked in more detail at the thermal emission from dust in the disks of two comparable Herbig Ae systems, AB Aur and HD 163296, using data from the *Infrared Space Observatory* (ISO). We saw that in the dust in both these systems, significant grain growth has already occurred. However, the degree in which this has happened, as well as the degree in which the dust has crystallized, differs greatly between these two systems of identical mass and age. This conclusion should not come as a great surprise, since studies in the past have shown that for pre-main sequence stars in young clusters, the presence of a disk itself is poorly correlated with stellar age. Clearly other parameters than stellar mass and age determine the dissipation speed of a circumstellar disk. Further research to find out what these other parameters are (influence of the wide circumstellar environment? presence of low-mass, perhaps planetary, companions?) is clearly needed. Another, more unexpected, conclusion reached in Chapter 5 is that the processes of grain growth and crystallization are poorly correlated. We have only briefly investigated the causes of grain growth and crystallization in this thesis. Because the physical mechanisms behind these processes are still poorly understood, it remains unclear what the poor correlation noted in this thesis tells us about the physical processes occurring in the circumstellar disks of HAeBes. It also remains unclear what the better tracer of the evolutionary state of the disk is: grain growth or crystallization? In the next few years, the answers to these questions may come from new theoretical work. In the more distant future, more sensitive infrared spectrometers, such as those on board SIRTF and SOFIA, but also Vizier on the VLT, will open up the opportunity to investigate these questions by not only studying the dust composition of the infrared brightest HAeBes, as was possible with ISO, but also study the wealth of HAeBes in the Orion complex. These new instruments will also push the amount of thermal emission required to do these studies down, so it will also be possible to study the more evolved systems with less circumstellar dust and trace the evolutionary processes described in this thesis to a later stage in the formation of planetary systems.

Another way to study the amount and dissipation of dust around Herbig Ae/Be stars would be through submillimeter photometry. In Chapter 6 we have followed this approach to study the dust in the star forming region associated with the Herbig stars R and T CrA, using 450 and 850 μm maps obtained with the newly installed *Submillimeter Common User Bolometer Array* (SCUBA) at the JCMT. An important conclusion from this chapter is that extended emission is present throughout the region at both 450 and 850 μm. Our SCUBA maps do not show an enhanced intensity at the positions of the Herbig Ae/Be stars R CrA and T CrA, showing that their intrinsic submm flux must be smaller than previously thought. In Chapter 6 we did find six point-like submm

sources in the R CrA region. Two of these could not be identified with a near-infrared source, making them valid new candidates for Class 0 sources. In view of the small extent of the mapped region, this number of at least two is surprisingly high. This leads us to conclude that either Class 0 sources cannot be unambiguously identified with protostars, or that protostellar collapse must be slower than predicted by the models.

11.3 Emission line studies of star forming regions

In Chapters 7–10 we studied the infrared emission line spectra of a number of star forming regions using data obtained with the *Infrared Space Observatory*, and concluded that the infrared atomic fine structure lines and the molecular emission lines are dominated by emission from photodissociation regions (PDRs) and/or shocks. In Chapters 7–9 we looked in some detail at individual star forming regions, of different mass and age, whereas in Chapter 10 we focussed more on the physical processes occurring in the sample as a whole.

The most striking aspect of the environment of the two massive young stars studied in Chapter 7, S106 and Cep A East, is how different the two are in terms of the emission line spectrum and the solid-state absorption. We concluded that it is not possible to explain the differences between the two in terms of a different orientation and the differences must be understood in terms of evolution, in which Cep A East, with an emission line spectrum dominated by shocks, is the more embedded, younger, of the two, and S106, with an emission line spectrum caused by the combination of its H II region and the adjoining PDR, is a more evolved young star seen nearly edge-on. In fact, if we would have observed the S106 system at a smaller inclination angle, it might have appeared as the more massive counterpart of the Herbig Be star BD+40°4124, studied in Chapter 8. In this chapter we saw that this star may have produced a low-density H II region in its wide circumstellar environment, whereas smaller patchy clouds in its neighbourhood may have escaped photoionization and remain observable as a PDR today.

In Chapter 8 we have also studied two other YSOs in the BD+40°4124 region, the Herbig Ae star LkHα 224 and the embedded YSO LkHα 225. The most remarkable aspect of LkHα 224 is its smooth infrared spectrum, devoid of any solid-state features. If we compare this spectrum with the rich solid-state emission spectra of the Herbig Ae stars AB Aur and HD 163296, studied in Chapter 5, this featureless infrared spectrum is even more striking. In Chapter 8 we explained this absence of dust features in LkHα 224 as being due to the presence of an optically thick disk. Yet it remains unclear what the evolutionary connection between the disks of these three systems is. A systematic study of the infrared spectra of a larger sample of HAeBes using the newest generation of infrared spectrometers will very likely give new clues to the answer of this question.

Another important new result reached in Chapter 8 is based on the ISO spectra of the embedded YSO LkHα 225. The emission line spectrum of this source could be well explained as arising in a shock driven by its outflow. The molecular absorption line spectrum of this source remains puzzling, however. We found that the line of sight

towards this object sets a new record for the gas to solid ratios of CO_2 and H_2O. The CO_2 gas/solid ratio is at least a factor 100 higher than that found in any other line of sight so far. With the data presented in this thesis we were unable to infer whether this unexpected result is because the molecular core in which LkHα 225 is located is more evolved than that towards other sources, or that this core is heavily disrupted by its vicinity to BD+40°4124. The answer to this question is of potentially great importance, because if it is found that this system is located in the most evolved molecular core known to date, it holds the potential to further our knowledge of the poorly understood physical and chemical processes involved with core collapse. The answer may come within the near future by studying gas/solid ratio's in the line of sight towards weaker infrared sources in the vicinity of LkHα 225, for which ISO lacked both the sensitivity and spatial resolution, with an instrument like Vizier on the VLT.

Another approach to finding out the reason of the anomalous solid/gas ratio in the line of sight towards LkHα 225 would be to perform similar studies on seemingly similar systems. One of the classical young stellar objects, the binary system of T Tau studied in Chapter 9, might be a prime example. This system also serves to illustrate how complex and confused the surroundings of YSOs can be. We found that to explain the emission line spectrum observed with ISO, we needed at least three sources of H_2 emission, probably all of them shocked gas driven by outflows from the two components of T Tau. A not well understood phenomenon is why the two components of T Tau seem to have a different orientation, whereas they are obviously physically connected. To extend the analogy with the multiple system LkHα 225, it would be worthwhile to study the kinematics of the gas in this latter system in more detail as well, to see whether the same enigmatic non-parallel orientations also occur here and thus tell us something the formation history of these highly unusual young stellar systems.

The most rigorous test of our interpretation of infrared emission line spectra as arising in PDRs and shocks was done in Chapter 10. Here we used ISO to study the circumstellar environment of 10 embedded YSOs and 11 Herbig Ae/Be stars. We found that the distinction between PDRs and shocks can be made with relative ease using infrared spectroscopy using the presence of [S I] emission (indicative of the presence of a shock), strong [C II] emission (PDR) and PAH emission (PDR). Based on these results we suggested an evolutionary scenario in which the circumstellar material around a young star changes from being heated mechanically by shocks into heated by radiation from the central star through a PDR as the star clears its surroundings.

In Chapter 10 we also tested current models in literature for PDRs and shocks by comparing their predicted infrared emission-line spectra with those observed with ISO. Qualitatively, we found good agreement between the observed emission line spectrum and that predicted by PDR models. However, the models appear to underestimate the temperatures reached in the H_2 emitting region. The results presented here also confirm earlier suspicions that the commonly observed [O I] 63.2 μm line can suffer from self-absorption in many regions where it is observed and hence should be used with caution to constrain PDR model parameters.

For shocks we also found qualitative agreement between the observed emission line spectrum and that predicted by models. However, the H_2 emission invariably

seems to produce two thermal components, whereas the plane-parallel J- and C-shock models we used for comparison only predict one such component. This need for a two-component structure was also found from the analysis of the atomic infrared fine structure lines. Clearly the employed simple shock models are too simplified to be used for a quantitative analysis and models that correctly describe the two-dimensional structure of a shock are needed to explain our observations.

11.4 Concluding Remarks

As the results presented in this thesis have shown, the development of new astronomical instrumentation like the ISO and Hipparcos satellites has rapidly increased our knowledge of the processes leading to star formation. Although the new results invariably raise new questions, we have come closer to the solutions of old problems and mysteries. Progress in understanding our own origins has been made.

In the foreseeable future many new instruments will be developed to study the origins of planetary systems like our own. With these future developments, it seems likely that the rapid progression of our knowledge of young stars will continue and remain to make the field of star formation one of the most exciting in astrophysics for decades to come.

Nederlandse Samenvatting

Sterren worden gevormd uit grote wolken van stof en gas die in de interstellaire ruimte voorkomen. Zo'n wolk stort uiteindelijk onder de invloed van zijn eigen zwaartekracht in elkaar tot het een bol van gas (het stof verdampt of blijft rond de ster zitten) heeft gevormd waarin in de kern de druk zo hoog is opgelopen dat waterstof in helium kan worden omgezet: een ster. Als een ster net gevormd is, bevindt zich rond de jonge ster nog materie uit de oorspronkelijke wolk. Dit proefschrift gaat over waarnemingen van dit circumstellaire materiaal (gas en stof) rond jonge sterren. Het is van belang om dit te bestuderen omdat we denken dat uit dit materiaal uiteindelijk planetenstelsels rondom andere sterren worden gevormd en we op deze manier wellicht te weten kunnen komen of die andere planetenstelsels lijken op het onze of juist helemaal niet en we ook meer kunnen leren over hoe ons eigen zonnestelsel is gevormd. In deze Nederlandse samenvatting zal ik proberen op ook voor leken begrijpelijke wijze uit te leggen wat we hierover hebben geleerd door middel van het onderzoek wat ik de afgelopen vier jaar heb gedaan.

Dit proefschrift is voornamelijk gebaseerd op waarnemingen gedaan met twee satellieten van de Europese ruimtevaartoganisatie ESA, *Hipparcos* en het infrarood ruimteobservatorium, *ISO*. De eerstgenoemde satelliet was in staat om heel nauwkeurig de posities van sterren aan de hemel te meten. Omdat de aarde om de zon draait, lijkt het of alle sterren aan de hemel elk jaar een klein stukje heen en weer bewegen als je ze vanaf de aarde of een satelliet als *Hipparcos* die om de aarde heen draait bekijkt. De grootte van die beweging, de zogenaamde parallax, vertelt je hoe ver zo'n ster van ons verwijderd is. In Hoofdstuk 2 en 3 van dit proefschrift heb ik deze parallaxgegevens van een aantal Herbig Ae/Be sterren, massieve jonge sterren die voor het eerst bestudeerd zijn door de Amerikaanse astronoom George Herbig in de jaren zestig, en de gegevens over de helderheid van deze sterren die *Hipparcos* ook opleverde geanalyseerd. Hieruit blijkt dat als je hun gemeten helderheid corrigeert voor afstand, Herbig Ae/Be sterren helderder zijn dan sterren van gelijke temperatuur die niet zo jong meer zijn. Dit is een resultaat wat ook verwacht werd omdat we denken dat deze jonge sterren nog aan het samentrekken zijn. Ze zijn dus nog groter dan de oudere sterren en omdat ze een groter stralend oppervlak hebben zijn de ook helderder. Nu kunnen we dus stellen dat de helderheid van een jonge ster, in combinatie met de tem-

peratuur van de ster, een maat is voor hoe oud zo'n ster is en in Hoofdstuk 2 en 3 zijn van een aantal sterren leeftijden bepaald. Nu was van deze sterren al bekend dat ze ook nog een schijf bestaande uit stof en gas om zich heen hebben. Het stof in zo'n schijf wordt verwarmd door de centrale ster, en begint dan infrarood- of warmtestraling uit te zenden. Door de bestaande gegevens over de infraroodstraling van de bestudeerde jonge sterren te combineren met de nieuw bepaalde leeftijden, kon ik in Hoofdstuk 2 laten zien dat er op een gegeven moment in de evolutie van een jonge ster eerst minder infraroodstraling met een golflengte rond 10 μm lijkt te worden geproduceerd, waarna ook infraroodstraling van kortere golflengte afneemt. Dit kan verklaard worden door aan te nemen dat bepaalde stukken uit de schijf lijken te verdwijnen, bijvoorbeeld doordat in dit gedeelte van de schijf zich een planeet heeft gevormd.

In Hoofstuk 3 heb ik ook beter gekeken naar de helderheid van de Herbig Ae/Be sterren die door de *Hipparcos* satelliet zijn gemeten. Het blijkt dat van meer dan 65% de helderheid niet constant is, maar variaties vertoont. Verder bleek dat grote variaties alleen voorkomen bij relatief koele sterren. Deze grote variaties worden waarschijnlijk veroorzaakt door grote wolken van stof die zich in en uit onze gezichtslijn naar de ster bewegen en daardoor het licht van de ster verzwakken. Tot nu toe werd gedacht dat deze stofwolken zich in de schijf rond de ster bevinden. In Hoofdstuk 3 toon ik aan dat dit effect alleen het al dan niet voorkomen van die variaties in helderheid niet kan verklaren. In Hoofstuk 4 kijk ik in meer detail naar de variaties in helderheid van één jonge ster, V351 Ori, gebruik makend van waarnemingen die gedurende 10 jaar zijn vergaard op de Europese Zuidelijke Sterrenwacht (ESO) in Chili. Het blijkt dat dit object gedurende de tijd dat wij hem hebben waargenomen veranderd is van een ster die wel grote variaties in helderheid vertoont in een ster die vrijwel constant is, terwijl de hoeveelheid infraroodstraling die we van deze ster ontvangen in de tussentijd niet veranderd is. Ook dit gedrag valt moeilijk te verklaren met obscuratie van sterlicht door de stofwolken in de schijf rondom de ster.

Hoofstuk 5 is het eerste hoofdstuk in dit proefschrift waar we waarnemingen analyseren gedaan met *ISO*. Deze satelliet is gebouwd om voor het eerst nauwkeurig de hoeveelheid infraroodstraling die we ontvangen van objecten aan de hemel als functie van golflengte te kunnen meten. Dit kan niet vanaf de aarde gebeuren omdat de dampkring een groot gedeelte van deze straling blokkeert. In Hoofstuk 5 analyseer ik met behulp van *ISO* gegevens het stof in de schijf rond twee jonge sterren, AB Aur en HD 163296. Volgens de met *Hipparcos* uitgevoerde studie in Hoofdstuk 2 en 3 zouden deze twee sterren als twee druppels water op elkaar moeten lijken. We vinden echter dat het stof rond AB Aur bestaat uit silicaten, ijzer-oxide en polycyclische aromatische koolwaterstoffen (PAHs), hele kleine koolstofrijke stofdeeltjes, terwijl het stof rond HD 163296 bestaat uit silicaten, ijzer-oxide en ijs. Verder vinden we dat de silicaten in AB Aur een amorfe (de atomen zijn niet netjes geordend in een rooster) structuur hebben, terwijl een klein gedeelte van de silicaten in HD 163296 uit kristallen bestaat. Ook blijken de stofdeeltjes rond HD 163296 gemiddeld veel groter te zijn dan die rond AB Aur. Het blijkt dus dat de leeftijd en massa van de centrale ster (die voor deze beide sterren gelijk is) ons niet alles verteld over wat er is gebeurd met de stofdeeltjes in de schijf. Ook blijkt dat de processen van kristallisatie en de groei van stofdeeltjes,

waarvan we denken dat die ook in ons eigen zonnestelsel hebben plaatsgevonden toen het nog jong was, niet noodzakelijkerwijs gekoppeld zijn.

In Hoofstuk 6 analyseer ik veel kouder stof op een plek waarvan we denken dat er op dit moment sterren worden gevormd, het R CrA gebied, met behulp van kaarten die ik op een golflengte van 450, 800 en 850 μm van dit gebied heb gemaakt met behulp van de *James Clerk Maxwell Telescope* (JCMT) op Hawaii. Het blijkt dat het hele gebied straalt op deze hele lange golflengtes, waar we naar heel erg koud stof zitten te kijken. Er zijn echter ook minimaal zes compacte bronnen, waarschijnlijk jonge sterren, in het gebied die veel helderder stralen bij deze lange golflengtes. Daarvan zijn er zeker twee niet zichtbaar in het optisch of infrarood. Normaal gesproken worden deze bronnen die alleen bij heel erg lange golflengtes zichtbaar zijn geïdentificeerd met heel erg jonge sterren waarvan de vormende wolk nog bezig is in te storten. In het R CrA gebied vind ik echter minimaal twee van deze bronnen, wat uitermate onwaarschijnlijk zou moeten zijn omdat het ineenstorten volgens de theorie heel erg snel zou moeten gaan. Of de door de theorie voorspelde tijdschaal, of de identificatie van de alleen bij lange golflengtes zichtbare bronnen met zich vormende sterren moet dus onjuist zijn.

In de hoofstukken 7 tot 10 keren we terug naar infrarood waarnemingen gedaan door de *ISO* satelliet, maar nu kijken we naar infrarood straling van gas rondom jonge sterren in plaats van emissie door stofdeeltjes. Het onderscheid tussen beide vormen van emissie is eenvoudig te maken omdat stof op vrijwel alle infraroodgolflengtes straalt, terwijl gas alleen maar straalt op scherp bepaalde golflengtes (een foton wordt door een atoom uitgezonden als een electron "van plaats veranderd", en de quantumfysica leert ons dat dat niet willekeurig kan gebeuren, maar altijd in bepaalde stapjes, waardoor de energie, en dus de golflengte, van het foton ook maar bepaalde waarden aan kan nemen). Om infrarood straling van gas waar te kunnen nemen met de instrumenten aan boord van *ISO* moet het gas een temperatuur bereiken van enkele honderden graden boven het absolute nulpunt. We kunnen drie mechanismen bedenken waardoor het geval zou kunnen zijn. Allereerst kunnen de energierijke fotonen van een hete ster electronen uit hun atoom bevrijden, waarna ze weer met andere deeltjes kunnen botsen en op die manier het gas verwarmen. Omdat de atomen in zo'n H II gebied een gedeelte van hun electronen verliezen, krijgen ze een negatieve elektrische lading, of worden ze geïonisserd.

Een tweede mogelijkheid om een gebied in de ruimte tot enkele honderden graden te verwarmen is door middel van het fotoelektrisch effect: Als een atoom door licht wordt beschenen dat volgens de klassieke natuurkunde niet genoeg energie per foton bevat om een electron los te maken, voorspelt de quantumfysica dat er een kans is dat dit toch gebeurd. Dit fotoelektrisch effect is van belang omdat vrijwel al het gas in de interstellaire ruimte bestaat uit de elementen waterstof en helium. Alle fotonen die genoeg energie bezitten om waterstof te ioniseren zullen dus bijdragen aan de vorming aan een H II gebied en niet kunnen ontsnappen. Fotonen met minder energie kunnen het H II gebied echter ongestoord passeren, maar via het fotoelektrisch effect toch bijdragen aan de verwarming van het gas in het fotodissociatie-gebied (PDR) daarbuiten.

Een derde mogelijkheid om gas in de interstellaire ruimte te verwarmen is door middel van een schok. Jonge sterren winnen niet alleen massa door inval van materie

uit hun schijf, maar ze verliezen ook materie die via de polen van het stersysteem terug de ruimte wordt ingeblazen. Als deze sterk samengeperste "wind" met hoge snelheid (tot enkele honderden kilometers per seconde) op de omringende materie botst, kan ook deze materie worden verwarmd en zo lijnstraling in het infrarood produceren.

In Hoofdstuk 7 heb ik de *ISO* spectra van twee zware jonge sterren, S106 en Cep A Oost, vergeleken en er bleek dat deze twee objecten een heel verschillend emissielijnspectrum en heel veschillende absorpties door vaste stoffen vertonen. Het emisielijnspectrum van S106 bleek te kunnen worden verklaard door een model voor een H II gebied en een PDR, terwijl dat van Cep A Oost gedomineerd wordt door schokken. De verschillen tussen deze twee jonge systemen kunnen eigenlijk niet verklaard worden door aan te nemen dat we ze onder verschillende hoeken zien, maar kunnen alleen verklaard worden door aan te nemen dat het ene systeem, Cep A Oost, jonger is dan het andere en uiteindelijk zal evolueren in een systeem dat lijkt op S106. Het systeem S106 zou mogelijk net zo geëvolueerd kunnen zijn als dat van de minder massieve jonge ster BD+40°4124, bestudeerd in Hoofdstuk 8.

In Hoofdstuk 8 heb ik ook twee andere systemen in hetzelfde stervormingsgebied als BD+40°4124 bestudeerd, de Herbig Ae ster LkHα 224 en het ingebedde jonge object LkHα 225. Het emissielijn-spectrum van LkHα 225 kan goed worden verklaard als veroorzaakt door geschokt gas. Het absorptiespectrum van deze ster is echter raadselachtig. De verhouding van het gas in CO_2 en H_2O tot het ijs in deze stoffen is veel hoger dan ooit in enige andere gezichtslijn is gevonden. Het zou kunnen dat de wolk waarin LkHα 225 zich bevindt veel warmer is, en daarom meer geëvolueerd, dan andere wolken. Een andere verklaring is dat de nabijheid van de massieve, hete jonge ster BD+40°4124 de buitenlagen van de wolk, waar zich het koudste materiaal bevindt, heeft verwijderd. Met de huidige gegevens kunnen we niet concluderen welke verklaring de juiste is, maar dit is een dusdanig belangwekkende ontdekking dat deze vraag in de toekomst zeker moet worden onderzocht.

In Hoofstuk 9 heb ik het infrarode spectrum van waarschijnlijk de meest bekende jonge ster aan de hemel, T Tauri, bestudeerd. Hieruit leidde ik af dat in dit jong systeem, waarvan al bekend was dat het uit een dubbelster-systeem bestaat, er twee bronnen van geschokt gas moeten zijn. Het blijkt dus dat waarschijnlijk beide sterren in het T Tauri systeem een uitstroom van materie vertonen die vervolgens een schok veroorzaken als ze in aanraking komen met het omringende materiaal.

In Hoofdstuk 10 tenslotte bestudeer in de *ISO* spectra van een grotere groep jonge sterren. Ik vind hier dat we met de drie hierboven beschreven fenomenen, H II gebieden, PDRs en geschokt gas, elk spectrum kwalitatief goed kunnen verklaren. Quantitatief echter lijken modelberekeningen de temperaturen die bereikt worden in PDRs en geschokt gas te onderschatten. Het onderscheid tussen gebieden gedomineerd door PDRs en schokken, tot nu toe problematisch, blijkt met behulp van de *ISO* gegevens eenvoudig te maken. Met behulp hiervan suggereer ik in Hoofdstuk 10 een evolutionair scenario waarin het infrarood spectrum van jonge sterren eerst gedomineerd wordt door geschokt gas, waarna als de ster z'n omgeving schoonveegt het PDR dicht bij de ster zichtbaar wordt en het spectrum gedomineerd wordt door straling van het PDR.

Dankwoord

Dit proefschrift had niet tot stand kunnen komen zonder de steun van vele mensen. Allereerst wil ik mijn ouders en de rest van mijn familie bedanken voor alle liefde, steun en aanmoediging die ze me de afgelopen 30 jaar hebben gegeven. Verder gaat mijn dank uit naar mijn promotor, Xander Tielens, voor vele inspirerende gesprekken en e-mails, zijn schier onuitputtelijke geduld met mijn persoontje gedurende de afgelopen drie jaar en niet te vergeten zijn fantastische kijk op de dingen, zowel binnen als buiten de sterrenkunde. Tevens ben ik eeuwige dank verschuldigd aan mijn co-promotor, Rens Waters, voor de vele discussies, gesprekken, aanwijzingen en niet te vergeten het af en toe betalen van een rekening.

Het proefschrift dat hier ligt is voornamelijk gebaseerd op gegevens vergaard met twee satellieten van de Europese Ruimtevaartorganisatie ESA, *Hipparcos* en *ISO*. Zonder het voorbereidende werk en de vooruitziende blik van Pik-Sin Thé, Herman Tjin A Djie, Christoffel Waelkens en Paul Wesselius had ik niet over deze gegevens kunnen beschikken en had dit proefschrift niet geschreven kunnen worden. Aan de analyse en verwerking van de gegevens die in dit proefschrift zijn gepresenteerd hebben ook vele mensen bijgedragen of me de weg gewezen. Met name de co-auteurs van de verschillende artikelen die als hoofdstukken in dit proefschrift zijn verwerkt zijn een niet aflatende bron van inspiratie, steun, kennis en een volle INBOX geweest: Claude Catala, Dolf de Winter, Ewine van Dishoeck, Göran Sandell, Herman Tjin A Djie, Jeroen Bouwman, Luigi Spinoglio, Paul Wesselius, Peter Blondel, Pik-Sin Thé, Rens Waters, Sean Dougherty en Xander Tielens: bedankt voor de hulp!

Verder wil ik natuurlijk iedereen op het Anton Pannekoek Instituut bedanken voor het creëren van een geweldige sfeer en werkomgeving en niet te vergeten voor alle taart. In het bijzonder wil ik alle leden en ex-leden van het "circus Rens" bedanken voor hun steun, koekjes, brownies, taart, ijs, thee en aanverwante zaken. Alex, Ciska, Issei, Jacco, Jan, Jeroen, Frank, Pat, Peer, Robert, Sacha: bedankt. Ik zal jullie missen! Ook Arjan Volp en Finne Fortuin, het dynamische duo studenten dat ik het afgelopen jaar hier heb mogen begeleiden, worden bij deze bedankt. Ik vond het in ieder geval heel erg leuk, en ik hoop dat jullie er uiteindelijk ook zo over denken. O ja, en Marc: nog bedankt voor de moorkoppen. Ze waren lekker!

Een apart woord van dank is er voor mijn paranimf, en kamergenoot op het sterrenkundig instituut, Frank Molster. Hoewel ik eigenlijk niet goed weet of ik je hier

nu moet gaan bedanken voor de (als ik het goed heb uitgerekend, tenminste) 2000 uur die we samen afgekletst hebben, de 1500 mokken thee die je voor me hebt gehaald, de 750 keer dat je m'n sleutelnummer hebt doorgebeld en de 3 uur die ik naar je CD's en bandjes heb mogen luisteren. Ok, dan in ieder geval bedankt voor de vele wetenschappelijke discussies, de fysieke verdediging bij de promotie en het me op de hoogte houden van alle instituuts-roddels! Ook mijn andere paraminf, en grote broer, Ron van den Ancker, wil ik hierbij hartelijk bedanken. Zo zie je waar het overhoren van je kleine broertje over de kaart van de planeten uit de jeugd-encyclopedie nog toe kan leiden!

Dit dankwoord zou niet compleet zijn zonder iemand te bedanken die voor mijn start in de jonge-sterren business heel belangrijk is geweest, en wiens visie op de sterrenkunde en het leven in het algemeen ik bijzonder op prijs stel. Dolf, als jij me niet besmet had met het onderzoeks-virus, had m'n leven er nu waarschijnlijk heel anders uitgezien! Bedankt voor je steun, vriendschap en de bijna dagelijkse e-mails. Muchas gracias, Dolfito!

Een belangrijk "dank-je-wel" is er ook voor de organisaties die me de afgelopen jaren van financiële middelen hebben voorzien. In mijn levensonderhoud is in deze periode voorzien door NWO beurzen 781.76.015 en 614.41.003 aan Ewine van Dishoeck en een NWO *Pionier* beurs aan Rens Waters. Voor het mogelijk maken van het vele gereis dank ik het Leids Kerkhoven-Bosscha Fonds (LKBF), het Shell Reisfonds voor promovendi, de Stichting Ruimte Onderzoek Nederland (SRON), de Europese Zuidelijke Sterrenwacht (ESO) en NASA Ames Research Center.

Tenslotte wil ik iedereen bedanken die ik vergeten ben te noemen in het bovenstaande dankwoord. Mijn eeuwige excuses dat ik je ben vergeten! Het ligt niet aan jou, maar aan mijn vergeetachtigheid!